JYU DISSERTATIONS 188

Faluke Aikebaier

New Forms of Superconductivity

UNIVERSITY OF JYVÄSKYLÄ
FACULTY OF MATHEMATICS
AND SCIENCE

JYU DISSERTATIONS 188

Faluke Aikebaier

New Forms of Superconductivity

Esitetään Jyväskylän yliopiston matemaattis-luonnontieteellisen tiedekunnan suostumuksella julkisesti tarkastettavaksi yliopiston Ylistönrinteen salissa FYS1 tammikuun 31. päivänä 2020 kello 12.

Academic dissertation to be publicly discussed, by permission of the Faculty of Mathematics and Science of the University of Jyväskylä, in Ylistönrinne, auditorium FYS1, on January 31, 2020 at 12 o'clock noon.

JYVÄSKYLÄN YLIOPISTO
UNIVERSITY OF JYVÄSKYLÄ

JYVÄSKYLÄ 2020

Editors
Timo Sajavaara
Department of Physics, University of Jyväskylä
Timo Hautala
Open Science Centre, University of Jyväskylä

Permanent link to this publication: http://urn.fi/URN:ISBN:978-951-39-8036-8

ISBN 978-951-39-8036-8 (PDF)
URN:ISBN:978-951-39-8036-8
ISSN 2489-9003 Jyväskylä University Printing House, Jyväskylä 2020

Preface

This thesis is based on my research work carried out in the condensed matter theory group lead by Professor Tero Heikkilä, in the Department of Physics and Nanoscience Center at the University of Jyväskylä, Finland.

This work is an outcome of fruitful and pleasant stay in the beautiful city of Jyväskylä, with the guidance and companionship of many people.

First and foremost, I would like to express my deepest gratitude to my supervisor Professor Tero Heikkilä. I am very grateful to him for giving me the chance to start a career in theoretical condensed matter physics. It was a joy to learn and carry out research in his group. I am indebted to Tero's guidance, patience, and continuous support both at work and in life.

Besides my supervisor, I am obliged to my coauthors, Dr. Ville Kauppila, Dr. Mihail Silaev, Dr. Pauli Virtanen, Dr. Subrata Chakraborty, Mr. Mikel Rouco, Dr. Vitaly Golovach, Dr. Elia Strambini, Dr. Jagadeesh Moodera, Dr. Francesco Giazotto, and Dr. Sebastian Bergeret. I would like to acknowledge the reviewers, Dr. Irina Bobkova and Dr. Mircea Trif. I am also thankful to the wonderful colleagues that I had over the years, Dr. Philippe Djorwé, Mr. Souvik Agasti, Dr. Timo Hyart, Mr. Teemu Peltonen, Mr. Risto Ojajärvi, Mr. Kalle Kansanen, and Dr. Yao Lu.

In addition, I would like to extent my appreciation to the kind help and friendship of Katri, Eskimo, and others during our stay in Jyväskylä.

Importantly, I offer my sincerest thanks to my parents for their support and love during all these years. I would like to express my warmest thanks to my wife, Kadirya. Without her support and love, life would be much difficult. I am genuinely thankful for her sacrifice and the support of my parents in law over the years. Last but not least, I would like to thank my son, Fazil, he has always been my best motivation.

The financial support of Ellen and Artturi Nyyssönen Foundation is greatly acknowledged.

Helsinki, January, 2020

Faluke Aikebaier

Abstract

Flat band superconductivity in strained Dirac materials and transport properties of superconductors with a spin-splitting field are studied in this thesis.

Flat band superconductivity is a route to high temperature superconductivity. Strain induced flat band in Dirac materials provides a new mechanism to the flat band superconductivity. Superconductors with a spin-splitting field reveal novel features which do not exist or very small in non spin-split superconductors, for example, long-range spin accumulation and thermoelectric effects. Exploring other effects is beneficial for understanding the transport phenomena in such systems.

For the flat band superconductivity in strained Dirac materials, the Bogoliubov-de Gennes equation is used to study the properties of the strained Dirac materials in the superconducting state, including the inhomogeneous pair potential, local density of states and a finite supercurrent.

For the superconductors with a spin-splitting field, quasiclassical Green's function method is used to study the transport properties of such systems. The properties studied in this thesis include those in equilibrium and out of equilibrium. The non-collinearity of the spin-splitting fields between two spin-split superconductors introduces new features to the tunnelling conductance and gives rise to a finite Josephson current in the absence of external voltage. In the presence of a supercurrent, the short-range charge imbalance is converted to long-range spin accumulation in the presence of a homogeneous spin-splitting field. The inhomogeneous spin-splitting field alters many physical observables, such as the spin current density, domain wall size, and density of states. As a precursor to the domain wall motion in a superconductor with an inhomogeneous spin-splitting field, the domain wall motion in a diffusive weak ferromagnet reveals characteristic features like time dependent domain wall velocity for the force much larger than the torque, and occurring of the intrinsic pinning eventually for the torque much larger then the force.

The study on flat band superconductivity in strained Dirac materials show how this model results an inhomogeneous superconductivity, including its various properties. The study on the transport properties of superconductors with a spin-splitting field, by considering the effect of supercurrent, noncollinearity and inhomogeneity of the spin-splitting fields, fill many gaps in the previous research.

Author's address Faluke Aikebaier
Department of Physics and Nanoscience Center
University of Jyväskylä
Finland

Supervisors Professor Tero Heikkilä
Department of Physics and Nanoscience Center
University of Jyväskylä
Finland

Reviewers Dr Irina Bobkova
Institute of Solid State Physics
Russian Academy of Sciences
Russia

Dr Mircea Trif
MagTop, Institute of Physics
Polish Academy of Sciences
Poland

Opponent Dr Manuel Houzet
NAC and PHELIQS
CEA and Grenoble Alpes University
France

List of Publications

I V. J. Kauppila, F. Aikebaier, T. T. Heikkilä, *Flat Band Superconductivity in Strained Dirac Materials*, Phys. Rev B. 93. 214505 (2016)

II M. Rouco, S. Chakraborty, F. Aikebaier, V. N. Golovach, E. Strambini, J. S. Moodera, F. Giazotto, T. T. Heikkilä, and F. S. Bergeret, *Charge Transport through Spin-Polarized Tunnel Junction between Two Spin-Split Superconductors*, Phys. Rev. B 100, 184501 (2019)

III Faluke Aikebaier, Mihail A. Silaev, T. T. Heikkilä, *Supercurrent Induced Charge-Spin Conversion in Spin-Split Superconductors*, Phys. Rev. B 98, 024516 (2018)

IV Faluke Aikebaier, P. Virtanen, T. T. Heikkilä, *Superconductivity near a Magnetic Domain Wall*, Phys. Rev. B 99, 104504 (2019)

V Faluke Aikebaier, T. T. Heikkilä, *Domain Wall Motion in a Diffusive Weak Ferromagnet*, submitted

The author has derived all the formulas, carried out all the analytical and numerical calculations, and wrote most of the article in Article III and V. The author has derived most of the formulas, carried out all the analytical and numerical calculations, and wrote most of the article in Article IV. In Article I and II, the author participated in deriving the formulas and carrying out the analytical and numerical calculations.

Contents

1 Introduction **1**

2 Fundamental concepts **3**
2.1 Fundamentals of superconductivity . . . 3
2.1.1 BCS theory . . . 3
2.1.2 Properties of superconductors . . . 8
2.2 Fundamentals of ferromagnetism . . . 15
2.2.1 Models of ferromagnetism . . . 15
2.2.2 Domain structure . . . 17

3 Flat band superconductivity in strained Dirac materials **22**
3.1 Flat band superconductivity . . . 22
3.2 Strained Dirac materials . . . 23
3.3 Bogoliubov-de Gennes equation . . . 25
3.4 Superconducting state . . . 26

4 Superconductors with a spin-splitting field **29**
4.1 Spin-splitting in superconductors . . . 29
4.2 Quasiclassical Green's function approach . . . 32
4.2.1 Quasiclassical approximation . . . 32
4.2.2 Diffusive limit . . . 34
4.2.3 Matsubara technique . . . 35
4.2.4 Keldysh technique . . . 36
4.3 Homogeneous magnetization . . . 39
4.3.1 Effects in equilibrium . . . 40
4.3.2 Effects out of equilibrium . . . 47
4.4 Inhomogeneous magnetization . . . 52
4.4.1 Effects in equilibrium . . . 54
4.4.2 Effects out of equilibrium . . . 57

5 Domain wall motion in a diffusive weak ferromagnet **59**
5.1 Theory of Domain wall motion in brief . . . 59
5.2 Spin accumulation in a weak ferromagnet . . . 61
5.3 Force and torque . . . 63
5.4 Domain wall dynamics . . . 64

6 Summary & Outlook **68**

Appendix A: Kinetic Coefficients **71**

Appendix B: Numerical methods **73**
B.1 Self-consistent calculations 73
B.2 Boundary value problem 74
B.3 Other numerical methods 76

1 Introduction

Superconductivity is a fascinating quantum phenomenon. Below a critical temperature, many metals and alloys suddenly lose their electrical resistivity [1], and expel magnetic fields from their interior (Meissner effect) [2].

Following the phenomenological theories [3, 4] based on electromagnetic and thermodynamic properties respectively, a successful microscopic theory of superconductivity was laid by Bardeen, Cooper, and Schrieffer in 1957 [5], later commonly called the BCS theory. Since then, superconductivity has gone through huge development and has thrived as a field with many theoretical and applied aspects.

These aspects include searching for new superconducting materials, especially superconductors with higher critical temperatures, various properties of superconductors, nonequilibrium superconductivity, and new features of superconductors making contact with nonsuperconducting materials, as well as their immediate and potential applications in technology.

This thesis focuses on two rapidly evolved aspects, flat band superconductivity and superconductors with a spin-splitting field, which could be considered as new forms of superconductivity.

Ever since the discovery of superconductors, the attempt on searching for high temperature superconductors has never stopped. Flat band superconductors pave a new way on such efforts. Flat band superconductors are a type of superconductors with flat energy bands in the normal state around the Fermi level, which causes a very high density of states. Since the electrons around the Fermi level form bound pairs (Cooper pairs) and condense into the superconducting state below the critical temperature, a high density of states around the Fermi level indicates a stronger superconductivity, and according to the BCS theory, a stronger superconductivity implies a higher critical temperature.

Another long-standing struggle is the combination of superconductivity and ferromagnetism. This combination could be achieved in hybrid nanostructures via mutual proximity effects. In the case of a superconductor and a ferromagnetic insulator, properties of the superconductor are modified by an induced spin-splitting field. One significant feature of such superconductors is the spin splitting of the density of states. This type of superconductors have very interesting properties, like thermoelectric ef-

fects and long-range spin accumulations, which are very small or absent without the spin-splitting field.

In this thesis, the discussion on flat band superconductivity is centred on strained Dirac materials, and the discussion on the superconductors with a spin-splitting field covers their properties both in equilibrium and out of equilibrium, together with homogeneous and inhomogeneous spin-splitting fields. The outline of the thesis is as follows. In chapter 2, some fundamental properties of superconductivity and ferromagnetism are introduced. These properties are related to the discussions in the rest of the thesis. The flat band superconductivity in strained Dirac materials, including various properties are discussed in chapter 3. Transport properties of superconductors with a spin-splitting field are discussed in chapter 4. In this section, the equilibrium and nonequilibrium properties are separately discussed, both in the cases of homogeneous and inhomogeneous spin-splitting fields. As a nonequilibrium problem in the case of an inhomogeneous spin-splitting field in the normal state, domain wall motion in a weak ferromagnet is discussed independently in chapter 5. In chapter 6, the main results in this thesis and an outlook for the future work are shortly described.

2 Fundamental concepts

Before starting the discussions on the new forms of superconductivity, it is worthwhile to review the fundamental properties of superconductivity and ferromagnetism. In this chapter some of these properties are introduced. For superconductivity, the discussions start by the key concepts of the BCS theory, and review some of the basic features of superconductivity. For ferromagnetism, the Heisenberg and Stoner models are introduced briefly, and the domain structure of ferromagnet including the formation of the domain walls are discussed.

2.1 Fundamentals of superconductivity

2.1.1 BCS theory

The free electron model is successful in describing many properties of metals, but it fails to explain some others, especially at low temperatures. To go beyond the free electron model, we need to take into account the correlations between electrons. In electrostatics, the direct interaction (Coulomb interaction) between electrons is repulsive. However, in certain conditions the effective interaction between electrons could be attractive. For example, the phonon mediated electron-electron interaction [5]. The BCS theory starts from such an effective attraction between electrons.

The BCS theory does not concern the origin of the attractive interaction, which can overcome the Coulomb repulsion, but rather the consequence of it. It is also assumed such an attractive interaction takes place for electrons within an energy range. This range for the phonon-mediated interaction is the phonon energy (Debye energy), $\hbar\omega_D$ (BCS cutoff energy) [5]. Through this interaction, no matter how weak it is, electrons in the ground state pair themselves into bound pairs around the Fermi level, known as Cooper pairs, which can condense into a superconducting state.

For many low temperature superconductors, the attractive interaction is spin-independent, which leads to spin-singlet superconductivity. This thesis considers such superconductors. Moreover, if the interaction is weak compared to both the Fermi energy and phonon energy, then it can be represented as a point-like interaction. Then the

Hamiltonian of a system with an attractive interaction can be written as

$$H = \sum_{\sigma} \int d\boldsymbol{r} \psi_{\sigma}^{\dagger}(\boldsymbol{r}) H_0(\boldsymbol{r}) \psi_{\sigma}(\boldsymbol{r}) - g \int d\boldsymbol{r} \psi_{\uparrow}^{\dagger}(\boldsymbol{r}) \psi_{\downarrow}^{\dagger}(\boldsymbol{r}) \psi_{\downarrow}(\boldsymbol{r}) \psi_{\uparrow}(\boldsymbol{r}), \tag{2.1}$$

where

$$H_0(\boldsymbol{r}) = \frac{1}{2m} \left(\frac{\hbar}{i} \nabla - e\mathbf{A} \right)^2 + U(\boldsymbol{r}) - \epsilon_F$$

is the single-particle Hamiltonian of the free electron gas, $\mathbf{A}$ is the vector potential, $U(\boldsymbol{r})$ is a potential describing deviations from a regular crystal lattice caused by, for example, disorder, and ϵ_F is the Fermi energy. Here $\psi_{\sigma}^{(\dagger)}(\boldsymbol{r})$ is the second quantized field operator which annihilates (creates) an electron at position $\boldsymbol{r}$, and g characterizes the strength of the attractive interaction.

The theoretical approach for the treatment of the interacting part of the Hamiltonian in Eq. (2.1) in the BCS theory is the mean field approximation. This means that one could replace product of operators as $AB \approx \langle A \rangle B + A \langle B \rangle - \langle A \rangle \langle B \rangle$. By choosing $A = \psi_{\uparrow}^{\dagger}(\boldsymbol{r}) \psi_{\downarrow}^{\dagger}(\boldsymbol{r})$ and $B = \psi_{\downarrow}(\boldsymbol{r}) \psi_{\uparrow}(\boldsymbol{r})$, the Hamiltonian in Eq. (2.1) can be written as

$$H_{\mathrm{BCS}} \approx \sum_{\sigma} \int d\boldsymbol{r} \psi_{\sigma}^{\dagger}(\boldsymbol{r}) H_0(\boldsymbol{r}) \psi_{\sigma}(\boldsymbol{r}) + \int d\boldsymbol{r} \left[\Delta^*(\boldsymbol{r}) \psi_{\downarrow}(\boldsymbol{r}) \psi_{\uparrow}(\boldsymbol{r}) + \Delta(\boldsymbol{r}) \psi_{\uparrow}^{\dagger}(\boldsymbol{r}) \psi_{\downarrow}^{\dagger}(\boldsymbol{r}) \right] - E_0, \tag{2.2}$$

where the superconducting pair potential is defined as

$$\Delta(\boldsymbol{r}) = g \langle \psi_{\uparrow}(\boldsymbol{r}) \psi_{\downarrow}(\boldsymbol{r}) \rangle, \tag{2.3}$$

and

$$E_0 = \int d\boldsymbol{r} \frac{|\Delta(\boldsymbol{r})|^2}{g}$$

describes the energy difference between the normal and superconducting states.

We can use the Bogoliubov transformation to diagonalize the mean-field Hamiltonian. The field operators can be written in terms of fermionic annihilation and creation operators $\gamma_{\boldsymbol{k}\sigma}^{(\dagger)}$ (Bogoliubov operators) as

$$\psi_{\uparrow}(\boldsymbol{r}) = \sum_{\boldsymbol{k}} \left[\gamma_{\boldsymbol{k}\uparrow} u_{\boldsymbol{k}}(\boldsymbol{r}) - \gamma_{\boldsymbol{k}\downarrow}^{\dagger} v_{\boldsymbol{k}}^*(\boldsymbol{r}) \right] \tag{2.4a}$$

$$\psi_{\downarrow}(\boldsymbol{r}) = \sum_{\boldsymbol{k}} \left[\gamma_{\boldsymbol{k}\downarrow} u_{\boldsymbol{k}}(\boldsymbol{r}) + \gamma_{\boldsymbol{k}\uparrow}^{\dagger} v_{\boldsymbol{k}}^*(\boldsymbol{r}) \right], \tag{2.4b}$$

where $\gamma_{\boldsymbol{k}\sigma}^{(\dagger)}$ annihilates (creates) a particle in state $\boldsymbol{k}$ with spin σ. They satisfy the fermionic anticommutation relations

$$\{ \gamma_{\boldsymbol{k}\sigma}, \gamma_{\boldsymbol{k}'\sigma'}^{\dagger} \} = \delta_{\boldsymbol{k}\boldsymbol{k}'} \delta_{\sigma\sigma'},$$

$$\{\gamma^{(\dagger)}_{\boldsymbol{k}\sigma}, \gamma^{(\dagger)}_{\boldsymbol{k}'\sigma'}\} = 0.$$

It is also easy to show that the coefficients $u_{\boldsymbol{k}}(\boldsymbol{r})$ and $v_{\boldsymbol{k}}(\boldsymbol{r})$ satisfy

$$\sum_{\boldsymbol{k}} [u_{\boldsymbol{k}}(\boldsymbol{r}')u^*_{\boldsymbol{k}}(\boldsymbol{r}) + v_{\boldsymbol{k}}(\boldsymbol{r})v^*_{\boldsymbol{k}}(\boldsymbol{r}')] = \delta(\boldsymbol{r} - \boldsymbol{r}').$$

The Bogoliubov transformation leads to the Bogoliubov-de Gennes (BdG) equation

$$\begin{pmatrix} H_0(\boldsymbol{r}) & \Delta(\boldsymbol{r}) \\ \Delta^*(\boldsymbol{r}) & -H_0^\dagger(\boldsymbol{r}) \end{pmatrix} \begin{pmatrix} u_{\boldsymbol{k}}(\boldsymbol{r}) \\ v_{\boldsymbol{k}}(\boldsymbol{r}) \end{pmatrix} = \epsilon_{\boldsymbol{k}} \begin{pmatrix} u_{\boldsymbol{k}}(\boldsymbol{r}) \\ v_{\boldsymbol{k}}(\boldsymbol{r}) \end{pmatrix}. \tag{2.5}$$

In the normal state, this is nothing but the Schrödinger equation for electrons and holes. Therefore, the Bogoliubov-de Gennes equation is a correspondence of the Schrödinger equation in the superconducting state.

Substituting the field operators in Eq. (2.4) to the expressions of the pair potential in Eq. (2.3), and remembering the fact that

$$\langle \gamma^{(\dagger)}_{\boldsymbol{k}\sigma} \gamma^{(\dagger)}_{\boldsymbol{k}'\sigma'} \rangle = 0$$

$$\langle \gamma^\dagger_{\boldsymbol{k}\sigma} \gamma_{\boldsymbol{k}'\sigma'} \rangle = \delta_{\boldsymbol{k}\boldsymbol{k}'}\delta_{\sigma\sigma'} f(\epsilon_{\boldsymbol{k}}),$$

where $f(\epsilon_{\boldsymbol{k}})$ is the Fermi distribution function

$$f(\epsilon_{\boldsymbol{k}}) = \frac{1}{e^{\epsilon_{\boldsymbol{k}}/(k_B T)} + 1}, \tag{2.7}$$

we can write

$$\Delta(\boldsymbol{r}) = g \sum_{\boldsymbol{k}} v^*_{\boldsymbol{k}}(\boldsymbol{r}) u_{\boldsymbol{k}}(\boldsymbol{r}) \tanh\left(\frac{\epsilon_{\boldsymbol{k}}}{2k_B T}\right). \tag{2.8}$$

We can see that the solutions of the Bogoliubov-de Gennes equation depend on the superconducting pair potential $\Delta(\boldsymbol{r})$, and $\Delta(\boldsymbol{r})$ also depends on them. This means $\Delta(\boldsymbol{r})$ has to be determined self-consistently.

The Bogoliubov-de Gennes equation can be solved for the case of a homogeneous pair potential $\Delta(\mathbf{r}) = \Delta$. By assuming $u_{\boldsymbol{k}}(\boldsymbol{r}) = u^0_{\boldsymbol{k}} e^{i\boldsymbol{k}\cdot\boldsymbol{r}}$ and $v_{\boldsymbol{k}}(\boldsymbol{r}) = v^0_{\boldsymbol{k}} e^{i\boldsymbol{k}\cdot\boldsymbol{r}}$ the results are

$$\epsilon_{\boldsymbol{k}} = \pm\sqrt{\xi^2_{\boldsymbol{k}} + \Delta^2} \tag{2.9}$$

and

$$u^0_{\boldsymbol{k}} = \frac{1}{\sqrt{2}}\sqrt{1 + \frac{\xi_{\boldsymbol{k}}}{\epsilon_{\boldsymbol{k}}}} \tag{2.10a}$$

$$v^0_{\boldsymbol{k}} = \frac{1}{\sqrt{2}}\sqrt{1 - \frac{\xi_{\boldsymbol{k}}}{\epsilon_{\boldsymbol{k}}}}, \tag{2.10b}$$

where $\xi_{\boldsymbol{k}} = \hbar^2\boldsymbol{k}^2/(2m) - \epsilon_F$ is the normal state energy. Here Eq. (2.9) gives the energy spectrum of the superconducting state. We can also determine the density of states as

$$N_s(\epsilon) = N_0 \frac{|\epsilon|}{\sqrt{\epsilon^2 - \Delta^2}} \Theta(|\epsilon| - \Delta), \tag{2.11}$$

where $N_0 = mk_F/(2\pi^2\hbar^2)$ is the density of states at the Fermi level, and $\Theta(x)$ is the Heaviside step function. The energy spectrum in Eq. (2.9) and the density of states in Eq. (2.11) are plotted in Fig. 2.1(a,b). We can see the energy gap in the spectrum is $E_g = 2\Delta$ and the BCS divergence at $\epsilon = \pm\Delta$.

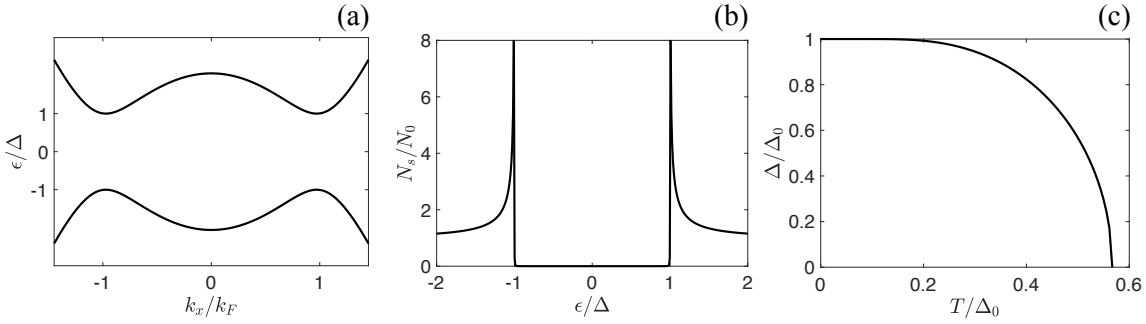

Figure 2.1: (a) BCS energy spectrum of one direction in momenta k_x. The spectrum is the same in other directions in an isotropic system. (b) Density of states of a bulk superconductor. (c) Temperature dependence of the superconducting pair potential.

Substituting the results in Eq. (2.10) to Eq. (2.8), and using the relations

$$\sum_{\boldsymbol{k}} \to \int \frac{\hbar d\boldsymbol{k}}{(2\pi\hbar)^3} = 2N_0 \int_0^{E_c} d\xi_{\boldsymbol{k}} \tag{2.12}$$

obtain

$$\Delta = \frac{g}{2(2\pi)^3} \int d\boldsymbol{k} \frac{\Delta}{\sqrt{\xi_{\boldsymbol{k}}^2 + \Delta^2}} \tanh\left(\frac{\epsilon_{\boldsymbol{k}}}{2k_BT}\right) \tag{2.13}$$

$$\Rightarrow 1 = \gamma \int_\Delta^{E_c} \frac{d\epsilon_{\boldsymbol{k}}}{\sqrt{\epsilon_{\boldsymbol{k}}^2 - \Delta^2}} \tanh\left(\frac{\epsilon_{\boldsymbol{k}}}{2k_BT}\right), \tag{2.14}$$

where $\gamma = gN_0$ is the interaction constant, and $E_c = \hbar\omega_D$ is the phonon energy.

Equation (2.14) gives the temperature dependence of the superconducting pair potential and the critical temperature T_c. The numerical result is given in Fig. 2.1(c). At zero temperature it can be solved analytically. In this case, $\tanh[\epsilon/(2k_BT)] \to 1$, and we get

$$\frac{1}{\gamma} = \int_\Delta^{E_c} \frac{d\epsilon_{\boldsymbol{k}}}{\sqrt{\epsilon_{\boldsymbol{k}}^2 - \Delta^2}} = \log\left(\frac{2E_c}{\Delta}\right).$$

We denote $\Delta(T=0)=\Delta_0$, and obtain

$$\Delta_0 = 2E_c e^{-1/\gamma}.$$

On the other hand, at $T=T_c$ the pair potential $\Delta=0$, and we have

$$\frac{1}{\gamma} = \int_0^{E_c} \tanh\left(\frac{\epsilon_{\boldsymbol{k}}}{2k_BT_c}\right)\frac{d\epsilon_{\boldsymbol{k}}}{\epsilon_{\boldsymbol{k}}}.$$

This can be solved as

$$k_BT_c = \frac{2e^C}{\pi}E_c e^{-1/\gamma},$$

where $C=0.577$ is the Euler constant. Then the zero temperature pair potential can be written as

$$\Delta_0 = \pi e^{-C}T_c \approx 1.764 k_BT_c. \tag{2.15}$$

This is one of the best well known predictions of the BCS theory. It relates the critical temperature to the superconducting pair potential at zero temperature, and most of the conventional superconductors satisfy this relation at least approximately.

The pair potential at zero temperature Δ_0 is also related to the spatial range of the Cooper pairs, called the superconducting coherence length, usually denoted by ξ_0. The BCS theory also gives an estimate to this length, which is

$$\xi_0^{\text{clean}} = \frac{\hbar v_F}{\pi\Delta_0}, \tag{2.16}$$

where v_F is the Fermi velocity. This result is for clean superconductors, namely, when the coherence length ξ_0 is much smaller than the electron mean free path l_{el}. For the opposite limit $\xi_0 \gg l_{el}$, the coherence length is given by

$$\xi_0^{\text{dirty}} = \sqrt{\frac{\hbar D}{2\Delta_0}}, \tag{2.17}$$

where $D=v_F l_{el}/3$ is the diffusion constant.

The coherence length is usually of the order of 10^3 nanometers, which is much larger than the atomic scale. Therefore, one Cooper pair is in the center of many others (millions or even more). This long range nature of the Cooper pairs is an important characteristic of the superconducting state.

The above are some of the most essential features of superconductivity. There are also many other properties, which can be explained by the BCS theory. In the next section, we present some of the properties relevant to this thesis.

2.1.2 Properties of superconductors

Magnetic properties

A superconductor reacts in peculiar ways to a magnetic field. For example, it expels a magnetic field from its interior below its critical temperature (Meissner effect) [2].

Early phenomenological London theory was able to explain the Meissner effect [3]. A magnetic field decays in a superconductor exponentially in a length λ_L, called the London penetration depth. The BCS theory calculated this depth as [5]

$$\lambda_L = \sqrt{\frac{m_e}{\mu_0 n_s e^2}}, \tag{2.18}$$

where m_e is the mass of an electron, e is the charge of the electron, μ_0 is the vacuum permeability, and n_s is the superconducting electron density.

A magnetic field could also destroy the superconductivity. The BCS theory also determined such a critical magnetic field. For a bulk superconductor, the critical field is given by the (Helmholtz) free energy density difference between the normal and superconducting phases. From the Gibbs free energy density in the presence of a magnetic field, we can write

$$\frac{H_c^2}{2\mu_0} = f_n - f_s,$$

where f_i is the free energy density for $i = n, s$ normal and superconducting states, respectively. For a homogeneous superconductor [5]

$$\begin{aligned} f_s &= -4N_0 \int_0^\infty d\xi_{\boldsymbol{k}} \epsilon_{\boldsymbol{k}} f(\epsilon_{\boldsymbol{k}}) + 2N_0 \int_0^{E_c} d\xi_{\boldsymbol{k}} \left(\xi_{\boldsymbol{k}} - \frac{\xi_{\boldsymbol{k}}^2}{\epsilon_{\boldsymbol{k}}} \right) - \frac{\Delta^2}{g}, \\ &= -2N_0 \int_\Delta^\infty d\epsilon_{\boldsymbol{k}} \frac{2\epsilon_{\boldsymbol{k}}^2 - \Delta^2}{\sqrt{\epsilon_{\boldsymbol{k}}^2 - \Delta^2}} f(\epsilon_{\boldsymbol{k}}) - \frac{1}{2}\Delta^2 N_0. \end{aligned}$$

Equation (2.14) is used in the second equal sign. The normal state free energy density can be obtained by setting $\Delta = 0$ as

$$f_n = -4N_0 \int_0^\infty d\xi_{\boldsymbol{k}} \xi_{\boldsymbol{k}} f(\xi_{\boldsymbol{k}}) = -\frac{\pi^2}{3} N_0 (k_B T)^2.$$

Then the critical field is determined by

$$\frac{H_c^2}{2\mu_0} = -\frac{\pi^2}{3} N_0 (k_B T)^2 + 2N_0 \int_\Delta^\infty d\epsilon_{\boldsymbol{k}} \frac{2\epsilon_{\boldsymbol{k}} - \Delta^2}{\sqrt{\epsilon_{\boldsymbol{k}}^2 - \Delta^2}} f(\epsilon_{\boldsymbol{k}}) + \frac{1}{2}\Delta^2 N_0. \tag{2.19}$$

The critical field calculated from Eq. (2.19) is plotted in Fig. 2.2(a). Here the critical field is normalized to the critical field at zero temperature

$$\frac{H_c^2(T=0)}{2\mu_0} = \frac{1}{2}\Delta_0^2 N_0 \;\Rightarrow\; H_c^0 = \sqrt{\mu_0 N_0}\Delta_0.$$

Superconductors with the above critical field are called type I superconductors. There are also type II superconductors which have two critical fields. The most important characteristic of such superconductors is the formation of magnetic vortices between the lower and upper critical fields [6]. In this thesis, we only consider type I superconductors.

For thin film superconductors, a perpendicular magnetic field also creates magnetic vortices. But a parallel magnetic field enhances the critical field compared to that of the bulk in type I superconductors [7]. For thin films with thickness less than the London penetration depth in Eq. (2.18), the Meissner effect is negligible. In this case, the critical field of a superconductor is determined by the normal state paramagnetism [8, 9]. This is shortly discussed in Sec. 4.1.

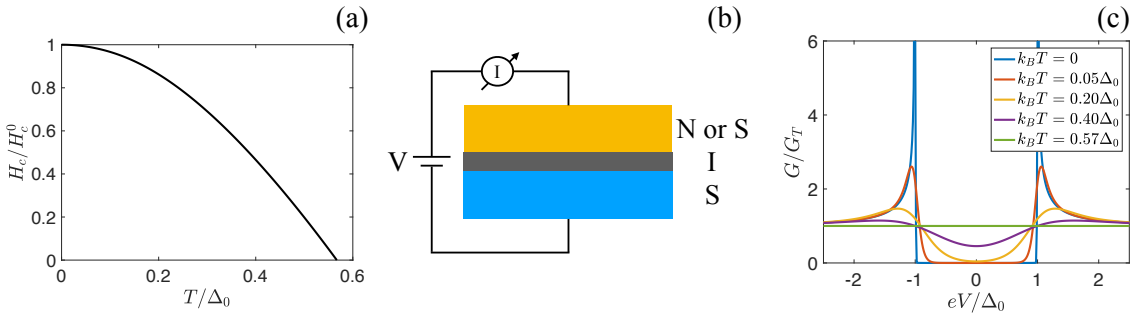

Figure 2.2: (a) Temperature dependence of the critical field. (b) Schematics of the normal metal (superconductor)-insulator-superconductor junction. (c) Tunnelling conductance of the NIS junction.

Tunnelling

Tunnelling is a quantum mechanical phenomenon where a particle passes through a potential barrier. If two metals are separated by a thin insulator, electrons can pass through from one metal to the other when a voltage difference is applied, and the current-voltage relation obeys the Ohm's low.

If one of the metals is replaced by a superconductor [Fig. 2.2(b)], due to the existence of the superconducting gap, no quasiparticles pass through unless the voltage reaches a threshold value equal to the superconducting pair potential [10]. Therefore, the energy

gaps in superconductors can be measured by normal metal-insulator-superconductor (NIS) junctions.

The (quasiparticle) tunnelling current for a NIS junction can be expressed as [11]

$$I(V) = \frac{G_T}{e} \int_{-\infty}^{+\infty} d\epsilon N_s(\epsilon) \left[f(\epsilon - eV) - f(\epsilon) \right], \tag{2.20}$$

where V is the applied voltage, eV is the resulting difference in the chemical potentials between the superconductor and normal metal, G_T is the conductance of the tunnelling barrier, and $f(\epsilon)$ is the Fermi distribution function in Eq. (2.7).

Another quantity for measuring the energy gap is the tunnelling conductance. Differentiating the tunnelling current with respect to the applied voltage V yields

$$G = \frac{dI}{dV} = G_T \int_{-\infty}^{+\infty} d\epsilon N_s(\epsilon) \frac{\partial f(\epsilon - eV)}{\partial (eV)}. \tag{2.21}$$

The tunnelling conductance for different temperatures is plotted in Fig. 2.2(c). It looks very much like the superconducting density of states, especially at low temperatures. This can be seen as follows. The derivative of the Fermi distribution function in the integrand can be written as

$$\frac{\partial f(\epsilon - eV)}{\partial (eV)} = \frac{1}{4k_B T} \mathrm{sech}^2 \left(\frac{\epsilon - eV}{2k_B T} \right). \tag{2.22}$$

This is a a Bell-shaped function of ϵ peaked at eV with a width $4k_BT$. For $T \to 0$, it is equivalent to a Dirac delta function. Then we have

$$\frac{G}{G_T} \xrightarrow{T \to 0} N_s(e|V|).$$

Therefore, the tunnelling conductance can also be used to measure the density of states directly at a low temperature.

In Sec. 4.3.1 the tunnelling conductance is calculated for junctions of a superconductor with a spin-splitting field with a normal metal (NIS) and a ferromagnet (FIS). In the case for a FIS junction, the expression for the tunnelling current in Eq. (2.20) is extended to include the polarization of the ferromagnet. In Article II, the expression of the tunnelling conductance is derived for a SIS junction, where both of the superconductors are with spin-splitting fields.

Supercurrent

The Cooper pairs are effectively bosons, and they condense into a Bose condensate with a wave function

$$\Psi = |\Psi| e^{i\varphi}, \tag{2.23}$$

where the amplitude determines the particle density $n_s/2 = |\Psi|^2$, and the phase φ characterizes the coherence of the Cooper pairs since a single wave function represents all the pairs. Similarly, we can introduce a phase to the superconducting pair potential as

$$\Delta(\boldsymbol{r}) = |\Delta(\boldsymbol{r})|e^{i\varphi(\boldsymbol{r})}.$$

The expression of the current in quantum mechanics in terms of the wave function is given by

$$\boldsymbol{j} = \frac{e^*}{2m^*}\left(\Psi^*\hat{\boldsymbol{p}}\Psi + \Psi\hat{\boldsymbol{p}}^\dagger\Psi^*\right),$$

where $e^* = 2e$, $m^* = 2m_e$ for Cooper pairs, and $\hat{\boldsymbol{p}}$ is the momentum operator. For charged particles $\hat{\boldsymbol{p}} = -i\hbar\nabla - e^*\boldsymbol{A}/c$, where c is the speed of light and $\boldsymbol{A}$ is the vector potential. Using Eq. (2.23), the current becomes

$$\boldsymbol{j} = -\frac{e^2 n_s}{m_e c}\left(\boldsymbol{A} - \frac{\hbar c}{2e}\nabla\varphi\right). \tag{2.24}$$

If the total vector potential $\boldsymbol{A}^t = \boldsymbol{A} - \hbar c\nabla\varphi/(2e)$ in Eq. (2.24) is strong in a superconductor, the magnetic field associated with $\boldsymbol{A}^t$ may reach the critical field and destroy superconductivity. The related current in this case is called the critical current.

In the absence of a magnetic field

$$\boldsymbol{j}_s = \frac{e n_s \hbar}{2m_e}\nabla\varphi. \tag{2.25}$$

This means that a supercurrent appears when the condensed wave function (through its phase) slowly changes in space.

The Cooper pair density n_s can be found from a detailed calculation. With the field operators, the supercurrent can be expressed as

$$\boldsymbol{j}_s = \frac{e}{2m_e}\sum_\sigma \langle\psi_\sigma^\dagger(\boldsymbol{r})\hat{\boldsymbol{p}}\psi_\sigma(\boldsymbol{r}) + \psi_\sigma(\boldsymbol{r})\hat{\boldsymbol{p}}^\dagger\psi_\sigma^\dagger(\boldsymbol{r})\rangle.$$

Using the Bogoliubov transformation in Eq. (2.4), $\boldsymbol{j}_s$ becomes

$$\boldsymbol{j}_s = \frac{e}{m_e}\sum_{\boldsymbol{k}}\{f(\epsilon_{\boldsymbol{k}})u_{\boldsymbol{k}}^*(\boldsymbol{r})\hat{\boldsymbol{p}}u_{\boldsymbol{k}}(\boldsymbol{r}) + [1 - f(\epsilon_{\boldsymbol{k}})]\, v_{\boldsymbol{k}}(\boldsymbol{r})\hat{\boldsymbol{p}}v_{\boldsymbol{k}}^*(\boldsymbol{r}) + \text{c.c.}\}. \tag{2.26}$$

If the position dependence of the pair potential is only via the phase, namely,

$$\Delta(\boldsymbol{r}) = \Delta e^{i\varphi(\boldsymbol{r})},$$

then the BdG equation can be solved with the ansatz $u_{\boldsymbol{k}}(\boldsymbol{r}) = u_{\boldsymbol{k}}^0 e^{i\boldsymbol{k}\cdot\boldsymbol{r}}e^{i\varphi/2}$ and $v_{\boldsymbol{k}}(\boldsymbol{r}) = v_{\boldsymbol{k}}^0 e^{i\boldsymbol{k}\cdot\boldsymbol{r}}e^{-i\varphi/2}$ as

$$\epsilon_{\boldsymbol{k}}^s = \pm\sqrt{\left[\xi_{\boldsymbol{k}} + \frac{\hbar^2(\nabla\varphi)^2}{8m_e}\right]^2 + \Delta^2} + \frac{\hbar^2\boldsymbol{k}\cdot\nabla\varphi}{2m_e}.$$

For a slowly varying phase in space

$$\epsilon_{\boldsymbol{k}}^{s} \simeq \pm\sqrt{\xi_{\boldsymbol{k}}^{2}+\Delta^{2}} + \frac{\hbar^{2}\boldsymbol{k}\cdot\nabla\varphi}{2m_{e}} = \epsilon_{\boldsymbol{k}} + \frac{\hbar^{2}\boldsymbol{k}\cdot\nabla\varphi}{2m_{e}}.$$

Now the supercurrent becomes

$$\begin{aligned}\boldsymbol{j}_{s} =& \frac{e\hbar}{m_{e}}\sum_{\boldsymbol{k}}\{f(\epsilon_{\boldsymbol{k}}^{s})|u_{\boldsymbol{k}}^{0}|^{2} + [1-f(\epsilon_{\boldsymbol{k}}^{s})]\,|v_{\boldsymbol{k}}^{0}|^{2}\}(\nabla\varphi) \\ & - \frac{2e\hbar}{m_{e}}\sum_{\boldsymbol{k}}\boldsymbol{k}\{f(\epsilon_{\boldsymbol{k}}^{s})|u_{k}^{0}|^{2} - [1-f(\epsilon_{\boldsymbol{k}}^{s})]\,|v_{\boldsymbol{k}}^{0}|^{2}\}.\end{aligned} \tag{2.27}$$

By adding and subtracting terms with $f(\epsilon_{\boldsymbol{k}})$, we can rewrite the above expression as

$$\boldsymbol{j}_{s} = \frac{e\hbar}{m_{e}}\sum_{\boldsymbol{k}}\{f(\epsilon_{\boldsymbol{k}})|u_{\boldsymbol{k}}^{0}|^{2}+[1-f(\epsilon_{\boldsymbol{k}})]\,|v_{\boldsymbol{k}}^{0}|^{2}\}\nabla\varphi+\frac{e\hbar}{m_{e}}\sum_{\boldsymbol{k}}[f(\epsilon_{\boldsymbol{k}}^{s})-f(\epsilon_{\boldsymbol{k}})]\,(|u_{\boldsymbol{k}}^{0}|^{2}-|v_{\boldsymbol{k}}^{0}|^{2})\nabla\varphi$$

$$-\frac{2e\hbar}{m_{e}}\sum_{\boldsymbol{k}}\boldsymbol{k}\{f(\epsilon_{\boldsymbol{k}})|u_{k}^{0}|^{2} - [1-f(\epsilon_{\boldsymbol{k}})]\,|v_{\boldsymbol{k}}^{0}|^{2}\} - \frac{2e\hbar}{m_{e}}\sum_{\boldsymbol{k}}\boldsymbol{k}\,[f(\epsilon_{\boldsymbol{k}}^{s})-f(\epsilon_{\boldsymbol{k}})]\,(|u_{\boldsymbol{k}}^{0}|^{2}+|v_{\boldsymbol{k}}^{0}|^{2})$$

In the above expression, the second term vanishes since $|u_{\boldsymbol{k}}^{0}|^{2}-|v_{\boldsymbol{k}}^{0}|^{2}$ is an odd function of $\xi_{\boldsymbol{k}}$ and the third term is zero since $\boldsymbol{k}$ sums up with plus and minus sign. We define the total electron density and normal electron density as

$$n = \langle\psi_{\sigma}^{\dagger}(\boldsymbol{r})\psi_{\sigma}(\boldsymbol{r})\rangle = 2\sum_{\boldsymbol{k}}\{f(\epsilon_{\boldsymbol{k}})|u_{\boldsymbol{k}}^{0}|^{2} + [1-f(\epsilon_{\boldsymbol{k}})]\,|v_{\boldsymbol{k}}^{0}|^{2}\},$$

$$n_{n}\nabla\varphi = 4\sum_{\boldsymbol{k}}\boldsymbol{k}\,[f(\epsilon_{\boldsymbol{k}}^{s})-f(\epsilon_{\boldsymbol{k}})]\,(|u_{\boldsymbol{k}}^{0}|^{2}+|v_{\boldsymbol{k}}^{0}|^{2}) = \frac{2\hbar^{2}}{m_{e}}\sum_{\boldsymbol{k}}\boldsymbol{k}^{2}\partial_{\epsilon_{\boldsymbol{k}}}f(\epsilon_{\boldsymbol{k}})\nabla\varphi$$

for $\hbar^{2}(\nabla\varphi)^{2}/2m_{e} \ll \xi_{\boldsymbol{k}}$. Then the superconducting electron density

$$n_{s} = 2\sum_{\boldsymbol{k}}\left\{f(\epsilon_{\boldsymbol{k}})|u_{\boldsymbol{k}}^{0}|^{2} + [1-f(\epsilon_{\boldsymbol{k}})]\,|v_{\boldsymbol{k}}^{0}|^{2} - \frac{\hbar^{2}\boldsymbol{k}^{2}}{m_{e}}\partial_{\epsilon_{\boldsymbol{k}}}f(\epsilon_{\boldsymbol{k}})\right\}$$

leads to the expression for the supercurrent in Eq. (2.25). This can be evaluated for $T \to 0$, where $\partial_{\epsilon_{\boldsymbol{k}}}f(\epsilon_{\boldsymbol{k}}) \to 0$, and we have

$$n = n_{s} = 2N_{0}\Delta_{0}.$$

In Sec. 3.4, the supercurrent in a pure flat band $\xi_{\boldsymbol{k}} = 0$ is discussed shortly. In Article I, a supercurrent is calculated for a flat band superconductor (strained Dirac materials) by adding a phase gradient to the superconducting pair potential.

Josephson tunnelling

If the normal metal in the tunnelling junction in Fig. 2.2(b) is replaced by a superconductor (SIS), the tunnelling current depends on the density of states in both superconductors. This brings new features to the tunnelling conductance, like extending the peaks location. However, more interesting effect happens if the two superconductors have a phase difference.

In this case, when $V = 0$ a supercurrent appears across the junction satisfying [12]

$$I_J = I_c \sin(\varphi_1 - \varphi_2),$$

where I_c is the critical current for this junction. This is called the dc Josephson effect. In the case of $\Delta_1 = \Delta_2 = \Delta$, a microscopic approach yields the Ambegaokar-Baratoff relation [13] for I_c as

$$I_c = \frac{G_T \pi \Delta}{2e} \tanh\left(\frac{\Delta}{2k_B T}\right). \tag{2.28}$$

If a voltage V is applied across the Josephson junction, the superconducting phase difference is determined by

$$\frac{d\varphi}{dt} = \frac{2eV}{\hbar},$$

where $\varphi = \varphi_1 - \varphi_2$. Solution of this equation is given by

$$\varphi(t) = \varphi(0) + \frac{2eVt}{\hbar}. \tag{2.29}$$

Then the Josephson current becomes

$$I_J = I_c \sin\varphi(t).$$

This introduces an oscillatory behaviour of the Josephson current as a function of time. This is called the ac Josephson effect.

There are various systems and devices based on the Josephson effects. In this thesis, however, we only focus on the above fundamental model of the Josephson effects. In Sec. 4.3.1 and Article II, the Josephson current is evaluated for a system of two superconductors with noncolinear spin-splitting fields.

Nonequilibrium effects

In thermal equilibrium, the quasiparticle states are occupied with a probability described by the Fermi distribution function in Eq. (2.7). An external perturbation,

however, causes a distortion to this distribution. As a response to this perturbation, nonequilibrium excitations arise in the superconductor.

It is convenient to express these nonequilibrium excitations in terms of their deviation from thermal equilibrium as

$$\delta f_k = f_k - f(\epsilon).$$

Here, δf_k represents two sets of nonequilibrium excitations, due to temperate and charge density, respectively [14]. These excitations are shown in Fig. 2.3.

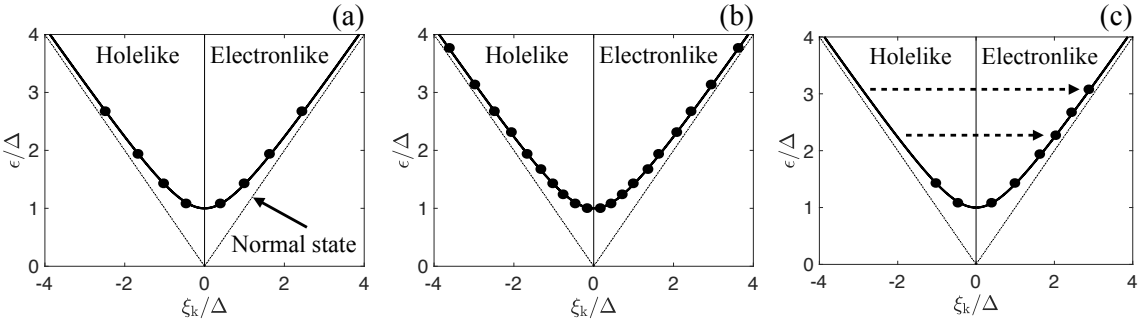

Figure 2.3: (a) Energy spectrum of quasiparticles in thermal equilibrium with the occupied states labelled with filled circles. The thin straight curve represents the normal state energy $\xi_k = \hbar^2 \boldsymbol{k}^2/(2m) - \epsilon_F$. The occupied sates are evenly distributed for electronlike $\xi_k > 0$ and holelike $\xi_k < 0$ branches. (b) Excitation of the even mode. (c) Excitation of the odd mode with electronlike-holelike branch transitions.

The nonequilibrium excitation due to a temperature change in Fig. 2.3(b) is even with respect to the Fermi level. It represents changes in quasiparticles populations on both electronlike and holelike branches in the spectrum. It is called the longitudinal or energy mode and we label this mode as f_L. It is an antisymmetric function of energy with respect to the Fermi level. The nonequilibrium excitation due to a charged perturbation in Fig. 2.3(c) is odd with respect to the Fermi level. It introduces a branch imbalance to the spectrum. It is called the transverse or charge mode and we label it as f_T. It is a symmetric function of energy with respect to the Fermi level.

The nonequilibrium properties of superconductors are related to these modes. For example, a charge imbalance created by injection of electric current from a normal metal injector is related to the charge mode f_T [15], and the energy mode f_L is related to the steady state enhancement of superconductivity in the presence of a microwave field [16]. The coupling between these two modes also leads to very interesting nonequilibrium effects. For example, a supercurrent flowing along a temperature gradient is known to induce a charge imbalance [17, 18].

In Sec. 4.3.2, the nonequilibrium charge f_T and energy f_L modes are extended to include the spin degrees of freedom for superconductors with a homogeneous spin-splitting field. The spin and spin energy modes are excited in such cases, and the

coupling between these modes in the presence of supercurrent leads to the charge-spin conversion in Article III.

2.2 Fundamentals of ferromagnetism

2.2.1 Models of ferromagnetism

In the absence of an external magnetic field, the magnetic moments of materials are directed randomly, which results to zero net magnetic moment. Below a critical temperature, however, magnetic moments of some materials start to align. If the alignment is parallel (hence with a nonzero net magnetization, also called spontaneous magnetization), these materials are called ferromagnets, and the related critical temperature is called Curie temperature.

Ferromagnetism originates from the exchange interaction between the magnetic moments, due to the electron-electron Coulomb interaction together with the Pauli exclusion principle. If one assumes that the atoms are well separated so that the overlap of the atomic wave functions is very small, the exchange interaction can be described by the Heisenberg Hamiltonian [19, 20]

$$H_{\text{Heisenberg}} = -\sum_{i,j} J_{ij} \boldsymbol{S}_i \cdot \boldsymbol{S}_j, \tag{2.30}$$

where the sum runs over the lattice sites i, j, J_{ij} is the exchange integral, which is positive for ferromagnets, and $\boldsymbol{S}_{i/j}$ is the spin operator.

In the presence of an external magnetic field, the magnetic moments interact with the field, and this interaction also contributes to the Hamiltonian of the system. The Zeeman Hamiltonian is given by

$$H_{\text{Zeeman}} = -2\mu_B \sum_i \boldsymbol{H}_i \cdot \boldsymbol{S}_i,$$

where $\mu_B = e\hbar/(2m_e)$ is the Bohr magneton and $\boldsymbol{H}_i$ is the local magnetic field acting on the ith spin. If the external field is applied in the z-axis direction, then the total Hamiltonian for a ferromagnet can be written as

$$H_F = -\sum_{i,j} J_{ij} \boldsymbol{S}_i \cdot \boldsymbol{S}_j - 2\mu_B H \sum_i S_i^z. \tag{2.31}$$

The Heisenberg model works well with many materials and phenomena. However, solving it is not an easy task. Approximations are always needed. The mean field

approximation simplifies the problem substantially, but it is a crude approximation to the Heisenberg model. Although it gives an insight on the qualitative physical picture of the model, it fails to explain many features, especially at temperatures close to the Curie temperature [21, 22]. There are also more advanced approximations, but this is not the focus of this thesis. The focus is rather on the phenomenological level, and the transport properties in the semiclassical regime. Therefore, there is no need to discuss the solutions of the Heisenberg model.

The energy spectrum and density of states of ferromagnets are complicated. However, we can use a simplified model (Stoner model) to discuss the features of different types of ferromagnets [23].

Most of the ferromagnets are metals. For a ferromagnetic metal below the Curie temperature, the spontaneous magnetization splits the electron bands. The splitting of the electron bands leads to the splitting of the density of states, see Fig. 2.4(b). For a comparison, the density of states of a paramagnetic metal is shown in Fig. 2.4(a). The degree of the splitting in the density of states, namely, the degree of the alignment of spins in a ferromagnet, can be represented by the spin polarization as

$$P = \frac{N_0^{\uparrow} - N_0^{\downarrow}}{N_0^{\uparrow} + N_0^{\downarrow}}, \tag{2.32}$$

where N_0^s is the density of states at the Fermi level for spin $s = \uparrow / \downarrow$.

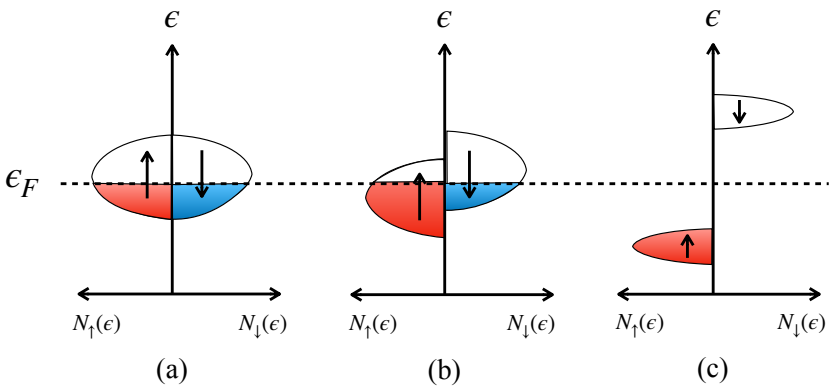

Figure 2.4: Schematic description of the density of states for different types of ferromagnets. (a) Paramagnetic metal, (b) ferromagnetic metal, (c) ferromagnetic insulator.

Although they are not as common as ferromagnetic metals, ferromagnetic insulators also exist and have very unique properties. For example, Europium chalcogenides have simple cubic structure, low Curie temperature, and splitting of the conduction band [24], as shown in Fig. 2.4(c). Europium chalcogenides are required for many applications. For example, they have been used as spin filters in various devices with tunnel junctions.

2.2.2 Domain structure

A large ferromagnetic material with a constant magnetization creates a magnetic field outside of itself (stray field) and hence a large magnetostatic energy. In order to reduce this energy, a ferromagnet splits itself into many domains, with different magnetization directions [25]. When an external magnetic field is applied, the domains tend to align with the direction of the field.

Domains are separated by domain walls, with a size much smaller than that of the domains. In the domain walls, the direction of the magnetization rotates smoothly from one domain to the other.

The formation of the domains is associated with a competition of various types of energies. The most relevant ones are the exchange energy, anisotropy energy, and the magnetostatic energy. The exchange energy prefers parallel configuration of the magnetization direction, while the anisotropy energy tends to align the magnetization to a particular direction. The magnetostatic energy is indeed the reason of the formation of the domains, it also determines the shape of the domain walls. Below, these energies are introduced separately.

Exchange (nonuniformity) energy

The exchange energy results from the exchange interaction. This energy is related to the Heisenberg model in Eq. (2.30). It can be derived from Heisenberg model in some limiting cases [26]. It is usually expressed phenomenologically as the gradient of the magnetization unit vector $\boldsymbol{m}$ as

$$U_{ex} = Q\left[\left(\frac{\partial \boldsymbol{m}}{\partial x}\right)^2 + \left(\frac{\partial \boldsymbol{m}}{\partial y}\right)^2 + \left(\frac{\partial \boldsymbol{m}}{\partial z}\right)^2\right], \tag{2.33}$$

where

$$Q = \frac{nJS^2}{a}$$

is called the exchange stiffness constant. In which, a is the lattice constant, S is the amplitude of the spins, J is the exchange integral for nearest-neighbour exchange interaction, and n is a constant. For a simple cubic lattice $n = 1$, for a body-centered cubic lattice $n = 2$, and for a face-centered cubic lattice $n = 4$.

Anisotropy energy

Magnetic anisotropy represents the contribution of magnetization direction to the energy of the system. It is the origin of hysteresis and coercivity.

The anisotropy energy density is given by a series powers of the direction cosines of the magnetization unit vector $\boldsymbol{m}$. It is invariant under time reversal and depends on the crystal structure [27].

For cubic crystals, since $\boldsymbol{m} \cdot \boldsymbol{m} = 1$, the anisotropy energy density is expressed as [25]

$$U_{\text{aniso}}^{\text{cubic}} = K_{c1}(m_x^2 m_y^2 + m_x^2 m_z^2 + m_y^2 m_z^2) + K_{c2} m_x^2 m_y^2 m_z^2 + ...,$$

where K_{c1} and K_{c2} are the first- and second-order cubic anisotropy constants.

For uniaxial and biaxial crystals, the anisotropy energy density can be written as [27]

$$U_{\text{ansio}}^{\text{uniaxial}} = K_{u1}(m_x^2 + m_y^2) + K_{u2}(m_x^2 + m_y^2)^2 + ...,$$

where K_{u1} and K_{u2} are the first- and second-order uniaxial or biaxial anisotropy constants.

The anisotropy constants are functions of temperature, and their magnitude generally decreases with increasing order. Moreover, using symmetry analysis, one can show that the anisotropy constants of different crystals are convertable. Namely, we can write the anisotroy constants for the uniaxial crystals in terms of the ones for the cubic crystals. For example [22],

$$K_{u1} = K_{c1}$$
$$K_{u2} = -\frac{7K_{c1}}{8} + \frac{K_{c2}}{8}.$$

Due to their simple form, we use the uniaxial and biaxial anisotropy energy density for discussions. If we use spherical coordinates for the unit vector,

$$\boldsymbol{m} = (\sin\alpha\cos\phi, \sin\alpha\sin\phi, \cos\alpha), \tag{2.35}$$

then the anisotropy energy density up to the second order can be written as

$$U_{\text{aniso}} = K_1 \sin^2\alpha + K_2 \sin^4\alpha. \tag{2.36}$$

The sign of the anisotropy constants determines the magnetization direction [27]. If $K_1 > 0$, the magnetization direction is along the z-axis, and this is called the direction of easy magnetization. Such ferromagnets are called easy-axis type. If $K_1 < 0$, the magnetization direction lies in the xy-plane (basal plane of the crystal), then the ferromagnets are called easy-plane type.

The second order anisotropy contant K_2 contributes corrections to the direction of magnetization [28]. For $K_1 > 0$ and $K_2 > -K_1$, the z-axis is the easy axis. For $K_1 > 0$, $K_2 < -K_1$ and $K_1 < 0$, $K_2 < -K_1/2$, the xy-plane is easy plane. The case of $-2K_2 < K_1 < 0$ makes the ferromagnet an easy-cone type. In this case, the magnetization direction lies outside of the basal plane and has an angle between the z-axis.

Domain wall

With the exchange energy and anisotropy energy, we are able to solve for the general domain wall structure and energy. It is energetically favourable for a ferromagnet that the rotation of the magnetization direction happens in a plane. This is because, rotation in three dimensional space causes extra energy [27]. This means that one of the component of the unit vector $\boldsymbol{m}$ of the magnetization direction is zero and α is a function of one coordinate x only.

The total energy up to the first order in the anisotropy energy density is given by

$$E_{dw} = \int_{-\infty}^{\infty} d^3x(U_{ex} + U_{\text{aniso}}) = W \int_{-\infty}^{\infty} dx(Q\alpha'^2 + K_1 \sin^2 \alpha),$$

where W is the cross sectional area of the ferromagnet. Minimizing this energy with respect to $\alpha(x)$, the corresponding Euler's equation gives

$$Q\alpha'' - K_1 \sin\alpha \cos\alpha = 0.$$

This equation can be solved with the boundary conditions $\alpha(-\infty) = 0$ and $\alpha(+\infty) = \pi$ as

$$\alpha(x) = \cos^{-1}\left[-\tanh\left(\frac{x}{\lambda}\right)\right], \tag{2.37}$$

where $\lambda = \sqrt{Q/K_1}$ is the domain wall size. With this solution, the domain wall energy can be written as

$$E_{dw} = 4W\sqrt{K_1 Q}.$$

Also another type of a rotation angle can be found in the literature,

$$\alpha(x) = \frac{\pi}{\lambda}\left(x + \frac{\lambda}{2}\right)\Theta\left(x + \frac{\lambda}{2}\right)\Theta\left(\frac{\lambda}{2} - x\right) + \pi\Theta\left(x - \frac{\lambda}{2}\right), \tag{2.38}$$

where Θ is the heaviside step function. This simplified ansatz for the domain wall structure allows an SU(2) type transformation in transport equations, and brings many conveniences to the analytics to the problem. With this domain wall structure, the domain wall size and energy are given by

$$\lambda = \sqrt{\frac{2Q}{K_1}}\pi,$$

$$E_{dw} = W\sqrt{2K_1 Q}\pi.$$

This energy is just slightly larger than the one of the domain wall structure in Eq. (2.37).

Types of the domain wall

As already mentioned above, in domain walls the rotation of magnetization happens in a plane, and this can be represented by setting, for example, $\phi = 0$ or $\pi/2$ in the magnetization unit vector in Eq. (2.35). The first choice is called the Néel wall, which describes the rotation of the magnetization happening in the plane of the domain wall. The second is called the Bloch wall, in which the magnetization rotates out of the plane of the domain wall. The schematics of these domain walls are shown in Fig. 2.5(a).

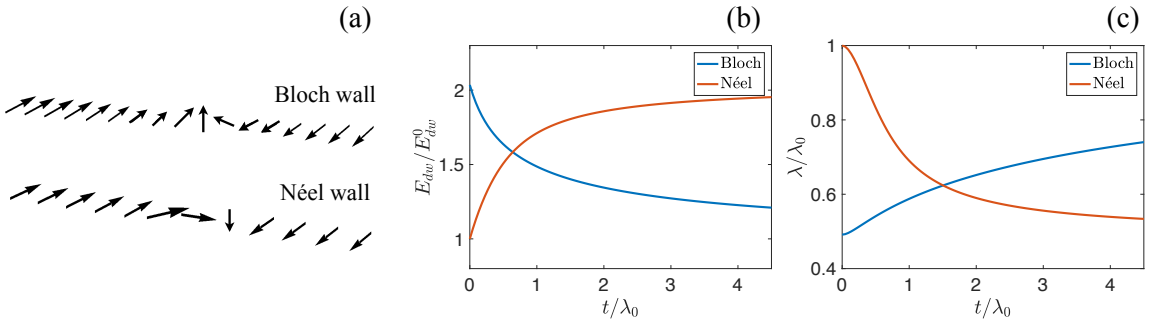

Figure 2.5: (a) Schematic view of the two types of domain wall structure. (b) Minimized domain wall energy and (c) domain wall size for two types of domain wall structure, as a function of thickness of a ferromagnet.

The prefered types of the domain walls is determined by the magnetostatic energy caused by the stray field. Since the demagnetizing factor depends on the shape of a material, the magnetostatic energy density of the two types of the domain walls are slightly different [29]

$$U_{\text{mag}}^{\text{Bloch}} = \frac{\lambda}{\lambda + t}\frac{\mu_0 M_a^2}{2}$$

$$U_{\text{mag}}^{\text{Néel}} = \frac{t}{\lambda + t}\frac{\mu_0 M_a^2}{2},$$

where t is the thickness of the ferromagnet, and M_a is the average magnetization of the ferromagnet.

We can use the rotation angle in Eq. (2.38), and take the anisotropy energy density for a uniaxial crystal up to the second order to calculate the total energy. Note that

for a thin film $K_1 \to K_1 + K_s/t$, where K_s is the surface anisotropy constant [30]. Then we get

$$E_{dw}^{\text{Bloch}} = F_1 + \frac{\lambda^2}{\lambda + t}\frac{\mu_0 M_a^2}{2}W$$

$$E_{dw}^{\text{Néel}} = F_1 + \frac{t\lambda}{\lambda + t}\frac{\mu_0 M_a^2}{2}W,$$

where

$$F_1 = \frac{Q\pi^2}{\lambda}W + \frac{1}{2}K_{\text{eff}}\lambda W, \tag{2.41}$$

and $K_{\text{eff}} = K_1 + K_s/t + 3K_2/4$.

Minimization of these two energies with respect to the domain wall size λ produces the domain wall energies and sizes for the two types of the domain walls. The results are plotted in Fig. 2.5(b,c). For simplicity, we assume $|K_s|/t \ll |K_1|$ and normalize the domain wall energy and domain wall size with the solutions in the absence of the magnetostatic energy

$$\lambda_0 = \sqrt{\frac{2Q}{K_{\text{eff}}}}\pi, \tag{2.42a}$$

$$E_{dw}^0 = W\sqrt{2K_{\text{eff}}Q}\pi. \tag{2.42b}$$

We can see that, although its domain wall size is larger, Néel wall is preferred energetically for thin ferromagnets, while the Bloch walls appear in bulk ferromagnets ($t \to \infty$). Moreover, for thin ferromagnets with $t \ll \lambda$, the contribution of the magnetostatic energy to the domain wall size is very small, and the domain wall size is determined by λ_0 in Eq. (2.42a). Namely, the exchange energy and anisotropy energy are enough to the energetics of a Néel wall for a thin ferromagnet. If we relax the assumption $|K_s|/t \ll |K_1|$, there would be some corrections to the domain wall energy and domain wall sizes at small t, but the overall behaviour is not changed.

In Sec. 4.4, the induced exchange field in a superconductor making contact with a ferromagnetic insulator is considered to be inhomogeneous. The inhomogeneity is represented by a Néel domain wall since it is energetically favorable for thin films.

3 Flat band superconductivity in strained Dirac materials

Ensuing some of the fundamental properties of superconductivity, the first topic in the new forms of superconductivity, flat band superconductivity, is discussed in this chapter. The discussions start from presenting the general ideas of the flat band superconductivity, and then the strained Dirac materials are introduced briefly. The superconducting state, including the Bogoliubov-de Gennes equation, of strained Dirac materials are discussed at the end.

3.1 Flat band superconductivity

As shown in Sec. 2.1.1, in the BCS theory the size of the superconducting pair potential of a homogeneous superconductor is suppressed exponentially. At zero temperature

$$\Delta_0 = 2E_c e^{-1/(gN_0)},$$

where N_0 is the density of states at the Fermi level. Since the BCS theory predicts Δ_0 be of the same order as the critical temperature T_c [Eq. (2.15)], aiming to increase the density of states is a way in searching for superconductors with higher critical temperatures.

One way to pursue is an extreme case when $\xi_{\boldsymbol{k}} = 0$, namely a dispersionless normal state energy (flat band). In this case Eq. (2.13) becomes

$$\Delta = \frac{g}{2}\int \frac{d\boldsymbol{k}}{(2\pi)^d} \tanh\left(\frac{\Delta}{2k_BT}\right) = \frac{gV_d}{2(2\pi)^d} \tanh\left(\frac{\Delta}{2k_BT}\right), \tag{3.1}$$

where d is the dimensionality of the system, and V_d is the volume (area or length) of the flat band in the momentum space. At zero temperature, this equation results to a superconducting pair potential that is linear in the interaction strength g, so that the flat band system may give rise to a very high T_c.

The best known flat bands are the Landau levels [31]. However, the strong magnetic field also suppresses the superconductivity as discussed in Sec. 2.1.2, so that Landau levels are not applicable to the flat band superconductivity. The first model of flat

band superconductivity was given by Khodel and Shaginyan, in a case where the flat bands are induced by interactions between the fermions as a result of merging of different fermionic levels [32].

There are also other types of flat bands that are not due to the interaction. Flat bands or partially flat bands (with higher order energy dispersion around the Fermi level) are formed at the surface states of some topological semimetals [33–35]. One example is the rhombohedral graphite [36], where the formation of the flat band happens on the surface of a multilayered rhombohedral structure with a large number of layers.

Another possible formation of the topological flat bands appears at certain strained surfaces or interfaces with misfit dislocations. Examples of these types of flat bands were used to explain the appearance of superconductivity at the interfaces of combinations of nonsuperconducting materials containing misfit dislocation [37–39], and the superconductivity in graphite interfaces with Bernal stacking [40]. A strain induced flat band can be also realized in graphene and other Dirac materials [41, 42]. In this case, a periodic strain field plays the role of an effective gauge field and forms partially flat bands without breaking the time-reversal symmetry. We discuss this type of flat band superconductivity is this chapter.

3.2 Strained Dirac materials

The Dirac materials are a class of materials whose low-energy excitations behave like massless Dirac fermions and obey the Dirac Hamiltonian [43]. In energy spectrum, Dirac materials have conical dispersions near zero energy, called Dirac cones. The zero energy takes place at two or more inequivalent Dirac points in the momentum space, the area around these points is called valley.

The Hamiltonian of a Dirac material with a periodic strain field around a Dirac cone discussed in Ref. [42] (Tang-Fu model) is given by

$$H_{TF} = \hbar v_F \hat{k}_x \sigma_1 + \hbar v_F \left[\hat{k}_y + A_y(x)\right] \sigma_2, \tag{3.2}$$

where v_F is the Fermi velocity of the Dirac material, and σ_i is the ith Pauli spin matrix, which acts on the pseudospin degree of freedom. Here the strain induced gauge field $A_y(x)$ is a component of the effective vector potential $\boldsymbol{A} \propto (0, A_y(x), 0)$ with a strain period L so that $A_y(x + L) = A_y(x)$ and $\int_0^L A_y(x) = 0$.

The form of the periodic strain field (pseudo vector potential) is given by [42]

$$A_y(x) = \frac{\beta}{L} \cos\left(\frac{2\pi x}{L}\right),$$

where β is a dimensionless parameter describing the strength of the strain. The estimated realistic values for the massless Dirac fermions are between $\beta \approx 20 \sim 40$.

The Hamiltonian in Eq. (3.2) describes the physics at one valley, the sign of the strain field is reversed for the partner valley. We can use the Bloch theorem to transform this Hamiltonian in the momentum space as

$$H_{TF}(\boldsymbol{k}) = \hbar v_F \left(\frac{2\pi m}{L} + k_x\right)\sigma_1\delta_{ml} + \hbar v_F k_y \sigma_2 \delta_{ml} + \hbar v_F \frac{\beta}{2L}\sigma_2(\delta_{m,l-1} + \delta_{m,l+1}), \quad (3.3)$$

where m, l are the Bloch indices. Here k_x ranges between $-\pi/L$ to π/L.

Diagonalization of this Hamiltonian yields the energy spectrum $\xi_{\boldsymbol{k}}$, which is plotted in Fig. 3.1(a) for different values of β. See Appendix B.3 for the numerical method used for the diagonalization. We can see that the partially flat band appears around $k_y \in [-\beta/(2L), \beta/(2L)]$. However, for very small values of k_y, the dispersion is linear. This linear dispersion and the emergence of the flat band can be understood within a perturbation model. For $\hat{k}_y = 0$, Eq. (3.2) has the following zero energy solutions [44]

$$\Psi_+ = \begin{pmatrix}0\\1\end{pmatrix} \exp\left[\int_0^x A(x')dx'\right] = \begin{pmatrix}0\\1\end{pmatrix} \exp\left[\frac{\beta \sin(2\pi x/L)}{2\pi}\right]$$
$$\Psi_- = \begin{pmatrix}1\\0\end{pmatrix} \exp\left[-\int_0^x A(x')dx'\right] = \begin{pmatrix}1\\0\end{pmatrix} \exp\left[-\frac{\beta \sin(2\pi x/L)}{2\pi}\right].$$

Then we treat $\hat{k}_y$ as a perturbation and obtain

$$\frac{\xi_{k_y} L}{\hbar v_F} = \pm C k_y, \quad (3.4)$$

where

$$C = I_0^{-1}(\beta/\pi).$$

Here $I_0(x)$ is the zeroth modified Bessel function of the first kind. Then $C \to 0$ for $\beta \gg \pi$, and a flat band is formed.

The density of states in Fig. 3.1(b) can be numerically determined as

$$N(\epsilon) = \frac{1}{n_{\boldsymbol{k}}} \sum_{\boldsymbol{k}} \delta(\epsilon - \xi_{\boldsymbol{k}}),$$

where $\delta(x)$ is the Dirac delta function, and $n_{\boldsymbol{k}}$ is the total number of $\boldsymbol{k}$-vectors used in the calculations. We can see that the density of states is very high at $k_y L = 0$, and the peak is higher for larger β.

The topological properties of materials are characterized by topological invariants. Here we calculate the winding number for the strain induced flat band [45]

$$\nu = \frac{1}{4\pi i} \int_{-\pi/L}^{\pi/L} dk_x \mathrm{Tr}[\sigma_3 H_{TF}^{-1}(\boldsymbol{k}) \partial_{k_x} H_{TF}(\boldsymbol{k})].$$

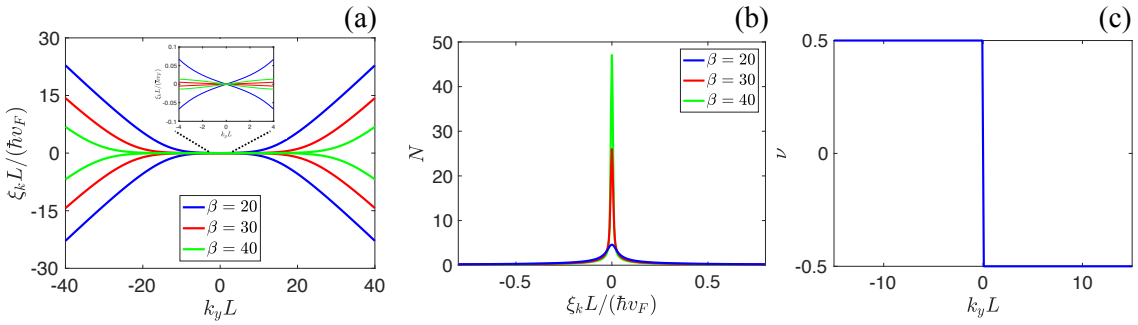

Figure 3.1: (a) Strain induced flat band energy spectrum at $k_x = 0$ and (b) the density of states. (c) Winding number of the induced flat band for $\beta = 30$.

The winding number $\nu = 0$ describes topologically trivial states, and $\nu \neq 0$ corresponds to topological nontrivial states. We can see from Fig. 3.1(c) that as $k_y L$ changes sign at $k_y L = 0$, the strain induced flat band transforms from one topological state $\nu = 0.5$ to an other $\nu = -0.5$.

3.3 Bogoliubov-de Gennes equation

The superconducting state of the strain induced flat band is described by the Bogoliubov-de Gennes equation in Eq. (2.5). In the momentum space, we can write

$$H_{\mathrm{BdG}} = \begin{pmatrix} H_{TF}(\boldsymbol{k}) & \Delta_{ml} \\ \Delta^*_{ml} & -H_{TF}(\boldsymbol{k}) \end{pmatrix}, \tag{3.5}$$

where $\Delta^{(*)}_{ml} = \Delta^{(*)}_n \delta_{l,m\pm n}$. Here Δ_n is a 2×2 matrix due to the pseudospin degress of freedom. If we assume in lattice coupling, we can write

$$\Delta_n = \begin{pmatrix} \Delta_{n\uparrow} & 0 \\ 0 & \Delta_{n\downarrow} \end{pmatrix}.$$

The Hamiltonian in Eq. (3.5) represents the superconductivity at one valley. The other valley also contributes to the superconductivity. Therefore, the self-consistent determination of Δ_n from Eq. (2.8) in the momentum space is given by

$$\Delta_n = \Delta_n^K + \Delta_n^{-K}, \tag{3.6}$$

where

$$\Delta_n^K = g \sum_{\boldsymbol{k}} \sum_m \sum_b u_{b,m}(\boldsymbol{k}) \sigma_0 v^*_{b,m-n}(\boldsymbol{k}) \tanh\left(\frac{\epsilon_{b,\boldsymbol{k}}}{2k_B T}\right)$$

$$\Delta_n^{-K} = g \sum_{\boldsymbol{k}} \sum_m \sum_b v_{b,m}^*(\boldsymbol{k}) \sigma_0 u_{b,m-n}(\boldsymbol{k}) \tanh\left(\frac{\epsilon_{b,\boldsymbol{k}}}{2k_B T}\right),$$

where m is the Bloch index, b is the band index, K represents the valley, and σ_0 is the unit matrix in the pseudospin space.

The superconducting pair potential determined in Eq. (3.6) leads to three types of superconductivity, depending on the size of the interaction strength g. When $g \ll \hbar v_F C L$, the superconductivity is of the type found in pure Dirac materials [46, 47]. When $\hbar C L \ll g \ll \hbar v_F L/\beta$, the system is in the pure flat-band regime, and only the lowest energy bands contribute to superconductivity. Our focus is this regime in this chapter. When $g \geqslant \hbar v_F L/\beta$, also higher bands contribute to superconductivity. This situation was considered in Ref. [48] in strained graphene where an inhomogeneous superconducting state was also found.

Note that there is a quantum critical point in the case of $g \ll \hbar v_F C L$, below which superconductivity does not take place. This can be seen as follows. Due to the Dirac cone structure, it is reasonable to assume that the energy spectrum in k_x axis also has the form of Eq. (3.4). Then Eq. (2.13) becomes

$$1 = \frac{4g}{2(2\pi)^2} \int d\boldsymbol{k} \frac{1}{\sqrt{[\hbar v_F C \sqrt{k_x^2 + k_y^2/L}]^2 + \Delta^2}} \tanh\left(\frac{\epsilon_{\boldsymbol{k}}}{2k_B T}\right),$$

where the pseudospin and the valley degeneracies are included. At the quantum critical point, $\Delta = 0$, we can use the polar coordinate to evaluate this integral at $T = 0$ as

$$1 = \frac{g_{\min}}{2\pi^2 L} \int_0^{k_c} k dk \int_0^{2\pi} d\phi \frac{1}{\hbar v_F C k/L} = \frac{g_{\min} k_c}{\pi \hbar v_F C}.$$

Since the flat appears around $k_y \in [-\beta/(2L), \beta/(2L)]$, we choose the momentum cutoff as $k_c = \beta/(2L)$, this yields

$$g_{\min} = \frac{2\pi C}{\beta} \hbar v_F L. \tag{3.7}$$

Then for $g < g_{\min}$, there is no superconducting state of the system.

3.4 Superconducting state

Equation. (3.6) is used to calculate the superconducting pair potential as shown in Fig. 3.2. The numerical methods used for the diagonalization of the Hamiltonian, the self-consistency calculations and the integrations are discussed in Appendix B. The

position averaged $\Delta = (1/L)\int_0^L dx\Delta(x)$ is plotted in Fig. 3.2(a) for different β, as a function of g. We can see the superconductivity is stronger for larger β. For $\beta = 20$, we can see the visible quantum critical point described in Eq. (3.7) as $g_{\min} \approx 0.003\hbar v_F L$. For larger β, the dependence of Δ_{ave} on g is approximately linear as $\Delta_{\text{ave}} \approx \beta g/(2L^2)$.

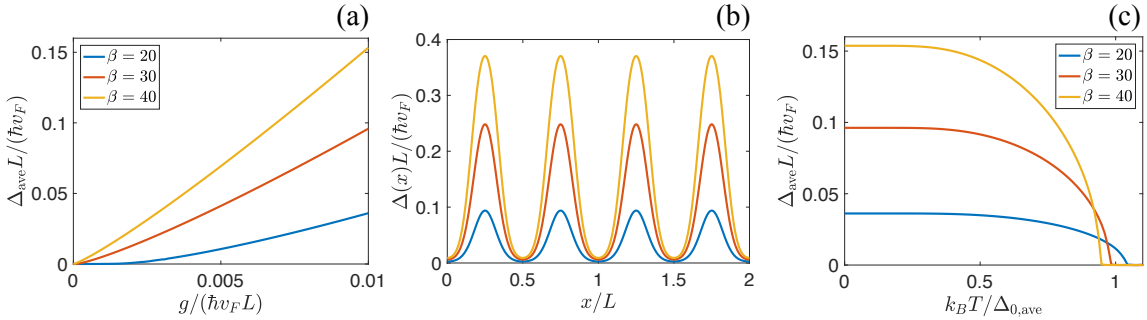

Figure 3.2: (a) Averaged superconducting pair potential Δ_{ave} as a function of interaction strength g for different β. (b) Profile of $\Delta(x)$ for the same values of β with (a). (c) Temperature dependence of Δ_{ave}.

Next, the profiles of the superconducting pair potential for a fixed $g = 0.01\hbar v_F L$ for different β are shown in Fig. 3.2(b). There two peaks show up in the profile for each strain period, due to the pseudospin degree of freedom. Note that the minima is finite in the profiles. The temperature dependence of the averaged $\Delta(x)$ is plotted Fig. 3.2(c). We can see that the critical temperature is approximately equal to Δ_{ave}, namely, the superconducting pair potential is of the same order with the critical temperature as in the BCS theory. Thus, the dependence of T_c on g is also linear. We can therefore expect a high T_c in the flat band regime.

The energy spectrum and density of states of the superconducting state are shown in Fig. 3.3. As the superconducting pair potential is stronger for larger β, the energy gap in the spectrum is also larger. At $\epsilon_{\boldsymbol{k}=0} = 2\Delta_{\text{ave}}$, the gap reaches its maximum. The density of states show a peculiar two-peaked shape for larger β. However, for $\beta = 20$, the weaker superconductivity leads to a single peak structure in the density of states. These features could act as a possible experimental signature for superconductivity described by this model.

One last thing to examine is the supercurrent. The supercurrent in flat band materials is also interesting. The dispersionless spectrum, in principle, leads the vanishing of the supercurrent. This can be seen as follows. The supercurrent expression in Eq. (2.27) can be written as

$$\boldsymbol{j}_s = -2e\sum_{\boldsymbol{k}}\{f(\epsilon^s_{\boldsymbol{k}})v^e_g - [1 - f(\epsilon^s_{\boldsymbol{k}})]\, v^h_g\},$$

where

$$v^{e(h)}_g = \mp\frac{1}{\hbar}\partial_{\boldsymbol{k}}\xi_{\boldsymbol{k}\mp\nabla\varphi/2} = \begin{cases} u^*_{\boldsymbol{k}}(\boldsymbol{k})\hat{p}u_{\boldsymbol{k}}(\boldsymbol{r})/m_e \\ v_{\boldsymbol{k}}(\boldsymbol{k})\hat{p}v^*_{\boldsymbol{k}}(\boldsymbol{r})/m_e \end{cases}$$

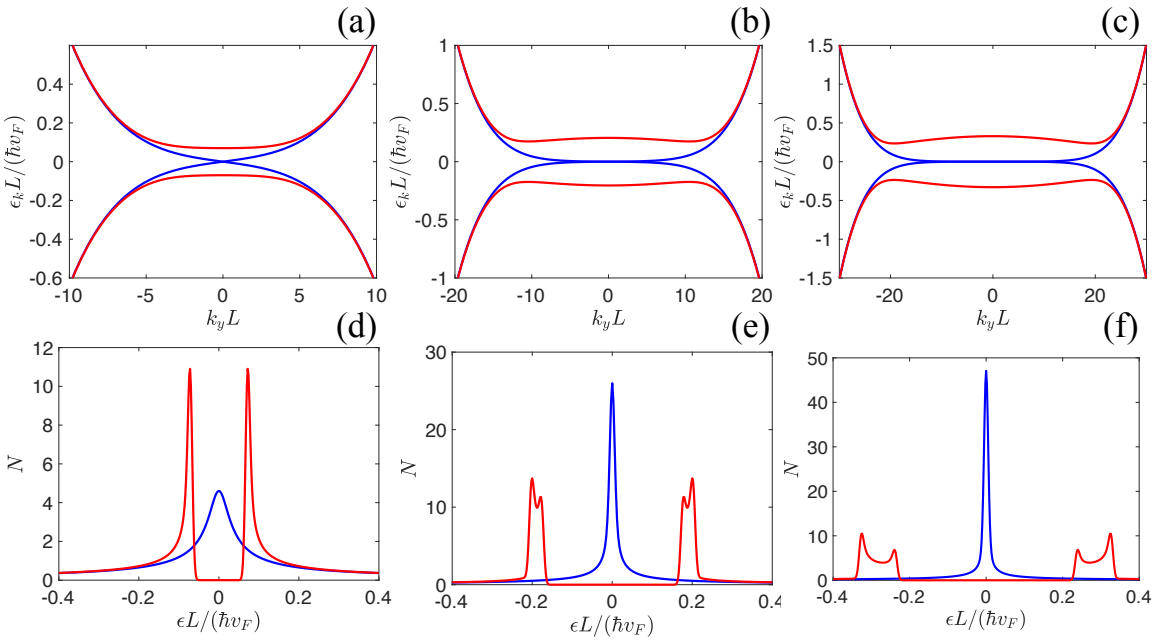

Figure 3.3: Energy spectrum and density of states both in the normal and superconducting state for (a,d) $\beta = 20$, (b,e) $\beta = 30$, (c,f) $\beta = 40$.

is the group velocity for electronlike (holelike) quasiparticles. For flat bands then $v_g^{e(h)} = 0$, the supercurrent becomes zero. Therefore, it is reasonable to think that the paired electrons are localized in flat bands, and unable to carry supercurrent. However, a finite supercurrent is predicted in the superconducting state of multilayered rhombohedral graphene [49] and in general for a topological flat band due to an additional geometric contribution to the superfluid weight [50]. Then one can expect a finite supercurrent due to the topological nature [Fig. 3.1(c)] of strain induced flat band in Dirac materials.

The expression for the supercurrent in strained Dirac materials can be written as

$$\boldsymbol{j}_s = \frac{ev_F}{L} \sum_{\boldsymbol{k},b} \left[f_{\boldsymbol{k},b} u^*_{\boldsymbol{k},b} \boldsymbol{\sigma} u_{\boldsymbol{k},b} + (f_{\boldsymbol{k},b} - 1) v^*_{\boldsymbol{k},b} \boldsymbol{\sigma} v_{\boldsymbol{k},b} \right],$$

where $f_{\boldsymbol{k},b}$ is the Fermi distribution function for quasiparticles occupying the bth band at momentum $\boldsymbol{k}$. The averaged supercurrent and its various properties are shown in Article I.

In Dirac materials, such as, graphene, the superconductivity was shown with strong doping, and with a critical temperature of a few Kelvin [51, 52]. Strain induced flat bands, however, offers a promising alternative for the appearance of superconductivity in Dirac materials with a very high critical temperature even in the absence of doping. A detailed discussion on the prediction of the critical temperature of a strained graphene can be found in Article I.

4 Superconductors with a spin-splitting field

Transport properties of superconductors with a spin-splitting field are discussed in this chapter. After presenting the spin-splitting in a superconductor at the beginning, the Quasiclassical Green's function method is reviewed shortly. Thereupon, the equilibrium and nonequilibrium effects related to Article II to Article IV are summarized.

4.1 Spin-splitting in superconductors

In the presence of an applied magnetic field, the critical field is determined by Eq. (2.19). However, for very thin films with thickness less than the London penetration depth in Eq. (2.18), the Meissner effect is negligible under a parallel magnetic field. Then the critical field is determined by an other mechanism.

A normal metal experiences a paramagnetic effect under a Zeeman field [21]. If the parallel magnetic field destroys the superconductivity of a thin film at a critical field, then the corresponding normal state beyond this critical field must be related to the paramagnetism, and the parallel magnetic field is equivalent to a Zeeman field.

The free energy density of a metal at the critical field is lowered by a magnetic energy density, and this energy density should be equal to the superconducting free energy density as

$$f_s = f_n - MH_c,$$

where H_c is the critical field, and M is the related magnetization density. It can be written in terms of the density of states at the Fermi level as [21]

$$M = \mu_B^2 H N_0.$$

Then we have

$$f_n - f_s = N_0(\mu_B H_c)^2.$$

We can write Eq. (2.19) as

$$N_0(\mu_B H_c)^2 = -\frac{\pi^2}{3} N_0 (k_B T)^2 + 2N_0 \int_\Delta^\infty d\epsilon_{\boldsymbol{k}} \frac{2\epsilon_{\boldsymbol{k}} - \Delta^2}{\sqrt{\epsilon_{\boldsymbol{k}}^2 - \Delta^2}} f(\epsilon_{\boldsymbol{k}}) + \frac{1}{2}\Delta^2 N_0.$$

At $T = 0$, it becomes

$$(\mu_B H_c)^2 = \frac{1}{2}\Delta^2 \Rightarrow \mu_B H_c = \frac{\Delta}{\sqrt{2}}. \tag{4.1}$$

This is known as the Chandrasekhar-Clogston limit [8, 9].

Superconductors with a Zeeman field have another very important property. Since a Zeeman field splits the energy spectrum for two spin species, the density of states also splits [53–57]. This is shown in Fig. 4.1. The Zeeman field splits the density of states for each spin species. In this case, the density of states in Eq. (2.11) becomes

$$\frac{N_s(\epsilon)}{N_0} = \frac{1}{2}\frac{|\epsilon + h|}{\sqrt{(\epsilon + h)^2 - \Delta^2}}\Theta(|\epsilon + h| - \Delta) + \frac{1}{2}\frac{|\epsilon - h|}{\sqrt{(\epsilon - h)^2 - \Delta^2}}\Theta(|\epsilon - h| - \Delta), \tag{4.2}$$

where $h = \mu_B|H|$ is the effective Zeeman splitting in energy and H is the applied parallel field (Zeeman field). Due to the splitting of the spectrum and the density of states, H is also called the spin-splitting field.

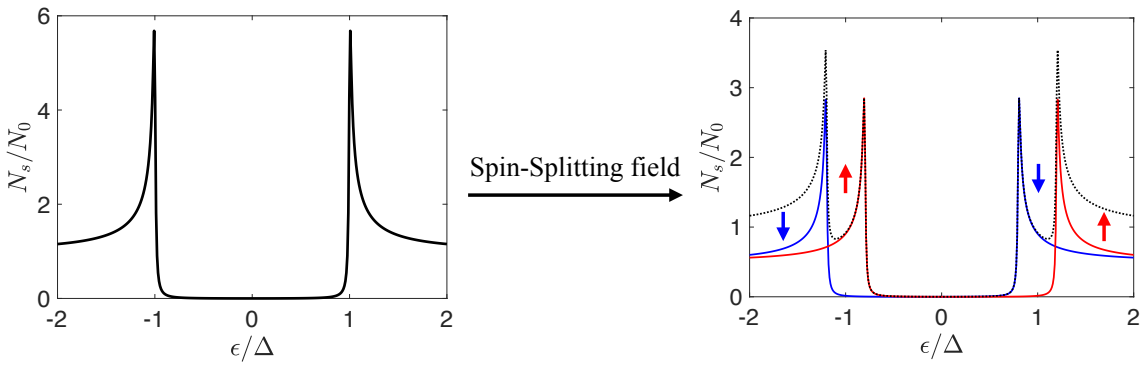

Figure 4.1: Spin splitting of the density of states. The peak at higher energy in the density of states is higher than the one at the lower energy, due to the contribution of both spin species.

The spin splitting can also be induced by making contact of a superconductor (S) with a ferromagnetic insulator (FI). In this case, the Hamiltonian of the S is shown in Eq. (2.2), and the Hamiltonian of the FI is shown in Eq. (2.30) together with a term describing anisotropy. Some of the properties of FI are discussed in Sec. 2.2.1. The coupling between the S and the FI can be considered by a model of localized magnetic moments of FI interacting with the spin of the conduction electrons of the S on the exchange interaction [58–62]

$$H_{ex} = -J_{ex}\sum_{ss'}\int d\boldsymbol{r}\psi_s^\dagger(\boldsymbol{r})[\boldsymbol{S}(\boldsymbol{r})\cdot\boldsymbol{\sigma}]_{ss'}\psi_{s'}(\boldsymbol{r}), \tag{4.3}$$

where $\psi^{(\dagger)}(\boldsymbol{r})$ is the destruction (creation) operator, $\boldsymbol{\sigma} = (\sigma_1, \sigma_2, \sigma_3)$ is a vector of Pauli spin matrices, s is the spin index, and J_{ex} is an effective parameter describing

the exchange interaction (s-d or s-f type). Here the integral goes only over the localized spin $\boldsymbol{S}(\boldsymbol{r})$ at the FI/S interface.

If we assume that the Curie temperature of the FI is much larger than the superconducting critical temperature ($T_{\text{Curie}} \gg T_c$), then the magnetization of the FI is not affected by the S. Thus, the effective spin-splitting field induced in the S is proportional to the averaged spin $\langle \boldsymbol{S}(\boldsymbol{r}) \rangle$. If the thickness t_S of the superconductor is much smaller than the superconducting coherence length ξ_0, the effective spin-splitting field can be expressed as [60, 62, 63]

$$\boldsymbol{h} = J_{ex} \langle \boldsymbol{S}(\boldsymbol{r}) \rangle \frac{a}{t_S},$$

where a is the lattice constant of the FI. This effective spin-splitting field creates a strong splitting in the density of states in Eq. (4.2) (in the case of a homogeneous spin-splitting field) in the presence of a small external magnetic field or even in its absence [64–69]. In this case, the spin-splitting field is also called the exchange field.

Superconductors with spin-splitting density of states have many novel features which are not present or very small in the absence of the spin-splitting field. For example, thermoelectric effects are negligibly small in conventional superconductors. However, huge thermoelectric effects (large values of figure of merit) were predicted and detected in superconductors with a spin-splitting field [70–74]. Another example is the long-range spin accumulation. Inside a metal, spins relax within a spin relaxation length. This length scale is even shorter in the superconducting state [75]. However, in superconductors with a spin-splitting field, spin accumulation persists in much longer distances than the spin relaxation length in the normal state [76–82]. These effects and other nonequilibrium properties of superconductors with a spin-splitting field are reviewed in Refs. [83, 84].

In the effects reviewed in Refs. [83, 84], the spin-splitting field induced in the superconductors is considered to be homogeneous. However, if it is induced by a FI, then the exchange field may be inhomogeneous due to the nonuniformity of the magnetization in the FI. The properties of superconductors with an inhomogeneous exchange field are less studied compared to the ones with a homogeneous exchange field. A recent study shows a peculiar tunnelling conductance in a FI/S structure, where the peak at the lower energy is higher than the one at the higher energy (opposite to the ones in Fig. 4.1), and the magnetic domain structure of the FI is considered responsible for this effect [85].

In this chapter, we discuss both equilibrium and out of equilibrium properties of superconductors with both homogeneous and inhomogeneous exchange fields.

4.2 Quasiclassical Green's function approach

As shown in Sec. 2.1.1 and in Chapter 3, the BdG equation works well with an effective mean-field Hamiltonian. However, in the presence of disorder, or for the nonequilibrium effects, for example, mentioned in Sec. 2.1.2, one needs easier theoretical treatments. The Green's function technique for the BCS theory provides a powerful tool for the description of nonequilibrium superconductivity, especially in the presence of disorder [86]. In this section, the basic principles of this method are reviewed.

4.2.1 Quasiclassical approximation

For superconductors with an exchange field, the Green's function is defined in the Nambu $\times$ spin space. Using the spinor $\hat{\psi}^\dagger = (\psi_\uparrow^\dagger, \psi_\downarrow^\dagger, -\psi_\downarrow, \psi_\uparrow)$, the Green's function can be written as an expectation value of a product of field operators

$$\hat{G}(\boldsymbol{r}_1, t_1; \boldsymbol{r}_2, t_2) = -i\langle T_C \hat{\psi}(\boldsymbol{r}_1, t_1)\hat{\psi}^\dagger(\boldsymbol{r}_2, t_2)\rangle, \tag{4.4}$$

where T_C means a time ordering on a time-loop contour C, and the average means the Gibbs statistical average. Within the BCS theory, this Green's function satisfies the Gorkov equation [87]

$$(\sigma_0 \hat{G}_0^{-1} - \sigma_0\hat{\Delta} - i\boldsymbol{h}\cdot\boldsymbol{\sigma}\tau_3 - \check{\Sigma})(\boldsymbol{r}_1, t_1; \boldsymbol{r}_2, t_2) \otimes \hat{G}(\boldsymbol{r}_2, t_2; \boldsymbol{r}_1', t_1') = \delta(\boldsymbol{r}_1, t_1, \boldsymbol{r}_1', t_1'), \tag{4.5}$$

where $\hat{\Sigma}$ is the self-energy, $\otimes$ represents a convolution over the coordinates, $\boldsymbol{\sigma}$ is a vector of Pauli matrices in the spin space, and τ_3 is the third Pauli matrix in the Nambu space. Here the superconducting pair potential has the following matrix structure

$$\hat{\Delta}(\boldsymbol{r}_1, t_1; \boldsymbol{r}_2, t_2) = \delta(\boldsymbol{r}_1, t_1; \boldsymbol{r}_2, t_2)\begin{pmatrix} 0 & \Delta \\ \Delta^* & 0 \end{pmatrix}$$

and $\hat{G}_0^{-1}$ is the Green's function of a free electron

$$\hat{G}_0^{-1}(\boldsymbol{r}_2, t_2; \boldsymbol{r}_1', t_1') = \delta(\boldsymbol{r}_1, t_1, \boldsymbol{r}_1', t_1')\left(i\tau_3\frac{\partial}{\partial t_1} + \frac{1}{2m}\hat{\boldsymbol{\partial}}_{\boldsymbol{r}_1}^2 + \epsilon_F\right),$$

where $\hat{\boldsymbol{\partial}}_{\boldsymbol{r}} = \nabla_{\boldsymbol{r}} - ie\boldsymbol{A}\tau_3$ is the gauge-invariant spatial derivative with the vector potential $\boldsymbol{A}$.

In Eq. (4.5), it is assumed that $\hbar = k_B = 1$. The identity matrix in the Nambu (τ_0) and spin space (σ_0) are also suppressed below. The matrix dimensions are fulfilled with these identity matrices where it is needed.

The Gorkov equation is indeed very powerful for studying various properties of superconductors. However, the double coordinate Green's functions are very cumbersome,

especially for inhomogeneous systems. Further approximations are needed to simplify the Gorkov equation. Quasiclassical method provides such a possibility by making use of the fact that the energy scale involved in the superconducting phenomena is much smaller than the characteristic energy of the normal state, namely the Fermi energy E_F. (Note that this may not be true for flat band superconductivity in Chapter 3 since the superconducting pair potential is enhanced.)

The Green's function in Eq. (4.4) oscillates as a function of the relative coordinate $\boldsymbol{r}_1 - \boldsymbol{r}_2$ with the scale of the Fermi wavelength λ_F [88], which is typically of the order of a nanometer. It is much smaller than the superconducting coherence length ξ_0 in Eq. (2.16). This is equivalent to the above mentioned limit $\Delta \ll E_F$. The information contained in this oscillation may be ignored, since the contributions of this oscillation to the effects in superconducting state are very small. This can be done by integrating over the relative coordinate $\boldsymbol{r} = \boldsymbol{r}_1 - \boldsymbol{r}_2$. This yields the Wigner transform of the Green's function

$$\hat{G}(\boldsymbol{R}, \boldsymbol{p}) = \int d\boldsymbol{r} e^{-i\boldsymbol{p}\cdot\boldsymbol{r}} \hat{G}\left(\boldsymbol{R} + \frac{\boldsymbol{r}}{2}, \boldsymbol{R} - \frac{\boldsymbol{r}}{2}\right),$$

where $\boldsymbol{R} = (\boldsymbol{r}_1 + \boldsymbol{r}_2)/2$ is the center-of-mass coordinate. This is a highly peaked function around $|\boldsymbol{p}| \approx p_F$. If we take the Fourier transform of this Green's function by writing $\boldsymbol{p} = p_F \hat{p}$, the momentum integral can be transformed into an energy integral as in Eq. (2.12).

The quasiclassical Green's function is defined as

$$\hat{g}(\hat{p}, \boldsymbol{R}) = \frac{i}{\pi} \int d\xi_{\boldsymbol{p}} \hat{G}(\xi_{\boldsymbol{p}}, \hat{p}, \boldsymbol{R}),$$

where $\xi_{\boldsymbol{p}} = p^2/(2m) - \epsilon_F$ is the normal state energy spectrum. With the quasiclassical Green's function, the Gorkov equation reduces to the Eilenberger equation (via the gradient expansion, see the derivation in Ref. [89] as an example). In the stationary case it is written as [90–92]

$$-\boldsymbol{v}_F \left[\hat{\boldsymbol{\partial}}_{\boldsymbol{R}}, \hat{g}(\hat{p}, \boldsymbol{R})\right] = \left[-i\epsilon\tau_3 + i\boldsymbol{h}\cdot\boldsymbol{\sigma}\tau_3 + \hat{\Delta} + \hat{\Sigma}, \hat{g}(\hat{p}, \boldsymbol{R})\right],$$

where $\boldsymbol{v}_F$ is the Fermi velocity, and the superconducting pair potential has the structure

$$\hat{\Delta} = \sigma_0 \begin{pmatrix} 0 & \Delta(\boldsymbol{R}) \\ \Delta^*(\boldsymbol{R}) & 0 \end{pmatrix}.$$

This equation has to be supplemented by the boundary condition $\hat{g}^2 = \hat{1}$ [93].

The Eilenberger equation is much easier to solve compared to the original Gorkov equation. The Green's function now depends on the center-of-mass coordinate and the direction of the quasiparticles. The Eilenberger equation is especially useful for clean superconductors.

4.2.2 Diffusive limit

The Eilenberger equation can be further simplified for the diffusive limit, namely, in the case when the elastic scattering self-energy is much larger than any other energy scales in the problem. This is equivalent to the case where elastic mean free path l_{el} is much smaller than all the other length scales, and the Green's function is nearly isotropic. This allows the expansion of the Green's function $\hat{g}(\hat{p}, \boldsymbol{R})$ with respect to $\hat{p}$ in spherical harmonics. Taking the lowest order in $\hat{p}$ (namely, only s-wave term) and angular averaging of the Eilenberger equation results in a diffusion equation, known as the Usadel equation [94]

$$D\nabla \cdot (\hat{g}\nabla\hat{g}) - \left[-i\epsilon\tau_3 + i\boldsymbol{h}\cdot\boldsymbol{\sigma}\tau_3 + \hat{\Delta} + \hat{\Sigma}, \hat{g}\right] = 0, \tag{4.6}$$

where D is the diffusion constant in Eq. (2.17). Here the quasiclassical Green's function is a function of $\boldsymbol{R}$ and the energy ϵ.

The self-energy consists of elastic and inelastic parts. In the simplest approximation, the inelastic part of the self-energy can be described by energy independent Dynes term [95]

$$\hat{\Sigma}_{\text{inel}} = \Gamma\tau_3,$$

where Γ is called the Dynes parameter. It affects the spectral properties of the system, for example, the density of states. Beyond this limit, the most relevant inelastic processes are the particle-particle and particle-phonon collisions. These collisions do not conserve the energy but conserve the total spin. These collisions for quasiclassical approximation are discussed in Ref. [96, 97].

There are two main contributions for elastic scattering, which conserve the energy. One arises from the nonmagnetic impurities, and which has already been taken into account in the diffusion constant by the electron mean free path l_{el}. Another one is scattering arising from magnetic impurities, which relax the spin. Two types of mechanisms are possible due to the spin-orbit coupling and spin-flip processes. Within the Born approximation, these terms can be expressed as [83, 84]

$$\hat{\Sigma}_{so} = \frac{1}{8\tau_{so}}\boldsymbol{\sigma}\cdot\hat{g}\boldsymbol{\sigma}, \tag{4.7}$$

$$\hat{\Sigma}_{sf} = \frac{1}{8\tau_{sf}}\boldsymbol{\sigma}\cdot\tau_3\hat{g}\tau_3\boldsymbol{\sigma},$$

where τ_{so} and τ_{sf} are the spin-orbit and spin-flip relaxation times, respectively. The spin-orbit coupling considered here is extrinsic, namely, originating from a random impurity potential. Since only the centrosymmetric superconductors are considered in this thesis, the intrinsic spin-orbit coupling originating from the lack of inversion symmetry is excluded.

In the case where the spin-splitting is induced by an external magnetic field, the contribution of the vector potential can be approximated as an effective self-energy as

$$\hat{\Sigma}_{orb} = \frac{1}{\tau_{orb}} \tau_3 \hat{g} \tau_3,$$

where τ_{orb} is the orbital depairing rate. For a superconducting thin film with thickness t_S, τ_{orb} can be determined in the case of a parallel magnetic field H [98, 99]. Moreover, in the presence of supercurrent, the effective vector potential (see Sec. 2.1.2) also contributes to τ_{orb} [100]. Then the orbital depairing rate can be written as

$$\frac{1}{\tau_{orb}} = \frac{D(eHt_S)^2}{6} + \frac{D\Delta(\nabla\varphi)^2}{2}, \tag{4.8}$$

where φ is the phase of the superconducting pair potential.

4.2.3 Matsubara technique

In thermal equilibrium, physical observables are independent of time. One can introduce an imaginary time $\tau = it$ to describe the time evolution of an operator to take into account a finite temperature. It was shown by Matsubara that the Green's function is time-ordered along this imaginary time within the interval $0 < \tau < 1/T$, where T is the temperature [101]. Then Eq. (4.4) can be written as

$$\hat{G}(\boldsymbol{r}_1, \boldsymbol{r}_2; \tau_1 - \tau_2) = \langle T_\tau \hat{\psi}(\boldsymbol{r}_1, \tau_1) \hat{\psi}^\dagger(\boldsymbol{r}_2, \tau_2) \rangle,$$

where T_τ means time-ordering in τ. It was also shown that, all the necessary information is contained in the Green's function for a discrete set of energies $\epsilon + i\Gamma = i\omega_n$ [101]. Here $\omega_n = (2n+1)\pi T$ are the Matsubara fermionic frequencies (energies) and n is an integer. Then the Usadel equation can be written as

$$D\nabla \cdot (\hat{g}\nabla\hat{g}) - \left[\omega_n \tau_3 + i\boldsymbol{h}\cdot\boldsymbol{\sigma}\tau_3 + \hat{\Delta} + \hat{\Sigma}_{so} + \hat{\Sigma}_{sf} + \hat{\Sigma}_{orb}, \hat{g}\right] = 0. \tag{4.9}$$

The convenience of the Matsubara technique is that the physical observables are directly related to the solution of the Usadel equation in Eq. (4.9). For example, the superconducting pair potential is determined by the self-consistency equation as

$$\Delta = \frac{1}{2}\pi T\gamma \sum_{\omega_n > 0}^{\omega_D} \mathrm{Tr}(\tau_1 \hat{g}), \tag{4.10}$$

where ω_D is the BCS cutoff energy. Another important quantity is the superconducting free energy related to its normal state. It can be written in terms of the quasiclassical

Green's function as [102] (also derived in Article IV)

$$f_{sn} = f_s - f_n = \pi T N_0 \sum_{\omega_n>0} \mathrm{Tr}\left\{(\omega_n + i\boldsymbol{h}\cdot\boldsymbol{\sigma})(\hat{1}-\tau_3\hat{g}) - \frac{1}{2}\hat{\Delta}\hat{g} + \frac{D}{4}(\nabla\hat{g})^2 \right.$$
$$+\frac{1}{16\tau_{so}}\left[3\cdot\hat{1} - (\boldsymbol{\sigma}\hat{g})\cdot(\boldsymbol{\sigma}\hat{g})\right] + \frac{1}{16\tau_{sf}}\left[3\cdot\hat{1} - (\boldsymbol{\sigma}\tau_3\hat{g})\cdot(\boldsymbol{\sigma}\tau_3\hat{g})\right] \quad (4.11)$$
$$\left.+\frac{1}{2\tau_{orb}}\left[\hat{1} - (\tau_3\hat{g})^2\right]\right\},$$

where $f_{sn} = f_{sn}[\boldsymbol{h}]$, $\hat{\Delta}$ and $\hat{g}$ are self-consistent values of the pair potential and the Green's function.

When a system which is driven out of equilibrium, a time dependent or a dissipative state is created due to the nonequilibrium distribution of excitations, for example f_T and f_L modes in Sec. 2.1.2. There are two ways to include these excitations. One is an analytical continuation from imaginary into the real frequency axis [96, 103], the other one is dealing with real-time Green's functions defined with special rules of time-ordering [104], known as the Keldysh technique as discussed in the next section.

4.2.4 Keldysh technique

If the system is in thermal equilibrium at a time $t_0 = -\infty$, then the time evolution of this system out of equilibrium is described by a forward and backward propagator (an expectation value of a product of field operators). It was shown by Keldysh that the proper time ordering T_C of the Green's function is achieved along a time contour with a forward and backward branch running parallel to the real-time axis [104]. This ordering splits the Green's function to different analytical parts, depending on which branch the time arguments are on. The auxiliary Green's functions are defined as

$$\hat{G}^{>}(\boldsymbol{r}_1,t_1;\boldsymbol{r}_2,t_2) = -i\langle\hat{\psi}(\boldsymbol{r}_1,t_1)\hat{\psi}^\dagger(\boldsymbol{r}_2,t_2)\rangle$$
$$\hat{G}^{<}(\boldsymbol{r}_1,t_1;\boldsymbol{r}_2,t_2) = i\langle\hat{\psi}^\dagger(\boldsymbol{r}_1,t_1)\hat{\psi}(\boldsymbol{r}_2,t_2)\rangle.$$

The physical observables related to nonequilibrium effects can be expressed in terms of these Green's functions. For convenience, we can take appropriate linear combinations of these Green's functions, by introducing retarded (advanced) Green's function $G^{R(A)}$ and the Keldysh Green's function G^K as

$$\hat{G}^R(\boldsymbol{r}_1,t_1;\boldsymbol{r}_2,t_2) = \Theta(t_1-t_1')[\hat{G}^{<}(\boldsymbol{r}_1,t_1;\boldsymbol{r}_2,t_2) - \hat{G}^{>}(\boldsymbol{r}_1,t_1;\boldsymbol{r}_2,t_2)]$$
$$\hat{G}^A(\boldsymbol{r}_1,t_1;\boldsymbol{r}_2,t_2) = -\Theta(t_1'-t_1)[\hat{G}^{<}(\boldsymbol{r}_1,t_1;\boldsymbol{r}_2,t_2) - \hat{G}^{>}(\boldsymbol{r}_1,t_1;\boldsymbol{r}_2,t_2)]$$
$$\hat{G}^K(\boldsymbol{r}_1,t_1;\boldsymbol{r}_2,t_2) = \hat{G}^{<}(\boldsymbol{r}_1,t_1;\boldsymbol{r}_2,t_2) + \hat{G}^{>}(\boldsymbol{r}_1,t_1;\boldsymbol{r}_2,t_2),$$

where $\Theta(t)$ is a Heaviside step function in time.

We take the quasiclassical approximation, and write these Green's function in a matrix form in the Keldysh space as [105]

$$\check{g} = \begin{pmatrix} \hat{g}^R & \hat{g}^K \\ 0 & \hat{g}^A \end{pmatrix}, \tag{4.12}$$

which satisfies the Usadel equation in the diffusive limit (in steady state)

$$D\nabla \cdot (\check{g}\nabla\check{g}) - \left[-i(\epsilon + i\Gamma)\tau_3 + i\boldsymbol{h}\cdot\boldsymbol{\sigma}\tau_3 + \check{\Delta} + \check{\Sigma}_{so} + \check{\Sigma}_{sf} + \check{\Sigma}_{orb}, \check{g}\right] = 0. \tag{4.13}$$

Here, the self-energies in the commutator follow the structure of the Green's function $\check{g}$ in Eq. (4.12), and the other terms are diagonal in the Keldysh space.

The retarded and advanced Green's functions contain the information on the eigenstates of the system, namely, energy dependent properties of the system. For example, the density of states for each spin species can be written as

$$N_s^{\uparrow/\downarrow} = \frac{1}{4} N_0 \mathrm{Re}\left\{\mathrm{Tr}\left[(\tau_3 \pm \sigma_s\tau_3)\,\hat{g}^R\right]\right\}, \tag{4.14}$$

where $s = 1, 2, 3$ represents the spin component. The retarded and advanced Green's functions are related as $\hat{g}^A = -\tau_3\hat{g}^{R\dagger}\tau_3$. The retarded (advanced) Green's function can also be obtained from the Matsubara Green's function by analytical continuation $i\omega_n \to \epsilon \pm i\Gamma$ with positive (negative) ω_n.

The Keldysh Green's function contains information on the nonequilibrium distribution functions. This can be seen from the normalization condition $\check{g}^2 = \check{1}$. It yields $(\hat{g}^R)^2 = (\hat{g}^A)^2 = \hat{1}$ and requires the Keldysh Green's function to be related to the retarded and advanced Green's functions via

$$\hat{g}^K = \hat{g}^R\hat{f} - \hat{f}\hat{g}^A, \tag{4.15}$$

where $\hat{f}$ is called the distribution matrix. It was shown that $\hat{f} = n_0\hat{1}$ in thermal equilibrium [106], where

$$n_0 = \tanh\left(\frac{\epsilon}{2T}\right) \tag{4.16}$$

is the equilibrium distribution function. Then, regarding to the nonequilibrium effects, the distribution matrix $\hat{f}$ must contain a nonequilibrium distribution of excitations.

If we substitute Eq. (4.15) into the Keldysh part of the Usadel equation in Eq. (4.13), we obtain a linear equation for $\hat{f}$ as follows

$$\begin{aligned} &D\left\{\nabla^2\hat{f} + \left(\hat{g}^R\nabla\hat{g}^R\right)\nabla\hat{f} - \nabla\left[\hat{g}^R\left(\nabla\hat{f}\right)\hat{g}^A\right] - \nabla\hat{f}\left(\hat{g}^A\nabla\hat{g}^A\right)\right\} \\ &+ i(\epsilon + i\Gamma)\hat{g}^R\left[\tau_3, \hat{f}\right] - i(\epsilon + i\Gamma)\left[\tau_3, \hat{f}\right]\hat{g}^A - \hat{g}^R\left[\hat{\Delta}, \hat{f}\right] + \left[\hat{\Delta}, \hat{f}\right]\hat{g}^A \\ &- i\hat{g}^R\left[\boldsymbol{h}\cdot\boldsymbol{\sigma}, \hat{f}\right] + i\left[\boldsymbol{h}\cdot\boldsymbol{\sigma}, \hat{f}\right]\hat{g}^A + \sum_{j=0,3}\sum_{i=1,2}\left[\frac{1}{8\tau_{sj}}\left(\hat{\Xi}_{ij}\hat{g}^A - \hat{g}^R\hat{\Xi}_{ij}\right)\right] = 0, \end{aligned} \tag{4.17}$$

where $\hat{\Xi}_{ij} = \sigma_i\tau_j\hat{g}^R[\hat{f},\sigma_i\tau_j] + [\hat{f},\sigma_i\tau_j]\hat{g}^A\sigma_i\tau_j$, and $\tau_{sj} = \tau_{so},\tau_{sf}$ for $j = 0,3$. In the derivation, the retarded and advanced part of the Usadel equation is substituted to the Keldysh part. We can see that there are no terms contributed from the orbital depairing mechanism. Namely, orbital depairing does not contribute to the spin-relaxation processes, rather it affects the equilibrium properties of the superconductor.

Since Eq. (4.17) is linear, it is convenient to parameterize the density matrix $\hat{f}$ for a general case of an inhomogeneous exchange field $\boldsymbol{h}$ as

$$\hat{f} = f_L + f_T\tau_3 + \sum_{j=1}^{3}(f_{Tj}\sigma_j + f_{Lj}\sigma_j\tau_3). \tag{4.18}$$

Here f_T and f_L are the charge and energy modes discussed in Sec. 2.1.2. The terms in the summation represent the nonequilibrium modes generalized for the spin-dependent case. For example, in the case of a homogeneous exchange field $\boldsymbol{h} = h\hat{z}$, f_{T3} represents the spin mode, and f_{L3} represents the spin energy mode. Moreover, their symmetries in energy also follows with T (symmetric) and L (antisymmetric) labelled modes.

We can further derive kinetic equations for each component of the distribution matrix $\hat{f}$. This can be done by multipling Eq. (4.17) by the different matrix components in Eq. (4.18) separately, and taking the trace of each matrix equation. This leads to a set of kinetic equations as follows [83, 84]

$$\nabla_k j_k^{sc} = H^{sc} + R^{sc} + S^{sc}, \tag{4.19}$$

where $k = x,y,z$ and s,c range between 0 to 3. The terms in the equation describe the spectral current tensor j_k^{sc}, the Hanle precession of spin caused by the exchange field H^{sc}, the conversion between the quasiparticles and the superconducting condensate R^{sc}, and the scattering processes with self energy S^{sc}, respectively. These terms are defined as

$$j_k^{sc} = \frac{1}{8}\mathrm{Tr}\left\{\sigma_s\tau_c\left[\nabla\hat{f} + \left(\hat{g}^R\nabla\hat{g}^R\right)\hat{f} - \hat{g}^R\left(\nabla\hat{f}\right)\hat{g}^A - \hat{f}\left(\hat{g}^A\nabla\hat{g}^A\right)\right]\right\} \tag{4.20a}$$

$$H^{sc} = \frac{1}{8}\mathrm{Tr}\left\{\sigma_s\tau_c\left(i\hat{g}^R\left[\boldsymbol{h}\cdot\boldsymbol{\sigma},\hat{f}\right] - i\left[\boldsymbol{h}\cdot\boldsymbol{\sigma},\hat{f}\right]\hat{g}^A\right)\right\} \tag{4.20b}$$

$$R^{sc} = \frac{1}{8}\mathrm{Tr}\left\{\sigma_s\tau_c\left(\hat{g}^R\left[\hat{\Delta},\hat{f}\right] - \left[\hat{\Delta},\hat{f}\right]\hat{g}^A\right)\right\} \tag{4.20c}$$

$$S^{sc} = \frac{1}{8}\mathrm{Tr}\left\{\sigma_s\tau_c\sum_{j=0,3}\sum_{i=1,2}\left[\frac{1}{8\tau_{sj}}\left(\hat{g}^R\hat{\Xi}_{ij} - \hat{\Xi}_{ij}\hat{g}^A\right)\right]\right\}. \tag{4.20d}$$

Solving these kinetic equations with proper boundary conditions, we can obtain all relevant observables from the Keldysh Green's function by using Eq. (4.15). For example, the superconducting pair potential can be determined self-consistently as

$$\Delta = \frac{\gamma}{16i}\int_{-E_c}^{E_c} d\epsilon\mathrm{Tr}\left[(\tau_1 - i\tau_2)\,\hat{g}^K(\epsilon)\right], \tag{4.21}$$

where E_c is the BCS cutoff energy. This equation contains both equilibrium and nonequilibrium contributions, as $\hat{g}^K = (\hat{g}^R - \hat{g}^A)\tanh[\epsilon/(2T)]$ in equilibrium. The nonequilibrium charge imbalance and spin accumulation can be calculated as

$$\mu(\boldsymbol{R}) = \int_{-\infty}^{\infty} \frac{d\epsilon}{16} \mathrm{Tr}[\hat{g}^K(\epsilon, \boldsymbol{R})] \tag{4.22}$$

$$\mu_s(\boldsymbol{R}) = \int_{-\infty}^{\infty} \frac{d\epsilon}{16} \mathrm{Tr}\{\sigma_s\tau_3[\hat{g}^K(\epsilon, \boldsymbol{R}) - \hat{g}^K_{eq}(\epsilon, \boldsymbol{R})]\}, \tag{4.23}$$

where $s = 1, 2, 3$ is the spin components. The energy integrals of the different components of the spectral current tensor yield charge, spin, energy, and spin-energy current densities [90]

$$J^c_k = \frac{\sigma_N}{2e} \int_{-\infty}^{\infty} d\epsilon j^{03}_k \tag{4.24a}$$

$$J^s_k = \frac{\sigma_N}{2e^2} \int_{-\infty}^{\infty} d\epsilon j^{s0}_k \tag{4.24b}$$

$$J^e_k = \frac{\sigma_N}{2e^2} \int_{-\infty}^{\infty} d\epsilon\epsilon j^{00}_k \tag{4.24c}$$

$$J^{se}_k = \frac{\sigma_N}{2e^2} \int_{-\infty}^{\infty} d\epsilon\epsilon j^{s3}_k, \tag{4.24d}$$

where $\sigma_N = 2e^2 D N_0$ is the normal state conductivity and N_0 is the density of states at the Fermi level.

The detailed forms of the kinetic equations and the nonequilibrium observables in particular cases are discussed in the following sections.

4.3 Homogeneous magnetization

The typical size of a domain in the ferromagnet is much larger than the superconducting coherence length ξ_0 of many superconductors. In such a situation, a homogeneous exchange field in a superconductor in a FI/S structure is a good assumption. This is also the case of an applied parallel magnetic field. With a homogeneous magnetization, the term representing the exchange field in the Usadel equation becomes $i\boldsymbol{h}\cdot\boldsymbol{\sigma}\tau_3 = ih\sigma_3\tau_3$. Moreover, the solution of the Usadel equation in equilibrium is independent of the gradient terms. Namely, only the commutator determines the solutions in Eqs. (4.9) and (4.13). For Eq. (4.13), we have

$$\left[-i(\epsilon + i\Gamma)\tau_3 + i\boldsymbol{h}\cdot\boldsymbol{\sigma}\tau_3 + \hat{\Delta} + \check{\Sigma}_{so} + \check{\Sigma}_{sf} + \check{\Sigma}_{orb}, \check{g}\right] = 0, \tag{4.25}$$

where

$$\hat{\Delta} = |\Delta| \left(\cos\varphi\tau_1 - \sin\varphi\tau_2\right),$$

and φ is the phase of the superconducting pair potential. This allows us to parameterize the retarded (or Matsubara) Green's function as

$$\hat{g}^R = g_{01}(\tau_1\cos\varphi - \tau_2\sin\varphi) + g_{03}\tau_3 + g_{31}\sigma_3(\tau_1\cos\varphi - \tau_2\sin\varphi) + g_{33}\sigma_3\tau_3, \tag{4.26}$$

where g_i are complex scalar functions. Substituting this equation to Eq. (4.14), we can write the total density of states and the density of states difference between the two spin species as

$$N_+ = N_\uparrow + N_\downarrow = \mathrm{Re}(g_{03}) \tag{4.27a}$$

$$N_- = N_\uparrow - N_\downarrow = \mathrm{Re}(g_{33}). \tag{4.27b}$$

In the absence of the spin relaxation processes, the Usadel equation in Eq. (4.25) can be solved analytically with the normalization condition $(\hat{g}^R)^2 = \hat{1}$. The solutions are

$$g_{01/31} = \frac{|\Delta|}{2}\left(\frac{1}{\sqrt{|\Delta|^2 - (\epsilon + i\Gamma - h)^2}} \pm \frac{1}{\sqrt{|\Delta|^2 - (\epsilon + i\Gamma + h)^2}}\right) \tag{4.28a}$$

$$\begin{aligned} g_{03/33} = -\frac{i}{2}\Bigg[&\epsilon\left(\frac{1}{\sqrt{|\Delta|^2 - (\epsilon + i\Gamma - h)^2}} \pm \frac{1}{\sqrt{|\Delta|^2 - (\epsilon + i\Gamma + h)^2}}\right) \\ &-h\left(\frac{1}{\sqrt{|\Delta|^2 - (\epsilon + i\Gamma - h)^2}} \mp \frac{1}{\sqrt{|\Delta|^2 - (\epsilon + i\Gamma + h)^2}}\right)\Bigg]. \end{aligned} \tag{4.28b}$$

The solutions in the Matsubara representation can be obtained by replacing $\epsilon + i\Gamma \to i\omega_n$. In the presence of spin relaxation processes, however, these solutions have to be determined numerically. Below, we solve the Usadel equation numerically and study the effects both in equilibrium and out of equilibrium in some particular cases. The numerical methods for solving the Usadel equation for homogeneous magnetization, and the integrations are summarized in Appendix B.3.

4.3.1 Effects in equilibrium

Superconducting pair potential

Matsubara Green's function technique is very efficient for calculating the superconducting pair potential in thermal equilibrium. With the parameterization in Eq. (4.26), the self-consistency equation in Eq. (4.10) becomes

$$|\Delta| = 2\pi T\gamma \sum_{\omega_n>0}^{\omega_D} g_{01}.$$

The sum over Matsubara frequency gives a temperature dependent cutoff $N_D = \omega_D/(2\pi T)$ to the sum over n. Consider the following relation

$$2\pi T \sum_{n=0}^{N_D(T)} \frac{1}{\omega_n} = 2\pi T \left(\sum_{n=0}^{N_D(T_c)} + \sum_{N_D(T_c)}^{N_D(T)} \right) \frac{1}{\omega_n} = \frac{1}{\gamma} + \log\left(\frac{T_c}{T}\right),$$

where the definition of γ is used in the first sum [91], and the second sum is evaluated with the harmonic series

$$\sum_{n=1}^{k} \frac{1}{n} \approx \log k.$$

Then the self-consistency equation becomes

$$|\Delta| \log\left(\frac{T}{T_c}\right) = 2\pi T \sum_{\omega_n>0} \left(g_{01} - \frac{|\Delta|}{\omega_n} \right). \tag{4.29}$$

The self-consistent calculation using this equation, together with the free energy density in Eq. (4.11) are shown in Fig. 4.2. The numerical methods used in the calculations are discussed in Appendix B.1. The Chandrasekhar-Clogston limit can also be determined analytically from the free energy in Eq. (4.11) in the absence of spin relaxation processes. In this case, with the parameterization in Eq. (4.26), the free energy becomes

$$f_{sn} = 4\pi T N_0 \sum_{\omega_n>0} \left[\omega_n(1-g_{03}) - \frac{1}{2}|\Delta| g_{01} - ihg_{33} \right].$$

Substituting the solutions in Eq. (4.28), and to the lowest order in temperature, we can determine the Chandrasekhar-Clogston limit as

$$f_{sn} \xrightarrow{T\to 0} -\pi T \frac{|\Delta|^2 - 2h_c^2}{2\sqrt{|\Delta|^2 - h_c^2}} = 0 \;\Rightarrow h_c = \frac{|\Delta|}{\sqrt{2}}.$$

We can see form Fig. 4.2(a) that the exchange field suppresses the superconducting pair potential $|\Delta|$ and the critical temperature T_c compared to the case $h = 0$. The effect of the spin-flip relaxation and the orbital depairing rate is similar. Both of the processes suppress $|\Delta|$ and T_c, and the critical field of the Chandrasekhar-Clogston limit, compared to the absence of the spin-relaxation processes [See Fig. 4.2(a,b)]. Although the spin-orbit relaxation also suppresses $|\Delta|$ and T_c compared to the case $h = 0$, the overall effect is reducing the effect of the exchange field (larger $|\Delta|$ compared to the absence of the spin-orbit relaxation), and increasing the critical field of the Chandrasekhar-Clogston limit. This can be seen from the red curve in Fig. 4.2(a,b). In the presence of a supercurrent, the dependence of $|\Delta|$ on the phase gradient is

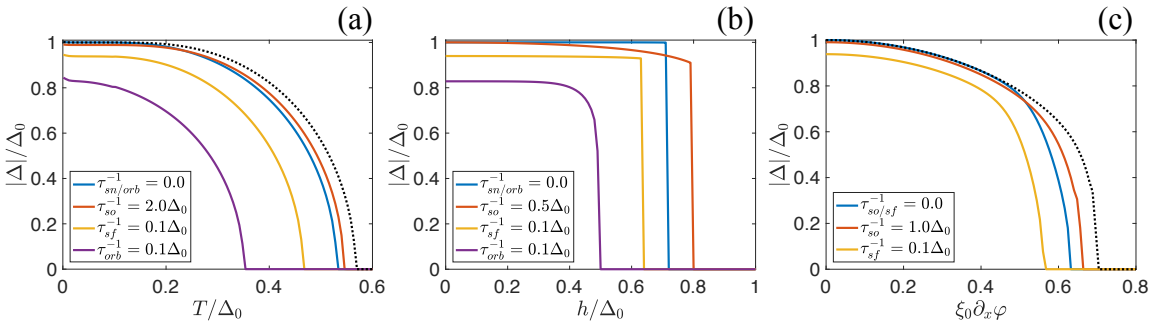

Figure 4.2: Superconducting pair potential as a function of temperature (a), exchange field (b), and the phase gradient (c). In (a) and (b), we defined the total spin-relaxation rate $\tau_{sn}^{-1} = \tau_{so}^{-1} + \tau_{sf}^{-1}$. The black dotted curve in (a) and (c) are the cases $h = 0$ and $\tau_{sn/orb}^{-1} = 0$. The parameters used in the calculations are $T = 0.05\Delta_0$ and $h = 0.3\Delta_0$ unless specified otherwise.

shown in Fig. 4.2(c). Here we consider a FI/S structure, so that the only contribution to the orbital depairing rate is the phase gradient $\xi_0\partial_x\varphi$. For different spin-relaxation processes, the phase gradient that makes $|\Delta| = 0$ corresponds to a critical phase gradient that destroys superconductivity.

Density of states

The density of states of a superconductor with a spin-splitting field can be calculated from Eq. (4.27). The results of the numerical calculations are shown in Fig. 4.3(b). We can see that the overall effect of the spin-relaxation processes is reshaping the peaks in the density of states. We also can see again that the spin-flip and orbital depairing rates suppress $|\Delta|$, and the spin-orbit relaxation reduce the effect of the spin-splitting field. This can be seen from the tendency of the combination of the two peaks around $\epsilon = \Delta_0$ in N_+ (blue curve).

Tunnelling conductance

The most common way to detect the spin splitting in a superconductor is by using a tunnelling junction. The tunnelling current through a NIS junction is given in Eq. (2.20). In the case of a ferromagnetic electrode with a non-vanishing spin polarization, this expression should be extended to include the polarization of the ferromagnetic electrode as [107]

$$I(V) = \frac{G_T}{e}\int_{-\infty}^{+\infty}(N_+ + PN_-)[f(\epsilon - eV) - f(\epsilon)], \tag{4.30}$$

where the polarization P is defined as

$$P = \frac{G_\uparrow - G_\downarrow}{G_\uparrow + G_\downarrow},$$

and G_s is the normal state conductance for spin $s = \uparrow / \downarrow$. In Fig. 4.3, the numerically calculated tunnelling conductance dI/dV is shown for a normal metal and ferromagnetic electrode, and the effects of different spin-relaxation processes are also considered. We can see that the tunnelling conductance with the normal metal electrode

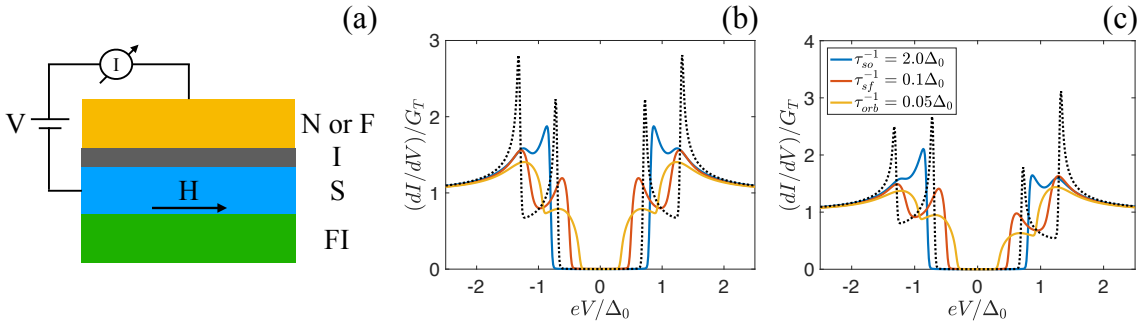

Figure 4.3: Tunnelling through a N(F)IS junction. (a) Schematics of the junction. Here the spin-splitting field is induced either by a parallel magnetic field H or a ferromagnetic insulator. (b) Tunnelling conductance with a normal metal electrode. (c) Tunnelling conductance with a ferromagnetic electrode with polarization $P = 0.2$. The black dotted line represents the tunnelling conductance in the absence of spin-relaxation processes. The parameters used in the calculations are $T = 0.01\Delta_0$ and $h = 0.3\Delta_0$.

(and hence $P = 0$) is proportional to the density of states of the superconductor, as discussed in Sec. 2.1.2. For the tunnelling conductance with the ferromagnetic electrode, the peaks are antisymmetric. This is due to the polarization of the conduction electrons in the ferromagnetic electrode. Therefore, the tunnelling conductance in this case can also be used to measure the polarization of the ferromagnetic materials.

Tunnel junction between two FI/S structures

As shown in Sec. 2.1.2, the tunnelling current through a SIS junction not only includes the quasiparticle tunnelling current, but a Josephson current is also created in the presence of a superconducting phase difference in the two superconductors. If we replace the superconductors in the SIS junction by superconductors with a spin-splitting field, new and interesting effects may arise due to the splitting of the density of states, especially from the noncollinearity of the spin-splitting fields. These effects are discussed in details in Article II. Below, the quasiparticle current and Josephson current are summarized.

In order to take into account the most general situation, we assume that the spin-splitting fields in the superconductors are induced by ferromagnetic insulators, and

a spin-polarized tunnelling barrier is placed in between the two FI/S structures, as shown in Fig. 4.4.

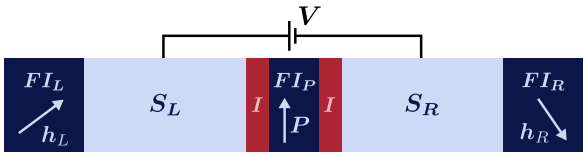

Figure 4.4: Schematics of a tunnel junction between two FI/S structures with a spin-polarized tunnelling barrier studied in Article II. The spin-splitting fields in the superconductors are induced by the neighbouring ferromagnetic insulators with different magnetization directions.

Here the spin-splitting field in the left (right) superconductor is induced by the left (right) ferromagnetic insulator with a magnetization direction $\boldsymbol{h}_L = h_L \boldsymbol{m}_L$ ($\boldsymbol{h}_R = h_R \boldsymbol{m}_R$). The spin-polarized tunnelling barrier is also a ferromagnetic insulator with polarization $\boldsymbol{P} = P\boldsymbol{m}_P$. The $\boldsymbol{m}_{L/R/P}$ is the unit vector pointing in the respective direction. In order to avoid magnetic proximity effect, the two superconductors are separated from the tunnelling barrier with thin insulators.

If we choose the polarization direction of the tunnelling barrier along the z axis $\boldsymbol{m}_P = (0, 0, 1)$, then the magnetization unit vectors of the two ferromagnetic insulators can be expressed as

$$\boldsymbol{m}_L = (\sin\alpha_L, 0, \cos\alpha_L)$$

$$\boldsymbol{m}_R = (\sin\alpha_R \cos\phi, \sin\alpha_R \sin\phi, \cos\alpha_R),$$

where $\alpha_{L/R}$ is the angle between the magnetization direction and the z axis, and ϕ is the magnetization angle in the xy plane. In the case of $\alpha_L = \alpha_R = 0$ or $\phi = 0$ and $\alpha_L = \alpha_R \pm (\pi)$, the magnetization directions in the two ferromagnetic insulators are in a collinear configuration. In the case of $\phi = 0$ and $\alpha_L \neq \alpha_R$, the magnetization directions in the two ferromagnetic insulators are in a coplanar configuration. The most general configuration is the case of $\alpha_L \neq \alpha_R$ and $\phi \neq 0$.

Since the two insulators separate the two superconductors from the tunnelling barrier, we can solve the Green's function in the two superconductors separately. The results can be used to calculate the total current through the double FI/S structure (see the derivation in Article IV)

$$I_t(t) = I + I_{J1} \sin\left(\varphi + \frac{2eVt}{\hbar}\right) + I_{J2} \cos\left(\varphi + \frac{2eVt}{\hbar}\right),$$

where I is the quasiparticle tunnelling current, I_{J1} is the usual Josephson critical current, and I_{J2} is the anomalous Josephson critical current. Below we discuss each component separately.

The quasiparticle tunnelling current can be expressed in terms of the solutions of the Green's functions as

$$\begin{aligned} I =& \frac{G_T}{2e}\int_{-\infty}^{+\infty} d\epsilon \Big[f(\epsilon - eV, T_L) - f(\epsilon, T_R)\Big]\Big\{N_+^L(\epsilon - eV)N_+^R(\epsilon) \\ &+ P\Big[N_+^L(\epsilon - eV)N_-^R(\epsilon)\boldsymbol{m}_R\cdot\boldsymbol{m}_P + N_-^L(\epsilon - eV)N_+^R(\epsilon)\boldsymbol{m}_L\cdot\boldsymbol{m}_P\Big] \\ &+ N_-^L(\epsilon - eV)N_-^R(\epsilon)\left[\boldsymbol{m}_L^{\parallel}\cdot\boldsymbol{m}_R^{\parallel} + \sqrt{1-P^2}\boldsymbol{m}_L^{\perp}\cdot\boldsymbol{m}_R^{\perp}\right]\Big\}, \end{aligned} \tag{4.32}$$

where

$$\begin{aligned} \boldsymbol{m}_{L/R}\cdot\boldsymbol{m}_P &= \cos\alpha_{L/R} \\ \boldsymbol{m}_L^{\parallel}\cdot\boldsymbol{m}_R^{\parallel} &= \cos\alpha_L\cos\alpha_R \\ \boldsymbol{m}_L^{\perp}\cdot\boldsymbol{m}_R^{\perp} &= \sin\alpha_L\sin\alpha_R\cos\phi. \end{aligned}$$

The integrand in the first line of Eq. (4.32) gives the usual quasiparticle tunnelling current in the absence of the exchange field. The terms proportional to $\boldsymbol{m}_{L/R}\cdot\boldsymbol{m}_P$ and $\boldsymbol{m}_L^{\parallel}\cdot\boldsymbol{m}_R^{\parallel}$ are related to the exchange field. These terms survive if the magnetization direction in the two ferromagnetic insulators are collinear. If we replace the left superconductor with a normal metal, these terms simply become $PN_-^R(\epsilon)\cos\alpha_R$, and Eq. (4.32) reduces to Eq. (4.30) in the case of $\alpha_R = 0$. The term $\boldsymbol{m}_L^{\perp}\cdot\boldsymbol{m}_R^{\perp}$ only exists in the noncollinear configuration.

We can see from Eq. (4.32) that the current strongly depends on the configurations of the spin-splitting fields. Drastic effects could take place if the magnetization directions differ by large angles. For simplicity, we fix $\alpha_L = 0$, and calculate the tunnelling conductance for different α_R by assuming the temperatures in the two superconductors are equal $T_L = T_R = T = 0.01\Delta_0$. The tunnelling conductance with different α_R are plotted in Fig. 4.5.

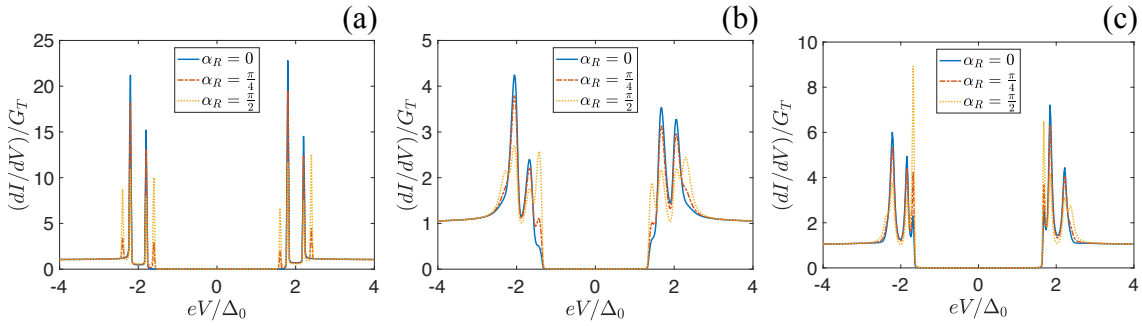

Figure 4.5: Tunnelling conductance of the system in Fig. 4.4 with polarization $P = 0.2$, (a) in the absence of spin-relaxation processes, (b) in the presence of spin-flip relaxation process $\tau_{sf}^{-1} = 0.05\Delta_0$, and (c) in the presence of spin-orbit relaxation process $\tau_{so}^{-1} = 0.5\Delta_0$. The strengths of the spin-splitting fields are $h_L = 0.1\Delta_0$ and $h_R = 0.3\Delta_0$, respectively.

We can see that in the collinear configurations of the spin-splitting fields, four peaks appear in the tunnelling conductance at $eV = \pm(\Delta_L + \Delta_R) \pm (h_L - h_R)$. This is an expected result since we assume that the strengths of the spin-splitting fields are different, and it is observed in many experiments with FI/S structures [64, 65, 85]. Interestingly, if the configurations are not collinear, four more peaks appear as $eV = \pm(\Delta_L+\Delta_R)\pm(h_L \pm h_R)$ and these peaks are higher for larger α_R. This is a new feature in the tunnelling conductance of two superconductors with spin-splitting fields.

The Josephson critical currents I_{J1} and I_{J2} can be expressed in terms of the solutions of the Green's functions as

$$I_{J1} = A_0\sqrt{1-P^2} + A_3\left[\sqrt{1-P^2}\boldsymbol{m}_L^{\parallel}\cdot\boldsymbol{m}_R^{\parallel} + \boldsymbol{m}_L^{\perp}\cdot\boldsymbol{m}_R^{\perp}\right] - B_3 P\boldsymbol{m}_P\cdot(\boldsymbol{m}_L\times\boldsymbol{m}_R)$$

$$I_{J2} = B_0\sqrt{1-P^2} + B_3\left[\sqrt{1-P^2}\boldsymbol{m}_L^{\parallel}\cdot\boldsymbol{m}_R^{\parallel} + \boldsymbol{m}_L^{\perp}\cdot\boldsymbol{m}_R^{\perp}\right] + A_3 P\boldsymbol{m}_P\cdot(\boldsymbol{m}_L\times\boldsymbol{m}_R),$$

where

$$\boldsymbol{m}_P\cdot(\boldsymbol{m}_L\times\boldsymbol{m}_R) = \sin\alpha_L\sin\alpha_R\sin\phi$$

and

$$A_i = \frac{G_T}{2e}\int_{-\infty}^{+\infty} d\epsilon\left\{f(\epsilon,T_R)\mathrm{Re}\left[g_{i1}^L(\epsilon-eV)\right]\mathrm{Im}\left[g_{i1}^R(\epsilon)\right] + f(\epsilon-eV,T_L)\mathrm{Im}\left[g_{i1}^L(\epsilon-eV)\right]\mathrm{Re}\left[g_{i1}^R(\epsilon)\right]\right\}$$

$$B_i = \frac{G_T}{2e}\int_{-\infty}^{+\infty} d\epsilon\left[f(\epsilon-eV,T_L) - f(\epsilon,T_R)\right]\mathrm{Im}\left[g_{i1}^L(\epsilon-eV)\right]\mathrm{Im}\left[g_{i1}^R(\epsilon)\right],$$

where $i = 0, 3$.

If we assume $T_L = T_R = T$, B_i terms are zero. Then the Josephson critical currents depend only on the A_i terms. The dependence of these terms on the spin-splitting fields and the spin-relaxation rates are plotted in Fig. 4.6. These terms can also be determined in the absence of spin-relaxation processes and in the case $h_L = h_R = h$ for $T \to 0$ as

$$A_0 = \frac{G_T\pi|\Delta|}{2e}\eta$$

$$A_3 = -\frac{G_T\pi|\Delta|}{2e}(\eta-1),$$

where

$$\eta = \frac{32|\Delta|^2\left(9h^4 - 32h^2|\Delta|^2 + 256|\Delta|^4\right)}{\left(16|\Delta|^2 - h^2\right)^3} - 1.$$

We can see from Fig. 4.6 and the expressions for A_is that $\eta = 1$ for $h = 0$, so that $A_3 = 0$ and A_0 gives the Ambegaokar-Baratoff relation in Eq. (2.28) at $T = 0$. Namely, A_3 is nonzero only in the presence of a spin-splitting field. This gives a correction to I_{J1} and a nonzero I_{J2} for a general configuration of the magnetization

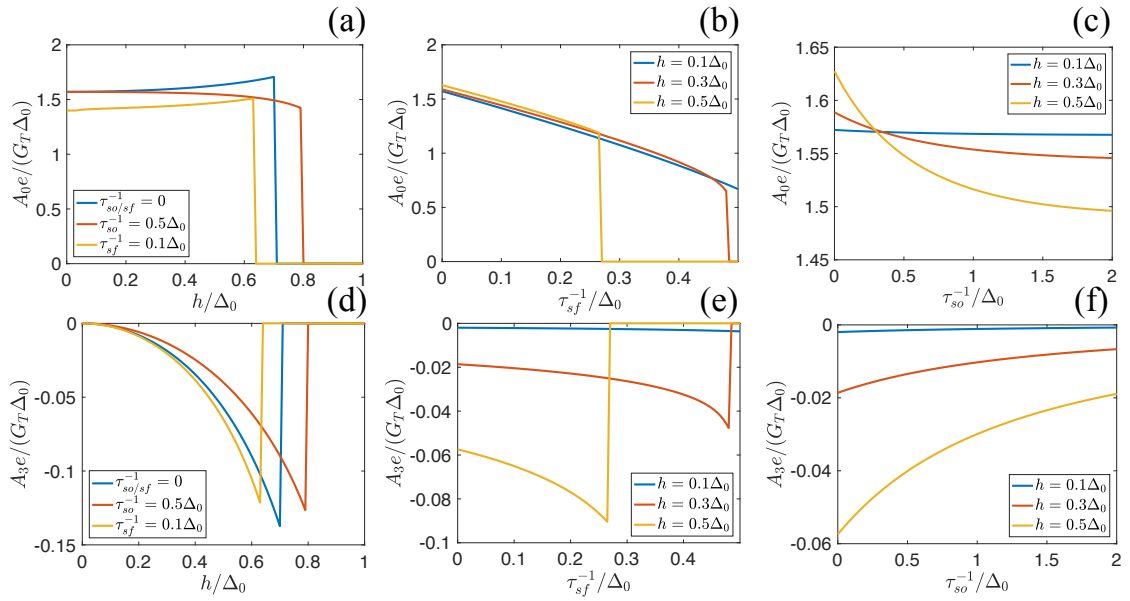

Figure 4.6: Integrals in the Josephson critical currents. The panels (a)-(c) are the spin-splitting field, spin-flip relaxation rate, and spin-orbit relaxation rate dependence of A_0. The panels (d)-(f) are the dependence of those of A_3. The calculations are done for $h_L = h_R = h$ and $\tau_{so/sf}^{-1,L} = \tau_{so/sf}^{-1,R} = \tau_{so/sf}^{-1}$ at a temperature $T_L = T_R = T = 0.01\Delta_0$.

directions. Moreover, for a strong polarization $P = 1$, I_{J2} is the only contribution to the Josephson current in the case $T_L = T_R$.

In nonmagnetic Josephson junctions, I_{J2} is nonzero when applying a voltage, and known as the cosine term [108, 109]. But here it is finite in the absence of a voltage with noncollinear spin-splitting fields. Then this is similar to the so-called anomalous Josephson current that appears in some systems with inhomogeneous magnetization and spin-orbit interaction [110].

4.3.2 Effects out of equilibrium

Many nonequilibrium effects in superconductors with a spin-splitting field are studied in a nonlocal lateral structure shown in Fig. 4.7(a). It consists of a superconducting wire, an injector electrode (normal or ferromagnetic), and a ferromagnetic detector electrode placed at a distance L_{det} from the injector electrode. The spin-splitting field is induced either by an in-plane magnetic field, or by a ferromagnetic insulator attached to the superconducting wire.

In this section, we study the nonequilibrium effects in such a structure in the presence of an externally induced supercurrent.

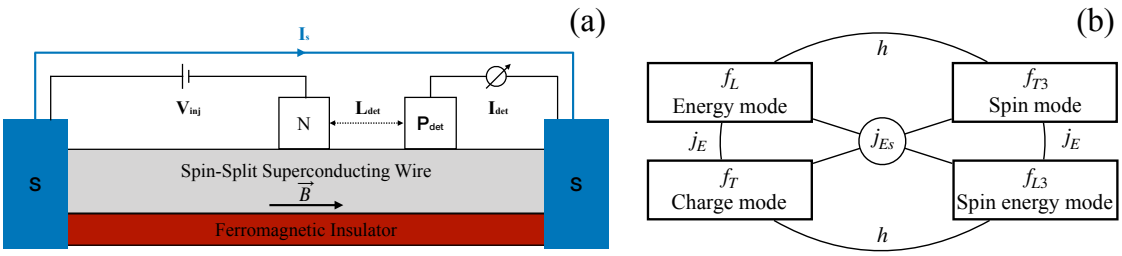

Figure 4.7: (a) The nonlocal lateral structure studied in Article III. A ferromagnetic detector is placed a distance L_{det} away from the normal metal injector on a superconducting wire with a spin-splitting field together with an externally induced supercurrent. (b) Couplings between different nonequilibrium modes via the spin-splitting field and the spectral supercurrents.

Kinetic equations

In the presence of supercurrent, the kinetic equations related to the nonequilibrium effects in Eq. (4.19) in a homogeneous magnetization become

$$\nabla \cdot \begin{pmatrix} j_e \\ j_s \\ j_c \\ j_{se} \end{pmatrix} = \begin{pmatrix} 0 & 0 & 0 & 0 \\ 0 & S_{T3} & 0 & 0 \\ 0 & 0 & R_T & R_{L3} \\ 0 & 0 & R_{L3} & R_T + S_{L3} \end{pmatrix} \begin{pmatrix} f_L \\ f_{T3} \\ f_T \\ f_{L3} \end{pmatrix}, \tag{4.37}$$

where

$$\begin{pmatrix} j_e \\ j_s \\ j_c \\ j_{se} \end{pmatrix} = \begin{pmatrix} D_L\nabla & D_{T3}\nabla & j_E\nabla\varphi & j_{Es}\nabla\varphi \\ D_{T3}\nabla & D_L\nabla & j_{Es}\nabla\varphi & j_E\nabla\varphi \\ j_E\nabla\varphi & j_{Es}\nabla\varphi & D_T\nabla & D_{L3}\nabla \\ j_{Es}\nabla\varphi & j_E\nabla\varphi & D_{L3}\nabla & D_T\nabla \end{pmatrix} \begin{pmatrix} f_L \\ f_{T3} \\ f_T \\ f_{L3} \end{pmatrix}. \tag{4.38}$$

Here the kinetic coefficients $D_{L/T/T3/L3}$, $R_{T/L3}$, and $S_{T3/L3}$ are defined in terms of the Green's function $\hat{g}^{R(A)}$. The definitions and the energy dependence of these coefficients are given in Appendix A. The terms with the phase gradient (considered to be a constant) are the spectral supercurrents, the total spectral supercurrent $j_E = j_E^{\uparrow} + j_E^{\downarrow}$ and spectral spin supercurrent $j_E = j_E^{\uparrow} - j_E^{\downarrow}$, where j_E^s is the spectral supercurrent for spin $s = \uparrow / \downarrow$. Note that the energy mode f_L does not have a source term. This is because we only consider systems with sizes much smaller than the inelastic relaxation length. This makes f_L mode long-ranged.

In equilibrium, $g^K = (g^R - g^A)n_0$, where n_0 is the equilibrium distribution function in Eq. (4.16). From the charge and spin-energy current densities in Eq. (4.24), the supercurrent I_s and spin-energy current I_{se} can be obtained as

$$I_s = \frac{\sigma_N W}{2e} \int_{-\infty}^{\infty} d\epsilon j_E \tanh\left(\frac{\epsilon}{2T}\right) \nabla\varphi \tag{4.39}$$

$$I_{se} = \frac{\sigma_N W}{2e^2} \int_{-\infty}^{\infty} d\epsilon\epsilon j_{Es} \tanh\left(\frac{\epsilon}{2T}\right) \nabla\varphi,$$

where W is the cross-sectional area of the superconducting wire. In the absence of spin relaxation processes, these integrals can be solved analytically at $T \to 0$. With the solutions in Eq. (4.28), we obtain

$$I_s = \frac{\sigma_N W \pi |\Delta|}{2e} \nabla\varphi$$

$$I_{se} = \frac{h}{e} I_s.$$

Out of equilibrium, we can see from Eq. (4.37) and Eq. (4.38) that all the nonequilibrium modes are coupled, as shown in Fig. 4.7(b). In the absence of the spin-splitting field, f_L and f_T modes are coupled by j_E. This coupling leads to charge imbalance in the presence of a temperature gradient [17, 18]. In the absence of the supercurrent, h couples f_L and f_{T3} (as well as f_T and f_{L3}). This coupling leads to the long-range spin accumulation due to the long-range feature of f_L [76–82]. The combinations of the above may lead to interesting effects. Especially, the coupling of f_T and f_{T3} through f_L. Since f_L is a long-range mode, it is possible to convert a short-range charge imbalance to a long-range spin accumulation. This effect is discussed in Article III. The summary of the discussions are given in this subsection.

In order to achieve the charge-spin conversion, we consider a nonmagnetic injector electrode attached at $x = 0$. The injection of quasiparticle current from the injector electrode requires suitable boundary conditions to solve the kinetic equations in Eq. (4.37).

Boundary conditions

The injection of matrix quasiparticle current is described by the boundary conditions at the tunnelling interface [111] extended to the spin-dependent case [83, 84]

$$\begin{pmatrix} [j_c] \\ [j_e] \\ [j_s] \\ [j_{se}] \end{pmatrix} = k_I \begin{pmatrix} N_+ & PN_- & PN_+ & N_- \\ PN_- & N_+ & N_- & PN_+ \\ PN_+ & N_- & N_+ & PN_- \\ N_- & PN_+ & PN_- & N_+ \end{pmatrix} \begin{pmatrix} [f_T] \\ [f_L] \\ [f_{T3}] \\ [f_{L3}] \end{pmatrix}, \tag{4.40}$$

where $k_I = 1/(R_{I\square}\sigma_N)$ is the injector transparency, $R_{I\square}$ is the injector interface resistance per unit area and σ_N is the normal state conductivity, P is the spin-polarization of the tunnelling barrier, $N_\pm$ is the density of states in Eq. (4.27).

The spectral currents on the left-hand side of Eq. (4.40) are the currents at the injector. The nonequilibrium modes on the right-hand side of Eq. (4.40) are the difference between nonequilibrium modes in the superconducting wire and the injector electrode

$[f_k] = f_k^S - f_k^{N/F}$, where $k = T, L, T3, L3$. For a normal metal injector, which we are considering, $[f_k^N] = (n_+, n_-, 0, 0)^\top$, where $\top$ means transpose, $n_\pm = [n_0(\epsilon - eV) \pm n_0(\epsilon + eV)]/2$ is the voltage-biased distribution function in the normal metal electrode, and n_0 is the equilibrium distribution function in Eq. (4.16).

Superconducting pair potential

The superconducting pair potential used to calculate the kinetic coefficients should be determined self-consistently. With the Keldysh technique, the self-consistent calculation is given in Eq. (4.21). With the parameterization in Eq. (4.26), it becomes

$$|\Delta| = \frac{\gamma}{2} \int_{-E_c}^{E_c} d\epsilon \left\{ \mathrm{Im}(g_{01}^R) f_L + \mathrm{Im}(g_{31}^R) f_{T3} + i \left[\mathrm{Re}(g_{01}^R) f_T + \mathrm{Re}(g_{31}^R) f_{L3} \right] \right\}.$$

If the superconductor couples to the injection electrode via a tunnelling junction, the spectral properties of the superconductor are not affected by the nonequilibrium modes within the leading order in the interface transmission. Then only the first term in the integrand (with $f_L = n_0$) is relevant for the self-consistent calculations, and $|\Delta|$ is the same as the superconducting pair potential in equilibrium, and its properties are discussed in Sec. 4.3.1.

Spin accumulation and nonlocal conductance

The injection of quasiparticle current from a normal metal injector creates charge imbalance and spin accumulation in the superconducting wire. With the parameterization in Eq. (4.26), these quantities in Eq. (4.22) and Eq. (4.23) become

$$\mu = \frac{1}{2} \int_0^\infty d\epsilon (N_+ f_T + N_- f_{L3}) \tag{4.41}$$

$$\mu_z = \frac{1}{2} \int_0^\infty d\epsilon [N_+ f_{T3} + N_- (f_L - n_0)]. \tag{4.42}$$

Due to the couplings between the nonequilibrium modes, injected quasiparticle current creates all the modes. The coupling between these modes leads to different nonequilibrium effects. The charge imbalance and spin accumulation representing different nonequilibrium effects are shown in Fig. 4.8. The numerical methods for solving the boundary value problems and the integration of array functions are introduced in Appendix B.2 and Appendix B.3, respectively.

As we can see from Eq. (4.41) and Eq. (4.42), via N_-, the spin-splitting field leads to the fact that f_{L3} and f_L modes contribute to the charge imbalance and spin accumulation, respectively. These are shown as the red curves in Fig. 4.8(a). Since f_L modes only relaxes with inelastic scattering processes, it is linear in position and also makes the spin accumulation long-ranged [79]. Through the supercurrent, the charge imbalance (spin accumulation) converts into the spin accumulation (charge imbalance). These are shown as the blue curves in Fig. 4.8(a). Since these conversions contain f_L mode, the supercurrent induced terms are also long-ranged.

We can see from the boundary conditions in Eq. (4.40) that the pure charge imbalance is odd in applied voltage, while the heat induced spin accumulation is even. Thus, in the linear response regime, the supercurrent solely induces the conversion between the charge imbalance to the spin accumulation. In article III, we study the dependence of spin accumulation in the linear response regime on various parameters.

In many experiments, the spin accumulation is detected by the nonlocal conductance. The nonlocal conductance is determined from the current through the detector in the case of a zero bias $V_{det} = 0$ at the detector

$$g_{nl} = \frac{dI_{det}}{dV_{inj}},$$

where

$$I_{det} = G_{det}\left(\mu + P_{det}\mu_z\right).$$

Here G_{det} is the detector interface conductance in the normal state, P_{det} is the polarization of the ferromagnetic detector, μ and μ_z are the charge imbalance and spin accumulation in Eq. (4.41) and Eq. (4.42), respectively.

The nonlocal conductance can be separated into four components in terms of the symmetry with respect to V_{inj} and P_{det} as

$$g_{nl} = g_{\text{charge}} + g^s_{\text{charge}} + (g_{\text{super}} + g_{\text{heat}})P_{det}.$$

Since g_{nl} is a result of differentiation of I_{det} with respect to V_{inj}, the pure charge imbalance g_{charge} is even with respect to V_{inj} and P_{det}. The supercurrent induced charge imbalance in the presence of a temperature gradient results to g^s_{charge}, which is odd in V_{inj}. The term g_{heat} is the long-range spin accumulation due to the heat injection. This term is odd in V_{inj} and P_{det}. Finally, g_{super}, which is odd in P_{det} and even in V_{inj}, is the term caused by the supercurrent induced charge-spin conversion.

With this symmetry analysis, we can subtract the terms which are odd in the detector polarization, and plot the results in Fig. 4.8(b,c). We can see that g_{heat} is antisymmetric with respect to V_{inj}, while g_{super} is symmetric. The total conductance is asymmetric due to these two contributions.

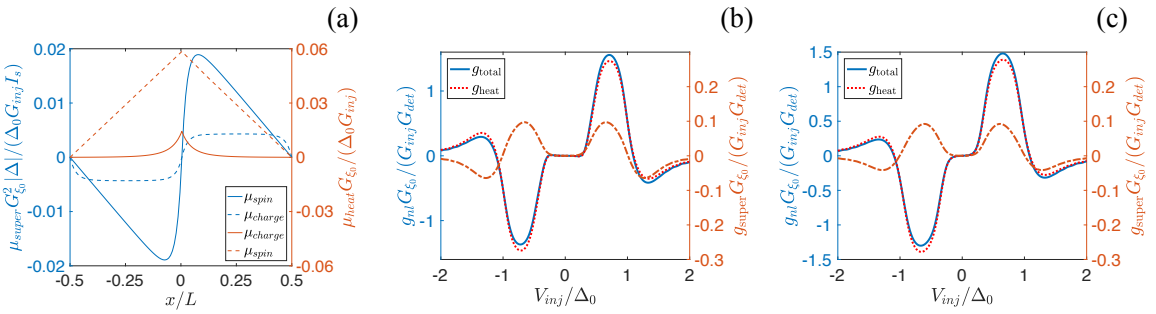

Figure 4.8: (a) Pure charge imbalance and heat induced spin accumulation (red) and supercurrent induced charge imbalance and spin accumulation (blue) at $T = 0.15\Delta_0$ and $V_{inj} = 0.1\Delta_0$. From Article III. The nonlocal conductance for spin-orbit relaxation dominated case in (b) and for spin-flip relaxation dominated case in (c) at $T = 0.05\Delta_0$ and $\xi_0\partial_x\varphi = 0.3$. The blue solid curve represents the total nonlocal conductance, the red dotted curve represents $g_{\rm heat}$, and $g_{\rm super}$ is plotted in a smaller scale. The spin relaxation rates in (b) are $\tau_{so}^{-1} = 0.0475\Delta_0$, $\tau_{sf}^{-1} = 0.0025\Delta_0$, and in (c) are $\tau_{so}^{-1} = 0.0125\Delta_0$, $\tau_{sf}^{-1} = 0.0375\Delta_0$. The other parameters used in the calculations are $h = 0.3\Delta_0$, and $L = 20\xi_0$.

4.4 Inhomogeneous magnetization

As discussed in Sec. 2.2.2, ferromagnets have domain structure. Namely, a ferromagnet may consist of many domains with different magnetization directions connected by domain walls. Thus, in a FI/S structure, the induced exchange field in the superconductor could also be inhomogeneous.

In this section, we relax the assumption of the previous section, a homogeneous magnetization, and study the effects of an inhomogeneity in a FI/S structure, especially domain walls. For simplicity, we consider an inhomogeneous exchange field induced in the superconductor as a domain wall structure separating two domains with opposite magnetization directions. The theoretical treatment of the Usadel equation in this case is developed in Article IV. The main steps are summarized in this section.

We consider a Néel domain wall [see Fig. 4.9(a)] induced in the superconductor, since it is energetically favourable in thin ferromagnets, as shown in Sec. 2.2.2. We use the rotation angle representing the domain wall structure in Eq. (2.38). It brings certain technical advantages when we solve the Usadel equation as shown below.

With this rotation angle, the exchange field in the Usadel equation in Eq. (4.9) can be written as

$$\boldsymbol{h} = h\left(\sin\alpha(x), 0, \cos\alpha(x)\right),$$

where h is the exchange field strength. Correspondingly, the gradient in the Usadel equation becomes a derivative in the x direction.

We can introduce a rotation matrix, to rotate the spin axis parallel to the local magnetization direction. Since the rotation of a Néel domain wall happens in the xz plane in the spin space, we can define the rotation matrix as

$$\hat{R} = e^{i\sigma_2\alpha(x)/2},$$

where $\alpha(x)$ is the rotation angle in Eq. (2.38). With this rotation matrix, we can rotate the quasiclassical Green's function $\hat{g}$ as

$$\hat{g} = \hat{R}^\dagger \hat{g}_0 \hat{R}, \tag{4.43}$$

so that the new Green's function $\hat{g}_0$ satisfies

$$D\hat{\partial}_x^A \cdot \left(\hat{g}_0 \hat{\partial}_x^A \hat{g}_0\right) - \left[\omega_n \tau_3 + ih\sigma_3\tau_3 + \hat{\Delta} + \hat{\Sigma}, \hat{g}_0\right] = 0, \tag{4.44}$$

where

$$\begin{aligned} \hat{\Delta} &= \Delta\tau_1, \\ \hat{\partial}_x^A Y &= \partial_x Y - [\hat{A}, Y], \end{aligned} \tag{4.45}$$

and

$$\hat{A} = \frac{i}{2}\sigma_2 \alpha'(x).$$

Here we use the Matsubara representation. For the Usadel equation in the real-time representation, the rotation matrix is doubled in the Keldysh space, and $\hat{g}_0$ takes the form of Eq. (4.12).

The long derivative contains an SU(2) type vector potential $\hat{A}$. It produces more terms in the first term in Eq. (4.44) compared to the Usadel equation in homogeneous magnetization in Eq. (4.25), as follows

$$D\hat{\partial}_x^A \cdot \left(\hat{g}_0 \hat{\partial}_x^A \hat{g}_0\right) = D\partial_x \left(\hat{g}_0 \partial_x \hat{g}_0\right) + D\left[\hat{A}, \hat{g}_0 \hat{A} \hat{g}_0\right] - D\left[\hat{A}, \hat{g}_0 \partial_x \hat{g}_0\right] - D\partial_x \left(\hat{g}_0 \hat{A} \hat{g}_0\right).$$

We are especially interested in the second term on the right hand side

$$D\left[\hat{A}, \hat{g}_0 \hat{A} \hat{g}_0\right] = \frac{1}{2}\alpha'(x)^2 D\left[\sigma_2 \hat{g}_0 \sigma_2, \hat{g}_0\right]. \tag{4.46}$$

This term has a similar form with the extrinsic spin-orbit relaxation in Eq. (4.7) in the Usadel equation, with a relaxation rate $\alpha'(x)^2 D/2$ but only in one spin direction. Thereby it is similar to the intrinsic (Rashba or Dresselhaus) spin-orbit coupling [112–114]. This means that the inhomogeneous exchange field acts like spin-orbit relaxation, and its effect would be similar to the one with spin-orbit relaxation discussed in the previous section. Moreover, the rotation of the magnetization also indicates an equilibrium spin current. Then this is similar to the equilibrium spin current for the case when the direction of the Zeeman field is perpendicular to the direction of the Rashba spin-orbit field in a superconducting wire [115].

The derivative of the rotation angle $\alpha'(x)$ is discontinuous at the domain wall boundaries $x = \pm\lambda/2$. This implies a discontinuity in the long derivative of $\hat{g}_0$ in Eq. (4.45). In order to describe this discontinuity we can integrate the Usadel equation in Eq. (4.44) at the boundary to obtain the boundary conditions for the Usadel equation as

$$\hat{g}_0\partial_x\hat{g}_0|_{x_b^\pm} - \hat{g}_0\partial_x\hat{g}_0|_{x_b^\mp} = \frac{1}{2}\alpha'(x)\left[\hat{g}_0 i\sigma_2, \hat{g}_0\right]|_{x_b^\pm}, \tag{4.47}$$

where $x_b = \pm\lambda/2$ and $\pm$ refer to the right and left sides of the boundary. Far away from the domain wall structure, the Usadel equation is the same with the one in the case of a homogeneous exchange field. The solutions in this case constitute the rest of the boundary conditions.

In order to solve the Usadel equation for a position dependent Green's function, we use an extended θ parameterization as in Ref. [116]

$$\hat{g}_0 = \cos\theta\left(M_0 + i\tan\theta\boldsymbol{M}\cdot\boldsymbol{\sigma}\right)\tau_3 + \sin\theta\left(M_0 - i\cot\theta\boldsymbol{M}\cdot\boldsymbol{\sigma}\right)\tau_1, \tag{4.48}$$

where $\boldsymbol{M} = (M_1, M_2, M_3)$. The advantage of using this parameterization is that the parameters θ, M_0, and $\boldsymbol{M}$ are all real in the Matsubara representation. The normalization condition $\hat{g}_0^2 = \hat{1}$ implies a constraint on these parameters

$$M_0^2 - \boldsymbol{M}^2 = 1. \tag{4.49}$$

With the parameterization in Eq. (4.48), the Usadel equation reduces to a set of differential equations for the parameters θ, M_0, and $\boldsymbol{M}$. With the boundary conditions in Eq. (4.47), these equations can be solved numerically. The numerical method for solving the boundary value problems are introduced in Appendix B.2.

The solutions of the differential equations are shown in Article IV for the Matsubara Green's function. For retarded Green's function, we can substitute $i\omega \to \epsilon + i\Gamma$ in the differential equations, and obtain complex solutions of these parameters. Finally, the unrotated Green's function in Eq. (4.43) (Matsubara or retarded), can be written as

$$\begin{aligned}\hat{g} = {} & \cos\theta\left[M_0 + i\tan\theta\cos\alpha(x)\boldsymbol{M}\cdot\boldsymbol{\sigma} + i\tan\theta\sin\alpha(x)\left(M_3\sigma_1 - M_1\sigma_3\right)\right]\tau_3 \\ & + \sin\theta\left[M_0 - i\cot\theta\cos\alpha(x)\boldsymbol{M}\cdot\boldsymbol{\sigma} - i\cot\theta\sin\alpha(x)\left(M_3\sigma_1 - M_1\sigma_3\right)\right]\tau_1.\end{aligned} \tag{4.50}$$

In the next section, this Green's function is used to calculate various physical quantities.

4.4.1 Effects in equilibrium

In this section, the equilibrium effects studied in Article IV is reviewed. We consider a FI/S structure containing a Néel domain wall, as shown in Fig. 4.9(a), and the domain wall center is at $x = 0$.

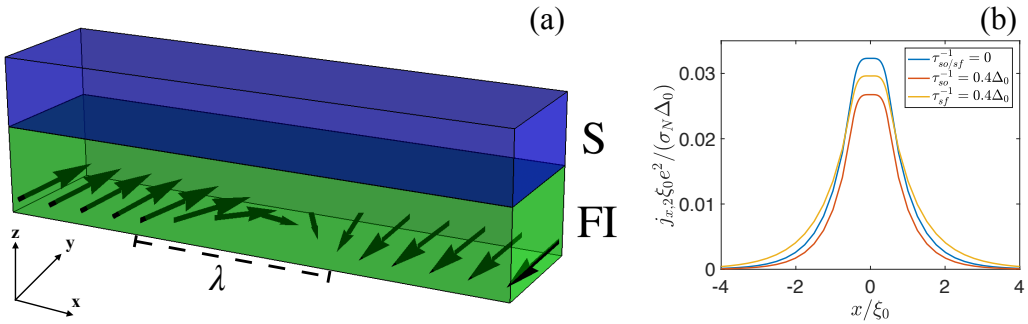

Figure 4.9: (a) Schematic view of the structure considered in Article IV. A superconductor is placed on top of a ferromagnetic insulator containing a domain wall. (b) Equilibrium spin current density for $\lambda = 0.5\xi_0$, $T = 0.05\Delta_0$, and $h = 0.3\Delta_0$. From Article IV.

Superconducting pair potential

In equilibrium, with the parameterization in Eq. (4.48), the self-consistency equation for the superconducting pair potential in Eq. (4.29) becomes

$$\Delta \log\left(\frac{T}{T_c}\right) = 2\pi T \sum_{\omega_n>0}\left(M_0 \sin\theta - \frac{\Delta}{\omega_n}\right). \tag{4.51}$$

We can see that Δ does not explicitly depend on the rotation angle $\alpha(x)$, since we only consider spin-singlet pairing.

The self-consistent Δ is position dependent around the domain wall structure. The effect of the spin-relaxation processes are similar with the case of a homogeneous exchange field in Sec. 4.3.1. However, the effects are weaker in the domain wall region, since the inhomogeneous exchange field acts as a spin-orbit relaxation as in Eq. (4.46), which already reduces the effect of the exchange field.

Equilibrium spin current density

Due to the inhomogeneity of the exchange field, the spin of the quasiparticles rotates with respect to the local magnetization. This produces a flow of spin, namely an equilibrium spin current density [117].

The spin current density in Eq. (4.24b) in the Matsubara representation can be written as

$$j_{k,s} = \frac{\sigma_N}{2e^2}\pi T i \sum_{\omega_n>0} \mathrm{Tr}\left[\sigma_s\left(\hat{g}\nabla_k\hat{g}\right)\right].$$

Since the rotation of the magnetization takes place along the spin y direction, the

only nonzero component of the spin current is along this direction

$$j_{x,2} = \frac{2\sigma_N}{e^2}\pi T \sum_{\omega_n>0} \left[\alpha'(x)\left(M_1^2 + M_3^2\right) + M_3\partial_x M_1 - M_1\partial_x M_3\right].$$

This is then consistent with the equilibrium spin current in a spin-split superconductor with Rashba spin-orbit field [115].

The position dependence of $j_{x,2}$ is shown in Fig. 4.9(b). We can see that inside the domain wall, the maximum spin current density is a constant, and smoothly goes to zero at the outside of the domain wall. Moreover, the spin-relaxation processes reduce the spin current density. The dependence of the spin current density on temperature, exchange field strength, and domain wall size are discussed in Article IV.

Effects of superconductivity on the domain wall size

In a thin ferromagnet, the (Néel) domain wall size and energy are given in Eq. (2.42). These are determined from the free energy F_1 in Eq. (2.41). The effect of the superconductivity which influences the formation of the domain wall should be added to F_1 when minimizing the total free energy. The contribution of the domain wall to the energetics of the system is given by the difference of the superconducting free energy in the case of inhomogeneous and homogeneous magnetization as

$$F_2 = F_{sn}(\boldsymbol{h}) - F_{sn}(\boldsymbol{h} = h\hat{z}),$$

where

$$F_{sn} = \int_{-\infty}^{\infty} f_{sn} dV = W \int_{-\infty}^{\infty} f_{sn} dx,$$

and W is the cross sectional area of the superconductor, and f_{sn} is the free energy density in Eq. (4.11). The free energy F_2 and the domain wall size determined from the total free energy $F = F_1 + F_2$ are discussed in detail in Article IV. The overall effect of the superconductivity on energetics of the system is to reduce it, especially for the domain walls with sizes of the order of ξ_0.

Density of states

With the parameterization in Eq. (4.48), the density of states for each spin species in Eq. (4.14) becomes (for $s = 3$)

$$N_{\uparrow/\downarrow} = \frac{1}{2} N_0 \mathrm{Re}\left[\cos\theta M_0 \pm (\cos\alpha M_3 - \sin\alpha M_1)\, i \sin\theta\right].$$

Here the parameters are complex since this expression is derived from the retarded Green's function. This density of states is position dependent and it is plotted in Fig. 4.10(a) at different positions around the domain wall for $\lambda = 0.1\xi_0$. We can see that the density of states is affected by the inhomogeneity of the exchange field, and it forms a shark-fin shape at the center of the domain wall.

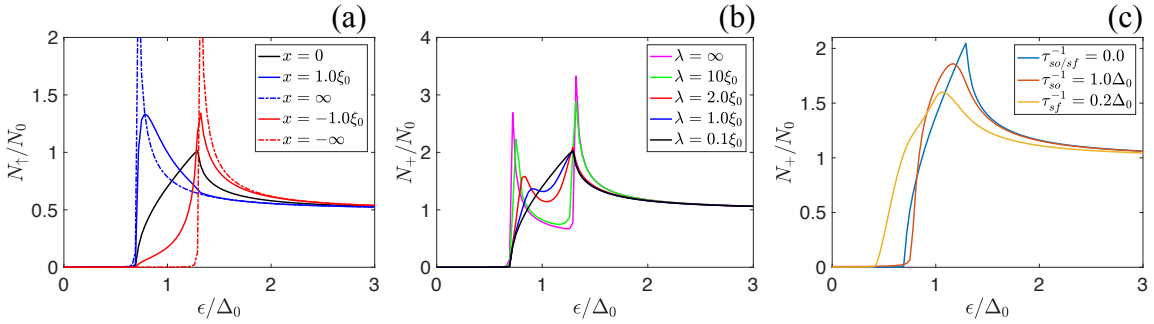

Figure 4.10: Density of states of a superconductor in the presence of a domain wall studied in Article IV. (a) The density of states for each spin species at different positions around the domain wall for $\lambda = 0.1\xi_0$. (b) The total density of states at the domain wall center for different domain wall sizes. (c) The effects of the spin-relaxation processes on the total density of states at the center of the domain wall for $\lambda = 0.1\xi_0$. The parameters used in the calculations are $T = 0.05\Delta_0$, and $h = 0.3\Delta_0$.

In Fig. 4.10(b), the total density of states at the center of the domain wall for different domain wall sizes are shown. We can see that as the domain wall size decreases, the inner peaks in the density of states are shifted to the outer ones, and the shark-fin structure is formed for a small domain wall size. Finally, the effects of the spin-relaxation processes on the density of states at the center of the domain wall are shown in Fig. 4.10(c).

4.4.2 Effects out of equilibrium

The most interesting nonequilibrium effect in the case of an inhomogeneous exchange field is the domain wall motion. The domain wall motion has been extensively studied in ferromagnets in recent years [118]. However, this topic is much less studied in the superconductor based hybrid structures. A thermally induced domain wall motion was recently studied in the presence of a temperature gradient in a clean ferromagnet/superconductor structure [119]. But in a FI/S structure, this effect has never been studied so far to the author's knowledge.

The currents inducing the domain wall motion in the superconductor are the currents in Eq. (4.24). This requires solutions of the nonequilibrium modes for an inhomogeneous magnetization. Although the rotation of the magnetization takes place in a plane, an equilibrium spin current exists in the perpendicular spin direction, as shown

in Sec. 4.4.1. As a result, all the nonquilibrium modes in Eq. (4.18) are nonzero in this case.

We can derive the kinetic equations for the nonequilibrium modes similar to the ones in Eq. (4.37). In the absence of the supercurrent, these equations decouple into two sets. One consists of the kinetic equations for f_T and f_{Ls} modes, the other for f_L and f_{Ts} modes, where $s = 1, 2, 3$. However, this is a rather complicated problem.

It is instructive to examine the normal state form of these kinetic equations. If we take the energy integral of the Usadel equation in Eq. (4.13), and take the trace after multiplying with Pauli spin matrices, we reach a spin diffusion equation as

$$D\partial_x^2 \boldsymbol{s} = \frac{1}{\tau_{sn}} \boldsymbol{s} - 2\boldsymbol{h} \times \boldsymbol{s}, \tag{4.52}$$

where $\boldsymbol{s} = (s_1, s_2, s_3)$ is a vector of spin accumulation. It is defined as

$$\boldsymbol{s}(\boldsymbol{r}) = N_0 \int d\epsilon \boldsymbol{f}(\boldsymbol{r}, \epsilon), \tag{4.53}$$

where $\boldsymbol{f} = (f_{T1}, f_{T2}, f_{T3})$.

This equation describes the spin accumulation in a weak ferromagnet with a domain wall structure. This is due to the fact that the exchange splitting is small in a weak ferromagnet, and hence the spin-relaxation rate and the diffusion constant are independent of the spin index.

In order to understand the domain wall motion in a superconductor with an inhomogeneous exchange field, it is useful to study the domain wall motion in a system in which the spin accumulation can be described by the above kinetic equation. As the domain wall motion in a ferromagnet is an independent topic, we discuss it in the next chapter.

5 Domain wall motion in a diffusive weak ferromagnet

In this chapter, continuing the previously discussed nonequilibrium effects in the case of inhomogeneous magnetization, the domain wall motion in a diffusive weak ferromagnet is discussed. First, the theory of domain wall motion is demonstrated briefly, and then the theoretical model is presented. After reviewing the force and torque acting on the domain wall shortly, the domain wall dynamics are discussed at the end.

5.1 Theory of Domain wall motion in brief

A domain wall appears between two magnetic domains with opposite magnetizations in a ferromagnet, as a result of the competition between the exchange energy and anisotropy energy, as discussed in Sec. 2.2.2.

When a current is injected to a ferromagnet, an electron could be reflected or transmitted from the domain wall. The reflection corresponds to a linear momentum transfer, and the transmission corresponds to a spin (angular momentum) transfer, due to the interaction between the localized spins with the conduction electrons by, for example, an s-d type interaction as in Eq. (4.3).

Due to the conservation of momentum, a momentum transfer process leads to a domain wall motion. Due to the above two momentum transfer processes, the domain wall motion cannot be simply described by a set of equations of motion of, for example, a particle. The Lorentz force, for example, is perpendicular to the magnetic field and velocity. A domain wall motion, as the magnetization direction rotates, also indicates an accompanying out-of-plane angle of the magnetization direction. This idea was proposed in the early phenomenological theoretical studies in Refs. [120–123]. After a series of experimental confirmations [124–128], a microscopic theory of domain wall motion was finally laid on more than a decade ago [129].

The equations of the domain wall motion are given by [118, 129]

$$\dot{\phi} + \alpha_0 \frac{\dot{X}}{\lambda} = \frac{\lambda}{\hbar N_w S} \left(F + F_{\text{pin}} \right) \tag{5.1a}$$

$$\dot{X} - \alpha_0 \lambda \dot{\phi} = \frac{K_\perp \lambda}{2\hbar} S \sin(2\phi) + \frac{\lambda}{\hbar N_w S} T_z, \tag{5.1b}$$

where S is the size of the localized spin, and ϕ is the out-of-plane angle of the magnetization in the domain wall, and it is a function of time. This angle requires a hard-axis anisotropy energy represented by $K_\perp$. The number of localized spins in the domain wall is $N_w = 2\lambda W/a^3$ in the case of a thin ferromagnet, where W is the cross-sectional area of the ferromagnet, and a is the lattice constant.

The force, representing the momentum transfer, and the torque, representing the spin transfer, are given by [118, 129]

$$F = -\int dV \nabla \boldsymbol{h} \cdot \boldsymbol{s}, \tag{5.2a}$$

$$T_z = -\int dV (\boldsymbol{h} \times \boldsymbol{s})_z, \tag{5.2b}$$

where $\boldsymbol{s}$ is the spin density, and $\boldsymbol{h}$ is the exchange field in the ferromagnet. Its amplitude $h = |\boldsymbol{h}|$, the exchange splitting is defined as $h = J_{ex} S$, where J_{ex} is the effective parameter describing the s-d type exchange interaction, see Eq. (4.3).

For the current driven domain wall motion, the force is much larger than the torque, in the case of a small domain wall, since in this case, the electron scattering is strong. In the opposite limit, for large domain walls, the electrons scattering is weak, and the torque is much larger than the force. This is known as the adiabatic limit [118].

The term F_{pin} represents the extrinsic pinning which modifies the easy axis anisotropy. For a point defect, it can be written as

$$F_{\text{pin}} = -\frac{dV_{\text{pin}}}{dX},$$

where

$$V_{\text{pin}} = \frac{N_w V_0}{\zeta^2} \left(X^2 - \zeta^2\right) \Theta(\zeta - |X|).$$

Here $\Theta(x)$ is the Heaviside step function, V_0 is the pinning strength per spin, and ζ is the pinning range.

The equations of motion of a domain wall in Eq. (5.1) are simple. The nonnontrival task is to evaluate the force and torque, especially the spin density. Once determining the spin density, and choosing the domain wall structure, we can discuss the domain wall dynamics by solving the equations of motion with proper initial conditions, usually chosen as $X(0) = 0$ and $\phi(0) = 0$.

In this chapter, we discuss the domain wall motion induced by a spin current in a weak ferromagnet, resulting from the induced spin accumulation. The spin accumulation

is the spin density $\boldsymbol{s}$ in the force and torque in this case. We determine the spin accumulation from the spin diffusion equation in Eq. (4.52).

One major difference of the spin current from the spin-polarized charge current (used in most of the domain wall motion studies) is that it decays within the spin-relaxation length l_s, due to the spin-relaxation processes. In fact, the spin-relaxation processes bring many effects in the domain wall motion induced from spin-polarized charge current. For example, it enhances nonadiabaticity of the domain wall close to the adiabatic limit [130, 131]. A spin current without the charge current going along may bring interesting effects to the domain wall motion.

5.2 Spin accumulation in a weak ferromagnet

In this chapter, we study the domain wall motion in the structure shown in Fig. 5.1. This structure consists of a weak ferromagnet containing a domain wall with size λ, and a strong ferromagnetic injector with polarization P_I. The injector is placed on the left of the domain wall structure at $z = 0$, where the magnetization is homogeneous. We consider the Néel domain wall since it is energetically preferred in thin films (see Sec. 2.2.2).

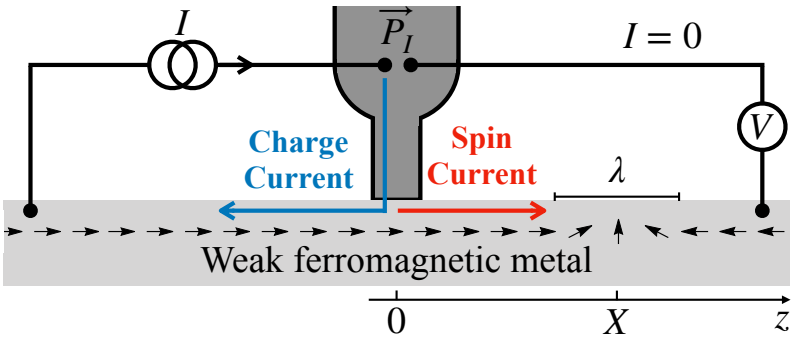

Figure 5.1: Schematics of a weak ferromagnet containing a domain wall considered in Article V. An injector is placed on the left side of the domain wall at a position $z = 0$, where the magnetization is homogeneous.

The domain wall structure is described in the exchange field as

$$\boldsymbol{h} = h\boldsymbol{m}(z - X), \tag{5.3}$$

where $\boldsymbol{m}(x)$ is given in Eq. (2.35) with the rotation angle α given in Eq. (2.38) by replacing $x \to z - X$.

The "weak" and "strong" ferromagnets are considered in terms of the size of the spin polarization in Eq. (2.32). For a weak ferromagnet with a small exchange splitting,

the density of states for each spin species at the Fermi level are equal $N_0^{\uparrow} \simeq N_0^{\downarrow}$, and hence $P \to 0$. This allows us to use a spin-independent transport equation to describe the spin accumulation in the weak ferromagnet.

When a spin polarized current is injected from the ferromagnetic injector, a spin accumulation is created in the weak ferromagnet. Due to the spin relaxation processes, this spin accumulation decays exponentially within the spin-relaxation length, $l_s = \sqrt{D\tau_s}$, where τ_s is the spin-flip relaxation time. The spin diffusion equation in Eq. (4.52) can also be derived from the Boltzmann equation in the diffusive limit, as we have shown in Article V. After including the Plank's constant, we rewrite the spin-diffusion equation as

$$\hbar D\partial_z^2 \boldsymbol{s} = \frac{\hbar}{\tau_s}\boldsymbol{s} - 2\boldsymbol{h} \times \boldsymbol{s}.$$

Similar to the trick in Sec. 4.4, we can use a rotation matrix to transform the spin-diffusion equation to a simpler form. Considering the out-of-plane angle ϕ, the rotation matrix can be defined as

$$\hat{R} = e^{i\sigma_2\alpha(z-X)/2}e^{i\sigma_3\phi/2},$$

so that we can write the spin accumulation as

$$\boldsymbol{s} = \hat{R}^{\dagger}\boldsymbol{s}_0\hat{R}. \tag{5.4}$$

Then the spin accumulation $\boldsymbol{s}_0 = (s_1^0, s_2^0, s_3^0)$ in the rotated spin space satisfies the following spin-diffusion equation

$$\hbar D\hat{\partial}_z^2 \boldsymbol{s}_0 = \frac{\hbar}{\tau_s}\boldsymbol{s}_0 - 2h\hat{z} \times \boldsymbol{s}_0, \tag{5.5}$$

where $\hat{z} = (0, 0, 1)$, and the long derivative is given in Eq. (4.45).

The boundary conditions for this equation representing the discontinuity of $\alpha'(z)$ can be obtained by integrating the boundary conditions in Eq. (4.47) in energy as

$$\partial_z s_1^0|_{z_b^{\pm}} - \partial_z s_1^0|_{z_b^{\mp}} = -\frac{\pi}{\lambda}s_3^0|_{z_b^{\pm}},$$

$$\partial_z s_2^0|_{z_b^{\pm}} - \partial_z s_2^0|_{z_b^{\mp}} = 0,$$

$$\partial_z s_3^0|_{z_b^{\pm}} - \partial_z s_3^0|_{z_b^{\mp}} = \frac{\pi}{\lambda}s_1^0|_{z_b^{\pm}},$$

where $z_b = \pm(X \pm \lambda/2)$, and $\pm$ refers to the right and left sides of the domain wall boundary.

The boundary conditions representing the injection of the spin-polarized current can be obtained by taking the energy integral of the boundary conditions in Eq. (4.40) [and also multiplied by N_0 as in Eq. (4.53)] as

$$\hbar D\partial_z s_1^0 = 0$$

$$\hbar D \partial_z s_2^0 = 0$$
$$\hbar D \partial_z s_3^0 = k_I \hbar D (s_3^0 - P_I V N_0).$$

Note that, the voltage V here represents a rescaled voltage at the injector V_{inj} by a factor η as $V = \eta V_{\mathrm{inj}}$ ($e = 1$). This is due to the fact that the spin accumulation in the weak ferromagnet is affected by the spin accumulation in the injector (strong) ferromagnet (see the detail in Article V).

Finally, the spin accumulation $\boldsymbol{s}_0$ in the rotated space can be transformed into the unrotated space by using Eq. (5.4). In detail, we have

$$s_1 = \cos\phi(s_1^0 \cos\theta + s_3^0 \sin\theta) - s_2^0 \sin\phi \tag{5.8a}$$
$$s_2 = s_2^0 \cos\phi + \sin\phi(s_1^0 \cos\theta + s_3^0 \sin\theta) \tag{5.8b}$$
$$s_3 = s_3^0 \cos\theta - s_1^0 \sin\theta. \tag{5.8c}$$

The position dependence of the components of $\boldsymbol{s}_0$ and $\boldsymbol{s}$ are shown in Article V. The numerical methods for solving the boundary value problems are introduced in Appendix B.2. In the preceding section, we use $\boldsymbol{s}$ to calculate the force and torque.

5.3 Force and torque

Substituting the spin accumulation in Eq. (5.8) and the exchange field in Eq. (5.3) to the expressions of the force and torque in Eq. (5.2), obtain

$$F = -\frac{h\pi W}{\lambda} \int dz s_1^0 \tag{5.9a}$$
$$T_z = -hW \int dz s_2^0 \sin\theta, \tag{5.9b}$$

where W is the cross-sectional area of the weak ferromagnet.

The dependence of the force and torque on various parameters as a function of the domain wall position X are shown in Article V. Due to the decaying feature of the spin current and spin accumulation, the force and torque also decay exponentially. Moreover, the amplitudes of the force and torque do not solely depend on the domain wall size λ, but they also depend on the spin-relaxation processes. For strong spin relaxation, the force is much larger then the torque unless λ is of the order of l_h. For weak spin relaxation, on the other hand, the torque is much larger than the force unless $\lambda \ll l_h$. These properties are different from the ones in the case of current driven domain wall motion [118].

5.4 Domain wall dynamics

The units of F and T_z/λ are hVN_0W. In order to make the equations of motion in Eq. (5.1) dimensionless, one can choose a unit time as

$$t_0 = \frac{2\hbar S}{a^3 N_0 h V}.$$

Multiplying Eq. (5.1) by t_0, and reorganising the terms, obtain (in the absence of the external pinning)

$$\frac{\dot{X}}{\lambda} = \frac{1}{1+\alpha_0^2}\left[\alpha_0 f + \frac{\tau_z}{\lambda} + k_\perp \sin(2\phi)\right] \tag{5.10a}$$

$$\dot{\phi} = \frac{1}{1+\alpha_0^2}\left[f - \alpha_0\frac{\tau_z}{\lambda} - \alpha_0 k_\perp \sin(2\phi)\right]. \tag{5.10b}$$

Here the unitless force, torque, and perpendicular anisotropy energy are defined as

$$f = -\frac{\pi}{\lambda V N_0}\int dx s_1^0$$

$$\tau_z = -\frac{1}{VN_0}\int dx s_2^0 \sin\theta$$

$$k_\perp = \frac{K_\perp S^2}{a^3 N_0 h V}.$$

Before solving these equations with the force and torque in Eq. (5.9), we first discuss the case of constant force and torque.

Constant force and torque

For constant force and torque, which are denoted as f_0 and τ_z^0, respectively, the equations of motion in Eq. (5.10) can be solved analytically with the initial conditions $X(0) = 0$ and $\phi(0) = 0$. Due to the lengthy form of the analytical expressions, only the numerical solutions are plotted in Fig. 5.2 and the analytical results in the limit $t \to \infty$ are used for discussions. The numerical methods for solving initial value problems are summarized in Appendix B.3.

In the case of the force much larger than the torque, $\dot{\phi} = 0$ for $f_0 < \alpha_0 k_\perp$ when $t \to \infty$. Substituting Eq. (5.10b) to Eq. (5.10a), we obtain a constant domain wall velocity

$$\dot{X} = \frac{\lambda f_0}{\alpha_0}. \tag{5.11}$$

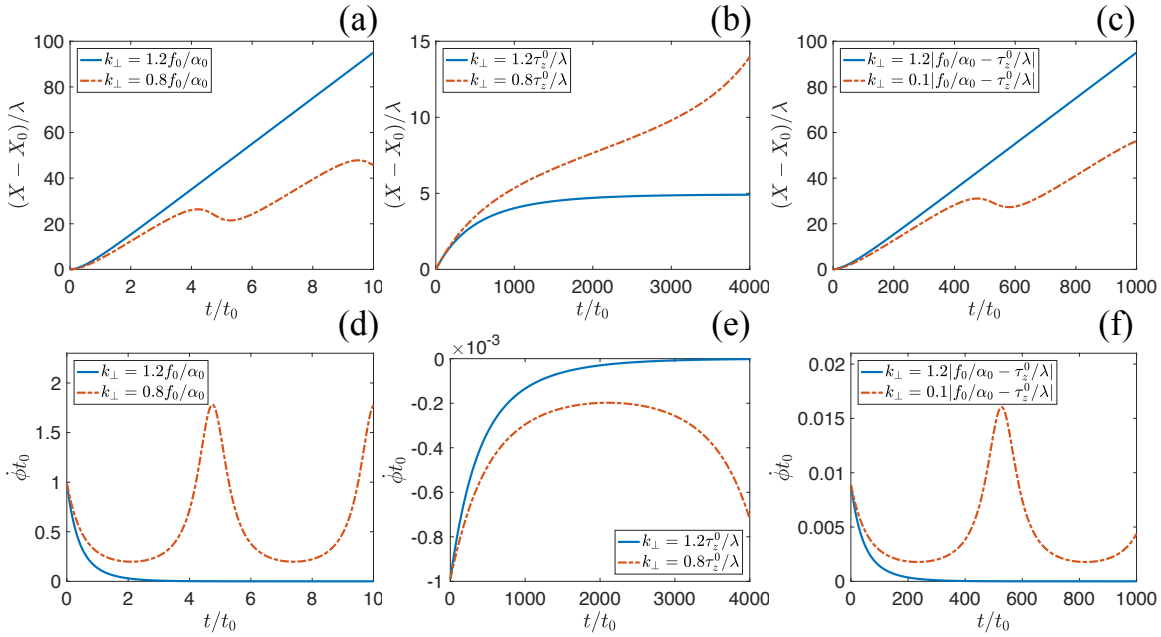

Figure 5.2: Domain wall motion with constant force and torque. In the left column (a,d), the domain wall motion is shown in the absence of the torque $f_0 = 1.0VhN_0W$, $\tau_z^0/\lambda = 0$ for $\lambda = 0.01l_h$. In the middle column (b,e), the domain wall motion is shown in the absence of the force $f_0 = 0$, $\tau_z^0\lambda = 1.0VhN_0W$ for $\lambda = 100l_h$. In the right column (c,f), the domain wall motion is shown in the presence of both force and torque $f_0 = 0.01VhN_0W$, $\tau_z^0/\lambda = 1.0VhN_0W$ for $\lambda = 100l_h$. The Gilbert damping parameter $\alpha_0 = 0.1$ is used in the calculation.

Using this result, we can also determine

$$\phi = \frac{1}{2}\arcsin\left(\frac{f_0}{\alpha_0 k_\perp}\right). \tag{5.12}$$

If $f_0 > \alpha_0 k_\perp$, however, $\dot{\phi}$ oscillates in time, and this leads to an oscillatory domain wall motion as can be seen from Fig. 5.2(a). This is known as the Walker breakdown [132].

In the case of the torque much larger than the force, we also have $\dot{\phi} = 0$ for $\tau_z^0 < k_\perp\lambda$ when $t \to \infty$. This makes the domain wall stop

$$\dot{X} = 0.$$

This means that the spin transfer is completely absorbed by the perpendicular anisotropy energy represented by $k_\perp$. This is known as the intrinsic pinning [129]. In this case, ϕ can be determined from Eq. (5.10b) as

$$\phi = -\frac{1}{2}\arcsin\left(\frac{\tau_z^0}{k_\perp\lambda}\right).$$

In the opposite regime $\tau_z^0 > k_\perp\lambda$, however, the domain wall keeps moving as the time evolves. The domain wall position as a function of time in this case is shown in Fig. 5.2(b).

In the presence of both force and torque, even a small force is enough to break the intrinsic pinning and the domain wall moves with a constant velocity for $k_\perp > |f/\alpha_0 - \tau_z^0/\lambda|$ as in Eq. (5.11). The out-of-plane angle ϕ in Eq. (5.12) becomes

$$\phi = \frac{1}{2}\arcsin\left[\frac{1}{k_\perp}\left(\frac{f_0}{\alpha_0} - \frac{\tau_z^0}{\lambda}\right)\right]. \tag{5.13}$$

In the opposite case, $k_\perp < |f/\alpha_0 - \tau_z^0/\lambda|$, the domain wall again moves in an oscillatory fashion, see Fig. 5.2(c,f).

Decaying force and torque

The force and torque in Eq. (5.9) decay exponentially as a function of X. The three cases of the domain wall motion, force much larger than the torque, the torque much larger than the force, and comparable force and torque, are plotted for a decaying force $f = f_0 e^{-X/l_s}$ and torque $\tau_z = \tau_z^0 e^{-X/l_s}$ in Fig. 5.3.

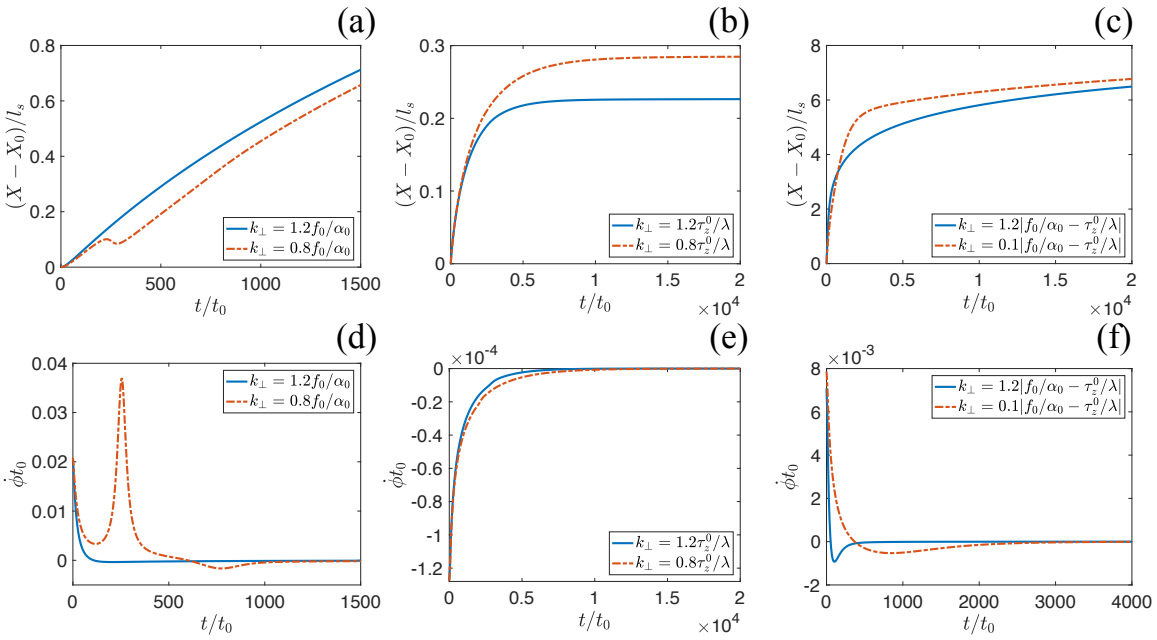

Figure 5.3: Domain wall motion with decaying force and torque studied in Article V. In the left column (a,d), the domain wall motion is shown for the case of the force much larger than the torque for $\lambda = 0.01 l_h$ and $l_s = 3.2 l_h$. In the middle column (b,e), the domain wall motion is shown for the case of the torque much larger than the force $\lambda = 20 l_h$ and $l_s = 100 l_h$. In the right column (c,f), the domain wall motion is shown for comparable force and torque for $\lambda = l_h$ and $l_s = 3.2 l_h$. The other parameters used in the calculations are $P_I = 0.5$, $k_I l_h = 0.5$, $X_0 = \lambda/2$, and $\alpha_0 = 0.1$. In the calculations $k_\perp = 1.2|f_0/\alpha_0 - \tau_z^0/\lambda|$.

In the case of the force much larger than the torque, similar consideration with Eq. (5.11) yields in the case of $\dot{\phi} \to 0$ and $f_0 < \alpha_0 k_\perp$ an equation for the domain

wall velocity

$$\dot{X} = \frac{\lambda f_0}{\alpha_0} e^{-X/l_s}. \tag{5.14}$$

This equation can be solved as

$$X = X(0) + l_s \log\left(1 + \frac{f_0 \lambda t}{l_s \alpha_0}\right),$$

and

$$\dot{X} = \frac{f_0 l_s \lambda}{l_s \alpha_0 + f_0 \lambda t}.$$

Here $X(0)$ is the domain wall position when $\dot{\phi} \to 0$. Comparing with Eq. (5.11), we can find that the domain wall velocity is decreased by an amount which depends on time and $\dot{X} \to 0$ for $t \to \infty$. We can also determine the out-of-plane angle from Eq. (5.10b) as

$$\phi = \frac{1}{2} \arcsin\left[\frac{f_0 l_s}{k_\perp} \frac{e^{-X(0)/l_s}}{l_s \alpha_0 + f_0 \lambda t}\right]. \tag{5.15}$$

Namely, ϕ is positive and approaches to 0 for $t \to \infty$. In the opposite case, $f_0 > \alpha_0 k_\perp$, the Walker breakdown takes place. However, as the force decays and thus smaller than $\alpha_0 k_\perp$ after some time T, the domain wall motion for $t > T$ is again governed by Eq. (5.14). This can be seen from Fig. 5.3(a,d).

In the case of the torque much larger than the force, the intrinsic pinning always takes place since as the torque decays there is always a time $\tau_z(T) < k_\perp \lambda$. Then for $t \to \infty$, we always have

$$\dot{X} = 0.$$

From the numerical result in Fig. 5.3(e), we can see that ϕ is negative in this case.

For comparable both force and torque, the intrinsic pinning is destroyed and the domain wall motion is again governed by Eq. (5.14). We can also determine

$$\phi = \frac{1}{2} \arcsin\left[\frac{1}{k_\perp}\left(\frac{f_0}{\alpha_0} - \frac{\tau_z^0}{\lambda}\right) \frac{\alpha_0 l_s}{l_s \alpha_0 + f_0 \lambda t} e^{-X(0)/l_s}\right]. \tag{5.16}$$

The numerical solutions of the equations of motion in this case can be seen from Fig. 5.3(c,f).

6 Summary & Outlook

This thesis studies novel effects in new forms of superconductivity. The new forms are rather distinct due to the different aim in their research. The research in flat band superconductivity aims to find materials or systems with higher critical temperature, while the research in superconductors with a spin-splitting field concentrates on transport properties at a low temperature.

Notwithstanding the objectives, the density of states plays important role in understanding the effects in both aspects. Benefited from the diverging density of states representing flat energy bands in the normal state, flat band systems form high temperature superconducting state below the critical temperature. The lifted spin degeneracy reveals in the superconducting density of states by the spin-splitting field leads to the novel features which do not exist or very small in usual (non spin-split) superconductors.

The thesis focuses on the strained Dirac materials for the flat band superconductivity, and various equilibrium and nonequilibrium properties of superconductors with homogeneous and inhomogeneous spin-splitting fields. The main results of the thesis and some unsolved problems are outlined below.

Flat-band superconductivity

In article I, we study superconductivity in Dirac materials with flat energy bands induced by a strain field. We discuss several properties of such systems in the superconducting state, including inhomogeneous superconducting pair potential, highly increased critical temperature compared to the case without the strain, peculiar two-peak shaped density of states, and a finite supercurrent.

The strain field considered in article I acts as a pseudo magnetic field, and it preserves the time reversal symmetry [42]. Hence it would be interesting to see the magnetic properties of the model in article I. Especially, for example in a strained graphene as a one atomic layer thickness system, a perpendicular magnetic field creates a magnetic vortex in the system. Moreover, the screening effects in the strain induced flat band is another unsolved problem. The screening properties of electrons is described by the dielectric constant, and the dielectric constant is related to the density of states [21]. The diverging density of states in the strained Dirac materials may lead to unexpected

effects.

The research in flat band superconductivity could be extended to other systems. Recently discovered superconductivity in twisted bilayer graphene with a twist angle (magic angle) about 1° [133] could be explained by flat band superconductivity [134], since the effect of the twist is to suppress the Fermi velocity and the flat bands are formed around the magic angle [135].

Equilibrium effects in superconductors with a spin-splitting field

The equilibrium effects in FI/S structures considered in this thesis include both the cases of homogeneous and inhomogeneous magnetization.

In the case of homogeneous magnetization, various equilibrium properties are reviewed in Refs. [83, 84], including FFLO state, static susceptibility, Fermi liquid effects, and cryptoferromagnetic state. In Article II, we studied the transport properties of junctions between two FI/S structure. We show that the noncollinearity of the spin-splitting fields between the two FI/S structures creates new features in the tunnelling conductance (eight-peak structure) and Josephson current (nonzero current in the absence of the external voltage). However, these effects are not shown in the experiment in Article II. This is due to the fact that the spin-splitting field induced in the superconductor is inhomogeneous, and the measured tunnelling current is determined by taking the average over the inhomogeneity in space.

Indeed, the inhomogeneous exchange field in a FI/S structure is more often encountered, especially in large samples. There are also many interesting effects in the case of inhomogeneous exchange field. For example in Ref. [85], the inhomogeneity of the FI is described by a multi domain structure, and it brings changes to the density of states and the tunnelling conductance. In Article IV, we consider a single domain wall separating two domains with opposite magnetization directions. We study several physical quantities altered due to the domain wall structure, such as domain wall size, equilibrium spin current, density of states, and the tunnelling conductance.

As we have shown in Article IV, superconductivity reduces the induced domain wall size. However, we restricted ourselves to a case of positive total free energy of the system. This remains the situation unsolved for when the total free energy is negative, and which leads to a dense multi domain structure [136]. Moreover, another unsolved problem is the effect of the supercurrent to the properties of a FI/S structure with a fixed domain wall, this would lead to an equilibrium spin supercurrent and further influence the domain wall size.

Nonequilibrium effects in superconductors with a spin-splitting field

Various nonequilibrium effects in superconductors with a homogeneous spin-splitting field are studied in recent years, and are reviewed in Refs. [83, 84]. The corresponding effects are rather small or absent in non spin-split superconductors, for example, thermoelectric effects and long-range spin accumulation. The work in Article III fills the gap of these effects in the presence of a supercurrent. We show that in a superconductor with a spin-splitting field, a supercurrent can convert charge imbalance to long-range spin accumulation, and this can be detected by studying different symmetry components in the nonlocal conductance.

A number of future research problems in the superconductors with a spin-splitting field are outlined in Refs. [83, 84]. These research directions contribute to the future applications in technology, for example, the thermoelectric radiation detector [137] based on the very large thermoelectric effects [72, 73].

Besides these effects, the untouched and also challenging problems out of equilibrium are in the case of inhomogenous spin-splitting field, for example, domain wall motion. As a precursor, we study the domain wall motion in a weak ferromagnet induced by a spin current as a result of spin accumulation in Article V. We evaluate the force and torque acting on the domain wall, and show that the domain wall motion in this case has its characteristic features, for example, time dependent domain wall velocity in the case of force much large than the torque, and achieving the intrinsic pinning in all cases in the case of the torque much larger than the force. The domain wall motion in the superconducting state is left for future work. Moreover, the equilibrium supercurrent may also induce the domain wall motion, and finally, the extension of these works in the presence of both supercurrent and spin accumulation.

To summarize, the new forms of superconductivity studied in this thesis contributed to the research community in the field of superconductivity. Strain induced flat band provides new ways of studying flat band superconductivity, and it has certain advantages to other suggesitons, for example, larger flat band areas in the momentum space compared to the twisted bilayer graphene [138].

The research in superconductivity with a spin-splitting field filled many gaps in this field. The research also going towards the directions have not yet been explored, such as the domain wall motion. It has also been used in other aspects of the superconductivity, like Majorana based quantum computing [139–141]. Very exciting and interesting problems are left to the future. The author sincerely hopes the research in this field to be continued by others.

Appendix A: Kinetic Coefficients

The kinetic coefficients in Eq. (4.38) are defined in Eq. (4.20a) for a homogeneous magnetization. With the parameterization in Eq. (4.26), they can be written as

$$D_L = \frac{D}{8}\mathrm{Tr}\left(\hat{1} - \hat{g}^R\hat{g}^A\right) = \frac{D}{2}(1 - |g_{01}|^2 - |g_{31}|^2 + |g_{03}|^2 + |g_{33}|^2)$$

$$D_{T3} = -\frac{D}{8}\mathrm{Tr}\left(\hat{g}^R\sigma_3\hat{g}^A\right) = D\mathrm{Re}(g_{03}g_{33}^* - g_{01}g_{31}^*)$$

$$D_T = \frac{D}{8}\mathrm{Tr}\left(\hat{1} - \hat{g}^R\tau_3\hat{g}^A\tau_3\right) = \frac{D}{2}(1 + |g_{01}|^2 + |g_{31}|^2 + |g_{03}|^2 + |g_{33}|^2)$$

$$D_{L3} = -\frac{D}{8}\mathrm{Tr}\left(\hat{g}^R\tau_3\sigma_3\hat{g}^A\tau_3\sigma_3\right) = D\mathrm{Re}(g_{01}g_{31}^* + g_{03}g_{33}^*)$$

$$j_E = \frac{D}{8}\mathrm{Tr}\left[\left(\hat{g}^R\partial_x\hat{g}^R - \hat{g}^A\partial_x\hat{g}^A\right)\tau_3\right] = D\left[\mathrm{Im}(g_{01}^2) + \mathrm{Im}(g_{31}^2)\right]$$

$$j_{Es} = \frac{D}{8}\mathrm{Tr}\left[\left(\hat{g}^R\partial_x\hat{g}^R - \hat{g}^A\partial_x\hat{g}^A\right)\tau_3\sigma_3\right] = 2D\mathrm{Im}(g_{01}g_{31})$$

The kinetic coefficients on the right hand side of Eq. (4.37) can also be written in terms of the components of the Green's function in Eq. (4.26)

$$R_T = \frac{|\Delta|}{8}\mathrm{Tr}\left[\left(\hat{g}^R + \hat{g}^A\right)\tau_1\right] = \mathrm{Re}(g_{01})|\Delta|$$

$$R_{L3} = \frac{|\Delta|}{8}\mathrm{Tr}\left[\left(\hat{g}^R + \hat{g}^A\right)\tau_1\sigma_3\right] = \mathrm{Re}(g_{31})|\Delta|$$

$$S_{T3} = \frac{1}{\tau_{sn}}\left\{\mathrm{Re}(g_{03})^2 - \mathrm{Re}(g_{33})^2 + \beta\left[\mathrm{Im}(g_{01})^2 - \mathrm{Im}(g_{31})^2\right]\right\}$$

$$S_{L3} = \frac{1}{\tau_{sn}}\left\{\mathrm{Re}(g_{03})^2 - \mathrm{Re}(g_{33})^2 - \beta\left[\mathrm{Re}(g_{01})^2 - \mathrm{Re}(g_{31})^2\right]\right\}$$

where

$$\tau_{sn}^{-1} = \tau_{sf}^{-1} + \tau_{so}^{-1}$$

$$\beta = \frac{\tau_{sf}^{-1} - \tau_{so}^{-1}}{\tau_{sf}^{-1} + \tau_{so}^{-1}}.$$

The energy dependence of these kinetic coefficients are shown in Fig. A.1.

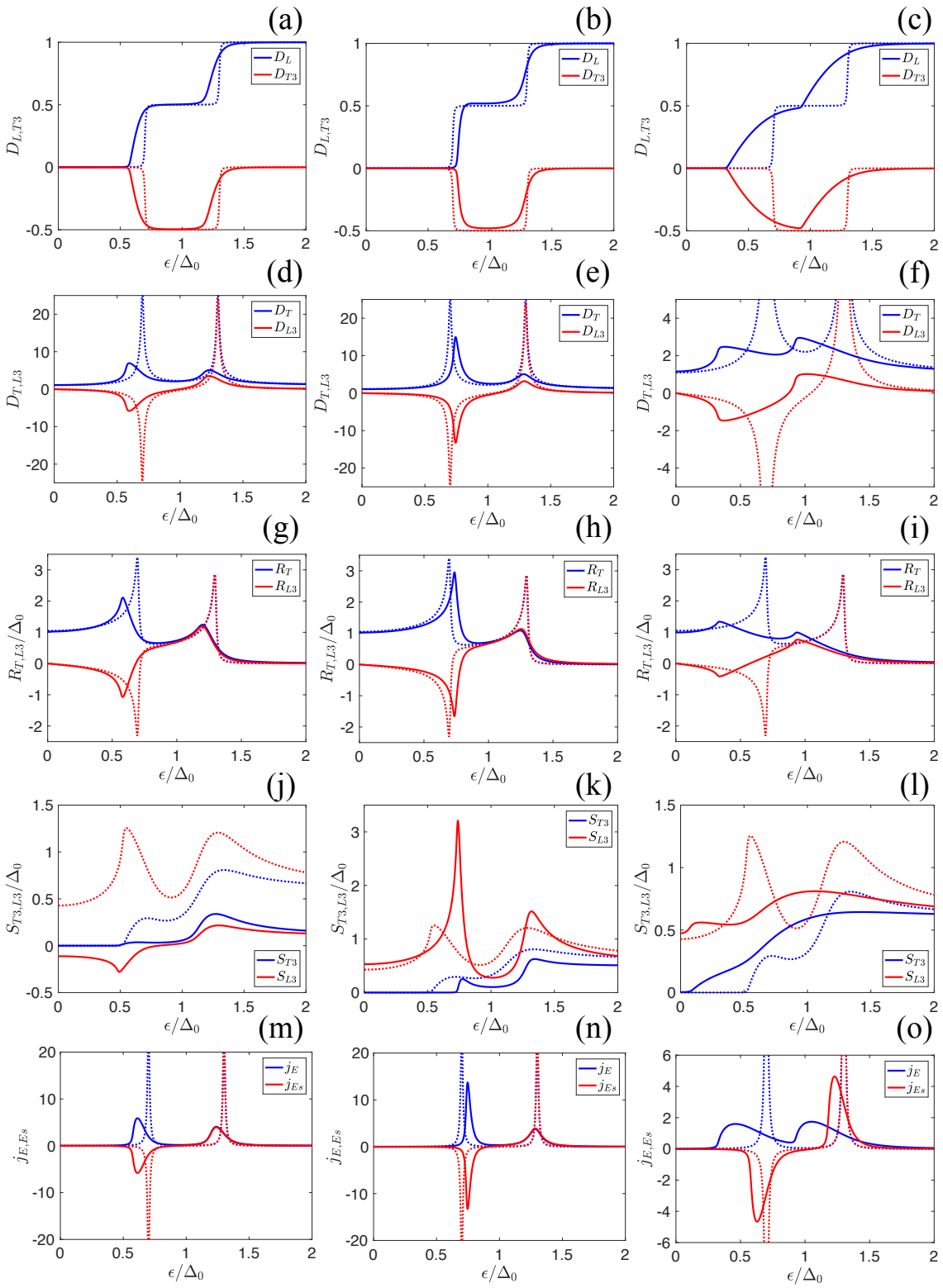

Figure A.1: Energy dependence of the kinetic coefficients with spin-flip , spin-orbit, and orbital depairing rates in left, center, and right columns, separately. The depairing rates are $\tau_{sf}^{-1} = 0.1\Delta_0$, $\tau_{so}^{-1} = 0.5\Delta_0$, and $\tau_{orb}^{-1} = 0.1\Delta_0$, respectively. The dashed curves show the energy dependence of the kinetic coefficients in the absence of the spin-relaxation processes with $\Gamma = 0.01\Delta_0$, except for $S_{T3/L3}$ with $\tau_{sf}^{-1} = 0.1\Delta_0$ and $\tau_{so}^{-1} = 0.5\Delta_0$.

Appendix B: Numerical methods

The numerical calculations in this thesis are carried out in MATLAB. Various numerical solvers in MATLAB are very convenient and efficient for the problems encountered in this thesis. For example, self-consistent calculations, diagonalizing matrices, solving nonlinear algebraic equations, solving differential equations, and integration of array functions. Here, we summarize the numerical methods regarding these problems.

B.1 Self-consistent calculations

The self-consistent calculations in this thesis is considered for determining the superconducting pair potential. We use the MATLAB solver package `nsola` to do these calculations. This solver is based on the Newton-Krylov iterative method to solve linear and nonlinear equations.

In order to use `nsola` to perform self-consistent calculations for the superconducting pair potential, one needs to provide the an error function, an initial guess, and error tolerances (both relative and absolute). The error function is defined as

$$\mathrm{erf} = \Delta_{\mathrm{new}} - \Delta_{\mathrm{old}},$$

where Δ_{new} is the obtained superconducting pair potential in each iteration, and Δ_{old} is the one in the previous iteration, in the first iteration Δ_{old} is then the initial guess $\Delta^{(0)}$.

For flat band superconductivity in strained Dirac materials in Chapter 3, the superconducting pair potential is determined from Eq. (3.6). The initial guess is chosen as the superconducting pair potential for pure flat bands $\xi_{\boldsymbol{k}} = 0$ in Eq. (3.1) at $T = 0$. Since the energy spectrum is periodic in k_x in the first Brillouin zone and flat bands are formed between $k_y \in [-\beta/(2L), \beta/(2L)]$, we can write $V_{d=2} = 2\pi\beta/L^2$, and considering the valley and pseudo spin degeneracies, Eq. (3.1) becomes

$$\Delta^{(0)} = \frac{g\beta}{\pi L^2}.$$

For the superconductors with a spin-splitting field in Chapter 4, the superconducting pair potential is determined from (depending on the parameterization) Eq. (4.29) and Eq. (4.51). The superconducting pair potential at zero temperature and spin-splitting field Δ_0 is chosen as the initial guess in these cases.

B.2 Boundary value problem

The kinetic equations in Eq. (4.37), and the Usadel equation in Eq. (4.44) [and hence Eq. (5.5)] are linear and nonlinear ordinary differential equations, respectively. The MATLAB built-in functions `bvp4c` and `bvp5c`, based on the most commonly used shooting method, are very efficient for solving these equations for a boundary value problem. The small price to be paid is that, one has to reduce the differential equations to the first order. For a set of differential equations, the reducing order leads to a first order matrix differential equations as

$$\partial_x \boldsymbol{f} = M\boldsymbol{f}, \tag{B.1}$$

where $\boldsymbol{f}$ is a vector of the solutions to be determined and M is a matrix. For nonlinear differential equations M is also a functional of $\boldsymbol{f}$. For the kinetic equations in Eq. (4.37), we can write

$$\boldsymbol{f} = (f_L, f_{T3}, f_T, f_{L3}, \partial_x f_L, \partial_x f_{T3}, \partial_x f_T, \partial_x f_{L3}),$$

and for the Usadel equation in Eq. (4.44), we can write

$$\boldsymbol{f} = (\theta, M_0, M_1, M_3, \partial_x\theta, \partial_x M_0, \partial_x M_1, \partial_x M_3). \tag{B.2}$$

For the spin-diffusion equation in Eq. (5.5), we can write

$$\boldsymbol{f} = (s_1^0, s_2^0, s_3^0, \partial_x s_1^0, \partial_x s_2^0, \partial_x s_3^0). \tag{B.3}$$

However, the examples of `bvp4c` and `bvp5c` for the matrix differential equations and the boundary conditions for a multiboundary problem is not easy to find. An example code is listed below. Note that, the user defined functions for `bvp4c` and `bvp5c` can only be defined for three variables, `x` (coordinate mesh of the superconducting or ferromagnetic wire), `y` (solutions to be determined), and `region` (representing the multiboundary). The other variables have dependence on the differential equations and boundary conditions have to be set as `global` variables.

The structure of the differential equations with eight solutions and four boundaries

(three regions) are written as follows [regarding Eq. (4.37) and Eq. (4.44)]

```
function[dxdy]=odefun(x,y,region)
global a b c d
switch region
   case 1
     dxdy=[eqn1_1(a,b,c,d); eqn2_1(a,b,c,d); ...; eqn8_1(a,b,c,d)];
   case 2
     dxdy=[eqn1_2(a,b,c,d); eqn2_2(a,b,c,d); ...; eqn8_2(a,b,c,d)];
   case 3
     dxdy=[eqn1_3(a,b,c,d); eqn2_3(a,b,c,d); ...; eqn8_3(a,b,c,d)];
end
```

Here `dxdy` represents the derivative of $\boldsymbol{f}$ in Eq. (B.1). The equations on the right-hand-side of `dxdy` represents the right-hand-side of the matrix differential equation in Eq. (B.1). For the kinetic equations in Eq. (4.37), these equations are the same for three regions, but for the Usadel equation in Eq. (4.44) [and hence Eq. (5.5)] the equations in `region 2` is different form `region 1` and `region 3`.

The structure of the boundary conditions for the differential equations with the above form are written as follows

```
function[res]=odebc(yL,yR)
global a b c d
res=[cond1(a,b,c,d,yL,yR),cond2(a,b,c,d,yL,yR),...,
     cond32(a,b,c,d,yL,yR)];
```

Here `yL` (`yR`) represents the value of the solutions at the left (right) boundary in each region. For the above differential equations with eight solutions and four boundaries, it is a 8×3 matrix. The boundary conditions in `res` include all the relevant boundary conditions. For example, for the kinetic equations in Eq. (4.37), the boundary conditions not only include the injection of the quasiparticles in Eq. (4.40). One also needs to consider the superconductor is in equilibrium far from the injector. This means $f_L = n_0$, where n_0 is the equilibrium distribution function in Eq. (4.16), and other nonequilibrium modes are zero. This mimics the situations in experiments that the ends of the superconducting wires are connected with wide electrodes within the inelastic scattering length. Similar consideration for the Usadel equation in Eq. (4.44) requires solving the Usadel equation in equilibrium in Eq. (4.25) for the parameterization in Eq. (4.48) in the Matsubara representation.

In order to increase the efficiency and accuracy of `bvp4c` and `bvp5c` for a nonlinear differential equation, one can also provide the analytical partial derivative of the right-hand-side the matrix differential equation in Eq. (B.1) as a Jacobian matrix as

$$\boldsymbol{J} = \left(\partial_{f_1}(M\boldsymbol{f}), \partial_{f_2}(M\boldsymbol{f}), ..., \partial_{f_n}(M\boldsymbol{f})\right),$$

where the components of f_i are the components of the vectors in Eq. (B.2) and Eq. (B.3).

Note also that for the Usadel equation in Eq. (4.44) in the real-time representation, one has to separate the real and imaginary parts to solve the differential equations. This doubles the number of variables in the numerical solutions.

B.3 Other numerical methods

For the diagonalization of the BdG Hamiltonian in Eq. (3.5), the MATLAB built-in function `eig` is used, which returns both eigenvalues and eigenvectors of the matrix. This allows one to calculate all the relevant physical quantities in Chapter 3.

The solutions of the Green's function in homogeneous magnetization in Eq. (4.25), in principle, can be solved using the nonlinear equation solver `nsola`. However, the MATLAB built-in function `fsolve` is also very efficient. We can write Eq. (4.25) in detailed form, write a set of nonlinear algebraic equations for the components of $\hat{g}^R$ in Eq. (4.26) or in Eq. (4.48). Moreover, the normalization condition $(\hat{g}^R)^2 = \hat{1}$ adds two constraints to these equations. The user defined function for these equations can only be defined for the components of $\hat{g}^R$. The other variables relevant for the solutions of the Usadel equation, like the exchange field and temperature, have to be set as `global` variables. The analytical solutions of $\hat{g}^R$ in Eq. (4.28) can be used as the initial guess for `fsolve`.

The numerical integration in MATLAB is also very convenient, especially for array functions. For example, the integrand of the spin accumulation in Eq. (4.42) is an array of position numerically. Using the MATLAB built-in function `integral`, the energy integral can be directly evaluated, by specifying the Name-Value argument as `ArrayValued`. Moreover, the BCS divergence in the integrand (numerically cured by the Dynes parameter Γ) can be evaluated more accurately by providing integration `Waypoints` in the Name-Value argument.

Finally, the initial value problem in Chapter 5. Since the spin current decays smoothly, the domain wall moves smoothly in time. This makes the dynamic equations of the domain wall motion in Eq. (5.1) are nonstiff differential equations. Then one can use the MATLAB built-in differential equation solver `ode45` to solve these differential equations.

References

[1] H. K. Onnes. The Resistance of Pure Mercury at Helium Temperatures,. *Commun. Phys. Lab. Univ. Leiden*, 12(120):1, 1911.

[2] W. Meissner and R. Ochsenfeld. Ein neuer Effekt bei Eintritt der Supraleitfähigkeit [A New Effect at the Onset of Superconductivity]. *Naturwissenschaften*, 21(44):787–788, 1933.

[3] F. London and H. London. The Electromagnetic Equations of the Superconductor. *Proceedings of the Royal Society of London. Series A: Mathematical and Physical Sciences*, 149(866):71–88, 1935.

[4] V. L. Ginzburg and L. D. Landau. On the Theory of Superconductivity. *Zh. Eksp. Teor. Fiz.*, 20:1064–1082, 1950.

[5] J. Bardeen, L. N. Cooper, and J. R. Schrieffer. Theory of Superconductivity. *Phys. Rev.*, 108(5):1175, 1957.

[6] A. A. Abrikosov. On the Magnetic Properties of Superconductors of the Second Group. *JETP*, 5:1174–1182, 1957.

[7] M. Tinkham. *Introduction to Superconductivity.* 2nd Edition, McGraw-Hill, New York, 1996.

[8] B. S. Chandrasekhar. A Note on the Maximum Critical Field of High-Field Superconductors. *Appl. Phys. Lett.*, 1(1):7–8, 1962.

[9] A. M. Clogston. Upper Limit for the Critical Field in Hard Superconductors. *Phys. Rev. Lett.*, 9(6):266, 1962.

[10] I. Giaever. Electron Tunneling Between Two Superconductors. *Phys. Rev. Lett.*, 5:464–466, 1960.

[11] I. Giaever and K. Megerle. Study of Superconductors by Electron Tunneling. *Phys. Rev.*, 122:1101–1111, 1961.

[12] B. D. Josephson. Possible New Effects in Superconductive Tunnelling. *Phys. Lett.*, 1(7):251 – 253, 1962.

[13] V. Ambegaokar and A. Baratoff. Tunneling Between Superconductors. *Phys. Rev. Lett.*, 10:486–489, 1963.

[14] A. Schmid and G. Schön. Linearized Kinetic Equations and Relaxation Processes of a Superconductor Near t_c. *J. Low Temp. Phys.*, 20(1-2):207–227, 1975.

[15] M. Tinkham and J. Clarke. Theory of Pair-Quasiparticle Potential Difference in Nonequilibrium Superconductors. *Phys. Rev. Lett.*, 28:1366–1369, 1972.

[16] T. M. Klapwijk, J. N. Van Den Bergh, and J. E. Mooij. Radiation-Stimulated Superconductivity. *J. of Low Temp. Phys.*, 26(3-4):385–405, 1977.

[17] A. Schmid and G. Schön. Generation of Branch Imbalance by the Interaction between Supercurrent and Thermal Gradient. *Phys. Rev. Lett.*, 43:793–795, 1979.

[18] J. Clarke, B. R. Fjordbøge, and P. E. Lindelof. Supercurrent-Induced Charge Imbalance Measured in a Superconductor in the Presence of a Thermal Gradient. *Phys. Rev. Lett.*, 43:642–645, 1979.

[19] W. Heisenberg. Zur Theorie des Ferromagnetismus. *Z. Phy.*, 49(9):619–636, 1928.

[20] Philip M. M. The Theory of Electric and Magnetic Susceptibilities. *Science*, 76(1971):326–328, 1932.

[21] N. W. Ashcroft and N. D. Mermin. *Solid State Physics*. Holt, Rinehart and Winston, NC, USA, 1976.

[22] R. Skomski. *Simple Models of Magnetism*. Oxford Graduate Texts. OUP Oxford, 2012.

[23] E. C. Stoner. Collective Electron Ferromagnetism. *Proc. R. Soc. A*, 165(922):372–414, 1938.

[24] P. Wachter. *Europium Chalcogenides: EuO, EuS, EuSe and EuTe*, volume 2 of *Handbook on the Physics and Chemistry of Rare Earths*. Elsevier, Amsterdam, Netherlands, 1979, 1979.

[25] C. Kittel. Physical Theory of Ferromagnetic Domains. *Rev. Mod. Phy.*, 21(4):541, 1949.

[26] S. Chikazumi and C. D. Graham. *Physics of Ferromagnetism*, volume 94. Oxford University Press, 2009.

[27] L. D. Landau, E. M. Lifshits, and L. P. Pitaevskii. *Electrodynamics of Continuous Media*. Course of theoretical physics. Butterworth-Heinemann, 1984.

[28] B. D. Cullity and C. D. Graham. *Introduction to Magnetic Materials*. Wiley: Hoboken, NJ, 2 edition, 2009.

[29] S. Middelhoek. Domain Walls in Thin Ni–Fe Films. *J. Appl. Phys.*, 34(4):1054–1059, 1963.

[30] R. L. Stamps. Mechanisms for Exchange Bias. *J. Phys. D.: Appl. Phys.*, 33(23):247–268, 2000.

[31] L. Landau. Diamagnetismus der Metalle. *Z. Phys.*, 64(9):629–637, 1930.

[32] V. A. Shaginyan and V. R. Khodel. Superfluidity in System with Fermion Condensate. *JETP Lett.*, 51(9), 1990.

[33] S. Ryu and Y. Hatsugai. Topological Origin of Zero-Energy Edge States in Particle-Hole Symmetric Systems. *Phys. Rev. Lett.*, 89:077002, 2002.

[34] A. P. Schnyder and S. Ryu. Topological Phases and Surface Flat Bands in Superconductors without Inversion Symmetry. *Phys. Rev. B*, 84:060504, 2011.

[35] T. T. Heikkilä, N. B. Kopnin, and G. E. Volovik. Flat Bands in Topological Media. *JETP Lett.*, 94(3):233, 2011.

[36] N. B. Kopnin, M. Ijäs, A. Harju, and T. T. Heikkilä. High-Temperature Surface Superconductivity in Rhombohedral Graphite. *Phys. Rev. B*, 87:140503, 2013.

[37] K. Murase, S. Ishida, S. Takaoka, T. Okumura, H. Fujiyasu, A. Ishida, and M. Aoki. Superconducting Behavior in PbTe-SnTe Superlattices. *Surf. Sci.*, 170(1):486 – 490, 1986.

[38] N. Y. Fogel, A. S. Pokhila, Y. V. Bomze, A. Y. Sipatov, A. I. Fedorenko, and R. I. Shekhter. Novel Superconducting Semiconducting Superlattices: Dislocation-Induced Superconductivity? *Phys. Rev. Lett.*, 86:512–515, 2001.

[39] N. Y. Fogel, E. I. Buchstab, Y. V. Bomze, O. I. Yuzephovich, A. Y. Sipatov, E. A. Pashitskii, A. Danilov, V. Langer, R. I. Shekhter, and M. Jonson. Interfacial Superconductivity in Semiconducting Monochalcogenide Superlattices. *Phys. Rev. B*, 66:174513, 2002.

[40] P. Esquinazi, T. T. Heikkilä, Y. V. Lysogorskiy, D. A. Tayurskii, and G. E. Volovik. On the Superconductivity of Graphite Interfaces. *JETP Lett.*, 100(5):336–339, 2014.

[41] M. A. H. Vozmediano, M. I. Katsnelson, and F. Guinea. Gauge Fields in Graphene. *Phys. Rep.*, 496(4):109 – 148, 2010.

[42] E. Tang and L. Fu. Strain-Induced Partially Flat Band, Helical Snake States and Interface Superconductivity in Topological Crystalline Insulators. *Nat. Phys.*, 10(12):964, 2014.

[43] G. G. Naumis, S. Barraza-Lopez, M. Oliva-Leyva, and H. Terrones. Electronic and Optical Properties of Strained Graphene and Other Strained 2d Materials: a Review. *Rep. Prog. Phys.*, 80(9):096501, 2017.

[44] T. T. Heikkilä and G. E. Volovik. Flat Bands as a Route to High-Temperature Superconductivity in Graphite. In *Basic Physics of Functionalized Graphite*, pages 123–143. Springer, 2016.

[45] G. E. Volovik. *Quantum Phase Transitions from Topology in Momentum Space*, pages 31–73. Springer, Berlin, Heidelberg, 2007.

[46] N. B. Kopnin and E. B. Sonin. BCS Superconductivity of Dirac Electrons in Graphene Layers. *Phys. Rev. Lett.*, 100:246808, 2008.

[47] Y. E. Lozovik, S. L. Ogarkov, and A. A. Sokolik. Theory of Superconductivity for Dirac Electrons in Graphene. *J. Exp. Theor. Phys.*, 110(1):49–57, 2010.

[48] M. V. Hosseini. Inhomogeneous Superconductivity in the Presence of Time-Reversal Symmetry. *Europhys. Lett.*, 110(4):47010, 2015.

[49] N. B. Kopnin. Surface Superconductivity in Multilayered Rhombohedral Graphene: Supercurrent. *JETP Lett.*, 94(1):81, 2011.

[50] S. Peotta and P. Törmä. Superfluidity in Topologically Nontrivial Flat Bands. *Nat. commun.*, 6:8944, 2015.

[51] G. Profeta, M. Calandra, and F. Mauri. Phonon-Mediated Superconductivity in Graphene by Lithium Deposition. *Nature phys.*, 8(2):131, 2012.

[52] J. Chapman, Y. Su, C. A. Howard, D. Kundys, A. N. Grigorenko, F. Guinea, A. K. Geim, I. V. Grigorieva, and R.R. Nair. Superconductivity in Ca-Doped Graphene Laminates. *Sci. Rep.*, 6:23254, 2016.

[53] R. Meservey, P. M. Tedrow, and P. Fulde. Magnetic Field Splitting of the Quasiparticle States in Superconducting Aluminum Films. *Phys. Rev. Lett.*, 25:1270–1272, 1970.

[54] P. M. Tedrow and R. Meservey. Spin-Dependent Tunneling into Ferromagnetic Nickel. *Phys. Rev. Lett.*, 26:192–195, 1971.

[55] R. Meservey, P. M. Tedrow, and Ronald C. Bruno. Tunneling Measurements on Spin-Paired Superconductors with Spin-Orbit Scattering. *Phys. Rev. B*, 11:4224–4235, 1975.

[56] D. Paraskevopoulos, R. Meservey, and P. M. Tedrow. Spin Polarization of Electrons Tunneling from 3*d* Ferromagnetic Metals and Alloys. *Phys. Rev. B*, 16:4907–4919, 1977.

[57] R. Meservey, D. Paraskevopoulos, and P. M. Tedrow. Tunneling Measurements of Conduction-Electron-Spin Polarization in Heavy Rare-Earth Metals. *Phys. Rev. B*, 22:1331–1337, 1980.

[58] A. I. Buzdin and L. N. Bulaevskii. Ferromagnetic Film on the Surface of a Superconductor: Possible Onset of Inhomogeneous Magnetic Ordering. *Sov. Phys. JETP*, 67(3):576–578, 1988.

[59] T. Tokuyasu, J. A. Sauls, and D. Rainer. Proximity Effect of a Ferromagnetic Insulator in Contact with a Superconductor. *Phys. Rev. B*, 38:8823–8833, 1988.

[60] M. G. Khusainov. Indirect RKKY Exchange and Magnetic States of Ferromagnet-Superconductor Superlattices. *Zh. Eksp. Teor. Fiz.*, 109(2):524, 1996.

[61] F. S. Bergeret, K. B. Efetov, and A. I. Larkin. Nonhomogeneous Magnetic Order in Superconductor-Ferromagnet Fultilayers. *Phys. Rev. B*, 62(17):11872–11878, 2000.

[62] Y. A. Izyumov, Y. N. Proshin, and M. G. Khusainov. Competition between Superconductivity and Magnetism in Ferromagnet/Superconductor Heterostructures. *Usp. Fiz. Nauk*, 45(2):109–148, 2002.

[63] P. G. De Gennes. Coupling between Ferromagnets through a Superconducting Layer. *Phys. Lett.*, 23(1):10 – 11, 1966.

[64] P. M. Tedrow, J. E. Tkaczyk, and A. Kumar. Spin-Polarized Electron Tunneling Study of an Artificially Layered Superconductor with Internal Magnetic Field: EuO-Al. *Phys. Rev. Lett.*, 56:1746–1749, 1986.

[65] X. Hao, J. S. Moodera, and R. Meservey. Spin-Filter Effect of Ferromagnetic Europium Sulfide Tunnel Barriers. *Phys. Rev. B*, 42:8235–8243, 1990.

[66] J. S. Moodera, T. S. Santos, and T. Nagahama. The Phenomena of Spin-Filter Tunnelling. *J. Phys. Condens. Matter*, 19(16):165202, 2007.

[67] Y. M. Xiong, S. Stadler, P. W. Adams, and G. Catelani. Spin-Resolved Tunneling Studies of the Exchange Field in EuS/Al Bilayers. *Phys. Rev. Lett.*, 106:247001, 2011.

[68] K. Senapati, M. G. Blamire, and Z. H. Barber. Spin-Filter Josephson Junctions. *Nat. Mater.*, 10(11):849, 2011.

[69] M. J. Wolf, C. Sürgers, G. Fischer, and D. Beckmann. Spin-Polarized Quasiparticle Transport in Exchange-Split Superconducting Aluminum on Europium Sulfide. *Phys. Rev. B*, 90:144509, 2014.

[70] P. Machon, M. Eschrig, and W. Belzig. Nonlocal Thermoelectric Effects and Nonlocal Onsager Relations in a Three-Terminal Proximity-Coupled Superconductor-Ferromagnet Device. *Phys. Rev. Lett.*, 110:047002, 2013.

[71] P. Machon, M. Eschrig, and W. Belzig. Giant Thermoelectric Effects in a Proximity-Coupled Superconductor-Ferromagnet Device. *New. J. Phys.*, 16(7):073002, 2014.

[72] A. Ozaeta, P. Virtanen, F. S. Bergeret, and T. T. Heikkilä. Predicted Very Large Thermoelectric Effect in Ferromagnet-Superconductor Junctions in the Presence of a Spin-Splitting Magnetic Field. *Phys. Rev. Lett.*, 112:057001, 2014.

[73] S. Kolenda, M. J. Wolf, and D. Beckmann. Observation of Thermoelectric Currents in High-Field Superconductor-Ferromagnet Tunnel Junctions. *Phys. Rev. Lett.*, 116:097001, 2016.

[74] S. Kolenda, C. Sürgers, G. Fischer, and D. Beckmann. Thermoelectric Effects in Superconductor-Ferromagnet Tunnel Junctions on Europium Sulfide. *Phys. Rev. B*, 95:224505, 2017.

[75] N. Poli, J. P. Morten, M. Urech, Arne Brataas, D. B. Haviland, and V. Korenivski. Spin Injection and Relaxation in a Mesoscopic Superconductor. *Phys. Rev. Lett.*, 100:136601, 2008.

[76] C. Quay, D. Chevallier, C. Bena, and M. Aprili. Spin Imbalance and Spin-Charge Separation in a Mesoscopic Superconductor. *Nature Phys.*, 9(2):84, 2013.

[77] F. Hübler, M. J. Wolf, D. Beckmann, and H. v. Löhneysen. Long-Range Spin-Polarized Quasiparticle Transport in Mesoscopic Al Superconductors with a Zeeman Splitting. *Phys. Rev. Lett.*, 109:207001, 2012.

[78] M. J. Wolf, F. Hübler, S. Kolenda, H. v. Löhneysen, and D. Beckmann. Spin Injection from a Normal Metal into a Mesoscopic Superconductor. *Phys. Rev. B*, 87:024517, 2013.

[79] M. Silaev, P. Virtanen, F. S. Bergeret, and T. T. Heikkilä. Long-Range Spin Accumulation from Heat Injection in Mesoscopic Superconductors with Zeeman Splitting. *Phys. Rev. Lett.*, 114:167002, 2015.

[80] T. Krishtop, M. Houzet, and J. S. Meyer. Nonequilibrium Spin Transport in Zeeman-Split Superconductors. *Phys. Rev. B*, 91:121407, 2015.

[81] I. V. Bobkova and A. M. Bobkov. Long-Range Spin Imbalance in Mesoscopic Superconductors under Zeeman Splitting. *JETP Lett.*, 101(2):118–124, 2015.

[82] D. Chevallier, M. Trif, C. Dutreix, M. Guigou, C. H. L. Quay, M. Aprili, and C. Bena. Superconductor Spintronics: Modeling Spin and Charge Accumulation in out-of-Equilibrium NIS Junctions Subjected to Zeeman Magnetic Fields. *New J. Phys.*, 20(1):013014, 2018.

[83] F. S. Bergeret, M. Silaev, P. Virtanen, and T. T. Heikkilä. Colloquium: Nonequilibrium Effects in Superconductors with a Spin-Splitting Field. *Rev. Mod. Phys.*, 90:041001, 2018.

[84] T. T. Heikkilä, M. Silaev, P. Virtanen, and F. S. Bergeret. Thermal, Electric and Spin Transport in Superconductor/Ferromagnetic-Insulator Structures. *Prog. Surf. Sci.*, 94(3):100540, 2019.

[85] E. Strambini, V. N. Golovach, G. De Simoni, J. S. Moodera, F. S. Bergeret, and F. Giazotto. Revealing the Magnetic Proximity Effect in EuS/Al Bilayers through Superconducting Tunneling Spectroscopy. *Phys. Rev. Mater.*, 1:054402, 2017.

[86] L. P. Gorkov. On the Energy Spectrum of Superconductors. *Sov. Phys. JETP*, 7(505):158, 1958.

[87] A. A. Abrikosov, L. P. Gorkov, and I. E. Dzyaloshinski. Methods of Quantum Field Theory in Statistical Physics (p. 48), 1963.

[88] G. Eilenberger. Transformation of Gorkov's Equation for Type II Superconductors into Transport-Like Equations. *Z. Physik*, 214(2):195–213, 1968.

[89] A. Ozaeta. Transport Phenomena in Superconducting Hybrid Nanostructures. *Doctoral Dissertation*, 2014.

[90] W. Belzig, F. K. Wilhelm, C. Bruder, G. Schön, and A. D. Zaikin. Quasiclassical Green's Function Approach to Mesoscopic Superconductivity. *Superlattices Microstruct.*, 25(5):1251 – 1288, 1999.

[91] N. Kopnin. *Theory of Nonequilibrium Superconductivity*. International Series of Monographs on Physics. Clarendon Press, Oxford, 2001.

[92] J. A. X. Alexander, T. P. Orlando, D. Rainer, and P. M. Tedrow. Theory of Fermi-Liquid Effects in High-Field Tunneling. *Phys. Rev. B*, 31:5811–5825, 1985.

[93] U. Eckern and A. Schmid. Quasiclassical Green's Function in the BCS Pairing Theory. *J. Low Temp. Phys.*, 45(1-2):137–166, 1981.

[94] K. D. Usadel. Generalized Diffusion Equation for Superconducting Alloys. *Phys. Rev. Lett.*, 25:507–509, 1970.

[95] R. C. Dynes, V. Narayanamurti, and J. P. Garno. Direct Measurement of Quasiparticle-Lifetime Broadening in a Strong-Coupled Superconductor. *Phys. Rev. Lett.*, 41:1509–1512, 1978.

[96] G. M. Eliashberg. Inelastic Electron Collisions and Nonequilibrium Stationary States in Superconductors. *Sov. Phys. JETP*, 34(3):668–676, 1972.

[97] J. W. Serene and D. Rainer. The Quasiclassical Approach to Superfluid ^{3}He. *Phys. Rep.*, 101(4):221 – 311, 1983.

[98] P. G. de Gennes. *Superconductivity of Metals and Alloys*. Advanced Book Classics. Westview Press, Boulder, CO, 1999.

[99] W. Belzig, C. Bruder, and G. Schön. Local Density of States in a Dirty Normal Metal Connected to a Superconductor. *Phys. Rev. B*, 54:9443–9448, 1996.

[100] A. Anthore, H. Pothier, and D. Esteve. Density of States in a Superconductor Carrying a Supercurrent. *Phys. Rev. Lett.*, 90:127001, 2003.

[101] T. Matsubara. A New Approach to Quantum-Statistical Mechanics. *Prog. Theor. Phys.*, 14(4):351–378, 1955.

[102] P. Virtanen, A. Vargunin, and M. Silaev. Quasiclassical Expressions for the Free Energy of Superconducting Systems. *arXiv preprint arXiv:1909.00992*, 2019.

[103] G. M. Eliashberg. Nonstationary Equations for Superconductors with Low Concentration of Paramagnetic Impurities. *Sov. Phys. JETP*, 28(6):1298–1302, 1969.

[104] L. V. Keldysh. Diagram Technique for Nonequilibrium Processes. *Sov. Phys. JETP*, 20(4):1018–1026, 1965.

[105] J. Rammer and H. Smith. Quantum Field-Theoretical Methods in Transport Theory of Metals. *Rev. Mod. Phys.*, 58:323–359, 1986.

[106] A. I. Larkin and Y. U. N. Ovchinnikov. Nonlinear Conductivity of Superconductors in the Mixed State. *Sov. Phys. JETP*, 41(5):960–965, 1975.

[107] F. S. Bergeret, A. Verso, and A. F. Volkov. Electronic Transport through Ferromagnetic and Superconducting Junctions with Spin-Filter Tunneling Barriers. *Phys. Rev. B*, 86:214516, 2012.

[108] A. I. Larkin and Y. N. Ovchinnikov. Tunnel Effect between Superconductors in an Alternating Field. *Sov. Phys. JETP*, 24(11):1035–1040, 1967.

[109] Richard E. H. Cosine and Other Terms in the Josephson Tunneling Current. *Phys. Rev. B*, 10:84–94, 1974.

[110] I. V. Krive, S. I. Kulinich, R. I. Shekhter, and M. Jonson. Charge and Spin Effects in Mesoscopic Josephson Junctions (Review). *Low Temp. Phys.*, 30(7):554–567, 2004.

[111] M. Y. Kuprianov and V. F. Lukichev. Influence of Boundary Transparency on the Critical Current of "Dirty" SS'S Structures. *Zh. Eksp. Teor. Fiz.*, 94:149, 1988.

[112] F. S. Bergeret and I. V. Tokatly. Singlet-Triplet Conversion and the Long-Range Proximity Effect in Superconductor-Ferromagnet Structures with Generic Spin Dependent Fields. *Phys. Rev. Lett.*, 110:117003, 2013.

[113] F. S. Bergeret and I. V. Tokatly. Spin-Orbit Coupling as a Source of Long-Range Triplet Proximity Effect in Superconductor-Ferromagnet Hybrid Structures. *Phys. Rev. B*, 89:134517, 2014.

[114] C. Gorini, P. Schwab, R. Raimondi, and A. L. Shelankov. Non-Abelian Gauge Fields in the Gradient Expansion: Generalized Boltzmann and Eilenberger Equations. *Phys. Rev. B*, 82:195316, 2010.

[115] I. V. Tokatly, B. Bujnowski, and F. S. Bergeret. Correspondence between Bulk Equilibrium Spin-Currents and Edge Spin Accumulation in Wires with Spin-Orbit Coupling. *arXiv preprint arXiv:1901.07890*, 2019.

[116] D. A. Ivanov and Ya. V. Fominov. Minigap in Superconductor-Ferromagnet Junctions with Inhomogeneous Magnetization. *Phys. Rev. B*, 73:214524, 2006.

[117] D. C. Ralph and M. D. Stiles. Spin Transfer Torques. *J. Magn. Magn. Mater.*, 320(7):1190 – 1216, 2008.

[118] G. Tatara, H. Kohno, and J. Shibata. Microscopic Approach to Current-Driven Domain Wall Dynamics. *Phys. Rep.*, 468(6):213 – 301, 2008.

[119] I. V Bobkova, A. M. Bobkov, and W. Belzig. Thermally Induced Spin-Transfer Torques in Superconductor/Ferromagnet Bilayers. *arXiv preprint arXiv:1909.04418*, 2019.

[120] L. Berger. Low-Field Magnetoresistance and Domain Drag in Ferromagnets. *J. Appl. Phys.*, 49(3):2156–2161, 1978.

[121] L. Berger. Exchange Interaction between Ferromagnetic Domain Wall and Electric Current in very Thin Metallic Films. *J. Appl. Phys.*, 55(6):1954–1956, 1984.

[122] L. Berger. Motion of a Magnetic Domain Wall Traversed by Fast-Rising Current Pulses. *J. Appl. Phys.*, 71(6):2721–2726, 1992.

[123] L. Berger. Emission of Spin Waves by a Magnetic Multilayer Traversed by a Current. *Phys. Rev. B*, 54:9353–9358, 1996.

[124] J. Grollier, D. Lacour, V. Cros, A. Hamzić, A. Vaurès, A. Fert, D. Adam, and G. Faini. Switching the Magnetic Configuration of a Spin Valve by Current-Induced Domain Wall Motion. *J. Appl. Phys.*, 92(8):4825–4827, 2002.

[125] J. Grollier, P. Boulenc, V. Cros, A. Hamzić, A. Vaurès, A. Fert, and G. Faini. Switching a Spin Valve Back and Forth by Current-Induced Domain Wall Motion. *Appl. Phys. Lett.*, 83(3):509–511, 2003.

[126] M. Kläui, C. A. F. Vaz, J. A. C. Bland, W. Wernsdorfer, G. Faini, E. Cambril, and L. J. Heyderman. Domain Wall Motion Induced by Spin Polarized Currents in Ferromagnetic Ring Structures. *Appl. Phys. Lett.*, 83(1):105–107, 2003.

[127] N. Vernier, D. A Allwood, D. Atkinson, M. D. Cooke, and R. P. Cowburn. Domain Wall Propagation in Magnetic Nanowires by Spin-Polarized Current Injection. *Europhys. Lett.*, 65(4):526–532, 2004.

[128] A. Yamaguchi, T. Ono, S. Nasu, K. Miyake, K. Mibu, and T. Shinjo. Real-Space Observation of Current-Driven Domain Wall Motion in Submicron Magnetic Wires. *Phys. Rev. Lett.*, 92:077205, 2004.

[129] G. Tatara and H. Kohno. Theory of Current-Driven Domain Wall Motion: Spin Transfer versus Momentum Transfer. *Phys. Rev. Lett.*, 92:086601, 2004.

[130] S. Zhang and Z. Li. Roles of Nonequilibrium Conduction Electrons on the Magnetization Dynamics of Ferromagnets. *Phys. Rev. Lett.*, 93:127204, 2004.

[131] A. Thiaville, Y. Nakatani, J. Miltat, and Y. Suzuki. Micromagnetic Understanding of Current-Driven Domain Wall Motion in Patterned Nanowires. *Europhys. Lett.*, 69(6):990–996, 2005.

[132] N. L. Schryer and L. R. Walker. The Motion of 180° Domain Walls in Uniform DC Magnetic Fields. *J. Appl. Phys.*, 45(12):5406–5421, 1974.

[133] Y. Cao, V. Fatemi, S. Fang, K. Watanabe, T. Taniguchi, E. Kaxiras, and P. Jarillo-Herrero. Unconventional Superconductivity in Magic-Angle Graphene Superlattices. *Nature*, 556(7699):43, 2018.

[134] T. J. Peltonen, R. Ojajärvi, and T. T. Heikkilä. Mean-Field Theory for Superconductivity in Twisted Bilayer Graphene. *Phys. Rev. B*, 98:220504, 2018.

[135] E. Suárez Morell, J. D. Correa, P. Vargas, M. Pacheco, and Z. Barticevic. Flat Bands in Slightly Twisted Bilayer Graphene: Tight-Binding Calculations. *Phys. Rev. B*, 82:121407, 2010.

[136] A. I. Buzdin. Proximity effects in superconductor-ferromagnet heterostructures. *Rev. Mod. Phys.*, 77:935–976, 2005.

[137] T. T. Heikkilä, R. Ojajärvi, I. J. Maasilta, E. Strambini, F. Giazotto, and F. S. Bergeret. Thermoelectric Radiation Detector Based on Superconductor-Ferromagnet Systems. *Phys. Rev. Applied*, 10:034053, 2018.

[138] Teemu J. Peltonen and Tero T. Heikkilä. Flat-Band Superconductivity in Periodically Strained Graphene: Mean-Field and Berezinskii-Kosterlitz-Thouless Transition. *arXiv preprint arXiv:1910.06671*, 2019.

[139] D. Aasen, M. Hell, R. V. Mishmash, A. Higginbotham, J. Danon, M. Leijnse, T. S. Jespersen, J. A. Folk, Charles M. Marcus, K. Flensberg, and J. Alicea. Milestones Toward Majorana-Based Quantum Computing. *Phys. Rev. X*, 6:031016, 2016.

[140] C. Beenakker and L. Kouwenhoven. A Road to Reality with Topological Superconductors. *Nature Phys.*, 12(7):618, 2016.

[141] P. Virtanen, F. S. Bergeret, E. Strambini, F. Giazotto, and A. Braggio. Majorana Bound States in Hybrid Two-Dimensional Josephson Junctions with Ferromagnetic Insulators. *Phys. Rev. B*, 98:020501, 2018.

ORIGINAL PAPERS

I

FLAT BAND SUPERCONDUCTIVITY IN STRAINED DIRAC MATERIALS

by

V. J. Kauppila, F. Aikebaier &T. T. Heikkilä 2016

Phys. Rev B. 93. 214505 (2016)

DOI: http://doi.org/10.1103/PhysRevB.93.214505

PHYSICAL REVIEW B **93**, 214505 (2016)

Flat-band superconductivity in strained Dirac materials

V. J. Kauppila,[1,*] F. Aikebaier,[2] and T. T. Heikkilä[2]

[1]*Low Temperature Laboratory, Department of Applied Physics, Aalto University, P.O. Box 15100, FI-00076 Aalto, Finland*

[2]*University of Jyvaskyla, Department of Physics and Nanoscience Center, P.O. Box 35, FI-40014 University of Jyväskylä, Finland*

(Received 22 January 2016; revised manuscript received 17 March 2016; published 13 June 2016)

We consider superconducting properties of a two-dimensional Dirac material such as graphene under strain that produces a flat-band spectrum in the normal state. We show that in the superconducting state, such a model results in a highly increased critical temperature compared to the case without the strain, inhomogeneous order parameter with two-peak shaped local density of states and yet a large and almost uniform and isotropic supercurrent. This model could be realized in strained graphene or ultracold atom systems and could be responsible for unusually strong superconductivity observed in some graphite interfaces and certain IV-VI semiconductor heterostructures.

DOI: 10.1103/PhysRevB.93.214505

In conventional superconductors, the superconducting critical temperature T_c depends exponentially on the electronic density of states ν at the Fermi level, $T_c \sim e^{-1/(g\nu)}$, where g describes the strength of attractive interaction. Thus, when engineering materials for higher critical temperatures, it is natural to aim to increase the density of states. In two-dimensional systems such as graphene, a traditional approach for this is to utilize doping [1], which recently lead to a breakthrough as strongly doped graphene was found to be superconducting with T_c of a few Kelvin [2]. An extreme case of increased density of states is the flat-band state, where the electrons within some momentum regime are completely dispersionless, leading to diverging density of states at the corresponding energy. In various different models, this has been shown to result in a parametrically enhanced critical temperature that is linear in the electron-phonon coupling constant, $T_c \sim g$ [3,4]. It has also been shown that this type of an approximate flat-band state is realized in graphene and other Dirac materials under periodic strain [5,6].

Besides straining Dirac electrons, there have been several propositions for realizing systems with a flat band and possibly promoting superconductivity [7]. Such models include surface states of topological semimetals with an approximate chiral symmetry [8]. If the energy scale characterizing the deviation from the exact symmetry is weaker than that characterizing superconductivity, the mean field theory predicts flat-band superconductivity [9]. An example system belonging to this class is rhombohedral graphite. However, this type of superconductor is prone to fluctuations [10].

The most often encountered models leading to flat bands result from large magnetic fields and the associated Landau levels [11]. However, magnetic fields also break the time reversal symmetry and typically suppress (singlet) superconducting order, so they cannot directly be utilized. A recent approach was hence to study superconductivity in a time-reversal invariant attractive Harper-Hubbard model defined on a two-dimensional square lattice [12], with the most direct realization in ultracold gases.

Here we present a BCS-like model for superconductivity of Dirac electrons under the type of strain that produces a flat-band normal state. This model has quite possibly been already realized in interfaces between IV-VI semiconductor heterostructures where the strain is naturally created between a topological insulator and a trivial insulator due to lattice mismatch [5,13,14]. Another possible realization for this model is in graphene with a strain field, created either artificially or at an interface inside graphite [15]. The latter suggestion also builds on the recent experimental evidence that graphene can become superconducting under heavy doping [1,2]. Our proposal could potentially be used to increase the superconducting critical temperature much higher in the absence of external doping. Besides, our model can be studied in ultracold gases in optical lattices where transforming Dirac points with adjustable geometry has already been demonstrated [16] and where the interaction between the electrons can be tuned via Feshbach resonances [17,18].

To achieve the flat-band state, the strain field experienced by the Dirac electrons should be such that the resulting effective vector potential is of the form $\mathbf{A} \propto (0, A_y(x), 0)$, where $A_y(x)$, the vector potential in the y direction in the 2D lattice, changes sign periodically in x, the direction perpendicular to the vector potential. A strict periodical variation is not entirely necessary for this effect, but it allows for a more direct theoretical description of the effect. Here we follow Ref. [5] and use $A_y(x) = \frac{\beta}{L}\cos(2\pi x/L)$, where β is a dimensionless parameter describing the strength of the strain and L is the strain period. In graphene, this vector potential could be produced for example by an in-plane strain field of the form $u_y(x) = \frac{a\beta}{4\pi}\sin(2\pi x/L)$ (assuming graphene Grüneisen parameter $= 2$ [6], see Fig. 1(a)) or out-of-plane strain field of the form $h(x,y) = y + \frac{a\beta}{4\pi}\sin(2\pi x/L)$, where $a = 1.42$ Å is the graphene lattice constant. As a result, the low-energy Hamiltonian describing the Dirac electrons is given by

$$\hat{H}_0 = \hbar v_F \hat{p}_x \sigma_x + \hbar v_F (\hat{p}_y + A_y(x))\sigma_y, \tag{1}$$

where v_F is the Fermi velocity of the Dirac material. In condensed-matter systems, Dirac points appear in pairs (valleys in graphene physics). Equation (1) describes the physics at one valley, say $\mathbf{K}$, whereas the sign of A_y is reversed for the partner valley ($\mathbf{K}'$). The dispersion relation of this model has an approximate flat band for $p_x \in [-\pi/L, \pi/L]$ and $p_y \in [-\beta/(2L), \beta/(2L)]$. Inside the flat band, it has a weak dispersion of the form $E_{\mathbf{p}} = \hbar c|\mathbf{p}|$, where $c = v_F/I_0(\beta/\pi)$

*ville.kauppila@aalto.fi

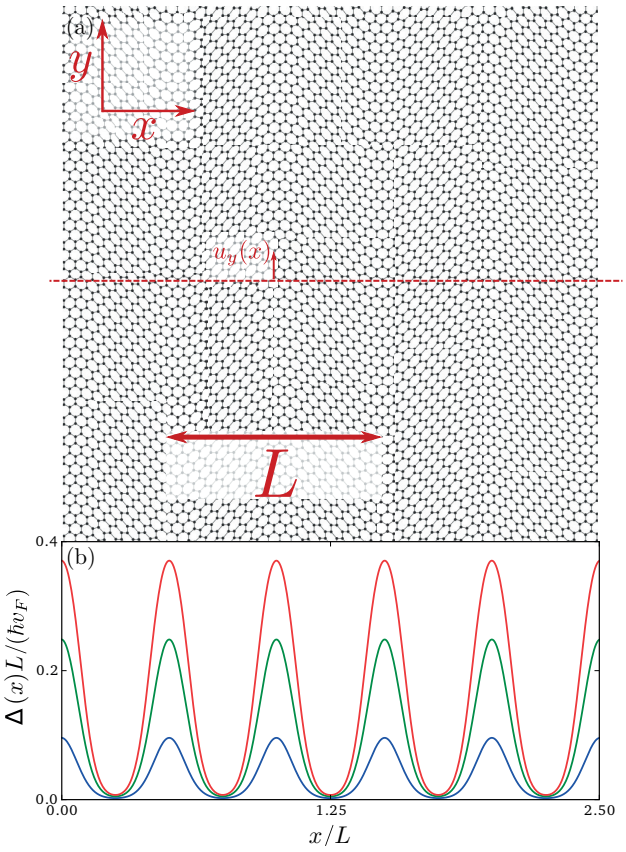

FIG. 1. (a) Schematic, highly exaggerated picture of a honeycomb lattice in strain field of the form $u_y(x) = \frac{a\beta}{4\pi}\sin(2\pi x/L)$, L being the strain period. (b) The profile of $\Delta(x)$ for $\beta = 20$ (blue), $\beta = 30$ (green), and $\beta = 40$ (red) and $g/(\hbar v_F L) = 0.01$.

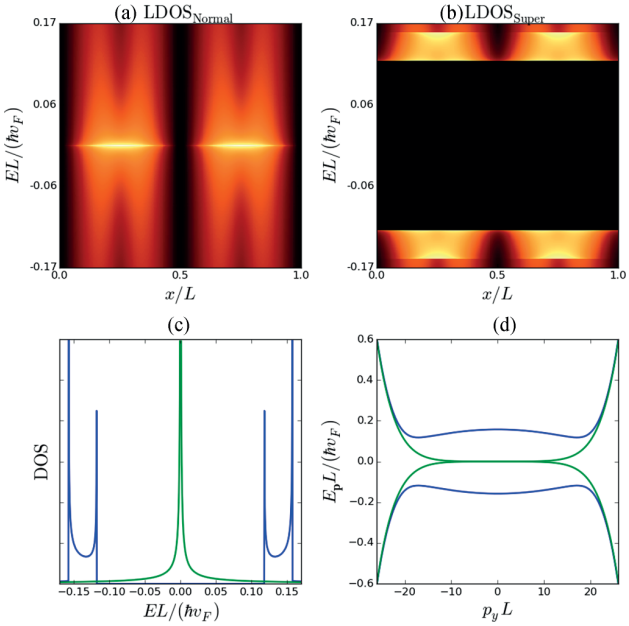

FIG. 2. Spectral properties of Dirac electrons in a periodic strain in normal and superconducting states with $\beta = 40$ and $g/(\hbar v_F L) = 0.005$. (a) Local density of states in the normal state. (b) Local density of states in the superconducting state. (c) Total density of states for the normal (green) and superconducting (blue) states. (d) The energy spectrum in both states.

and $I_n(x)$ is the modified Bessel function of the first kind [19]. For $\beta \gg \pi$, the speed becomes exponentially small, and the bands become asymptotically flat. This dispersion, along with the width of the flat band, determines the energy scale above which the model can be considered to have a flat band. The eigenstates of this Hamiltonian are localized at the points where the potential changes sign so that one sublattice is occupied at one sign change and the other sublattice at the opposite sign change. This can be seen in the density of states of the normal state shown in Fig. 2(a).

The Hamiltonian (1) is closely related to the Su-Schrieffer-Heeger (SSH) model for polyacetylene chains [20]. When the y-directional momentum p_y in (1) is zero, the model is exactly the SSH model with a domain wall and the associated topological zero energy state at each point where the potential changes sign. For finite p_y the domain walls move closer to each other and the zero energy states start to overlap until they are effectively destroyed at $p_y \approx \beta/(2L)$.

When we add an attractive interaction of coupling strength g to the model (1) (we assume here s-wave type coupling for simplicity [21]), the material has the possibility to enter a superconducting state described by the Bogoliubov-de Gennes equation

$$\begin{pmatrix} H_0 & \Delta(x) \\ \Delta^*(x) & -H_0 \end{pmatrix}\begin{pmatrix} u_n(\mathbf{r}) \\ v_n(\mathbf{r}) \end{pmatrix} = E_n \begin{pmatrix} u_n(\mathbf{r}) \\ v_n(\mathbf{r}) \end{pmatrix}. \tag{2}$$

The two degrees of freedom in the matrix are the Dirac particles, described by H_0 given in (1) with spinor wave functions $u_n(\mathbf{r})$, and Dirac holes, described by the Hamiltonian for holes, $-H_0$ with spinor wave functions $v_n(\mathbf{r})$. The form of the hole Hamiltonian follows from the fact that the hole partner for a particle in valley $\mathbf{K}$ is a conjugated particle at valley $-\mathbf{K}$ so that $H_0^{\text{holes}}(\mathbf{K}) = H_0^*(-\mathbf{K}) = -H_0(\mathbf{K})$. Below we suppress the subvalley indices and consider only $\mathbf{K}$ subvalley except when otherwise mentioned. The coupling between the particles and holes is described by a superconducting order parameter $\Delta(x)$, which, because of the periodic potential in the Hamiltonian, has a periodic dependence on the x coordinate. It can be found by solving the self-consistency equation

$$\Delta(x) = \frac{gL^2}{4\pi^2}\int_0^{2\pi/L} dp_x \int_0^{p_c} dp_y \sum_i \sum_n \times v^*_{i,n,\mathbf{p}}(x) u_{i,n\mathbf{p}}(x) \tanh\left[\frac{E_n(\mathbf{p})}{2k_B T}\right], \tag{3}$$

where we have summed over the two valleys which leads to both sublattices, labeled by i, contributing to the same Δ. The sum over the band index n can be restricted to those bands with energy below some cutoff energy, say the Debye energy due to the electron-phonon interaction.

With qualitative analysis of the energy scales of the model, we find three different regimes: (i) When $g \ll \hbar c L$, the small

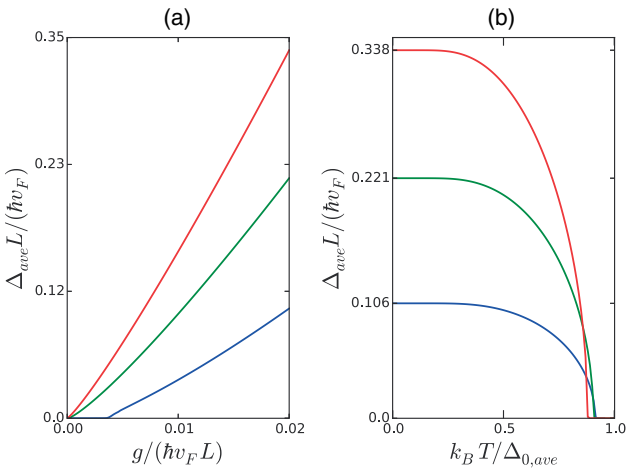

FIG. 3. (a) Dependence of Δ_{ave} on superconducting coupling with $\beta = 20$ (blue), $\beta = 30$ (green), and $\beta = 40$ (red). (b) Δ_{ave} as a function of temperature for $g/(\hbar v_F L) = 0.02$.

linear slope of the spectrum is visible and superconductivity is of the type found in pure Dirac materials [22,23] (for example, graphene). In particular, there is a quantum critical point at $g = \pi^2 \hbar c L/\beta$ below which superconductivity does not take place. (ii) When $\hbar c L \ll g \ll \hbar v_F L/\beta$, the system is in the pure flat-band superconductivity regime, only the lowest energy band contributing to the superconductivity. The critical temperature is enhanced and Δ is localized. This is the interesting regime where we focus below. (iii) When $g \gtrsim \hbar v_F L/\beta$, also higher (nonflat) bands contribute to superconductivity. A model resembling the one here in this third limit was considered in Ref. [24] in strained graphene where an inhomogeneous superconducting state was also found.

Because the density of states is peaked at the locations of the vector potential sign change, we expect that the superconducting order parameter is also localized close to these points. To demonstrate this, we calculate $\Delta(x)$ in the model (2) from the self-consistency calculation [19]. The resulting profile of $\Delta(x)$ is shown in Fig. 1(b).

In Fig. 3(b) we also plot the average of $\Delta(x)$ as a function of the coupling constant. For small couplings, where Δ is small and can "see" the small linear slope of the spectrum, there is a quantum critical point at $g \approx \pi^2 \hbar c L/\beta$ below which there is no superconductivity. In the figure, this point is only visible for $\beta = 20$ because for larger β the linear regime of the spectrum becomes exponentially smaller. For larger g, the system enters the flat-band regime. A simple constant Δ estimate yields for the order of magnitude estimate $\Delta \approx \beta g/(2L^2)$. This expression also shows the strong linear relationship between Δ and g that is apparent in the numerical calculation. From the numerics, we can also find that the critical temperature T_c is approximately given by the average value of Δ, i.e., $k_B T_c \approx (1/L)\int_0^L dx \Delta(x)$. This behavior is shown in Fig. 3(b). Due to the linear dependence between T_c and g we can therefore expect a high critical temperature in this parameter regime.

We also calculate the spectrum and local density of states in the superconducting state. At zero momentum, the spectrum has a gap of magnitude $|E_{\mathbf{p}=0}| \approx 2\Delta_{\max}$ which is the expected result for any superconductor. However, for small momenta, the slope of the spectrum is negative for excitations with positive momentum and energy, leading to a local minimum at $k_y = k_{\min} \sim \beta/(2L)$. The momentum dependence results from the localized $\Delta(x)$. In the density of states, the two local minima of the spectrum lead to a peculiar two-peaked shape shown in Fig. 2(a). This feature could act as a possible experimental signature for superconductivity described by this model.

For a flat band, the group velocity c of the electrons becomes very small for both normal and superconducting state [see Fig. 2(d)]. It would hence be natural to think of the paired electrons to be localized, unable to carry supercurrent. However, there are also other contributions to supercurrent besides those proportional to the group velocity [12]. We calculate the supercurrent by adding a phase gradient to the order parameter as $\Delta(x) \to \Delta(x)e^{i\mathbf{k}_s x}$ in which case the supercurrent is given by

$$\mathbf{J}(x) = \frac{ev_F}{L}\sum_{\mathbf{p},n}(f_{\mathbf{p},n}u^\dagger_{\mathbf{p},n}\sigma u_{\mathbf{p},n} + (f_{\mathbf{p},n}-1)v^\dagger_{\mathbf{p},n}\sigma v_{\mathbf{p},n}), \quad (4)$$

where $f_{\mathbf{p},n}$ is the number of quasiparticles occupying the nth band at momentum $\mathbf{p}$. At $T = 0$, $f[E_n(\mathbf{p})] = 1$ for $E_n(\mathbf{p}) < 0$ and 0 otherwise.

For $|\mathbf{k}_s L| \ll 1$, we find that the supercurrent is approximately of the form $J_i(x) \approx a_i \Delta_{\max} k_{s,i}$, where $i \in \{x,y\}$ and $a_x = 0.17$, $a_y = 0.19$ are fitted constants that describe the weak anisotropy of the current. This result is shown in Fig. 4. While current in the x direction must be independent of y due to translational invariance, it can be inhomogeneous in the y direction. In the inset of Fig. 4 we show the profile of current flowing in the y direction. Interestingly, it is only weakly inhomogeneous even though the superconducting order parameter varies strongly in space. The reason for this is that the current is proportional to the overlap of the wave functions of the two sublattices and the overlap is

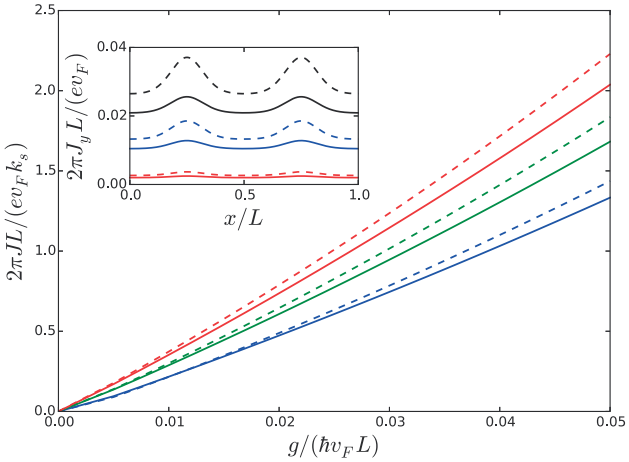

FIG. 4. Supercurrent in x and y directions (solid and dashed lines, respectively) as a function of the superconducting coupling for $\beta = 25$ (blue), $\beta = 30$ (green), and $\beta = 35$ (red). Inset: profile of the supercurrent in y direction for $\beta = 25$ (solid line) and $\beta = 30$ (dashed line) for $k_s L = 0.01, 0.05, 0.1$.

almost position independent. This behavior is analogous to what happens in a model for superconducting rhombohedral graphite [25].

Let us discuss the possible physical realizations of periodically strained Dirac fermions. So far, graphene has been shown to be superconducting when doped with calcium and possibly also with other elements [1,2,26]. In that case doping of the pure Dirac material is required to increase the density of states so that the quantum critical point disappears. If this is the main effect, then the scheme of a periodic strain discussed here should also make even undoped graphene superconducting because the flattening of the spectrum greatly lowers the superconducting coupling required to overcome the quantum critical point (by the factor $c/v_F = 1/I_0(\beta/\pi)$). Contrary to the pristine graphene (or other Dirac material), doping the strained graphene to move the chemical potential out of the flat-band regime would act to reduce the critical temperature.

Strain superlattice could explain the observations of the superconducting-type behavior at interfaces between graphite regions with different lattice orientations [27–29]. It is possible that such interfaces stabilize an array of screw dislocations, which would lead to the presence of periodically strained graphene at the interfaces.

We can estimate the value of the critical temperature in periodically strained graphene using the coupling constant obtained from experiments [2,26]. As shown in Ref. [19], we would get T_c as large as 420 K for $\beta = 30$ and $L = 10$ nm. In this estimate, we neglect the effects from the strain superlattice or the doping in the experiments on g, and therefore it should be taken only as indicative. Such effects are left for further work.

Another class of materials where flat-band superconductivity due to straining has already been suggested is layered structures made out of IV-VI semiconductors such as PbTe/SnTe, PbSe, PbS, PbTe/PbSe, PbS/YbS, and PbTe/YbS [13,14]. Our results here could be used to verify whether models previously suggested [5] indeed are valid in these materials.

Besides superconductivity, flat bands can promote also other types of states, such as magnetism [30], depending on the dominant interaction channel. Moreover, in such two-dimensional systems the long-range correlations are most likely suppressed by some mechanism, which would limit the observation of superconductivity in large samples. Besides the phase fluctuations leading to Kosterlitz-Thouless physics, another mechanism for suppressing correlations would be those affecting the strain lattice. Therefore, on length scales long compared to such elastic correlation length, the system would most likely be described by a set of Josephson coupled superconducting islands. The exact elastic correlation lengths are materials dependent and therefore out of the scope of the present work. We also note that in the case of strained graphene, other pairing symmetries have been considered [31].

We thank Grigori Volovik and Pablo Esquinazi for fruitful discussions. This work was supported by the Academy of Finland through its Center of Excellence program Project No. 284594, and by the European Research Council (Grant No. 240362-Heattronics).

[1] G. Profeta, M. Calandra, and F. Mauri, Nat. Phys. **8**, 131 (2012).
[2] J. Chapman, Y. Su, C. Howard, D. Kundys, A. Grigorenko, F. Guinea, A. Geim, I. Grigorieva, and R. Nair, Sci. Rep. **6**, 23254 (2016).
[3] N. B. Kopnin, T. T. Heikkilä, and G. E. Volovik, Phys. Rev. B **83**, 220503 (2011).
[4] V. Khodel and V. Shaginyan, JETP Lett. **51**, 553 (1990).
[5] E. Tang and L. Fu, Nat. Phys. **10**, 964 (2014).
[6] M. A. Vozmediano, M. Katsnelson, and F. Guinea, Phys. Rep. **496**, 109 (2010).
[7] T. T. Heikkilä and G. E. Volovik, arXiv:1504.05824.
[8] T. Heikkilä, N. B. Kopnin, and G. E. Volovik, JETP Lett. **94**, 233 (2011).
[9] N. B. Kopnin, M. Ijäs, A. Harju, and T. T. Heikkilä, Phys. Rev. B **87**, 140503 (2013).
[10] V. J. Kauppila, T. Hyart, and T. T. Heikkilä, Phys. Rev. B **93**, 024505 (2016).
[11] L. Landau, Z. Phys. **64**, 629 (1930).
[12] S. Peotta and P. Törmä, Nat. Commun. **6**, 8944 (2015).
[13] N. Y. Fogel, E. I. Buchstab, Y. V. Bomze, O. I. Yuzephovich, A. Y. Sipatov, E. A. Pashitskii, A. Danilov, V. Langer, R. I. Shekhter, and M. Jonson, Phys. Rev. B **66**, 174513 (2002).
[14] N. Y. Fogel, A. S. Pokhila, Y. V. Bomze, A. Y. Sipatov, A. I. Fedorenko, and R. I. Shekhter, Phys. Rev. Lett. **86**, 512 (2001).
[15] P. Esquinazi, T. Heikkilä, Y. Lysogorskiy, D. Tayurskii, and G. Volovik, JETP Lett. **100**, 336 (2014).
[16] L. Tarruell, D. Greif, T. Uehlinger, G. Jotzu, and T. Esslinger, Nature (London) **483**, 302 (2012).
[17] I. Bloch, J. Dalibard, and W. Zwerger, Rev. Mod. Phys. **80**, 885 (2008).
[18] C. Chin, R. Grimm, P. Julienne, and E. Tiesinga, Rev. Mod. Phys. **82**, 1225 (2010).
[19] See Supplemental Material at http://link.aps.org/supplemental/10.1103/PhysRevB.93.214505 for the technical details of our model.
[20] A. J. Heeger, S. Kivelson, J. Schrieffer, and W.-P. Su, Rev. Mod. Phys. **60**, 781 (1988).
[21] Typically phonon mediated superconductivity in graphene is ascribed to lead to s-wave pairing, whereas other origins for the attractive interactions may lead to more exotic pairings, see Ref. [32] online for the discussion in the context of doped graphene. The recent experimental evidence [1,2] on superconductivity has been interpreted to be phonon mediated.
[22] N. B. Kopnin and E. B. Sonin, Phys. Rev. Lett. **100**, 246808 (2008).
[23] Y. E. Lozovik, S. Ogarkov, and A. Sokolik, J. Exp. Theor. Phys. **110**, 49 (2010).
[24] M. V. Hosseini, Europhys. Lett. **110**, 47010 (2015).
[25] N. B. Kopnin, JETP Lett. **94**, 81 (2011).
[26] A. V. Fedorov, N. I. Verbitskiy, D. Haberer, C. Struzzi, L. Petaccia, D. Usachov, O. Y. Vilkov, D. Vyalikh, J. Fink, M. Knupfer *et al.*, Nat. Commun. **5**, 3257 (2014).
[27] T. Scheike, W. Böhlmann, P. Esquinazi, J. Barzola-Quiquia, A. Ballestar, and A. Setzer, Adv. Mater. **24**, 5826 (2012).

[28] A. Ballestar, J. Barzola-Quiquia, T. Scheike, and P. Esquinazi, New J. Phys. **15**, 023024 (2013).
[29] P. Esquinazi, N. García, J. Barzola-Quiquia, P. Rödiger, K. Schindler, J.-L. Yao, and M. Ziese, Phys. Rev. B **78**, 134516 (2008).
[30] H.-H. Lin, T. Hikihara, H.-T. Jeng, B.-L. Huang, C.-Y. Mou, and X. Hu, Phys. Rev. B **79**, 035405 (2009).
[31] B. Roy and V. Juričić, Phys. Rev. B **90**, 041413 (2014).
[32] A. M. Black-Schaffer and C. Honerkamp, J. Phys.: Condens. Matter **26**, 423201 (2014).

II

CHARGE TRANSPORT THROUGH SPIN-POLARIZED TUNNEL JUNCTION BETWEEN TWO SPIN-SPLIT SUPERCONDUCTORS

by

M. Rouco, S. Chakraborty, F. Aikebaier, V. N. Golovach, E. Strambini, J. S. Moodera, F. Giazotto, T. T. Heikkilä & F. S. Bergeret 2019

Phys. Rev. B 100, 184501 (2019)

DOI: http://doi.org/10.1103/PhysRevB.100.184501

Charge transport through spin-polarized tunnel junction between two spin-split superconductors

Mikel Rouco,[1,*] Subrata Chakraborty,[2,3,†] Faluke Aikebaier,[2] Vitaly N. Golovach,[1,4,5] Elia Strambini,[6] Jagadeesh S. Moodera,[7] Francesco Giazotto,[6,‡] Tero T. Heikkilä,[2,§] and F. Sebastian Bergeret[1,5,‖]

[1]*Centro de Física de Materiales (CFM-MPC), Centro Mixto CSIC-UPV/EHU, Manuel de Lardizabal 5, E-20018 San Sebastián, Spain*

[2]*Department of Physics and Nanoscience Center, University of Jyväskylä, P.O. Box 35 (YFL), FI-40014 Jyväskylä, Finland*

[3]*Department of Physics, Queens College of the City University of New York, Queens, New York 11367, USA*

[4]*IKERBASQUE, Basque Foundation for Science, 48013 Bilbao, Basque Country, Spain*

[5]*Donostia International Physics Center (DIPC), Manuel de Lardizabal 4, E-20018 San Sebastian, Spain*

[6]*NEST Istituto Nanoscienze-CNR and Scuola Normale Superiore, I-56127 Pisa, Italy*

[7]*Department of Physics and Francis Bitter Magnet Lab, Massachusetts Institute of Technology, Cambridge, Massachusetts 02139, USA*

(Received 21 June 2019; revised manuscript received 1 October 2019; published 4 November 2019)

We investigate transport properties of junctions between two spin-split superconductors linked by a spin-polarized tunneling barrier. The spin-splitting fields in the superconductors (S) are induced by adjacent ferromagnetic insulating (FI) layers with arbitrary magnetization. The aim of this study is twofold. On the one hand, we present a theoretical framework based on the quasiclassical Green's functions to calculate the Josephson and quasiparticle current through the junctions in terms of the different parameters characterizing it. Our theory predicts qualitative new results for the tunneling differential conductance, dI/dV, when the spin-splitting fields of the two superconductors are noncollinear. We also discuss how junctions based on FI/S can be used to realize anomalous Josephson junctions with a constant geometric phase shift in the current-phase relation. As a result, they may exhibit spontaneous triplet supercurrents in the absence of a phase difference between the S electrodes. On the other hand, we show results of planar tunneling spectroscopy of a EuS/Al/AlO_x/EuS/Al junction and use our theoretical model to reproduce the obtained dI/dV curves. Comparison between theory and experiment reveals information about the intrinsic parameters of the junction, such as the size of the superconducting order parameter, spin-splitting fields and spin relaxation, and also about properties of the two EuS films, such as their morphology, domain structure, and magnetic anisotropy.

DOI: 10.1103/PhysRevB.100.184501

I. INTRODUCTION

Superconducting films with spin-split density of states have been used for a long time to determine the spin polarization of ferromagnetic metals tunnel-coupled to the superconductor (S) [1–7]. Originally, the spin splitting was induced by applying in-plane magnetic fields to thin superconducting films. These fields had to be large, of the order of few tesla, in order to obtain sizable splittings. Interestingly, as shown in the late 1980s, such spin splitting can also be observed at rather small, or even zero, magnetic fields in superconducting Al layers adjacent to ferromagnetic insulators (FI) [8,9]. In this case, the splitting is attributed to the exchange interaction at the FI/S interface [10]. Additionally, those first works on FI/S structures showed that thin FI layers can also be used as very efficient spin filters, with potential application as sources for highly spin-polarized spin currents [11].

More recently, nonequilibrium properties of superconductors with a spin-split density of states have attracted a renewed attention [12–18]. In such systems, two additional spin-dependent modes appear and couple to the widely studied nonequilibrium energy and charge modes [16,19]. FI/S structures have also been suggested for several applications, as highly efficient thermoelectric elements [20,21], bolometers [22], thermometers [23], cryogenic RAM memories [24], and different caloritronic devices to access the electronic heat current in nanostructures [25–29].

Most of these applications require both superconductors with spin-split density of states and highly polarized spin-filter interfaces. This motivates the present work, in which we explore both theoretically and experimentally FI/S junctions. Theoretically, we develop a general model to describe the coupling of two spin-split superconductors through an additional spin-filter barrier. Our model takes into account self-consistently magnetic disorder, spin-orbit coupling, and orbital effects of the magnetic field, as well as noncollinear spin-splitting fields. On the one hand, our model predicts new features in FI/S-based junctions: Additional coherent peaks in the differential conductance when the FI layers are monodomain with noncollinear magnetization, and the possible realization of an anomalous Josephson junction with pure triplet supercurrents at zero phase bias. On the other hand, our model provides a tool to interpret transport experiments on tunneling junctions with FI/S electrodes.

*mikel.rouco@ehu.eus
†schrkmv@gmail.com
‡francesco.giazotto@sns.it
§tero.t.heikkila@jyu.fi
‖fs.bergeret@csic.es

Experimentally, we measure the tunneling conductance of an EuS/Al/AlO_x/EuS/Al junction as a function of the applied voltage and magnetic field. The differential tunneling conductance, dI/dV, shows sharp peaks whose heights depend on the effective spin splitting induced in both Al layers and the spin filtering of the barrier. Below, we perform a self-consistent calculation that allows us to determine unambiguously the main parameters governing the transport of the junction

The work is organized as follows. In the next section, we present the measurements of the tunneling conductance of the junction under consideration as a function of the magnetic field. In Sec. III, we present a theoretical model based on the quasiclassical Green's functions for the description of the transport properties of a generic FI/S/I/FI/I/S/FI junction. In Sec. IV, we discuss the Josephson current through such junctions with emphasis on the anomalous behavior when the FI magnetizations are noncollinear. In Sec. V, we focus on the quasiparticle current and the tunneling differential conductance. The latter is compared to the experimental data, and a discussion of the results follows. We present our conclusions in Sec. VI.

II. TUNNELING CONDUCTANCE OF A EuS/Al/AlO_x/EuS/Al JUNCTION

In this section, we present our measurements of the current-voltage (I-V) characteristic of a EuS(4)/Al(4)/AlO_x/EuS(1.2)/Al(4.3)[1] junction (thickness in nanometers), see inset in Fig. 1(a). The samples consist of cross bars fabricated by electron-beam evaporation on an in situ metallic shadow mask with a typical junction area of $290 \times 290\ \mu m^2$ [30].

The tunneling spectroscopy is obtained by measuring the I-V characteristic in a dc two-wire setup, as sketched in the inset of Fig. 1(a). From this measurement we determine the differential conductance, dI/dV, via numerical differentiation. The measurements are done at cryogenic temperatures in a filtered cryogen-free dilution refrigerator. We first cool down the sample from room temperature to 25 mK in a nonmagnetic environment. Before applying any external magnetic field, we measure the I-V characteristic [Fig. 1(a)] and extract the dI/dV shown by the solid line in Fig. 1(b). We then apply an in-plane magnetic field (up to 160 mT) strong enough to align the magnetization of both EuS layers, and start decreasing it. During this process, we measure the I-V characteristic and determine the tunneling conductance at each value of the applied magnetic field. The full dependence is shown in the color plot of Fig. 2(d). Panels (a)–(c) in Fig. 2 correspond to different vertical cuts of Fig. 2(d) at the positions indicated by the arrows placed at the bottom of the figure.

The obtained tunneling conductance clearly shows the four-peak structure expected from the spin-split superconducting density of states (DOS) [9]. Notice that these peaks are also observed before applying any magnetic field, Fig. 1(b). The position of the peaks in Figs. 2(a)–2(c) is always symmetric with respect to the sign of the applied voltage, however, after the first magnetization of the junction, their heights are not. This behavior contrasts with the one shown in Fig. 1(b) for the demagnetized sample. The asymmetry is a fingerprint of spin-polarized tunneling through the middle EuS thin layer

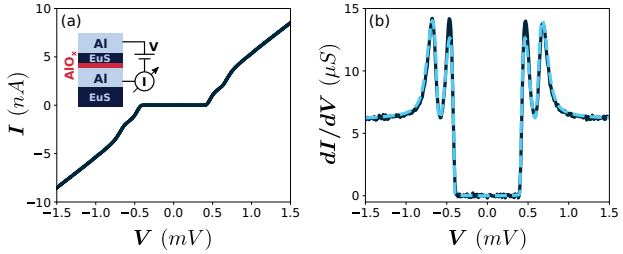

FIG. 1. Tunneling spectroscopy of a FI/S/I/FI/S junction before applying an external magnetic field. (a) Typical current (I) vs voltage (V) characteristic of the junction measured at 25 mK. (b) Numerical derivative of the I-V characteristic extracted from the data in (a) (black line). The blue dashed line is obtained from our theoretical model presented in Sec. III. The parameters used for the fitting are: $G_T = 6\ \mu$S, $\Delta_0 = 320\ \mu$eV, $h_L = 0$, $h_R = 100\ \mu$eV, $\tau_{sf}^{-1} = 0.08\Delta_0$, and $\tau_{so}^{-1} = \tau_{orb}^{-1} = 0$. In the demagnetized regime, the effective spin splitting in the upper Al layer is negligibly small. The spin splitting arises from the very large domain structure of the bottom EuS layer, with size much larger than the superconducting coherence length ξ_0. The measured peak structure resembles the one measured in Ref. [30] without the spin-filtering effect at work [see discussion after Eq. (37) for more details].

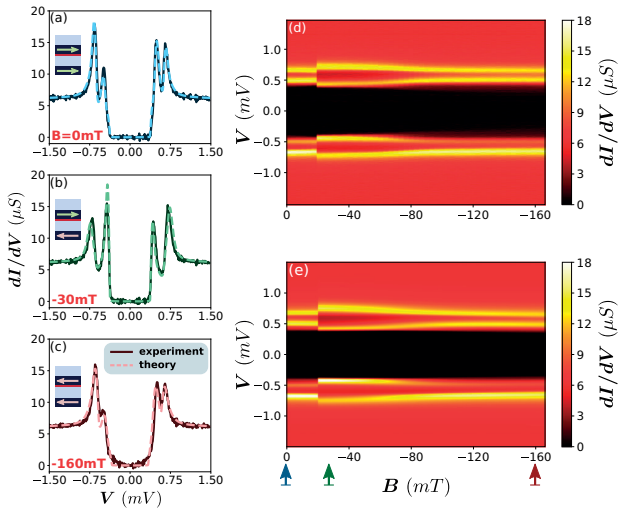

FIG. 2. Magnetic-field dependence of the tunneling conductance of the spin-polarized junction. Before the measurement, the system is polarized with a positive magnetic field ($B = 160$ mT). The differential conductance is then measured at different values of magnetic fields from 0 to -160 mT. (a), (b), and (c) show three different curves measured at 0, -20, and -160 mT, respectively. (d) shows the full measured B dependence. (e) is the fitting resulting from the theoretical model.

[1]During growth, the oxidation of the aluminum layer was not controlled. Therefore it does not necessarily have the stoichometry of Al_2O_3.

[7–9], which only after magnetization turns out to be apparent. In contrast, and according to the physical picture provided in Sec. V, when the sample is demagnetized, the thin EuS barrier layer consists of magnetic domains smaller than the coherence length with random polarization directions. This leads to a negligibly small value of the induced spin-splitting field on the upper superconductor and no spin-filtering effect on the current after averaging over the junction area.

The separation between the peaks at positive (or negative) voltage, Figs. 1(b) and 2(a)–2(c), provides information about the size of the spin-splitting energy induced in the Al layers. This splitting is proportional to the effective exchange energy between the spins localized at the EuS/Al interface and the Al conduction electrons [31].

We observe a sudden increase of the spin-splitting energy at −20 mT [Fig. 2(d)], which occurs when the system switches to the antiparallel configuration. As it turns out from our theoretical discussion in Sec. V, it is the bottom EuS layer that switches first and abruptly. By further increasing the magnetic field B the parallel configuration is recovered gradually with a smooth switching of the middle EuS magnetization. The two rather different switching behaviors of the EuS films can be attributed to a different magnetic configuration and anisotropy of the two films due to different deposition conditions, which crucially depends on the growth morphology [24,32].

Whereas the peak positions can be explained by using a simple tunneling model [7], detailed features such as the width and height of the peaks can only be understood by taking into account different scattering and depairing mechanisms and performing a self-consistent calculation of the superconducting order parameter. With this aim, in the next sections we present a theoretical model that allows us to describe the dI/dV curves, extract the values of the different parameters, and provide a physical picture that explains the full behavior shown in Fig. 2(d).

III. THE MODEL

In this section, we present a theoretical model to describe the electronic transport in junctions with spin-split superconductors and spin-filtering barriers. The goal of this section is twofold. On the one hand, to obtain general results for the current in tunnel junctions between two spin-split superconductors in the presence of a spin-filtering barrier. On the other hand, we provide a complete description of the experimental results presented in the previous section.

We consider a generic junction, sketched in Fig. 3. It consists of two spin-split superconductors separated by a spin-polarized tunneling barrier. The spin-split superconductors correspond to two S/FI bilayers, whereas the tunneling barrier is an additional FI layer with adjacent thin insulating layers to decouple it magnetically from the superconductors.

To describe the current through the junction below, we use the tunneling Hamiltonian approach, such that the system is described by

$$H = H_L + H_R + H_T . \tag{1}$$

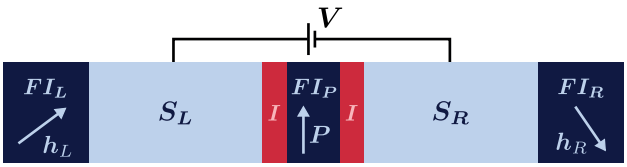

FIG. 3. Schematic of a tunnel junction between two spin-split superconductors with a spin polarized tunneling barrier and biased at a voltage V. The left (right) superconductor S_L (S_R) experiences a spin-splitting field $\boldsymbol{h}_L$ ($\boldsymbol{h}_R$) by an attached ferromagnetic insulator layer FI_L (FI_R). The spin polarized tunneling barrier, with polarization $\boldsymbol{P}$, is another ferromagnetic insulator (FI). To avoid the magnetic proximity effect, the superconductors are separated from the spin-polarized tunneling barrier by insulating layers (I). The superconductor S_L (S_R) is at temperature T_L (T_R).

Here, $H_{L(R)}$ describes the left(right) superconducting electrode attached to a FI and H_T the tunneling of electrons between the superconductors [33].

In order to compute the current one needs to determine the spectral properties of the decoupled FI-S electrodes. We model them by assuming that the interaction between the localized magnetic moments in the FI and the conduction electrons in the S layer creates an effective exchange field in the latter [18,31,34,35]. If the superconducting films are thinner than the coherence length such exchange field can be assumed to be homogeneous in the S and, hence, the S electrodes are described by

$$H_{L(R)} = H_{\rm BCS} + \mathbf{h}_{L(R)} \cdot \hat{\boldsymbol{\sigma}} , \tag{2}$$

where $\mathbf{h}_{L(R)} = h_{L(R)}\mathbf{n}_{L(R)}$ is the exchange field pointing in the direction of the unit vector $\mathbf{n}_{L(R)}$, $\hat{\boldsymbol{\sigma}}$ is the vector of Pauli matrices and $H_{\rm BCS}$ is the BCS Hamiltonian that also includes random impurities, magnetic, nonmagnetic, and those with spin-orbit coupling [36].

For the tunneling Hamiltonian [the last term of Eq. (1)] we assume that the tunneling through the barrier is spin dependent; in other words, that the electron tunneling probability depends on whether its spin is oriented parallel or antiparallel with respect to the barrier magnetization [37].

We consider a general case where the directions of the magnetization in each of the three FIs are independent of each other. A voltage V is applied across the junction and, in principle, the temperatures of the two FI/S electrodes are different $T_L \neq T_R$. Here, the indices L and R denote the left and right electrodes, respectively.

The effective splitting of the left and right superconductors in Fig. 3 is given by the induced exchange fields $\boldsymbol{h}_L = h_L\boldsymbol{n}_L$ and $\boldsymbol{h}_R = h_R\boldsymbol{n}_R$, respectively, whereas the spin filtering is described by the polarization vector $\boldsymbol{P} = P\boldsymbol{n}_P$ with $P \equiv \frac{G_\uparrow - G_\downarrow}{G_\uparrow + G_\downarrow}$ and $0 \leqslant P \leqslant 1$. The vectors $\boldsymbol{n}$ are unit vectors pointing in the respective directions, the magnitude of the exchange fields $h_{L/R}$ has energy units and $G_{\uparrow(\downarrow)}$ stands for the tunneling conductance through the junction for carriers with up (down) spin along the direction of $\mathbf{n}_P$.

Without loss of generality, we set the barrier magnetization along the z axis, $\boldsymbol{n}_P = (0, 0, 1)$, such that the magnetization orientations of the adjacent S/FI bilayers can be parametrized

by three angles, $\theta_{L,R}$ and γ:

$$\boldsymbol{n}_L = (\sin\theta_L, 0, \cos\theta_L) \tag{3}$$

and

$$\boldsymbol{n}_R = (\sin\theta_R\cos\gamma, \sin\theta_R\sin\gamma, \cos\theta_R). \tag{4}$$

In a collinear configuration, i.e., $\theta_L = \theta_R = 0$, the current through the junction can be straightforwardly calculated from the well-known tunneling expression [7]. We next generalize the latter for noncollinear magnetizations. Moreover, in order to include the effects of spin relaxation and depairing, we use the quasiclassical Green's functions (GFs) for an accurate description of the spectrum of the S/FI electrodes.

A. Quasiclassical Green's functions for spin-split superconductors

In this section, we present the quasiclassical Green's functions and the expression for the current as a function of the applied voltage and temperature bias (see also Ref. [18]) for an arbitrary magnetic configuration of the junction shown in Fig. 3. We restrict our analysis to the tunneling limit, which corresponds to the experimental situation when a FI is used as a barrier. In such case, one can treat each FI/S electrode in Fig. 3 independently. In other words, we can calculate the GFs, $\check{g}_L(\epsilon)$ and $\check{g}_R(\epsilon)$, for each electrode. Moreover, one can first consider the case in which $V = 0$ and $\varphi = 0$, where φ is the phase difference between the superconductors. Finite φ and V can then be added as gauge factors.

We use the Green's functions defined in the Keldysh⊗Nambu⊗spin space.[2] These are are 8×8 matrices that satisfy the normalization condition

$$\check{g}_s^2 = 1\ . \tag{5}$$

In the Keldysh space, they can be written as [38]

$$\check{g}_s = \begin{pmatrix} \check{g}_s^R & \check{g}_s^K \\ 0 & \check{g}_s^A \end{pmatrix}, \tag{6}$$

where $s = \{L, R\}$ labels left and right sides of the junction, $\check{g}_s^R$ stands for the retarded component of the GFs, $\check{g}_s^A = -\hat{\tau}_3\check{g}_S^{R\dagger}\hat{\tau}_3$ is the advanced component, and due to the normalization condition, the Keldysh component can be written as

$$\check{g}_s^K = \check{g}_s^R\check{f}_s - \check{f}_s\check{g}_s^A. \tag{7}$$

In these expressions, the "checks" $\check{}$ indicate the full 8×8 matrices, whereas $\hat{}$ are used for 4×4 matrices in Nambu spin space, and $\hat{}$ for 2×2 matrices. $\hat{\tau}_i$ is the ith Pauli matrix in Nambu space and $\hat{f}_s$ stands for the electron distribution function in electrode s. In equilibrium, the latter is proportional to the unit matrix in Nambu and spin space and reads

$$\check{f}_s(\epsilon) \equiv f_0(\epsilon, T_s) = \tanh\frac{\epsilon}{2k_BT_s}, \tag{8}$$

where k_B is the Boltzmann's constant and T_s is the temperature on the s side of the junction. In our notation, whenever we do not specify any matrix structure via Pauli matrices, it is implied that the matrix is proportional to the unit matrix in the corresponding space.

We now calculate the GFs in the electrodes, which we assume in thermal equilibrium. In the diffusive limit, they obey the Usadel equation [39] with a local spin splitting pointing in z direction and, as it was indicated after Eq. (6) and in Eq. (7), we only need to compute their retarded component. Then, to calculate the current through the junction with noncollinear magnetizations we will have to transform the GFs by using spin-rotation operators.

The Usadel equation for the retarded component of a homogeneous S/FI electrode in the spin local frame reads

$$\left[i\epsilon\hat{\tau}_3 - ih_s\hat{\tau}_3\hat{\sigma}_3 - \Delta_s\hat{\tau}_1 - \check{\Sigma}_s,\ \check{g}_s^R\right] = 0, \tag{9}$$

where $\hat{\sigma}_i$ is the ith Pauli matrix in the spin space and Δ_s is the self-consistent superconducting order parameter (see Appendix A for details). The self-energy $\check{\Sigma}_s$ consists of three contributions:

$$\check{\Sigma}_s = \check{\Sigma}_s^{\rm so} + \check{\Sigma}_s^{\rm sf} + \check{\Sigma}_s^{\rm orb}, \tag{10}$$

the spin relaxation due to spin-orbit coupling, $\check{\Sigma}_s^{\rm so}$, and spin-flip relaxation, $\check{\Sigma}_s^{\rm sf}$, and the orbital depairing, $\check{\Sigma}_s^{\rm orb}$, due to the external magnetic fields. Explicitly, each contribution within the relaxation time approximation reads

$$\check{\Sigma}_s^{\rm so} = \frac{\hat{\boldsymbol{\sigma}}\cdot\check{g}_s^R\cdot\hat{\boldsymbol{\sigma}}}{8\tau_s^{\rm so}}, \tag{11}$$

$$\check{\Sigma}_s^{\rm sf} = \frac{\hat{\boldsymbol{\sigma}}\cdot\hat{\tau}_3\check{g}_s^R\hat{\tau}_3\cdot\hat{\boldsymbol{\sigma}}}{8\tau_s^{\rm sf}}, \tag{12}$$

$$\check{\Sigma}_s^{\rm orb} = \frac{\hat{\tau}_3\check{g}_s^R\hat{\tau}_3}{\tau_s^{\rm orb}}, \tag{13}$$

where $\tau_s^{\rm so}$, $\tau_s^{\rm sf}$, and $\tau_s^{\rm orb}$ stand for spin-orbit, spin-flip, and orbital depairing relaxation times, respectively, and we use the notation $\hat{\boldsymbol{\sigma}}\cdot\check{A}\cdot\hat{\boldsymbol{\sigma}} = \sum_{i=1}^3\hat{\sigma}_i\check{A}\hat{\sigma}_i$.

The general solution of the Usadel equation (9), is then given by four components in the Nambu spin space:

$$\check{g}_s^R = (F_{0s} + F_{3s}\hat{\sigma}_3)\hat{\tau}_1 + (G_{0s} + G_{3s}\hat{\sigma}_3)\hat{\tau}_3. \tag{14}$$

The components proportional to τ_3 are the normal components. They determine the quasiparticle spectrum and enter the expression for the quasiparticle current. The off-diagonal terms in Nambu space, here proportional to τ_1, are the anomalous GFs and describe the superconducting condensate. They determine the Josephson current through the junction of Fig. 3. The anomalous GFs have two components: F_{0s} describes the singlet condensate, whereas the component F_{3s} describes the triplet component with zero total spin projection. Because we are considering diffusive systems, both components have s-wave symmetry. This implies that the triplet component is odd in frequency [40]. In Sec. V, we numerically solve the Usadel equation, Eq. (9), together with the normalization condition, Eq. (5), and the self-consistent expression for Δ_s (see Appendix A).

We next derive the expression for the tunneling current in terms of the above GFs.

[2]To simplify the notation we skip throughout the text the direct product symbol ⊗.

B. Tunneling current

In the previous section, we present the quasiclassical GFs, $\check{g}_s(\epsilon)$, in a local reference frame where $V = 0$, $\varphi = 0$ and the exchange field is parallel to the z axis. We now use these results to calculate the total electric current across the Josephson junction, sketched in Fig. 3, in the presence of a finite voltage and phase difference, and a noncollinear magnetic configuration. This can be done by a gauge transformation and a spin-rotation of the GFs.

In the presence of a voltage, the phase of a superconductor evolves in time as

$$\varphi(t) = \varphi + \frac{2eV}{\hbar}t \ , \tag{15}$$

where φ is the dc phase. We define the corresponding gauge matrix

$$\hat{U}(t) = \exp(-i\varphi(t)\hat{\tau}_3) \ . \tag{16}$$

If we assume that the voltage is applied on the left superconductor and the magnetizations of the two S/FI and the spin-filter barrier are noncollinear [see Eqs. (3) and (4)], we can obtain the GFs $\check{\check{g}}$ from those obtained in in Sec III A via the following transformations:

$$\check{\check{g}}_L(t-t') = \hat{R}_L \, \hat{U}(t) \, \check{g}_L(t-t') \, \hat{U}(t')^\dagger \, \hat{R}_L^\dagger, \tag{17}$$

$$\check{\check{g}}_R(t-t') = \hat{R}_R \, \check{g}_R(t-t') \, \hat{R}_R^\dagger. \tag{18}$$

Here, the operators $\hat{R}_s$ describe spin rotations in the left and right electrodes:

$$\hat{R}_L = \exp(-i\theta_L\hat{\sigma}_y/2), \tag{19}$$

$$\hat{R}_R = \exp(-i\gamma\hat{\sigma}_z/2)\exp(-i\theta_R\hat{\sigma}_y/2) \ , \tag{20}$$

and the time-dependent Green's functions in Eqs. (19) and (20) are obtained from the GFs in frequency space:

$$\check{g}_s(t-t') = \frac{1}{2\pi}\int_{-\infty}^{\infty} d\epsilon \ \check{g}_s(\epsilon) \ e^{i\epsilon(t-t)} \ . \tag{21}$$

From Eqs. (17) and (18), we can now write the full expression for the time-dependent electric current across the junction shown in Fig. 3 [41]:

$$I_c(t) = \frac{G_T\pi}{16e}\,\mathrm{Tr}(\hat{\tau}_3[\check{\check{g}}_L \circ \check{\Gamma}\check{\check{g}}_R\check{\Gamma}]^K), \tag{22}$$

where G_T is the normal state conductance of the junction, $[\cdot\circ\cdot]$ is a commutator of convolutions,[3] the superscript K stands for the Keldysh component of the commutator, and Tr stands for the trace over the Nambu×spin spaces.

[3] When the operators depend only on the difference of times the convolution is defined as

$$(A\circ B)(t) = \int_{-\infty}^{\infty} dt' A(t-t')B(t'-t).$$

Consequently, the commutator reads

$$[A\,;B] = (A\circ B)(t) - (B\circ A)(t).$$

Equation (22) is valid in the tunneling limit. The matrix $\check{\Gamma}$ describes the effect of the spin-filtering layer and is defined as

$$\check{\Gamma} = u + v\hat{\sigma}_3\hat{\tau}_3 \ , \tag{23}$$

where the parameters u and v depend on the polarization of the barrier P as follows:

$$u = \sqrt{\frac{1+\sqrt{1-P^2}}{2}}, \tag{24}$$

$$v = \sqrt{\frac{1-\sqrt{1-P^2}}{2}}. \tag{25}$$

One can easily check from these expressions that $u^2 + v^2 = 1$, $2uv = P$, and $u^2 - v^2 = \sqrt{1-P^2}$.

After a lengthy but straightforward algebra, we obtain from Eq. (22) the charge current through the junction which can be written as the sum of three components:

$$I_c(t) = I + J_1 \sin\left(\varphi + \frac{2eVt}{\hbar}\right) + J_2\cos\left(\varphi + \frac{2eVt}{\hbar}\right). \tag{26}$$

Here, I is the quasiparticle tunneling current and the remaining part is the Josephson current. Specifically, J_1 is the usual Josephson critical current. The third term is proportional to the cosine of $\varphi(t)$. In a nonmagnetic Josephson junction, this term is finite only at nonzero bias. In the literature, it is known as the $\cos\varphi$ term and has been widely studied [42–44]. Interestingly, in a magnetic junction, this term can be nonzero even when $V = 0$. In this case, this term leads to the so-called anomalous Josephson current that appears in certain magnetic system with spin-orbit coupling or inhomogeneous magnetization [45–55] and is discussed in more detail in Sec. IV.

From Eq. (22), we derive the expressions for the three components of the current in terms of the GFs. For the quasiparticle tunneling current, first term in Eq. (26), we obtain

$$\begin{aligned} I = \frac{G_T}{2e}\int_{-\infty}^{\infty} d\epsilon [f_0(\epsilon+eV,T_L) - f_0(\epsilon,T_R)] \\ \times \{P[\mathcal{N}_{0L}(\epsilon+eV)\mathcal{N}_{3R}(\epsilon)\boldsymbol{n}_R\cdot\boldsymbol{n}_P \\ + \mathcal{N}_{3L}(\epsilon+eV)\mathcal{N}_{0R}(\epsilon)\boldsymbol{n}_L\cdot\boldsymbol{n}_P] \\ + \mathcal{N}_{0L}(\epsilon+eV)\mathcal{N}_{0R}(\epsilon) + \mathcal{N}_{3L}(\epsilon+eV)\mathcal{N}_{3R}(\epsilon) \\ \times [\boldsymbol{n}_L^\parallel\cdot\boldsymbol{n}_R^\parallel + \sqrt{1-P^2}\,\boldsymbol{n}_L^\perp\cdot\boldsymbol{n}_R^\perp]\}, \end{aligned} \tag{27}$$

where $\mathcal{N}_{is}(\epsilon) \equiv \mathrm{Re}[G_{is}(\epsilon)]$ is the semisum ($i = 0$) and semidifference ($i = 3$) of the spin-up/spin-down densities of states (DOS). In deriving this expression we have used the vector equalities presented in Appendix B.

For the second and third terms in Eq. (26), we obtain

$$\begin{aligned} J_1 = A_0\sqrt{1-P^2} + A_3[\sqrt{1-P^2}\,\boldsymbol{n}_L^\parallel\cdot\boldsymbol{n}_R^\parallel \\ + \boldsymbol{n}_L^\perp\cdot\boldsymbol{n}_R^\perp] - B_3\,P\boldsymbol{n}_P\cdot(\boldsymbol{n}_L\times\boldsymbol{n}_R) \end{aligned} \tag{28}$$

and

$$\begin{aligned} J_2 = B_0\sqrt{1-P^2} + B_3[\sqrt{1-P^2}\,\boldsymbol{n}_L^\parallel\cdot\boldsymbol{n}_R^\parallel \\ + \boldsymbol{n}_L^\perp\cdot\boldsymbol{n}_R^\perp] + A_3\,P\boldsymbol{n}_P\cdot(\boldsymbol{n}_L\times\boldsymbol{n}_R), \end{aligned} \tag{29}$$

where A_i and B_i ($i = 1, 3$) are expressed in terms of the real and imaginary parts of the anomalous GFs $F_{is}(\epsilon)$:

$$A_i = \frac{G_T}{2e}\int_{-\infty}^{\infty} d\epsilon [f_0(\epsilon, T_R)\mathrm{Re}[F_{iL}(\epsilon + eV)]\mathrm{Im}[F_{iR}(\epsilon)] + f_0(\epsilon + eV, T_L)\mathrm{Im}[F_{iL}(\epsilon + eV)]\mathrm{Re}[F_{iR}(\epsilon)]], \quad (30)$$

$$B_i = \frac{G_T}{2e}\int_{-\infty}^{\infty} d\epsilon [f_0(\epsilon + eV, T_L) - f_0(\epsilon, T_R)] \times \mathrm{Im}[F_{iL}(\epsilon + eV)]\mathrm{Im}[F_{iR}(\epsilon)]. \quad (31)$$

Equations (26)–(31) determine the total current through the junction and are used in the next sections. We start by analyzing the Josephson current in magnetic junctions.

IV. ANOMALOUS JOSEPHSON CURRENT

An interesting situation occurs when $V = 0$, $\varphi = 0$, $T_L = T_R$ and the magnetization vectors of the three FI layers are not in the same plane. In this case, $I = 0$, $B_0 = B_3 = 0$ and the only term contributing to the current J_2 is the one proportional to A_3 in Eq. (29). The latter is finite when $\boldsymbol{n}_P \cdot (\boldsymbol{n}_L \times \boldsymbol{n}_R) \neq 0$, i.e., when three vectors are not coplanar. In this case a finite Josephson current may flow through the junction even if the dc phase difference φ is zero. This is the so-called anomalous Josephson current and the junction is referred as a φ_0 junction. The latter has been widely studied in magnetic junctions with spin-orbit coupling [45,50,51,53,56–58] or multilayer metallic ferromagnets [54,55,59–64].

In this section, we discuss the possible observation of the anomalous Josephson junction in FI/S-based junctions. This effect was not yet seen in the samples discussed here, because the large value of the normal-state resistance made it impossible to measure any Josephson current at the temperature of the experiments. However, similar type of samples with increased junction transparency would be good candidates for measuring the anomalous φ_0 effect.

Because we assume a unique temperature, $T_L = T_R = T$, and the junction is in equilibrium ($V = 0$), quasiparticle current is zero and one can write the expression for the Josephson current in terms of a sum over Matsubara frequencies. The anomalous functions proportional to the Pauli matrix σ_3 correspond to the odd-in-frequency triplet components of the condensate, $F_3(i\omega_n) = -F_3(-i\omega_n)$, whereas those proportional to σ_0 arise from the singlet components $F_0(i\omega_n) = F_0(-i\omega_n)$ [65]. The total current, Eq. (26), can then be written as

$$J_1 = \pi T \frac{\pi G_T}{2e}\sum_{\omega}\left[\sqrt{1-P^2}\left(F_0^2 + F_3^2 \boldsymbol{n}_L^{\parallel}\cdot\boldsymbol{n}_R^{\parallel}\right) + F_3^2 \boldsymbol{n}_L^{\perp}\cdot\boldsymbol{n}_R^{\perp}\right], \quad (32)$$

$$J_2 = \pi T \frac{\pi G_T}{2e} P \boldsymbol{n}_P \cdot (\boldsymbol{n}_L \times \boldsymbol{n}_R)\sum_{\omega} F_3^2. \quad (33)$$

The contribution proportional to $\sin\varphi$ contains the conventional singlet Josephson current that vanishes when the barrier is fully polarized $P = 1$. If the magnetizations and the barrier magnetization are noncollinear, there is an additional contribution stemming entirely from the interference of the triplet component of the condensate, as discussed in Refs. [37,41].

The anomalous current in Eq. (33) is also a pure triplet current which requires noncoplanar vectors, i.e., a finite triple product $\boldsymbol{n}_P \cdot (\boldsymbol{n}_L \times \boldsymbol{n}_R)$, and it is proportional to the polarization of the barrier. The well-defined splitting and strong barrier polarization make the EuS/Al material combination suitable for the realization of such magnetic anomalous junctions.

In the limit $T \to 0$, we obtain analytic results for the Josephson current by assuming equal amplitudes of the exchange fields, $h_L = h_R \equiv h$, and neglecting all relaxation processes, $\tau_{\mathrm{so}}^{-1} = \tau_{\mathrm{sf}}^{-1} = \tau_{\mathrm{orb}}^{-1} = 0$:

$$J_1 = \frac{\pi G_T \Delta}{2e}[\sqrt{1-P^2}\eta + (\sqrt{1-P^2}\boldsymbol{n}_L^{\parallel}\cdot\boldsymbol{n}_R^{\parallel} + \boldsymbol{n}_L^{\perp}\cdot\boldsymbol{n}_R^{\perp})(\eta - 1)], \quad (34)$$

$$J_2 = \frac{\pi G_T \Delta}{2e} P(\eta - 1)\boldsymbol{n}_P \cdot (\boldsymbol{n}_L \times \boldsymbol{n}_R), \quad (35)$$

where Δ is the real self-consistent superconducting order parameter at zero temperature and exchange field h and

$$\eta \equiv \frac{32\Delta^2(256\Delta^4 - 32\Delta^2 h^2 + 9h^4)}{(16\Delta^2 - h^2)^3} - 1. \quad (36)$$

In the case where $h = 0$ (and, therefore, $\boldsymbol{n}_L = \boldsymbol{n}_R = 0$), the coefficient $\eta = 1$ and Eq. (34) yields the well-known Ambegaokar-Baratoff [66] formula for the Josephson current with a prefactor $\sqrt{1-P^2}$ due to the barrier polarization.

V. QUASIPARTICLE CURRENT AND DIFFERENTIAL CONDUCTANCE

In this section, we discuss the quasiparticle current, Eq. (27), and use our theoretical framework to describe the experimental data shown in Figs. 1 and 2. In the following discussion, we identify the layer at the bottom (top) in the experimental setup, Fig. 1, with the left (right) electrode of the model in Fig. 3.

The experimental setup corresponds to a situation in which the EuS barrier serves two purposes: On the one hand, it acts as a spin-filtering barrier and, on the other hand, it causes the spin splitting in one of the superconductors (the right one in Fig. 3). This means that the orientation of barrier magnetization coincides with the direction of the exchange field in the right superconductor, $\boldsymbol{n}_P = \boldsymbol{n}_R$, while the magnetization $\boldsymbol{n}_L$ is, in principle, independent of the magnetization of the barrier. The left superconductor (S_L) is in a good contact with the outer EuS, which induces a finite h_L. At the other interface between S_L and the tunneling barrier, a thin oxide layer is formed, preventing the exchange coupling [9]. Thus, for our specific sample, the thinnest FI layer in the middle is a tunneling barrier (1.2 nm) which induces the spin splitting only on the right superconductor and polarizes the current, whereas the thicker EuS layer (4 nm) causes the spin splitting in the left Al film.

Because the two EuS layers are of different thicknesses and they were grown on two different substrates, it is expected that the magnetization switching is different, as well as the strength of the induced exchange splittings in the superconductors, $h_R \neq h_L$. We assume the same superconducting order parameter, spin orbit and spin flip relaxation times for both

Al films. Moreover, the temperatures are assumed to be equal, $T_L = T_R = T$.

Because of the high normal-state resistance of the tunneling barrier (∼160 kΩ), no Josephson current through the junction could be measured, as shown in the left panel of Fig. 1. In particular, the Josephson energy $E_J = \hbar J_1/(2e)$ was of the order of the temperature and, therefore, the thermal fluctuations of the phase smeared out the Josephson effect. The current shown in that figure corresponds only to the quasiparticle contribution and it can be determined from Eq. (27) for $\boldsymbol{n}_R \cdot \boldsymbol{n}_P = 1$ and $\boldsymbol{n}_R^{\perp} = 0$. We can parametrize the magnetic configuration of the junction by a single angle θ between the splitting field in the left and right superconductor: $\boldsymbol{n}_R \cdot \boldsymbol{n}_L = \boldsymbol{n}_P \cdot \boldsymbol{n}_L = \cos\theta$.

From Eq. (27), we compute the current and, after differentiation with respect to V, we obtain the differential tunneling conductance dI/dV. In Fig. 4, we show its dependence on the voltage for different values of the angle θ and certain values of spin splitting fields and spin relaxation times. For a collinear configuration of magnetizations, $\cos\theta = \pm 1$, the differential conductance shows the four-peak structure, observed in most of experiments on EuS/Al based structures [7–9,30,67]. These peaks appear at voltages $eV = \pm(\Delta_L + \Delta_R) \pm (h_L - \cos\theta h_R)$.

However, if the magnetizations of the FIs are noncollinear, we find a qualitatively new result (see the solid black line in Fig. 4). Instead of four peaks, the differential conductance shows eight peaks for any value of θ between 0 and π. These two different behaviors can be understood as follows:

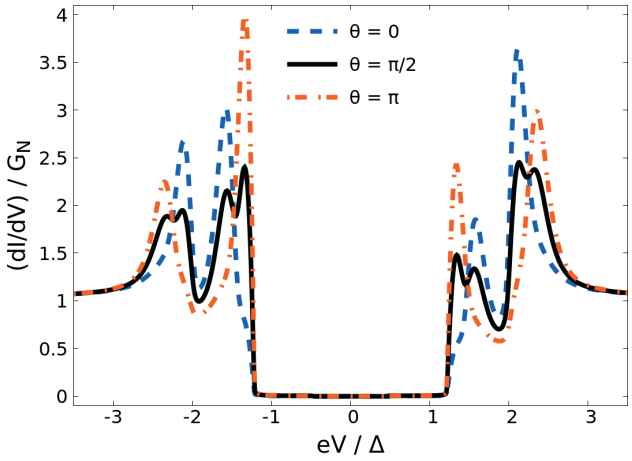

FIG. 4. Normalized differential conductance spectrum of the $FI_L/S_L/I/FI_R/S_R$ junction calculated from our theoretical model. Both superconductors are assumed to have the same order parameter, Δ_0. The polarization of the barrier is parallel to the exchange field induced in the right superconductor, $\boldsymbol{n}_P \parallel \boldsymbol{n}_R$, while the exchange field of the left superconductor forms an angle θ with $\boldsymbol{n}_R$. The dashed lines correspond to collinear situations, (blue) $\theta = 0$ and (red) $\theta = \pi$, while the solid black line corresponds to a noncollinear one, $\theta = \pi/2$. The remaining parameters used in the calculation are $\tau_{so}^{-1} = \tau_{orb}^{-1} = 0$ and $\tau_{sf}^{-1} = 0.08\Delta_0$ for the relaxation times in both superconductors, Zeeman splitting values of $h_L = 0.35\Delta_0$ and $h_R = 0.10\Delta_0$, a polarization of $P = 0.25$ and a global temperature of $k_B T = 0.01\Delta_0$.

In the collinear case, the spin component along the single direction of magnetization is globally conserved and the two spin species tunnel independently. When the polarization of the tunneling barrier is noncollinear with the magnetization of one of the electrodes, tunneling does not conserve spin. The additional peaks in the dI/dV stem from the projection of the electron spin of one of the electrodes onto the local spin basis in the other electrode. The peaks in dI/dV then appear at $eV = \pm(\Delta_L + \Delta_R) \pm (h_L \pm h_R)$

This unusual situation occurs when the induced exchange field, and hence the magnetization of the EuS films, is spatially homogeneous, so that the eight-peak structure of dI/dV shown in Fig. 4 can only be observed if the EuS are monodomain magnets with noncollinear magnetizations. In our EuS/Al samples the situation is rather different. As discussed in Ref. [30], EuS films consist of an ensemble of crystallites with intrinsic magnetization [68]. Therefore, before applying any external magnetic field, the magnetic configuration of the EuS layers consists of randomly oriented magnetic domains. Typically the size of EuS/Al tunnel junctions (here ∼290 × 290 μm^2) is much larger than the size of these domains and, therefore, the measured tunneling current is determined by an average over the angle θ, $\langle I\rangle_\theta \equiv \int_0^\pi \frac{d\theta}{\pi} I$, which reads

$$\langle I\rangle_\theta = \frac{G_T}{2e}\int_{-\infty}^{\infty} d\epsilon [f_0(\epsilon + eV, T_L) - f_0(\epsilon, T_R)] \times [\mathcal{N}_{0L}(\epsilon + eV)\mathcal{N}_{0R}(\epsilon) + P\mathcal{N}_{0L}(\epsilon + eV)\mathcal{N}_{3R}(\epsilon)]. \quad (37)$$

We use this averaging procedure to fit the experimental data shown in Fig. 1, which corresponds to the situation before any magnetic field has been applied. As discussed above, the finite spin-filtering coefficient P results in an asymmetry in the dI/dV curve with respect to the sign of V. However, Fig. 1 shows a quite symmetric curve. This can be explained by assuming that the domain size in the upper thin EuS layer is smaller than ξ_0 and, therefore, the possible splitting in the corresponding superconductor (R in our case) averages out. The absence of a Zeeman field in the right superconductor leads to an equal density of states for up and down electrons and, hence, $\mathcal{N}_{3R}(\epsilon) = 0$. Consequently, the second term on the second line of Eq. (37) does not contribute to the current, which now does not depend on the spin polarization of the tunneling barrier.

The theory curve in Fig. 1(b) (blue line), is obtained for $G_T = 6\,\mu S$, which is the value of the conductance measured at sufficiently large voltages (see the right panel of Fig. 1). The superconducting gap at zero field and zero temperature is set to $\Delta_0 = 320$ μeV in both Al layers. According to previous studies on the spin relaxation processes in aluminum layers [17,69,70], we set the spin-orbit relaxation time to $\tau_{so}^{-1} = 0.005\Delta_0$. The spin-flip relaxation is however enhanced due to the magnetic disorder caused by the adjacent EuS layer and we chose $\tau_{sf}^{-1} = 0.08\Delta_0$ in both Al layers. Since the measurements in Fig. 1 are for zero field then $\tau_{orb}^{-1} = 0$. The best fitting is obtained for $h_L = 100$ μeV (bottom layer in the experiment), whereas $h_R = 0$ as explained above. The EuS at the bottom is a thicker film and its magnetic domain size is of the order of, or even larger than, the superconducting

coherence length ξ_0 [30]. Therefore it induces a sizable exchange splitting in the bottom Al layer.

We now focus on the results of Fig. 2 when an external field is applied. These measurements are done after the first magnetization of EuS, i.e., after a strong enough in-plane magnetic field is applied ($B = 160$ mT). After this, we switched off the B-field and measured the I-V characteristic varying the magnetic field from $B = 0$ to $B \approx -160$ mT. The differential conductance obtained by a numerical differentiation is shown with solid lines in panels (a)–(c) of Fig. 2 for $B = 0$, $B = -30$ mT and $B = -160$ mT, respectively. A full overview of the dI/dV is presented as a color map in panel Fig. 2(d).

From the four-peak structure of dI/dV and the theoretical prediction in Fig. 4, we can conclude that the average induced exchange fields in the left and right superconductors are collinear. After the application of the initial strong magnetic field, the magnetizations of both EuS are aligned in the direction of B. By decreasing the field until it switches its direction, the magnetization of the FIs may also switch at their corresponding coercive fields leading to the usual ferromagnetic hysteresis loop. Such switching events can be seen from the evolution of the peak positions in the dI/dV map in Fig. 2(d).

We calculate the current using Eq. (27) and fit the data shown in Fig. 2. We use for the values of the spin-splitting fields for large magnetic fields (saturation of the magnetization of the EuS films) $h_L^{\rm sat} = 120$ μeV and $h_R^{\rm sat} = 30$ μeV. The difference between the values of the exchange fields after and before the first magnetization of the EuS layers is consistent with the result in Ref. [30]. In order to describe the evolution of the conductance peaks with the magnetic field, we assume that the exchange field follows the evolution of the local magnetization. In particular, for the color plot in Fig. 2(e), we assume that $h_L(B) = h_L^{\rm sat}\, y_L(B)$ and $h_R(B) = h_R^{\rm sat}\, y_R(B)$, whereas spin polarization of the barrier is chosen to be $P(B) = 0.25\, y_R(B)$. Here, $y_L(B) = 1 - 2\theta(B + 20)$ and $y_R(B) = \tanh \frac{B+70}{40}$ are two empirical functions that describe the evolution of the magnetization in the bottom and top EuS layers as a function of the magnetic field B given in mT, where $\theta(x)$ is the step function.

We also take into account the orbital depairing in the superconducting layers due to the applied magnetic field, determined by [71,72]

$$\tau_{\rm orb}^{-1} = \left(\frac{\pi d \xi_0 B}{\sqrt{6}\Phi_0}\right)^2 \Delta_0, \tag{38}$$

where Φ_0 is the magnetic flux quantum, $d \approx 4$ nm is the width of the Al layers and $\xi_0 \approx 200$ nm is the superconducting coherence length.

The results of our fitting procedure are the dashed lines in panels (a), (b), and (c) of Fig. 2 and the color map in panel (e). All in a good agreement with the experimental data.

At first glance our fitting suggests an unexpected behavior: The thin EuS layer switches its magnetization slower than the thicker one. Here we provide a plausible explanation for this behavior, which can be caused by the different polycrystalline structures of EuS layers grown under different conditions. The 4-nm-thick EuS (bottom layer in Fig. 2) is grown on an Al_2O_3 substrate, while the 1.2-nm barrier is grown directly on the previously oxidized underlying Al layer. As the oxidation of this layer is not controlled, its stoichiometry is completely different to the one on top of the substrate. Most likely, the thin layer consists of a more disordered set of crystallites and islands, resembling a superparamagnet. Such a large structural roughness could also arise from the propagation of defects created during growth in the bottom EuS and Al layers. If the RMS roughness is larger than half thickness of the top EuS layer, the layer would become discontinuous. Thus, the different thicknesses of the two EuS layers plays an important role in determining their magnetic properties as well. Presumably, the crystallites in the thick EuS layer are magnetically well coupled, while in the thin magnetic layer they form decoupled magnetic islands. Consequently, the EuS in the bottom would form magnetic domains on a scale much larger than the crystallite size, which leads to the sharp switching of the magnetization observed around $B = -20$ mT in Fig. 2(d). In the thin EuS layer, by contrast, the macroscopic magnetization is an average over the magnetization of the crystallites. Due to disorder, the anisotropy is also random and such crystallites would not switch simultaneously, resulting into the gradual magnetization reversal that we observe from $B \approx -60$ mT to ≈ -100 mT in Fig. 2(d). Moreover, the assumption of an island-like structure due to the growth morphology [32] can also explain the low polarization of the FI layer (25%) in comparison with previous results of near to 80% polarization [8,67]. Indeed, it seems that the coverage of the EuS barrier is not complete and, in addition to the spin polarized current, there is a parallel direct tunneling current through the AlO_x layer.

VI. CONCLUSIONS

We present an exhaustive analysis of tunnel junctions between spin-split superconductors coupled via a spin-polarized barrier. With the help of a theoretical model, we compute the spectral properties of the S/FI electrodes and determine the current through a FI/S/I/FI/I/S/FI junction, where the middle FI layer serves as a spin filter. Our theory predicts a previously unknown behavior of the differential tunneling conductance when the FI layers are noncollinear. Moreover, we suggest how to use these structures for the realization of so-called φ_0 junctions. In addition, our theory provides an accurate description of the differential conductance measurements of an EuS/Al/AlO_x/EuS/Al tunnel junction. We obtain diverse information from the comparison between theory and experiment. On the one hand we can determine the values for the induced spin-splitting fields, spin-filter efficiency, magnetic disorder, spin-orbit coupling, and orbital effects in the superconductors. On the other hand, from the magnetic field dependence of the $dI/dV(V)$ curves, we can extract information about the magnetic structure of the two EuS layers, which turns out to be very different due to the rather different growth morphology of each layer.

ACKNOWLEDGMENTS

This work was supported by EU's Horizon 2020 research and innovation program under Grant Agreement No. 800923 (SUPERTED). M.R., V.N.G., and F.S.B., acknowledge financial support by the Spanish Ministerio de Ciencia, Innovacion

y Universidades through the Projects No. FIS2014-55987-P and No. FIS2017-82804-P and by the grant "Grupos Consolidados UPV/EHU del Gobierno Vasco" (Grant No. IT1249-19). E.S. and F.G acknowledge partial financial support from the European Union's Seventh Framework Programme (FP7/2007-2013)/ERC Grant No. 615187- COMANCHE, and by the Tuscany Region under the FARFAS 2014 Project SCIADRO. S.C, F.A, and T.T.H. acknowledge support from the Academy of Finland (Key Funding Projects No. 305256 and No. 317118). The work of JSM at MIT was supported by NSF Grant No. DMR-1700137, ONR Grant No. N00014-16-1-2657, and ARO Grant No. W911NF1920041.

APPENDIX A: SELF-CONSISTENCY EQUATION

The superconducting gap for each superconductor in the paper is obtained self-consistently. In the quasiclassical theory, the self-consistency equation is given by

$$\Delta_s = \frac{\lambda}{16i}\int_{-\Omega_D}^{\Omega_D} d\epsilon \mathrm{Tr}\big[(\tau_1 - i\tau_2)\check{g}_s^K(\epsilon)\big], \tag{A1}$$

where $s = \{L, R\}$ labels the superconductor, λ is the coupling constant and Ω_D is the Debye cutoff energy. Using the expression for the Keldysh component in Eq. (7) and the parametrization of the Green's functions shown in Eq. (14), we can rewrite the self-consistency equation of the superconducting gap as

$$\Delta_s = \frac{\lambda}{2}\int_{-\Omega_D}^{\Omega_D} d\epsilon\ \mathrm{Im}[F_{0s}(\epsilon)]\tanh\left(\frac{\epsilon}{2k_BT}\right), \tag{A2}$$

We use this self-consistent superconducting gap, together with the Usadel equation in Eq. (9) to calculate the Green's functions used in current calculations.

APPENDIX B: RELATIONS BETWEEN UNIT VECTORS

In order to derive the expressions for the quasiparticle current and supercurrents in Sec. III, we made use of following relations between the unit vectors pointing in the direction of the polarization of the barrier, $\boldsymbol{n}_P$, and induced the exchange fields in the left, $\boldsymbol{n}_L$, and right, $\boldsymbol{n}_R$, electrodes. We define the parallel and perpendicular components of the exchange fields with respect to the polarization vector:

$$\boldsymbol{n}_s^{\parallel} \equiv (\boldsymbol{n}_s \cdot \boldsymbol{n}_P)\boldsymbol{n}_P = \cos\theta_s \boldsymbol{n}_P, \tag{B1}$$

$$\boldsymbol{n}_s^{\perp} \equiv \boldsymbol{n}_s - \boldsymbol{n}_s^{\parallel}, \tag{B2}$$

where $s = \{L, R\}$ labels the position of the electrode. According to these definitions and the expressions for the unit vectors of the Zeeman fields in Eqs. (3) and (4), we obtain the following useful relations:

$$\boldsymbol{n}_L \cdot \boldsymbol{n}_R = \boldsymbol{n}_L^{\parallel} \cdot \boldsymbol{n}_R^{\parallel} + \boldsymbol{n}_L^{\perp} \cdot \boldsymbol{n}_R^{\perp}, \tag{B3}$$

$$\boldsymbol{n}_L^{\parallel} \cdot \boldsymbol{n}_R^{\parallel} = \cos\theta_L \cos\theta_R, \tag{B4}$$

$$\boldsymbol{n}_L^{\perp} \cdot \boldsymbol{n}_R^{\perp} = \sin\theta_L \sin\theta_R \cos\gamma, \tag{B5}$$

$$\boldsymbol{n}_P \cdot (\boldsymbol{n}_L \times \boldsymbol{n}_R) = \sin\theta_L \sin\theta_R \sin\gamma. \tag{B6}$$

[1] R. Meservey, P. M. Tedrow, and P. Fulde, Phys. Rev. Lett. **25**, 1270 (1970).
[2] R. Meservey, P. M. Tedrow, and R. C. Bruno, Phys. Rev. B **11**, 4224 (1975).
[3] P. M. Tedrow and R. Meservey, Phys. Rev. Lett. **26**, 192 (1971).
[4] P. M. Tedrow and R. Meservey, Phys. Rev. B **7**, 318 (1973).
[5] D. Paraskevopoulos, R. Meservey, and P. M. Tedrow, Phys. Rev. B **16**, 4907 (1977).
[6] R. Meservey, D. Paraskevopoulos, and P. M. Tedrow, Phys. Rev. B **22**, 1331 (1980).
[7] R. Meservey and P. M. Tedrow, Phys. Rep. **238**, 173 (1994).
[8] J. S. Moodera, X. Hao, G. A. Gibson, and R. Meservey, Phys. Rev. Lett. **61**, 637 (1988).
[9] X. Hao, J. S. Moodera, and R. Meservey, Phys. Rev. B **42**, 8235 (1990).
[10] T. Tokuyasu, J. A. Sauls, and D. Rainer, Phys. Rev. B **38**, 8823 (1988).
[11] J. S. Moodera, T. S. Santos, and T. Nagahama, J. Phys.: Condens. Matter **19**, 165202 (2007).
[12] F. Hübler, J. C. Lemyre, D. Beckmann, and H. v. Löhneysen, Phys. Rev. B **81**, 184524 (2010).
[13] M. J. Wolf, C. Sürgers, G. Fischer, and D. Beckmann, Phys. Rev. B **90**, 144509 (2014).
[14] D. Beckmann, J. Phys.: Condens. Matter **28**, 163001 (2016).
[15] S. Kolenda, M. J. Wolf, and D. Beckmann, Phys. Rev. Lett. **116**, 097001 (2016).
[16] M. Silaev, P. Virtanen, F. S. Bergeret, and T. T. Heikkilä, Phys. Rev. Lett. **114**, 167002 (2015).
[17] F. S. Bergeret, M. Silaev, P. Virtanen, and T. T. Heikkilä, Rev. Mod. Phys. **90**, 041001 (2018).
[18] T. T. Heikkilä, M. Silaev, P. Virtanen, and F. S. Bergeret, Prog. Surf. Sci. **94**, 100540 (2019).
[19] A. Schmid and G. Schön, J. Low Temp. Phys. **20**, 207 (1975).
[20] P. Machon, M. Eschrig, and W. Belzig, Phys. Rev. Lett. **110**, 047002 (2013).
[21] A. Ozaeta, P. Virtanen, F. S. Bergeret, and T. T. Heikkilä, Phys. Rev. Lett. **112**, 057001 (2014).
[22] T. T. Heikkilä, R. Ojajärvi, I. J. Maasilta, E. Strambini, F. Giazotto, and F. S. Bergeret, Phys. Rev. Appl. **10**, 034053 (2018).
[23] F. Giazotto, P. Solinas, A. Braggio, and F. S. Bergeret, Phys. Rev. Appl. **4**, 044016 (2015).
[24] G. De Simoni, E. Strambini, J. S. Moodera, F. S. Bergeret, and F. Giazotto, Nano Lett. **18**, 6369 (2018).
[25] F. Giazotto and F. S. Bergeret, Appl. Phys. Lett. **102**, 132603 (2013).
[26] F. Giazotto, J. W. A. Robinson, J. S. Moodera, and F. S. Bergeret, Appl. Phys. Lett. **105**, 062602 (2014).
[27] F. Giazotto, T. T. Heikkilä, and F. S. Bergeret, Phys. Rev. Lett. **114**, 067001 (2015).
[28] M. Rouco, T. T. Heikkilä, and F. S. Bergeret, Phys. Rev. B **97**, 014529 (2018).

[29] S. Chakraborty and T. T. Heikkilä, J. Appl. Phys. **124**, 123902 (2018).
[30] E. Strambini, V. N. Golovach, G. De Simoni, J. S. Moodera, F. S. Bergeret, and F. Giazotto, Phys. Rev. Mater. **1**, 054402 (2017).
[31] X.-P. Zhang, F. S. Bergeret, and V. N. Golovach, Nano Lett. (2019).
[32] G.-X. Miao and J. S. Moodera, Appl. Phys. Lett. **94**, 182504 (2009).
[33] A. A. Abrikosov, *Fundamentals of the Theory of Metals* (Dover Publications, New York, 2017)
[34] M. G. Khusainov, Zh. Eksp. Teor. Fiz. **109**, 524 (1996) [JETP **82**, 278 (1996)].
[35] Yu. A. Izyumov, Yu. N. Proshin, and M. G. Khusainov, Phys. Usp. **45**, 109 (2002).
[36] K. Maki, Prog. Theor. Phys. **31**, 731 (1964).
[37] F. S. Bergeret, A. Verso, and A. F. Volkov, Phys. Rev. B **86**, 214516 (2012).
[38] D. N. Langenberg and A. I. Larkin, *Nonequilibrium superconductivity* (North-Holland, Amsterdam, 1986).
[39] K. D. Usadel, Phys. Rev. Lett. **25**, 507 (1970).
[40] F. S. Bergeret, A. F. Volkov, and K. B. Efetov, Phys. Rev. Lett. **86**, 4096 (2001).
[41] F. S. Bergeret, A. Verso, and A. F. Volkov, Phys. Rev. B **86**, 060506(R) (2012).
[42] R. E. Harris, Phys. Rev. B **10**, 84 (1974).
[43] A. I. Larkin and Y. N. Ovchinnikov, Zh. Eksp. Teor. Fiz. **51**, 1535 (1966) [JETP **24**, 1035 (1967)].
[44] A. Barone and G. Paterno, *Physics and Applications of the Josephson Effect* (Wiley, New York, 1982).
[45] A. Buzdin, Phys. Rev. Lett. **101**, 107005 (2008).
[46] A. Zazunov, R. Egger, T. Jonckheere, and T. Martin, Phys. Rev. Lett. **103**, 147004 (2009).
[47] A. Brunetti, A. Zazunov, A. Kundu, and R. Egger, Phys. Rev. B **88**, 144515 (2013).
[48] A. A. Reynoso, G. Usaj, C. A. Balseiro, D. Feinberg, and M. Avignon, Phys. Rev. Lett. **101**, 107001 (2008).
[49] K. N. Nesterov, M. Houzet, and J. S. Meyer, Phys. Rev. B **93**, 174502 (2016).
[50] F. Konschelle, I. V. Tokatly, and F. S. Bergeret, Phys. Rev. B **92**, 125443 (2015).
[51] F. Bergeret and I. Tokatly, Europhys. Lett. **110**, 57005 (2015).
[52] I. V. Bobkova, A. M. Bobkov, A. A. Zyuzin, and M. Alidoust, Phys. Rev. B **94**, 134506 (2016).
[53] T. Yokoyama, M. Eto, and Y. V. Nazarov, Phys. Rev. B **89**, 195407 (2014).
[54] M. A. Silaev, Phys. Rev. B **96**, 064519 (2017).
[55] M. A. Silaev, I. V. Tokatly, and F. S. Bergeret, Phys. Rev. B **95**, 184508 (2017).
[56] J.-F. Liu and K. S. Chan, Phys. Rev. B **82**, 125305 (2010).
[57] A. G. Mal'shukov, S. Sadjina, and A. Brataas, Phys. Rev. B **81**, 060502(R) (2010).
[58] Y. Lu and T. T. Heikkilä, Phys. Rev. B **100**, 104514 (2019).
[59] I. Margaris, V. Paltoglou, and N. Flytzanis, J. Phys.: Condens. Matter **22**, 445701 (2010).
[60] V. Braude and Y. V. Nazarov, Phys. Rev. Lett. **98**, 077003 (2007).
[61] A. Moor, A. F. Volkov, and K. B. Efetov, Phys. Rev. B **92**, 180506(R) (2015).
[62] R. Grein, M. Eschrig, G. Metalidis, and G. Schön, Phys. Rev. Lett. **102**, 227005 (2009).
[63] J.-F. Liu and K. S. Chan, Phys. Rev. B **82**, 184533 (2010).
[64] S. Mironov and A. Buzdin, Phys. Rev. B **92**, 184506 (2015).
[65] F. S. Bergeret, A. F. Volkov, and K. B. Efetov, Rev. Mod. Phys. **77**, 1321 (2005).
[66] V. Ambegaokar and A. Baratoff, Phys. Rev. Lett. **10**, 486 (1963).
[67] P. M. Tedrow, J. E. Tkaczyk, and A. Kumar, Phys. Rev. Lett. **56**, 1746 (1986).
[68] P. Tischer, IEEE Trans. Magn. **9**, 9 (1973).
[69] F. Jedema, H. Heersche, A. Filip, J. Baselmans, and B. Van Wees, Nature (London) **416**, 713 (2002).
[70] N. Poli, J. P. Morten, M. Urech, A. Brataas, D. B. Haviland, and V. Korenivski, Phys. Rev. Lett. **100**, 136601 (2008).
[71] A. Anthore, H. Pothier, and D. Esteve, Phys. Rev. Lett. **90**, 127001 (2003).
[72] P. G. de Gennes, *Superconductivity of Metals and Alloys*, Advanced Book Classics (Perseus, Cambridge, MA, 1999).

III

SUPERCURRENT INDUCED CHARGE-SPIN CONVERSION IN SPIN-SPLIT SUPERCONDUCTORS

by

Faluke Aikebaier, Mihail A. Silaev & T. T. Heikkilä 2018

Phys. Rev. B 98, 024516 (2018)

DOI: http://doi.org/10.1103/PhysRevB.98.024516

Supercurrent-induced charge-spin conversion in spin-split superconductors

Faluke Aikebaier,[*] Mihail A. Silaev,[†] and T. T. Heikkilä[‡]
Department of Physics and Nanoscience Center, University of Jyvaskyla, P.O. Box 35 (YFL), FI-40014 University of Jyväskylä, Finland

(Received 22 December 2017; revised manuscript received 27 March 2018; published 25 July 2018)

We study spin-polarized quasiparticle transport in a mesoscopic superconductor with a spin-splitting field in the presence of coflowing supercurrent. In such a system, the nonequilibrium state is characterized by charge, spin, energy, and spin-energy modes. Here we show that in the presence of both spin splitting and supercurrent, all these modes are mutually coupled. As a result, the supercurrent can convert charge imbalance, which in the presence of spin splitting decays on a relatively short scale, to a long-range spin accumulation decaying only via inelastic scattering. This effect enables coherent charge-spin conversion controllable by a magnetic flux, and it can be detected by studying different symmetry components of the nonlocal conductance signal.

DOI: 10.1103/PhysRevB.98.024516

I. INTRODUCTION

The nonequilibrium states in superconductors can be classified in terms of energy and charge modes [1,2] as a direct result of the particle-hole formalism in BCS theory. In magnetic systems the relevant nonequilibrium modes are related to the quasiparticle spin. In spin-split superconductors all these modes need to be considered, and the quasiparticle diffusion couples pairs of modes [3–5]. The earlier description of such spin-resolved modes includes only the direct quasiparticle transport, whereas the effect of supercurrent was not considered. However, a supercurrent flowing along a temperature gradient is known to induce a charge imbalance [6–9]. Here we combine these two effects and show how supercurrent couples all nonequilibrium modes. We show how this leads to a large coherently controllable charge-spin conversion induced by supercurrent. In particular, we use the theoretical framework [3] based on the quasiclassical Keldysh-Usadel formalism for superconductors with a spin-splitting field h and consider the presence of a constant phase gradient $\nabla\varphi$ in the superconducting order parameter. This leads to supercurrent and shows up in the kinetic equations as spectral charge and spin supercurrents. These coherent supercurrent terms couple spin and charge transport, generating spin from charge injection. The effect is long ranged compared to the spin-relaxation length in the normal state and becomes very large at the critical temperature and exchange field. It can be detected by studying the different symmetry components of the nonlocal conductance.

The spin-charge conversion studied here occurs only under nonequilibrium conditions and does not require spin-orbit interaction. Therefore it is qualitatively different from the direct [10–12] and inverse [13–16] equilibrium magnetoelectric effects proposed for noncentrosymmetric superconductors, Josephson junctions [17–19], and superconducting hybrid systems [20] with spin-orbit coupling. Experimental verification of these spin-orbit-induced effects is limited to recent observations of the anomalous Josephson effect through a quantum dot [21] and Bi_2Se_3 interlayer [22,23]. To our knowledge, the direct magnetoelectric effect, also known as the Edelstein effect, in noncentrosymmetric superconductors has not been observed to date. In normal conductors, such as GaAs semiconductors, this effect is known as the inverse spin-galvanic effect and has been detected using Faraday rotation [24]. In contrast, the charge-spin conversion predicted in this work can be measured by purely electrical probes. Moreover, it is specific to superconducting metallic systems and does not rely on the combination of inversion symmetry breaking and spin-orbit coupling, which usually has a tiny effect in such materials.

II. QUALITATIVE DESCRIPTION OF THE CHARGE-SPIN CONVERSION

The supercurrent-generated coupling between different nonequilibrium states can be understood with the schematic in Fig. 1, showing the spin-split BCS spectrum $E_p + \sigma h \pm \boldsymbol{p}_F \boldsymbol{v}_s$ (where $\sigma = \pm 1$ for spin $\uparrow$ and $\downarrow$) for left- and right-moving quasiparticles with respect to the condensate velocity $\boldsymbol{v}_s$. The left- and right-moving states are defined according to their velocities $v_g \equiv \partial E_p/\partial \boldsymbol{p} \gtrless 0$. The balance between the two can be broken either by position-dependent nonequilibrium modes or by the presence of a supercurrent that induces an energy difference (Doppler shift) $\sim 2 p_F v_s$ between the states with $p \approx \pm p_F$, where p_F is the Fermi momentum.

In the absence of spin splitting, $h = 0$, the combination of these two effects allows for the creation of charge imbalance proportional to $\boldsymbol{v}_s \nabla T$ [6–9] where T is the temperature. This mechanism is illustrated qualitatively in Fig. 1(a). Due to the temperature gradient, left-moving quasiparticles [both electrons (el) and holes (hl)] with velocities $v_e = v_h = -v_g = -v_F\sqrt{E_p^2 - \Delta^2}/E_p$ have an excess temperature T_L compared to that of the right-moving particles T_R. From Fig. 1(a) one can see that due to the Doppler shift there are more occupied states in the electron branch. This results in the charge imbalance μ controlled by the Doppler shift $p_F v_s$.

[*]faluke.aikebaier@jyu.fi
[†]mikesilaev@gmail.com
[‡]tero.t.heikkila@jyu.fi

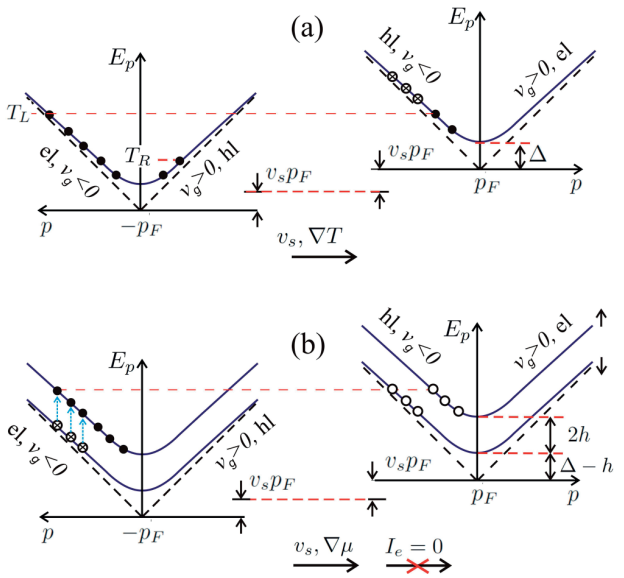

FIG. 1. Schematic pictures illustrating the couplings between different types of nonequilibrium states in a superconductor in the presence of the phase gradient driving the condensate to the velocity $\boldsymbol{v}_s$. (a) Generation of charge imbalance by the temperature gradient. (b) Generation of spin accumulation by the charge imbalance gradient $\nabla\mu$ under the restriction that energy current is absent $I_e = 0$. Shown in the plots are the quasiparticle electronlike (el) and holelike (hl) spectral branches in the superconductor in the presence of Doppler shifted energy $\pm p_F v_s$. The solid and open circles show the extra occupied and empty states compared to the equilibrium distribution, respectively, and the circles with crosses show the states which become depopulated due to the Doppler shift.

Now, let us turn to the system in the presence of velocity v_s and Zeeman splitting $h \neq 0$, shown in Fig. 1(b). Spin splitting the spectrum provides the possibility for a population difference between spin-↑ and -↓ branches. Therefore the supercurrent can couple charge and spin ($\mu_z \propto \boldsymbol{v}_s\nabla\mu$ or $\mu \propto \boldsymbol{v}_s\nabla\mu_z$) as well as excess energy and spin energy ($T_s \propto \boldsymbol{v}_s\nabla T$ or $T \propto \boldsymbol{v}_s\nabla T_s$). Here μ_z is the spin accumulation, and T_s is the spin energy accumulation [3]. Under general nonequilibrium conditions all these couplings are present. To separate the particular charge-spin conversion effect we must impose certain constraints on the distribution function changes due to the supercurrent-induced Doppler shift as in Fig. 1(b). As shown below [Eq. (18)], these constraints determine the particular symmetry components of the nonlocal conductance as functions of the injector voltage and polarization of the detector electrode. For example, let us assume a charge imbalance gradient $\nabla\mu \neq 0$ resulting in a larger (smaller) number of left-moving electrons (holes) in the absence of energy current I_e, so that the energies of left-moving (right-moving) quasiparticles are the same. In the absence of supercurrent these states occupy spin-up and -down branches symmetrically, yielding no spin accumulation. The Doppler shift results in qualitative changes in quasiparticle distributions. From Fig. 1(b) one can see that in order to have $I_e = 0$ without affecting the charge imbalance, the extra energy gained by placing electrons on the Doppler-shifted energy branch can be compensated only by utilizing the Zeeman energy and shifting some occupied states on the spin-down electron branch to the spin-up one (dashed arrows in Fig. 1). Together with compensating the energy difference between left- and right-moving states this shift produces a net spin polarization.

III. KINETIC THEORY IN THE PRESENCE OF SUPERCURRENT AND SPIN SPLITTING

Below, we quantify the physics described above using the kinetic equations [3] based on the quasiclassical Keldysh-Usadel formalism for superconductors with a spin-splitting field h to study the spin accumulation generated by the charge imbalance gradients. For concreteness, we consider the structure shown in Fig. 3(a) below. A superconducting wire with length L is placed between two superconducting reservoirs. We assume the presence of a Zeeman splitting along the wire due to either a magnetic proximity effect from a ferromagnetic insulator or an in-plane magnetic field. A current is injected in the wire from a normal-metal injector. A ferromagnetic detector with normal-state conductance $G_{\rm det}$ and spin polarization $P_{\rm det}$ is placed at distance $L_{\rm det}$ from the injector. Variants of this setup were realized, for example, in Refs. [25–27]. Here we assume that, in addition, a homogeneous supercurrent I_s flows along the wire. Either this current can be driven externally, or it can be induced by a magnetic field in a superconducting loop.

To study the properties of a mesoscopic superconductor with Zeeman splitting, we start from the Usadel equation [28] ($\hbar = k_B = 1$)

$$D\hat{\nabla}(\check{g}\hat{\nabla}\check{g}) + [\check{\Lambda} - \check{\Sigma}_{\rm so} - \check{\Sigma}_{\rm sf} - \check{\Sigma}_{\rm orb}, \check{g}] = 0, \qquad (1)$$

where D is the diffusion constant, $\check{g}$ is the quasiclassical Green's function, and the covariant gradient operator is $\hat{\nabla} = \nabla - iA[\tau_3, \cdot]$. In the commutator $\check{\Lambda} = i\epsilon\tau_3 - i(\boldsymbol{h}\cdot\boldsymbol{S})\tau_3 - \check{\Delta}$, ϵ is the quasiparticle energy, $\boldsymbol{h}$ is the spin-splitting field, $\boldsymbol{S} = (\sigma_1, \sigma_2, \sigma_3)$, and the Pauli matrix τ_j (σ_j) is in Nambu (spin) space. The exact form of the spin-splitting field term, as well as of the pair potential $\hat{\Delta}$, depends on the chosen Nambu spinor. We choose it to be

$$\Psi = (\psi_\uparrow(x),\ \psi_\downarrow(x),\ -\psi_\downarrow^\dagger(x),\ \psi_\uparrow^\dagger(x))^T, \qquad (2)$$

where T denotes a transpose. The advantage of using this spinor is that the Nambu structure has the same form for each spin component. The superconducting pair potential $\check{\Delta} = \hat{\Delta}\sigma_0$ should be obtained self-consistently (see Appendix A for details). We denote the Nambu-space matrix $\hat{\Delta}(x) = |\Delta|e^{i\varphi(x)\tau_3}\tau_1$, where x is the coordinate along the wire. Due to supercurrent, the phase φ becomes position dependent. We assume that the quasiparticle currents within the wire are so small that we can disregard the ensuing position dependence of $|\Delta|$. The last three terms in the commutator are $\check{\Sigma}_{\rm so} = (8\tau_{\rm so})^{-1}(\boldsymbol{S}\check{g}\boldsymbol{S})$, $\check{\Sigma}_{\rm sf} = (8\tau_{\rm sf})^{-1}(\boldsymbol{S}\tau_3\check{g}\tau_3\boldsymbol{S})$, and $\check{\Sigma}_{\rm orb} = \tau_{\rm orb}^{-1}\tau_3\check{g}\tau_3$, representing spin and charge imbalance relaxation due to the spin-orbit scattering, exchange interaction with magnetic impurities, and orbital magnetic depairing, respectively. The corresponding relaxation rates are $\tau_{\rm so}^{-1}$, $\tau_{\rm sf}^{-1}$, and $\tau_{\rm orb}^{-1}$.

We use the real-time Keldysh formalism and describe the quasiclassical Green's function as

$$\check{g} = \begin{pmatrix} \hat{g}^R & \hat{g}^K \\ \hat{0} & \hat{g}^A \end{pmatrix}, \tag{3}$$

where each component is a 4×4 matrix in the Nambu ⊗ spin space, $\hat{g}^{R(A)}$ is the retarded (advanced) Green's function, and $\hat{g}^K$ is the Keldysh Green's function describing the nonequilibrium properties. This function can be parameterized in the case of collinear magnetizations by $\hat{g}^K = \hat{g}^R\hat{f} - \hat{f}\hat{g}^A$, where the distribution matrix $\hat{f} = f_L + f_T\tau_3 + f_{T3}\sigma_3 + f_{L3}\sigma_3\tau_3$.

We consider Eq. (1) in the presence of the superconducting current along the wire. Removing the phase of the order parameter by gauge transformation allows us to write Eq. (1) in the gauge-invariant form, replacing the vector potential by the condensate momentum $\boldsymbol{q}_s = \nabla\varphi - 2\boldsymbol{A}$. The gradient term in Eq. (1) can be written in the form

$$\hat{\nabla}\cdot(\check{g}\hat{\nabla}\check{g}) = \nabla\cdot\hat{\boldsymbol{I}} + \frac{i}{2}[\tau_3, \boldsymbol{q}_s\hat{\boldsymbol{I}}], \tag{4}$$

$$\hat{\boldsymbol{I}} = \check{g}\nabla\check{g} + \frac{i\boldsymbol{q}_s}{2}(\check{g}\tau_3\check{g} - i\tau_3), \tag{5}$$

where $\hat{\boldsymbol{I}}$ is the matrix spectral current. We formulate the Keldysh part of this equation in terms of spectral currents: charge $j_c = \mathrm{Tr}(\tau_3\hat{I})$, energy $j_e = \mathrm{Tr}(\tau_0\hat{I})$, spin $j_s = \mathrm{Tr}(\sigma_3\hat{I})$, and spin energy $j_{\mathrm{se}} = \mathrm{Tr}(\sigma_3\tau_3\hat{I})$.

Kinetic equations derived from Eqs. (4) and (5) for these currents can be written in a matrix form:

$$\nabla\cdot\begin{pmatrix} j_e \\ j_s \\ j_c \\ j_{\mathrm{se}} \end{pmatrix} = \begin{pmatrix} 0 & 0 & 0 & 0 \\ 0 & S_{T3} & 0 & 0 \\ 0 & 0 & R_T & R_{L3} \\ 0 & 0 & R_{L3} & R_T + S_{L3} \end{pmatrix}\begin{pmatrix} f_L \\ f_{T3} \\ f_T \\ f_{L3} \end{pmatrix}, \tag{6}$$

where

$$\begin{pmatrix} j_e \\ j_s \\ j_c \\ j_{\mathrm{se}} \end{pmatrix} = \begin{pmatrix} D_L\nabla & D_{T3}\nabla & j_E q_s & j_{Es}q_s \\ D_{T3}\nabla & D_L\nabla & j_{Es}q_s & j_E q_s \\ j_E q_s & j_{Es}q_s & D_T\nabla & D_{L3}\nabla \\ j_{Es}q_s & j_E q_s & D_{L3}\nabla & D_T\nabla \end{pmatrix}\begin{pmatrix} f_L \\ f_{T3} \\ f_T \\ f_{L3} \end{pmatrix}. \tag{7}$$

The kinetic coefficients $D_{L/T/T3/L3}$, $R_{T/L3}$, and $S_{T3/L3}$ are defined in terms of the components of $\hat{g}^R$ and $\hat{g}^A$ (see Appendix B and more details in Ref. [3]). The terms $S_{T3/L3}$ are proportional to the total spin-relaxation rate in the normal state, $\tau_{\mathrm{sn}}^{-1} = \tau_{\mathrm{so}}^{-1} + \tau_{\mathrm{sf}}^{-1}$. The phase gradient provides two additional terms in Eq. (7): spectral supercurrent j_E [29] and spin supercurrent $j_{Es} = D\,\mathrm{Tr}[(\hat{g}^R\nabla\hat{g}^R - \hat{g}^A\nabla\hat{g}^A)\sigma_3\tau_3]/(8q_s)$. Further we use the gauge with $\boldsymbol{A} = 0$, so that $\boldsymbol{q}_s = \nabla\varphi$.

In equilibrium $f_L = \tanh(\epsilon/2T) \equiv n_0$, and other modes are absent. Then the spectral current terms yield nonzero charge supercurrent I_s and spin-energy current I_{se} as

$$I_s = G_{\xi_0}\xi_0 q_s\int_{-\infty}^{\infty} d\epsilon j_E\tanh\left(\frac{\epsilon}{2T}\right), \tag{8}$$

$$I_{\mathrm{se}} = G_{\xi_0}\xi_0 q_s\int_{-\infty}^{\infty} d\epsilon\epsilon j_{Es}\tanh\left(\frac{\epsilon}{2T}\right), \tag{9}$$

where $G_{\xi_0} = e^2 D\nu_F A/\xi_0$ is the normal-state conductance of the wire of one superconducting coherence length $\xi_0 = \sqrt{D/\Delta}$, with normal-state density of states ν_F and cross section A. We assume that the phase gradient is small, so that I_s is much below the critical current of the wire.

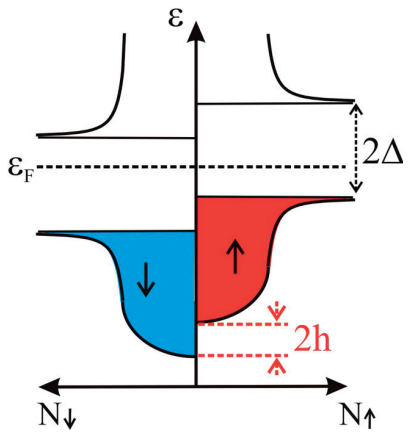

FIG. 2. Schematic picture illustrating the nonzero spin energy in the ground state of a spin-singlet superconductor with spin splitting. $N_{\uparrow,\downarrow}(\varepsilon)$ are the spin-up and -down densities of states as functions of the energy ε. The relative Zeeman shift of the electronic bands is $2h$. The case of $T = 0$ is shown, so that all states below the Fermi level ε_F are occupied.

The equilibrium spin-energy current, Eq. (9), arises due to the modification of the superconducting ground state in the presence of an exchange field. This is illustrated schematically in Fig. 2, which shows the occupied energy states in spin-up and spin-down subbands in a superconductor with a spin-splitting field. Here one can see that there is a relative energy shift between the spin-up and -down subbands. The overall energy difference between these states yields the nonvanishing spin energy density $\epsilon_\uparrow - \epsilon_\downarrow = hN_0$, where N_0 is the total electron density. Since all these particles are in the condensed state, the collective motion of the condensate results in the coherent spin-energy flow $I_{\mathrm{se}} = v_s N_0 h$. However, such an equilibrium spin-energy current is not directly observable and can be revealed through its coupling to the superconducting current and charge imbalance, as discussed below.

Out of equilibrium, the matrix in Eq. (7) couples the four modes together. The diffusion coefficients $D_{T3/L3} \neq 0$ for $h \neq 0$ combine pairwise f_T and f_{L3} (charge and spin energy) modes as well as f_L and f_{T3} (energy and spin) modes [4,5]. An additional coupling between f_L and f_T modes is introduced by j_E, mixing charge imbalance with energy. This coupling leads to the supercurrent-induced charge imbalance in the presence of a temperature gradient [7–9]. The presence of h and j_E combines these two effects together in Eq. (7) and allows for the conversion between charge imbalance and spin accumulation. In the next section we study the observable consequences of this conversion.

IV. SPIN-CHARGE CONVERSION IN A NONLOCAL SPIN VALVE

Kinetic theory developed in the previous section can be applied to predict the experimentally measurable consequence of the charge-spin conversion effect in the nonlocal spin-valve

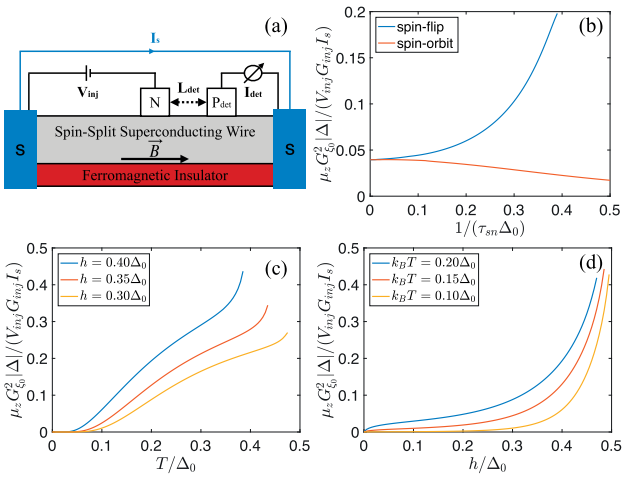

FIG. 3. (a) Schematic view of the setup. Here the spin-splitting field is induced from either the ferromagnetic insulator or external magnetic field $\boldsymbol{B}$. (b)–(d) Spin accumulation as a function of parameters $\mu_z = \mu_z(h, T, \tau_{sn})$ at the detector position $L_{det} = L/8$ in the linear-response regime (small V_{inj}). (b) The dependence on the spin-relaxation rate for $k_BT = 0.15\Delta_0$ and $h = 0.3\Delta_0$. (c) Temperature and (d) spin-splitting field dependence. The orbital depairing rate is $\tau_{orb}^{-1} = 0.176h^2/\Delta_0$. Here we normalize the induced spin signal by the supercurrent amplitude I_s.

setup shown in Fig. 3(a). It consists of a superconducting wire with externally induced supercurrent, an injector electrode attached at $x = 0$, and a ferromagnetic detector electrode attached at some distance $x = L_D$. The overall length of the wire L is fixed by the boundary conditions which require all nonequilibrium modes to vanish at $x = \pm L/2$.

Consider a nonferromagnetic injector electrode attached at $x = 0$. We describe the injection of matrix quasiparticle current using the boundary conditions at the tunneling interface [30] extended to the spin-dependent case [31]:

$$\begin{pmatrix} [j_c] \\ [j_e] \\ [j_s] \\ [j_{se}] \end{pmatrix} = \begin{pmatrix} N_+ & PN_- & PN_+ & N_- \\ PN_- & N_+ & N_- & PN_+ \\ PN_+ & N_- & N_+ & PN_- \\ N_- & PN_+ & PN_- & N_+ \end{pmatrix} \begin{pmatrix} [f_T] \\ [f_L] \\ [f_{T3}] \\ [f_{L3}] \end{pmatrix}. \tag{10}$$

Here the left-hand side of Eq. (10) contains the differences between currents in the superconducting wire on the left and on the right from the injector, $[j_k] = [j_k(x = +0) - j_k(x = -0)]/\kappa_I$, where $k = T, L, T3, L3$ and $\kappa_I = G_{inj}/(G_L L)$ is the injector transparency defined by the ratio of the normal-state conductance G_{inj} of the injector and the conductance $G_L L$ of the wire per unit length.

The right-hand side of Eq. (10) contains the differences of the distribution function components $[f]_k = f_k^{(S)} - f_k^{(N)}$ between the superconductor and normal-metal electrodes. The response matrix is here described by the spin polarization P and the energy-symmetric and energy-antisymmetric parts of the density of states, $N_+ = \mathrm{Tr\,Re}(\tau_3 \hat{g}^R)$ and $N_- = \mathrm{Tr\,Re}(\sigma_3 \tau_3 \hat{g}^R)$. In our particular case the normal-metal injector is characterized by the Fermi distribution function shifted by the applied bias voltage V_{inj}. Therefore we have $[f_L] = f_L - n_+$, $[f_T] = (f_T - n_-)$, $[f_{T3}] = f_{T3}$, and $[f_{L3}] = f_{L3}$, where $n_\pm = [n_0(\epsilon + V_{inj}) \pm n_0(\epsilon - V_{inj})]/2$.

The solutions of Eqs. (6) and (10) can be used to calculate the tunneling current I_{det} measured by a spin-polarized detector [4] with spin-filtering efficiency P_{det}:

$$I_{det} = G_{det}(\mu + P_{det}\mu_z), \tag{11}$$

$$\mu = \frac{1}{2}\int_{-\infty}^{\infty} d\varepsilon (N_+ f_T + N_- f_{L3}), \tag{12}$$

$$\mu_z = \frac{1}{2}\int_{-\infty}^{\infty} d\varepsilon [N_+ f_{T3} + N_-(f_L - f_{eq})]. \tag{13}$$

The contributions from the different nonequilibrium modes to μ and μ_z can be read off from the different symmetry components of I_{det} with respect to the injection voltage V_{inj} and the detector polarization P_{det}. The non-spin-polarized injector generates charge f_T and energy f_L modes [32], which are odd and even in the injection voltage, respectively. In spin-split superconductors the energy mode is coupled to the spin accumulation, producing a long-range spin signal with the symmetry [4] $\mu_z(V_{inj}) = \mu_z(-V_{inj})$. The supercurrent converts part of the charge imbalance to long-range spin accumulation with the opposite symmetry $\mu_z(V_{inj}) = -\mu_z(-V_{inj})$. Below we concentrate on the details of this mechanism.

First, we solve the kinetic equations using a perturbation expansion in the small parameter $\xi_0 q_s$, where $\xi_0 = \sqrt{D/\Delta}$ is the coherence length. For simplicity, we disregard inelastic scattering that would add an energy-nonlocal term in Eq. (6) and rather assume that $f_L = n_0$ at the ends of the wire. This mimics the typical experimental situation where the wire ends in wide electrodes, often at a distance that is small compared to the inelastic scattering length. In this case the solution of f_L includes a linear component. The solution of f_{T3}, however, is determined by the strength of spin relaxation. This calculation is detailed in Appendix C.

When $q_s = 0$, we find f_T and f_{L3} modes generating the charge imbalance μ. For $q_s \neq 0$ [see Eq. (7)] these solutions provide sources for the f_L and f_{T3} modes generating the spin accumulation μ_z in accordance with the qualitative mechanism illustrated in Fig. 1(b). This generation takes place close to the injectors before the charge imbalance relaxes due to the presence of an exchange field and depairing [3,33] [blue lines in Fig. 4(a)].

However, μ_z has a long-range part associated with the contribution of f_L, which consists of two qualitatively different parts. First, even in the absence of the supercurrent, there exists a long-range contribution related to the already known heating effect [4] given by

$$f_L^{heat}(x) = \alpha_{heat}(|x| - L), \tag{14}$$

where $\alpha_{heat} = N_+ n_+ / D_L$. Second, the long-range contribution excited due to the supercurrent is given approximatively by

$$f_L^{super} = \alpha_{super}[\mathrm{sgn}(x) - x/L]. \tag{15}$$

The amplitude α_{super} depends on the strength of relaxation described by $R_{T/L3}$ and $S_{T3/L3}$ in Eq. (6).

Note that the spatial structures of (14) and (15) are different because $f_L^{heat}(x)$ is an even function and $f_L^{super}(x)$ is an odd function of x [see Fig. 4(a)]. In addition, the amplitude of

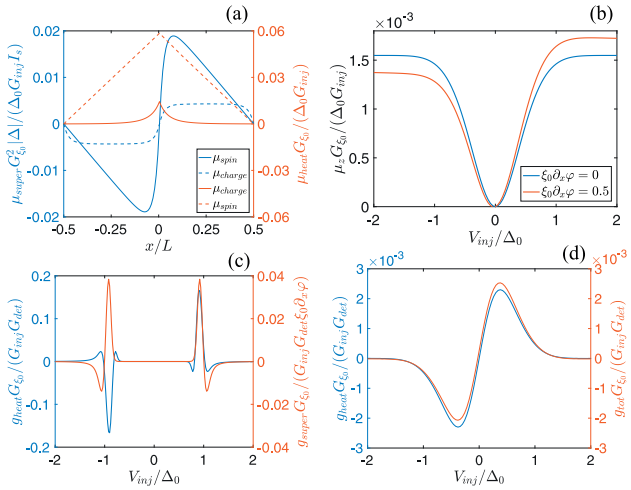

FIG. 4. Spin accumulation and nonlocal conductance. (a) Position dependence of heat-induced (red) and supercurrent-induced (blue) charge and spin imbalances. Here the results are calculated for $T = 0.15\Delta_0$, $h = 0.3\Delta_0$ at $V_{\rm inj} = 0.1\Delta_0$. The solid curves are odd in injection voltage, and dashed curves are even. (b) Injection voltage dependence on spin accumulation for $T = 0.25\Delta_0$. (c) Nonlocal conductance as a function of injection voltage in separate scales for heat- and supercurrent-induced effects (with $\xi_0\partial_x\varphi = 0.1$) for $T = 0.02\Delta_0$. (d) Heat-induced and total conductance as a function of injection voltage for $T = 0.25\Delta_0$ (with $\xi_0\partial_x\varphi = 0.5$). The parameters $\tau_{\rm so}^{-1} = 0.0475\Delta_0$, $\tau_{\rm sf}^{-1} = 0.0025\Delta_0$, $h = 0.05\Delta_0$, and $L = 20\xi_0$ are the same in (b)–(d).

the supercurrent-induced part is an odd function of the injector voltage $\alpha_{\rm super}(V_{\rm inj}) = -\alpha_{\rm super}(-V_{\rm inj})$. Therefore it exists already in the linear regime, whereas the heating (14) is a nonlinear effect since $\alpha_{\rm heat}(V_{\rm inj}) = \alpha_{\rm heat}(-V_{\rm inj})$. Further, as one can see from Eq. (14), the heating contribution grows linearly with the wire length L, while the supercurrent-related part (15) does not depend on the length L at distances $|x| \ll L$.

To gain further insight, we first study the spin accumulation using a numerical solution of the kinetic equations. In Figs. 3(b)–3(d), 4(a), and 4(b), we show the dependencies of the spin accumulation on various parameters $\mu_z = \mu_z(h, T, \tau_{\rm sn}, V_{\rm inj}, x)$ obtained from the numerical solutions of Eqs. (6) and (7). Note that from this plot it is clear that the effect exists entirely due to the modification of the quasiparticle spectrum by the spin splitting: As shown in Figs. 3(c) and 3(d), the spin signal μ_z disappears both for $h \to 0$ when there is no spin splitting and for $T \to 0$ when there are no quasiparticles. At the same time, Fig. 3(b) shows that the effect survives in the absence of spin-orbit or spin-flip scattering, i.e., for $\tau_{\rm sn} \to \infty$. Below we study in more detail the influence of spin relaxation on the behavior of different contributions to the spin accumulation.

A. Case without spin relaxation ($S_{T3,L3} = 0$)

The discussed mechanism of spin-charge conversion does not require any nonconservation of spin. This is qualitative distinction from previously discussed direct and inverse Edelstein effects which rely on the spin-orbit interaction [10–16]. In the absence of spin relaxation, $f_{T3} \propto x$ is also a long-range mode similar to the longitudinal one which in the absence of inelastic scattering is long range [see Eqs. (14) and (15)]. The combination of f_{T3} and f_L then yields (see details in Appendix C)

$$\mu_z = \xi_0\partial_x\varphi\,\frac{G_{\rm inj}}{G_{\xi_0}}\int_0^\infty d\epsilon n_-(\epsilon; V_{\rm inj}) \sum_{\sigma=\uparrow,\downarrow} \frac{\sigma N_\sigma^2 j_s^\sigma}{4D_L^\sigma R_T^\sigma} u_0(x). \tag{16}$$

Here $u_0(x) = -u_0(-x)$ is a function that decays linearly from unity close to the injector ($x = 0$) to zero at the reservoirs, and $n_- = [n_0(\epsilon + V_{\rm inj}) - n_0(\epsilon - V_{\rm inj})]/2$. Equation (16) describes the region $|x| > \lambda_{\rm cr}$, where $\lambda_{\rm cr}$ is the charge relaxation length. Here $N_{\uparrow/\downarrow} = N_+ \pm N_-$ are spin-up and -down densities of states, $D_L^{\uparrow/\downarrow} = D_L \pm D_{T3}$, $R_T^{\uparrow/\downarrow} = R_T \pm R_{L3}$, and $j_s^{\uparrow/\downarrow} = j_E \pm j_{Es}$. Moreover, $G_{\rm inj}$ and G_{ξ_0} are the normal-state conductances of the injector and of a wire with length ξ_0, respectively. The integrand in Eq. (16) is peaked at $\epsilon \approx \Delta \pm h$ due to the BCS divergence in N_σ, j_s^σ, and R_T^σ. This divergence can be cut off by the depairing parameter [34] Γ. Then taking $\epsilon = \Delta + h$ for spin-up $\sigma = \uparrow$ and $\epsilon = \Delta - h$ for spin-down $\sigma = \downarrow$ we obtain, $N_\sigma \approx \gamma_\sigma^{-1/2}/\sqrt{2}$, $j_S^\sigma \approx \gamma_\sigma^{-1}/2$, and $R_\sigma \approx \gamma_\sigma^{-1/2}/2$, with $\gamma_\sigma = \Gamma/(\Delta + \sigma h)$. Therefore the integrand scales as $(8\gamma_\sigma)^{-3/2}$, whereas the width of the peak is $\propto \Gamma$. Overall, this means a diverging integral scaling like $\sim\Gamma^{-1/2}$. Similar divergence was found in Ref. [6] for the supercurrent-induced charge imbalance in the absence of spin splitting.

In practice, the relevant depairing mechanism in the presence of spin splitting and supercurrent is the orbital depairing due to the combined effect of the supercurrent itself and of an in-plane magnetic field $\boldsymbol{B}$ on the spectrum of the superconductor [35–37], with rate $\tau_{\rm orb}^{-1} = D\Delta(\partial_x\varphi)^2/(2) + De^2B^2d^2/6$ for a film with thickness d. It does not relax the spin but affects the spectral properties of the superconductor by reshaping the singularities in the spectral quantities [3]. We can hence use $\tau_{\rm orb}^{-1}$ instead of Γ to cut the divergence and see that for very large phase gradients, μ_z becomes independent of $\partial_x\varphi$.

According to Eq. (16) the difference in the quantity $N_\sigma^2 j_s^\sigma/(D_L^\sigma R_T^\sigma)$ for spin-up and -down species describes the charge-spin conversion. We find that the charge imbalance in each spin subband is proportional to the energy integral of N_σ^2/R_T^σ. The charge in each subband is then converted to spin at a rate $\propto j_s^\sigma/D_L^\sigma$. The temperature and exchange field dependence of μ_z are given in Figs. 3(c) and 3(d), respectively. We can see that the linear response $\mu_z \to 0$ as $T \to 0$, which reflects the freezing out of the quasiparticle population [Fig. 3(c)]. However, this can be circumvented by considering the response at $V_{\rm inj} \sim \Delta$, as shown below. At the superconducting critical temperature T_c, the ratio μ_z/I_s diverges similarly to the supercurrent-induced charge imbalance in the presence of a temperature gradient [7,8]. Since T_c is lower for a higher exchange field, this divergence happens at a lower temperature in a higher exchange field. For a fixed temperature, the divergence of μ_z also happens at a critical exchange field [Fig. 3(d)] where superconductivity is suppressed [38,39].

B. Effect of spin relaxation

Spin-flip and spin-orbit relaxation affect both spectral and nonequilibrium properties of the superconductor. For the

spectral properties, spin-flip relaxation breaks the time-reversal symmetry and suppresses the superconducting pair potential and critical temperature, while spin-orbit scattering reduces the effect of the exchange field without suppressing the pair potential [3]. Both spin-flip and spin-orbit scattering also lead to the relaxation of f_{T3} [$S_{T3/L3}$ terms in Eq. (6)]. For strong spin relaxation, the contribution to μ_z thus results only from f_L and decays only via inelastic scattering. In this case (see details in Appendix C)

$$\mu_z = \xi_0 \partial_x \varphi_0 \frac{G_{\rm inj}}{G_{\xi_0}} \int_0^\infty d\epsilon n_-(\epsilon; V_{\rm inj}) \frac{(N_\uparrow^2 - N_\downarrow^2) j_E}{4 R_T D_L} u_1(x). \tag{17}$$

Here the linear function $u_1(x) = -u_1(-x) \approx u_0(x)$ for $|x| > \lambda_{\rm cr}$. However, the effects of spin-flip/spin-orbit scattering on the spectral functions also affect the resulting μ_z. The effect depends strongly on the type of scattering.

For pure spin-flip relaxation, contribution of f_L increases as a function of the spin-relaxation rate and diverges when the strong relaxation completely kills superconductivity. This can be seen in the relaxation rate dependence of μ_z in the linear-response regime in Fig. 3(b). For pure spin-orbit relaxation, the effect of the exchange field is suppressed, and thereby so is the charge-spin conversion.

V. SPIN ACCUMULATION AND NONLOCAL CONDUCTANCE

The charge-spin conversion can be detected by inspecting the nonlocal conductance $g_{\rm nl} = dI_{\rm det}/dV_{\rm inj}$ in the presence of the supercurrent I_s driven across the wire. Without supercurrent, this quantity was measured in Refs. [25–27]. We show an example of $g_{\rm nl}$ in Figs. 4(c) and 4(d). We separate it into different symmetry components vs $V_{\rm inj}$ and $P_{\rm det}$ as

$$g_{\rm nl} = g_{\rm ee} + g_{\rm eo} + (g_{\rm oe} + g_{\rm oo}) P_{\rm det}, \tag{18}$$

where $g_{\alpha e/o}(V_{\rm inj}) = \pm g_{\alpha e/o}(-V_{\rm inj})$ and $\alpha = e/o$ describe the symmetry vs $P_{\rm det}$. Since the derivative of the detector current with respect to $V_{\rm inj}$ flips the parity of the terms, the conductance due to the pure charge imbalance is even in both $V_{\rm inj}$ and $P_{\rm det}$ and hence is described by $g_{\rm ee}$. The term $g_{\rm oo} = g_{\rm heat}$ is the long-range spin accumulation due to the heat injection [4,5]. The supercurrent induces the term $g_{\rm eo}$ that describes the conversion of temperature gradients to charge [6–8], whereas $g_{\rm oe} = g_{\rm super}$ results from the supercurrent-induced charge-spin conversion. The symmetry of $g_{\rm super}$ results from the fact that it is related to spin imbalance (and therefore antisymmetric in $P_{\rm det}$) and originates from induced charge imbalance. In normal-metal spin injection experiments [40] only the term $g_{\rm oe}$ is nonzero, but it requires nonzero spin polarization $P_{\rm inj}$ of the injector. Here $P_{\rm inj} = 0$.

The term $g_{\rm super}$ should be compared to the contribution determined by effective heating [4] (14),

$$g_{\rm heat} = \frac{G_{\rm inj}}{G_{\xi_0}} \frac{L}{2\xi_0} u_3(x) \int_0^\infty d\epsilon \frac{\partial n_+}{\partial V_{\rm inj}} \frac{N_\uparrow^2 - N_\downarrow^2}{D_L}, \tag{19}$$

where $u_3(x) = u_3(-x)$ is a function that changes linearly from unity at the injector to zero at the reservoirs and $n_+ = (n_0(\epsilon + eV) + n_0(\epsilon - eV) - 2n_0)/2$. For $T \to 0$, $\partial n_\pm/\partial V_{\rm inj}$ approaches a δ function at $\epsilon = \pm eV$, and we can estimate the integrals by the values of the kinetic coefficients at those energies. For $eV \approx \Delta \pm h$ where the main signal resides, $g_{\rm super} \approx 2\xi_0 g_{\rm heat}/L$ for $\xi_0 \nabla\varphi \approx \tau_{\rm orb}^{-1}\Delta + \tau_{\rm sf}^{-1} + \tau_{\rm so}^{-1}$, i.e., when the supercurrent starts affecting the density of states. At higher temperatures and lower voltages $eV \lesssim k_B T$, where quasiparticle effects are visible even at linear response, $g_{\rm super}$ can dominate over $g_{\rm heat}$.

VI. CONCLUSION

In conclusion, we have shown how the nonequilibrium supercurrent in a spin-split superconductor can partially convert charge imbalance to spin imbalance. The resulting spin imbalance is long range, decaying only due to inelastic scattering. Here we have concentrated on a setup with collinear magnetizations. We expect that the generalization of our theory to the case with inhomogeneous magnetization would shed light on the possible coherently controllable nonequilibrium spin torques. We also expect to find analogous effects in superconducting proximity structures in the presence of spin splitting, i.e., combining the phenomena discussed in Refs. [41,42].

ACKNOWLEDGMENTS

We thank M. Houzet and M. Aprili for the question that started this project and T. Hyart and C. Quay for illuminating discussions. This work was supported by the Academy of Finland Center of Excellence (Project No. 284594), Research Fellow (Project No. 297439), and Key Funding (Project No. 305256) programs.

APPENDIX A: SELF-CONSISTENCY EQUATION FOR Δ

The pair potential Δ should be obtained self-consistently from

$$\Delta = \frac{\lambda}{16} \int_{-\Omega_D}^{\Omega_D} d\epsilon \, {\rm Tr}[(\tau_1 - i\tau_2)\hat{g}^K(\epsilon)], \tag{A1}$$

where λ is the coupling constant and Ω_D is the Debye cutoff energy. In the presence of both spin splitting and nonequilibrium distribution functions, this goes to the form [3]

$$\Delta = \frac{\lambda}{2} \int_{-\Omega_D}^{\Omega_D} d\varepsilon \big[{\rm Im} g_{01}^R f_L + {\rm Im} g_{31}^R f_{T3} + i\big({\rm Re} g_{01}^R f_T + {\rm Re} g_{31}^R f_{L3}\big)\big], \tag{A2}$$

where g_{ij}^R is the part of the retarded Green's function proportional to $\sigma_i \tau_j$. The results obtained in the main text use the self-consistent equilibrium gap but do not include the nonequilibrium corrections. For the gap amplitude $|\Delta|$ this approximation is justified in the case of low injection conductance $G_{\rm inj}$. However, with such a choice the charge current is, strictly speaking, not conserved in the presence of a constant phase gradient. This is because the quasiparticle injection modifies the phase of Δ [the last two terms in Eq. (A2)], and the true phase gradient corresponding to a constant charge current becomes position dependent. Such an effect is of a higher order in the phase gradient and within a perturbation approach can therefore be disregarded. We leave such higher-order effects for further work.

APPENDIX B: KINETIC COEFFICIENTS

The Green's function in Eq. (2) satisfies the normalization condition $\check{g}^2 = 1$, which allows us to parametrize the Keldysh Green's function as $\check{g}^K = \check{g}^R\check{f} - \check{f}\check{g}^A$, where the distribution matrix $\check{f} = f_L + f_T\tau_3 + f_{T3}\sigma_3 + f_{L3}\sigma_3\tau_3$. We also can parametrize the retarded Green's function as $\check{g}^R = g_{01}\tau_1 + g_{02}\tau_2 + g_{03}\tau_3 + g_{31}\sigma_3\tau_1 + g_{32}\sigma_3\tau_2 + g_{33}\sigma_3\tau_3$, and $\check{g}^A = -\tau_3\check{g}^{R\dagger}\tau_3$. Here g_i are complex scalar functions. From these, we identify $N_+ = \mathrm{Re}(g_{03})$ and $N_- = \mathrm{Re}(g_{33})$.

The kinetic coefficients D_i, R_i, and S_i in Eqs. (3) and (4) can be expressed in terms of the parameterized functions $\check{g}^R$ and $\check{g}^A$. D_i are

$$\begin{aligned}
D_L &= \frac{D}{2}(1 - |g_{01}|^2 - |g_{02}|^2 + |g_{03}|^2 - |g_{31}|^2 \\
&\quad - |g_{32}|^2 + |g_{33}|^2), \\
D_{T3} &= -D[\mathrm{Re}(g_{01}g_{31}^*) + \mathrm{Re}(g_{02}g_{32}^*) - \mathrm{Re}(g_{03}g_{33}^*)], \\
D_T &= \frac{D}{2}(1 + |g_{01}|^2 + |g_{02}|^2 + |g_{03}|^2 + |g_{31}|^2 \\
&\quad + |g_{32}|^2 + |g_{33}|^2), \\
D_{L3} &= D[\mathrm{Re}(g_{01}g_{31}^*) + \mathrm{Re}(g_{02}g_{32}^*) + \mathrm{Re}(g_{03}g_{33}^*)].
\end{aligned}$$

R_i are

$$\begin{aligned}
R_T &= \mathrm{Re}(g_{01})\Delta\cos\varphi - \mathrm{Re}(g_{02})\Delta\sin\varphi, \\
R_{L3} &= \mathrm{Re}(g_{31})\Delta\cos\varphi - \mathrm{Re}(g_{32})\Delta\sin\varphi.
\end{aligned}$$

S_i are

$$\begin{aligned}
S_{L3} &= \tau_{\mathrm{sn}}^{-1}\{\mathrm{Re}(g_{03})^2 - \mathrm{Re}(g_{33})^2 \\
&\quad + \beta[\mathrm{Im}(g_{01})^2 - \mathrm{Im}(g_{31})^2 + \mathrm{Im}(g_{02})^2 - \mathrm{Im}(g_{32})^2]\}, \\
S_{T3} &= \tau_{\mathrm{sn}}^{-1}\{\mathrm{Re}(g_{03})^2 - \mathrm{Re}(g_{33})^2 \\
&\quad + \beta[\mathrm{Re}(g_{31})^2 - \mathrm{Re}(g_{01})^2 + \mathrm{Re}(g_{32})^2 - \mathrm{Re}(g_{02})^2]\},
\end{aligned}$$

where $\tau_{\mathrm{sn}}^{-1} = \tau_{\mathrm{so}}^{-1} + \tau_{\mathrm{sf}}^{-1}$ and the parameter $\beta = (\tau_{\mathrm{so}} - \tau_{\mathrm{sf}})/(\tau_{\mathrm{so}} + \tau_{\mathrm{sf}})$ describes the relative strength of the spin-orbit and spin-flip scattering. For $\beta > 0$, spin-flip scattering dominates the spin-orbit scattering and vice versa for $\beta < 0$. These coefficients are independent of φ (the dependence of φ in R_i terms is canceled by the corresponding terms in g_i).

There are also two more coefficients in Eqs. (3) and (4), spectral supercurrent and spectral spin supercurrent, which depend on the phase gradient $\partial_x\varphi$:

$$\begin{aligned}
j_E\partial_x\varphi &= \tfrac{1}{8}D\,\mathrm{Tr}[(\check{g}^R\partial_x\check{g}^R - \check{g}^A\partial_x\check{g}^A)\tau_3], \\
j_{Es}\partial_x\varphi &= \tfrac{1}{8}D\,\mathrm{Tr}[(\check{g}^R\partial_x\check{g}^R - \check{g}^A\partial_x\check{g}^A)\sigma_3\tau_3].
\end{aligned}$$

These two terms are related to the nonzero charge supercurrrent and spin-energy current. Here and below we assume that the wire is in the x direction and all changes in the phase φ and the distribution functions take place in that direction.

APPENDIX C: PERTURBATION THEORY SOLUTIONS OF KINETIC EQUATIONS IN THE LINEAR ORDER BY $\xi_0\nabla\varphi$

The general solution of the kinetic equations in Eq. (3) can be written as

$$\begin{aligned}
&(f_L, f_{T3}, f_T, f_{L3})^T \\
&= (C_{01} + C_{02}x)\mathbf{v}_0^T + C_1e^{k_Lx}\mathbf{v}_1^T + C_2e^{-k_Lx}\mathbf{v}_2^T + C_3e^{k_{T1}x}\mathbf{v}_3^T \\
&\quad + C_4e^{-k_{T1}x}\mathbf{v}_4^T + C_5e^{k_{T2}x}\mathbf{v}_5^T + C_6e^{-k_{T2}x}\mathbf{v}_6^T,
\end{aligned} \tag{C1}$$

where $\mathbf{v}_0^T = (1,0,0,0)^T$; k_L, k_{T1}, and k_{T2} are the energy-dependent inverse length scales; the other $\mathbf{v}_i^T$ can be determined numerically; and C_i can be determined from the boundary conditions (10). For a small phase gradient, we can determine these coefficients analytically. Below we concentrate in particular on the solutions of the modes related to the supercurrent-induced spin imbalance and treat the supercurrent as a perturbation in the kinetic equations. At zeroth order Eq. (3) decouples into two sets of kinetic equations. First, we concentrate on the part that is odd in the injection voltage, describing charge imbalance. In this case, for a vanishing supercurrent the relevant distribution function components are f_T and f_{L3}. We denote their values in the absence of supercurrent by f_T^0 and f_{L3}^0. On the other hand, the supercurrent couples them to the other two functions f_L and f_{T3} and induces the change δf_L and δf_{T3}, which we calculate to linear order in the phase gradient. For f_T and f_{L3}, we get the first set of kinetic equations,

$$\begin{pmatrix} D_T & D_{L3} \\ D_{L3} & D_T \end{pmatrix}\begin{pmatrix} \partial_x^2 f_T^0 \\ \partial_x^2 f_{L3}^0 \end{pmatrix} = \begin{pmatrix} R_T & R_{L3} \\ R_{L3} & R_T + S_{L3} \end{pmatrix}\begin{pmatrix} f_T^0 \\ f_{L3}^0 \end{pmatrix}. \tag{C2}$$

In what follows, we choose Δ_0 to be the reference energy scale, and therefore the coherence length $\xi_0 = \sqrt{\hbar D/\Delta_0}$ becomes the reference length scale. That means, for example, that the dimensionless quantities describing spin relaxation are of the form $\tau_{\mathrm{sf}}\Delta_0$ and $\tau_{\mathrm{so}}\Delta_0$.

Using the boundary conditions (10), we obtain for $\kappa_I L \ll 1$

$$\begin{pmatrix} f_T^0 \\ f_{L3}^0 \end{pmatrix} = \kappa_I\xi_0 n_-(\epsilon, V_{\mathrm{inj}})\sum_{i=1,2} A_i e^{-k_{Ti}x/\xi_0}\begin{pmatrix} k_{Ri} \\ -1 \end{pmatrix}, \quad 0 \leqslant x \leqslant \frac{L}{2}, \tag{C3}$$

where the inverse length scales

$$k_{T1/2}^2 = \frac{D_T(2R_T - S_{L3}) - 2D_{L3}R_{L3} \pm \sqrt{4(D_TR_{L3} - D_{L3}R_T)^2 + 4D_{L3}(-D_TR_{L3} + D_{L3}R_T)S_{L3} + D_T^2S_{L3}^2}}{2\left(D_T^2 - D_{L3}^2\right)},$$

and the coefficients

$$A_i = \frac{\left[N_-\left(D_{L3} - D_Tk_{Ri'}\right) - N_+\left(D_T - D_{L3}k_{Ri'}\right)\right]}{4\left(D_{L3}^2 - D_T^2\right)\left(k_{Ri} - k_{Ri'}\right)k_{Ti}},$$

$$k_{R1/2} = \frac{D_T S_{L3} \mp \sqrt{4D_{L3}^2 R_T(R_T + S_{L3}) - 4D_{L3} D_T R_{L3}(2R_T + S_{L3}) + D_T^2\left(4R_{L3}^2 + S_{L3}^2\right)}}{2(D_T R_{L3} - D_{L3} R_T)}.$$

For the perturbed terms of f_L and f_{T3}, we get another set of kinetic equations,

$$\begin{pmatrix} D_L & D_{T3} \\ D_{T3} & D_L \end{pmatrix}\begin{pmatrix} \partial_x^2 \delta f_L \\ \partial_x^2 \delta f_{T3} \end{pmatrix} + \begin{pmatrix} j_E \partial_x \varphi & j_{Es} \partial_x \varphi \\ j_{Es} \partial_x \varphi & j_E \partial_x \varphi \end{pmatrix}\begin{pmatrix} \partial_x f_T^0 \\ \partial_x f_{L3}^0 \end{pmatrix} = \begin{pmatrix} 0 & 0 \\ 0 & S_{T3} \end{pmatrix}\begin{pmatrix} \partial_x^2 \delta f_L \\ \partial_x^2 \delta f_{T3} \end{pmatrix}. \tag{C4}$$

Using the solution in Eq. (C3), we obtain

$$\begin{aligned}\begin{pmatrix} \delta f_L \\ \delta f_{T3} \end{pmatrix} = \kappa_I \xi_0^2 \partial_x \varphi n_-(\epsilon, V_{\rm inj}) \sum_{i=1,2} \Bigg[& \frac{\alpha_i}{k_L^2 - k_{Ti}^2}\left(e^{-k_{Ti}x/\xi_0} - e^{-k_L x/\xi_0}\right)\begin{pmatrix} -D_{T3}/D_L \\ 1 \end{pmatrix} \\ & + \frac{\beta_i}{k_{Ti}^2}\left(\frac{2x}{L} - 1 + e^{-k_{Ti}x/\xi_0}\right)\begin{pmatrix} 1 \\ 0 \end{pmatrix}\Bigg], \quad 0 \leqslant x \leqslant \frac{L}{2},\end{aligned} \tag{C5}$$

where the inverse length scale

$$k_L^2 = \frac{S_{T3} D_L}{D_L^2 - D_{T3}^2}$$

and the coefficients

$$\alpha_i = \frac{[j_{Es}(D_{T3} + D_L k_{Ri}) - j_E(D_L + D_{T3} k_{Ri})][N_-(D_{L3} - D_T k_{Ri'}) - N_+(D_T - D_{L3} k_{Ri'})]}{2\left(D_T^2 - D_{L3}^2\right)\left(D_L^2 - D_{T3}^2\right)(k_{Ri} - k_{Ri'})},$$

$$\beta_i = \frac{(j_E k_{Ri} - j_{Es})[N_+(D_T - D_{L3} k_{Ri'}) - N_-(D_{L3} - D_T k_{Ri'})]}{2D_L\left(D_T^2 - D_{L3}^2\right)(k_{Ri} - k_{Ri'})}.$$

The spin accumulation generated from the supercurrent is

$$\begin{aligned}\mu_z &= \frac{1}{2}\int_0^\infty d\epsilon (N_+ \delta f_{T3} + N_- \delta f_L) \\ &= \frac{1}{2}\kappa_I \xi_0^2 \partial_x \varphi \int_0^\infty d\epsilon\, n_-(\epsilon, V_{\rm inj}) \sum_{i=1,2} \Bigg[\left(N_+ - N_- \frac{D_{T3}}{D_L}\right)\frac{\alpha_i}{k_L^2 - k_{Ti}^2}\left(e^{-k_{Ti}x/\xi_0} - e^{-k_L x/\xi_0}\right) \\ &\quad + N_- \frac{\beta_i}{k_{Ti}^2}\left(\frac{2x}{L} - 1 + e^{-k_{Ti}x/\xi_0}\right)\Bigg], \quad 0 \leqslant x \leqslant \frac{L}{2}.\end{aligned} \tag{C6}$$

In the extreme limit of $\tau_{\rm sn}^{-1} \to 0$, this result can be reduced to a simpler form. In this case, S_{T3} and S_{L3} terms in the kinetic equations are zero; therefore the $e^{-k_L x/\xi_0}$ term is replaced by a linear term with the same coefficients with δf_L. For the linear-response regime $n_-(\epsilon, V_{\rm inj}) = V_{\rm inj} \partial n_0/\partial\epsilon$, we get

$$\begin{aligned}\mu_z = V_{\rm inj} \kappa_I \xi_0^2 \partial_x \varphi \int_0^\infty d\epsilon \frac{\partial n_0}{\partial \epsilon} \Bigg[& \frac{N_\uparrow^2 j_s^\uparrow}{4 D_L^\uparrow R_T^\uparrow}\left(\frac{2x}{L} - 1 + e^{-\sqrt{R_T^\uparrow/D_T^\uparrow}x/\xi_0}\right) \\ & - \frac{N_\downarrow^2 j_s^\downarrow}{4 D_L^\downarrow R_T^\downarrow}\left(\frac{2x}{L} - 1 + e^{-\sqrt{R_T^\downarrow/D_T^\downarrow}x/\xi_0}\right)\Bigg], \quad 0 \leqslant x \leqslant \frac{L}{2},\end{aligned} \tag{C7}$$

where the $\uparrow$ and $\downarrow$ quantities are the addition and subtraction of the singlet and triplet components of the spectral quantities, $j_s^{\uparrow/\downarrow} = j_E \pm j_{Es}$, $N_{\uparrow/\downarrow} = N_+ \pm N_-$, $D_L^{\uparrow/\downarrow} = D_L \pm D_{T3}$, and $R_{\uparrow/\downarrow} = R_T \pm R_{L3}$.

It is straightforward to see that $\mu_z = 0$ for $h = 0$ since the quantity $N^2 j_s/(D_L R_T)$ is equal for both spin species. For nonzero h the difference in this quantity for different spin species gives the spin accumulation. However, without relaxation, this quantity is proportional to $1/\sqrt{\Gamma}$, which describes the broadening of the spectral quantities.

In practice, the relevant broadening renormalizing μ_z comes from the orbital effect due to either a magnetic field or

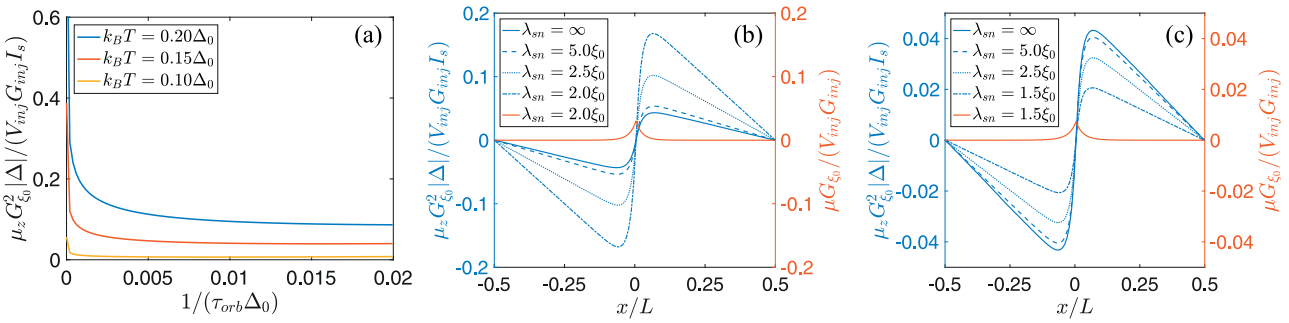

FIG. 5. Spin accumulation with and without relaxation in the linear-response regime. (a) The dependence on orbital depairing rate in the case without spin relaxation. Position dependence in the case of (b) pure spin-flip relaxation and (c) pure spin-orbit relaxation. An exchange field $h = 0.3\Delta_0$ is the same for all panels, and a temperature $T = 0.15\Delta_0$ is used in (b) and (c). The red curves describe the charge imbalance. The spin-relaxation length is defined as $\lambda_{sn} = \sqrt{\tau_{sn} D}$.

the phase gradient itself [35–37] or due to terms contributing to the spin relaxation [3]. The two first effects can be described by an orbital relaxation rate $\tau_{orb}^{-1} = (\xi_0 \partial_x \varphi)^2/2 + (De^2B^2d^2/6)$ [37], where B is the magnetic field and d is the film thickness. In the presence of spin relaxation described by the rate τ_{sn}^{-1}, an estimate for the overall broadening comes from $\Gamma \mapsto \tau_{orb}^{-1} + \tau_{sn}^{-1}$, but the exact amount depends on the relaxation mechanism and the size of the exchange field. As an example, we show the supercurrent-induced μ_z vs τ_{orb}^{-1} in Fig. 5(a). Since $\mu_z \propto (\xi_0 \partial_x \varphi)\Gamma^{-1/2}$, for large phase gradients satisfying $\xi_0 \partial_x \varphi \gg \sqrt{De^2B^2d^2/6 + \tau_{sn}^{-1}}$, the spin accumulation becomes independent of $\partial_x \varphi$.

However, spin relaxation also affects the decay of the nonequilibrium components of the distribution function via the relaxation terms $\sim S_{T/L3}$. In another extreme limit $\tau_{sn} \to \infty$, we can also have a simpler form of Eq. (C7). In this case $4D_{L3}(D_T R_{L3} - D_{L3} R_T)/D_T^2 \ll S_{L3}$, and

$$\mu_z = V_{inj} \kappa_I \xi_0^2 \partial_x \varphi \int_0^\infty d\epsilon \frac{\partial n_0}{\partial \epsilon} \frac{(N_\uparrow^2 - N_\downarrow^2) j_E}{4 R_T D_L} \times \left(\frac{2x}{L} - 1 + 2e^{-k_{T2} x/\xi_0} - e^{-k_L x/\xi_0} \right), \quad 0 \leqslant x \leqslant \frac{L}{2}. \tag{C8}$$

Here, except for the density of states, the triplet component of other spectral quantities do not contribute to the spin accumulation. The difference in the density of states for two spin species behaves differently for spin-orbit and spin-flip relaxations. Spin-orbit relaxation does not affect the pair potential but tries to lift the effect of the spin-splitting field. Therefore μ_z approaches zero for very strong relaxation [Fig. 5(c)]. In the case of spin-flip relaxation, it suppresses the pair potential; therefore spin accumulation diverges [Fig. 5(b)].

[1] M. Tinkham, *Introduction to Superconductivity* (Dover Publications, Mineola, New York, 2004).
[2] A. Schmid and G. Schön, J. Low Temp. Phys. **20**, 207 (1975).
[3] F. S. Bergeret, M. Silaev, P. Virtanen, and T. T. Heikkilä, Rev. Mod. Phys. (to be published), arXiv:1706.08245.
[4] M. Silaev, P. Virtanen, F. S. Bergeret, and T. T. Heikkilä, Phys. Rev. Lett. **114**, 167002 (2015).
[5] I. V. Bobkova and A. M. Bobkov, JETP Lett. **101**, 118 (2015).
[6] A. Schmid and G. Schön, Phys. Rev. Lett. **43**, 793 (1979).
[7] J. Clarke, B. R. Fjordbøge, and P. E. Lindelof, Phys. Rev. Lett. **43**, 642 (1979).
[8] C. Pethick and H. Smith, J. Phys. C **13**, 6313 (1980).
[9] C. J. Pethick and H. Smith, Phys. Rev. Lett. **43**, 640 (1979).
[10] V. M. Edelstein, Phys. Rev. Lett. **75**, 2004 (1995).
[11] V. M. Edelstein, Phys. Rev. B **67**, 020505 (2003).
[12] V. M. Edelstein, Phys. Rev. B **72**, 172501 (2005).
[13] V. Edel'shtein, Zh. Eksp. Teor. Fiz. **95**, 2151 (1989) [Sov. Phys. JETP **68**, 1244 (1989)].
[14] M. Houzet and J. S. Meyer, Phys. Rev. B **92**, 014509 (2015).
[15] K. V. Samokhin, Phys. Rev. B **70**, 104521 (2004).
[16] O. Dimitrova and M. V. Feigel'man, Phys. Rev. B **76**, 014522 (2007).
[17] A. Buzdin, Phys. Rev. Lett. **101**, 107005 (2008).
[18] F. Konschelle, I. V. Tokatly, and F. S. Bergeret, Phys. Rev. B **92**, 125443 (2015).
[19] I. V. Bobkova, A. M. Bobkov, A. A. Zyuzin, and M. Alidoust, Phys. Rev. B **94**, 134506 (2016).
[20] I. V. Bobkova and A. M. Bobkov, Phys. Rev. B **95**, 184518 (2017).
[21] D. B. Szombati, S. Nadj-Perge, D. Car, S. R. Plissard, E. P. A. M. Bakkers, and L. P. Kouwenhoven, Nat. Phys. **12**, 568 (2016).
[22] A. Assouline, C. Feuillet-Palma, N. Bergeal, T. Zhang, A. Mottaghizadeh, A. Zimmers, E. Lhuillier, M. Marangolo, M. Eddrief, P. Atkinson *et al.*, arXiv:1806.01406.
[23] A. Murani, A. Kasumov, S. Sengupta, Y. A. Kasumov, V. T. Volkov, I. I. Khodos, F. Brisset, R. Delagrange, A. Chepelianskii, R. Deblock, H. Bouchiat, and S. Guéron, Nat. Commun. **8**, 15941 (2017).
[24] Y. K. Kato, R. C. Myers, A. C. Gossard, and D. D. Awschalom, Phys. Rev. Lett. **93**, 176601 (2004).
[25] C. Quay, D. Chevallier, C. Bena, and M. Aprili, Nat. Phys. **9**, 84 (2013).
[26] F. Hübler, M. J. Wolf, D. Beckmann, and H. v. Löhneysen, Phys. Rev. Lett. **109**, 207001 (2012).
[27] M. J. Wolf, F. Hübler, S. Kolenda, H. v. Löhneysen, and D. Beckmann, Phys. Rev. B **87**, 024517 (2013).

[28] F. S. Bergeret, A. Volkov, and K. Efetov, Rev. Mod. Phys. **77**, 1321 (2005).
[29] T. T. Heikkilä, J. Särkkä, and F. K. Wilhelm, Phys. Rev. B **66**, 184513 (2002).
[30] M. Y. Kuprianov and V. Lukichev, Zh. Eksp. Teor. Fiz. **94**, 139 (1988) [Sov. Phys. JETP **67**, 1163 (1988)].
[31] F. S. Bergeret, A. Verso, and A. F. Volkov, Phys. Rev. B **86**, 214516 (2012).
[32] M. Tinkham and J. Clarke, Phys. Rev. Lett. **28**, 1366 (1972).
[33] F. Hübler, J. C. Lemyre, D. Beckmann, and H. v. Löhneysen, Phys. Rev. B **81**, 184524 (2010).
[34] R. C. Dynes, J. P. Garno, G. B. Hertel, and T. P. Orlando, Phys. Rev. Lett. **53**, 2437 (1984).
[35] P. G. de Gennes, *Superconductivity of Metals and Alloys*, Advanced Book Classics (Perseus, Cambridge, MA, 1999).
[36] W. Belzig, C. Bruder, and G. Schön, Phys. Rev. B **54**, 9443 (1996).
[37] A. Anthore, H. Pothier, and D. Esteve, Phys. Rev. Lett. **90**, 127001 (2003).
[38] B. S. Chandrasekhar, Appl. Phys. Lett. **1**, 7 (1962).
[39] A. M. Clogston, Phys. Rev. Lett. **9**, 266 (1962).
[40] F. J. Jedema, A. Filip, and B. Van Wees, Nature (London) **410**, 345 (2001).
[41] P. Virtanen and T. T. Heikkilä, Phys. Rev. Lett. **92**, 177004 (2004).
[42] P. Machon, M. Eschrig, and W. Belzig, Phys. Rev. Lett. **110**, 047002 (2013).

IV

SUPERCONDUCTIVITY NEAR A MAGNETIC DOMAIN WALL

by

Faluke Aikebaier, P. Virtanen & T. T. Heikkilä 2018

Phys. Rev. B 99, 104504 (2019)

DOI: http://doi.org/10.1103/PhysRevB.99.104504

Superconductivity near a magnetic domain wall

Faluke Aikebaier,[1,*] P. Virtanen,[2] and Tero Heikkilä[1]

[1]*Department of Physics and Nanoscience Center, University of Jyväskylä, P.O. Box 35 (YFL), FI-40014 University of Jyväskylä, Finland*

[2]*NEST, Istituto Nanoscienze-CNR and Scuola Normale Superiore, I-56127 Pisa, Italy*

(Received 20 December 2018; published 4 March 2019)

We study the equilibrium properties of a ferromagnetic insulator/superconductor structure near a magnetic domain wall. We show how the domain wall size is affected by the superconductivity in such structures. Moreover, we calculate several physical quantities altered due to the magnetic domain wall, such as the spin current density and local density of states, as well as the resulting tunneling conductance into a structure with a magnetic domain wall.

DOI: 10.1103/PhysRevB.99.104504

I. INTRODUCTION

One of the hallmarks of superconductivity is the Meissner effect, where a superconductor expels an external magnetic field from its interior [1]. Increasing the magnetic field, superconductivity gets suppressed and eventually destroyed by fields exceeding a critical field. However, the critical field of thin films in parallel magnetic field is greatly increased than that of the bulk superconductors, since the Meissner effect is negligibly small in this case [2]. Rather, the critical field is determined by the paramagnetic effect [3,4]. This effect suppresses superconductivity by aligning the electrons of Cooper pairs to be separated in energy. The magnetic field in this case then leads to a Zeeman effect.

One important consequence of the Zeeman field is the splitting of the density of states (DoS) in energy [5–9]. In the absence of the Zeeman field, the DoS of a superconductor shows a singularity at the energy which is equal to the superconducting pair potential. This singularity is separated by the Zeeman field for each spin species. The spin splitting can also be induced by making contact of a superconductor (S) with a ferromagnetic insulator (FI) [10–15]. In this case, the ferromagnetic insulator induces a strong exchange field with a small external magnetic field or even in its absence.

Various properties of superconductors with a spin-splitting density of states have been studied in recent years. An example is the strong thermoelectric effect with a thermopower predicted to exceed k_B/e and a possibility of obtaining large values of the figure of merit $ZT \gg 1$ at low temperatures [16–18]. Indications of this effect were also recently detected [19,20]. A spin accumulation in such a structure was detected at much longer distances than the relaxation lengths at the normal state [21–24]. Such effects are reviewed in Refs. [25,26].

In the above studies, the spin-splitting field induced in the superconductors is considered to be homogeneous. However, this is not always the case in a FI/S structure due to the nonuniformity of the ferromagnets. The nonuniformity can be described by a domain structure. Since the typical domain size in ferromagnets is much longer than the superconducting coherence length, the uniform magnetization is a good assumption in many cases. Here we relax this assumption and study the effects of inhomogeneity, especially domain walls.

The inhomogeneous exchange field also brings interesting effects to superconductivity. The existence of spin-singlet superconductivity in a magnetic domain wall in a ferromagnet (F) was studied several decades ago [27]. This effect also has been studied in S/F bilayers [28,29], where a superconducting material is placed on top of a ferromagnet with a domain structure. Decreasing the temperature, superconductivity first appears just above the domain wall. The experimental realization of such domain wall superconductivity was reported in Ref. [30]. The generation of a spin supercurrent in Josephson contacts with a domain wall is discussed in Ref. [31]. The reconstructed density of states at the end of the superconductor [32] and the magnetoelectric effects [33] in S/F bilayers with a magnetic texture were also studied recently. In the case of FI/S structures, a peculiar tunneling conductance was observed in a recent experiment and the magnetic domains in the ferromagnet were considered responsible for the experimental result [34].

Usually, the inhomogeneity of the exchange field induced by the ferromagnetic insulator in the superconductor can be represented by a multidomain structure, namely, alternating domains with opposite magnetization directions connected via domain walls. The theoretical model of the tunneling conductance in Ref. [34] concentrates on this case. Since the size of the domains is often much longer than the superconducting coherence length, whereas here we consider a single domain wall structure separating two domains with opposite magnetization directions. Moreover, the size of the domain wall in Ref. [34] was considered much smaller than the superconducting coherence length, here we also consider larger domain walls and study several physical quantities altered due to the inhomogeneity, such as the spin current density and the local density of states.

This paper is organized as follows. We introduce the FI/S structure containing a magnetic domain wall in Sec. II and solve the Usadel equation with an extended θ

*faluke.aikebaier@jyu.fi

parameterization. Equilibrium spin current density, as a direct consequence of the inhomogeneous exchange field, and its various properties are discussed in Sec. III. In Sec. IV we discuss the effect of superconductivity on the domain wall size, by considering the contribution of the superconducting free energy to the domain wall energy, and show that the maximal relative effect happens when the domain wall size is of the order of ξ_0, the superconducting coherence length (here defined at zero temperature and exchange field). For the possible measurement accessing this physics, we discuss the local density of states in Sec. V and the tunneling conductance across a nearby tunneling barrier in Sec. VI.

II. MODEL AND METHOD

A. Model

We study the properties of the structure in Fig. 1 in equilibrium. A superconducting wire is placed on top of a FI wire containing a magnetic domain wall. In many thin ferromagnets the domain wall structure energetically prefers a Néel type, in which the rotation of the magnetization happens in the plane of the domain wall. Therefore we consider a Néel domain wall with size λ. We make a variational ansatz and define the magnetization rotation angle as

$$\alpha(x) = \frac{\pi}{\lambda}\left(x+\frac{\lambda}{2}\right)\Theta\left(x+\frac{\lambda}{2}\right)\Theta\left(\frac{\lambda}{2}-x\right)+\pi\Theta\left(x-\frac{\lambda}{2}\right), \tag{1}$$

where Θ is the heaviside step function. The choice of $\alpha(x)$ in Eq. (1) as a linear function of x instead of the typically used hyperbolic functions that lead to a somewhat lower energy brings certain technical advantages. Its derivative is a constant inside the domain wall. This simplifies the Usadel equation, which describes the properties of the superconductor (see Sec. II B). The nonanalytic derivative of $\alpha(x)$ at the boundary of the domain wall can be transferred to the boundary conditions of the Usadel equation (see Sec. II C). Besides, the domain wall energy introduced by this choice of $\alpha(x)$ gives only slightly larger energy than the rotation angle constructed with hyperbolic functions (see Sec. IV).

The properties of a superconductor in the diffusive limit, namely, in the case when the elastic relaxation rate is much larger than any other energy scales in the problem, are described by the Usadel equation. In equilibrium, it is convenient to use the Usadel equation in the Matsubara representation ($\hbar = k_B = 1$)

$$D\nabla\cdot(\check{g}\nabla\check{g}) - [\omega_n\hat{\tau}_3 + i\boldsymbol{h}\cdot\boldsymbol{\sigma}\hat{\tau}_3 + \check{\Delta} + \check{\Sigma}, \check{g}] = 0, \tag{2}$$

where D is the diffusion constant, and $\check{g}$ is the quasiclassical Green's function satisfying the normalization condition $\check{g}^2 = \check{1}$. In the commutator, $\omega_n = (2n+1)\pi T$ is the Matsubara frequency, T is the temperature and n is an integer, $\boldsymbol{h}$ is the exchange field, $\boldsymbol{\sigma} = (\hat{\sigma}_1, \hat{\sigma}_2, \hat{\sigma}_3)$ is a vector of Pauli spin matrices, and $\check{\Delta} = \Delta\hat{\tau}_1$ is the superconducting pair potential. The self-energy $\check{\Sigma} = \check{\Sigma}_{so} + \check{\Sigma}_{sf}$, where $\check{\Sigma}_{so} = \boldsymbol{\sigma}\cdot\check{g}\boldsymbol{\sigma}/(8\tau_{so})$ and $\check{\Sigma}_{sf} = \boldsymbol{\sigma}\cdot\hat{\tau}_3\check{g}\hat{\tau}_3\boldsymbol{\sigma}/(8\tau_{sf})$ describe spin and charge imbalance relaxation due to the spin-orbit scattering and exchange interaction with magnetic impurities with corresponding relaxation times τ_{so} and τ_{sf}, and the Pauli matrices $\hat{\tau}_j(\hat{\sigma}_j)$ are in the Nambu (spin) space. We choose the Nambu spinor as

$$\Psi = (\psi_\uparrow(x) \quad \psi_\downarrow(x) \quad -\psi_\downarrow^\dagger(x) \quad \psi_\uparrow^\dagger(x))^\top,$$

where $\top$ denotes a transpose.

With the rotation angle described in Eq. (1), the exchange field can be written as

$$\boldsymbol{h} = h(\cos\alpha(x), 0, \sin\alpha(x)),$$

where h is the exchange field strength. With this choice, the exchange field depends only on x, and rotates in the xz plane, namely, $h_y = 0$ everywhere. Correspondingly, the gradient in Eq. (2) becomes a derivative in the x direction.

The Usadel equation we apply here is based on a lowest-order spherical harmonics expansion of the Green's function in terms of the momentum direction. Hence it cannot describe the domain wall superconductivity in a d-wave superconductor/ferromagnetic insulator multilayers [35]. The physics studied in Ref. [35] is hence outside the scope of the present work.

B. Rotation matrix

By introducing a position dependent rotation matrix, we can rotate the spin axis parallel to the local magnetization direction, so that the inhomogeneous exchange field in Eq. (2) can be treated as homogeneous. We define the rotation matrix as

$$\check{R} = e^{i\hat{\sigma}_2\alpha(x)/2},$$

where $\alpha(x)$ is the rotation angle in Eq. (1), and $\hat{\sigma}_2$ is the second Pauli matrix. Considering this rotation matrix, we define a new quasiclassical Green's function $\check{g}_0$

$$\check{g} = \check{R}^\dagger\check{g}_0\check{R}, \tag{3}$$

so that $\check{g}_0$ satisfies

$$D\check{\partial}_x^A\cdot\left(\check{g}_0\check{\partial}_x^A\check{g}_0\right) - [\omega_n\hat{\tau}_3 + ih\hat{\sigma}_3\hat{\tau}_3 + \check{\Delta} + \check{\Sigma}, \check{g}_0] = 0, \tag{4}$$

where

$$\check{\partial}_x^A X = \partial_x X - [A, X], \tag{5}$$

$$A = i\hat{\sigma}_2\alpha'(x)/2.$$

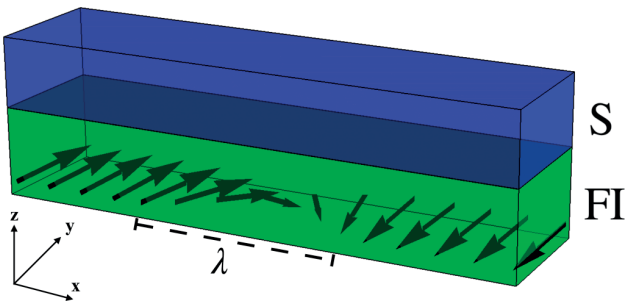

FIG. 1. Schematic view of the structure considered in this paper. A superconducting wire is placed on top of a FI wire containing a magnetic domain wall. The center of the domain wall is located at $x = 0$.

Thus the problem reduces to solving the Green's function $\check{g}_0$ for a homogeneous exchange field h, but with a redefined gradient with an SU(2) type vector potential A. Moreover, it is also straightforward to show that $\check{g}_0$ satisfies the normalization condition $\check{g}_0^2 = \check{g}^2 = \check{1}$.

The long derivative in Eq. (4) with the form in Eq. (5) introduces some extra terms with respect to the usual derivative and commutator terms in the Usadel equation. One of them is of the form

$$D[A, \check{g}_0 A \check{g}_0] = -\tfrac{1}{2}\alpha'(x)^2 D[\hat{\sigma}_2 \check{g}_0 \hat{\sigma}_2, \check{g}_0]. \tag{6}$$

This term has a similar form as the spin-orbit relaxation with a relaxation rate $\alpha'(x)^2 D/2$, but only in one spin direction. It is hence similar to the intrinsic (Rashba or Dresselhaus) spin-orbit coupling [36–38]. Since $\alpha'(x) \neq 0$ inside the domain wall, this term is a direct outcome of the existence of the inhomogeneous exchange field. In other words, inhomogeneous exchange field acts like a spin-orbit relaxation, reducing the effect of the exchange field without affecting the superconducting pair potential. This is shown on some physical quantities in the following sections.

C. Boundary condition

The long derivative $\partial_x^A g$ in the Usadel equation in Eq. (4) has to be continuous, so that a discontinuity in the derivative of $\alpha(x)$ implies a discontinuity in the derivative of $\check{g}$ at $x = \pm\lambda/2$. In order to describe this discontinuity, we integrate Eq. (4) at the boundary, obtaining

$$\check{g}_0 \partial_x \check{g}_0|_{x_b^\pm} - \check{g}_0 \partial_x \check{g}_0|_{x_b^\mp} = \tfrac{1}{2}\alpha'(x)[\check{g}_0 i\hat{\sigma}_2, \check{g}_0]|_{x_b^\pm}, \tag{7}$$

where $x_b = \pm\lambda/2$ and $\pm$ refers to the right and left side of the boundary. These boundary conditions together with the solutions in the case of a homogeneous exchange field far from the domain wall form the boundary conditions to the solutions of the Usadel equation in Eq. (4).

D. Parameterization

The quasiclassical Green's function $\check{g}$ and $\check{g}_0$ are 4×4 matrices in the Nambu $\otimes$ spin space. Since $\check{g}$ represents the Green's function for the inhomogeneous exchange field, we parametrize $\check{g}_0$ following the parametrization of the quasiclassical Green's function for inhomogeneous exchange field in Ref. [39],

$$\begin{aligned}\check{g}_0 = {} & \cos\theta\,\hat{\tau}_3(M_0 + i\tan\theta \boldsymbol{M}\cdot\boldsymbol{\sigma}) \\ & + \sin\theta\,\hat{\tau}_1(M_0 - i\cot\theta \boldsymbol{M}\cdot\boldsymbol{\sigma}).\end{aligned} \tag{8}$$

The advantage of using this parametrization is that θ and M_0 are real scalars and $\boldsymbol{M} = (M_1, M_2, M_3)$ is a real vector in the Matsubara representation. The normalization condition $\check{g}_0^2 = 1$ adds the constraint

$$M_0^2 - |\boldsymbol{M}|^2 = 1. \tag{9}$$

With the parametrization in Eq. (8), we get a set of differential equations from Eq. (4)

$$D\partial_x^2\theta + 2M_0(\Delta\cos\theta - \omega_n\sin\theta) - 2hM_3\cos\theta - \frac{1}{4\tau_{sf}}\left(2M_0^2 + 1\right)\sin(2\theta) = 0, \tag{10}$$

$$\begin{aligned}&D\left(\boldsymbol{M}\partial_x^2 M_0 - M_0\partial_x^2\boldsymbol{M}\right) + 2DM_0\alpha'(x)\begin{pmatrix}-\partial_x M_3\\ 0\\ \partial_x M_1\end{pmatrix} + DM_0\alpha'(x)^2\begin{pmatrix}M_1\\ 0\\ M_3\end{pmatrix} + 2\boldsymbol{M}(\Delta\sin\theta + \omega_n\cos\theta) \\ &- 2hM_0\sin\theta\begin{pmatrix}0\\ 0\\ 1\end{pmatrix} + \left[\frac{1}{\tau_{so}} + \frac{1}{2\tau_{sf}}\cos(2\theta)\right]M_0\boldsymbol{M} = 0.\end{aligned} \tag{11}$$

We can see directly from the vector differential equation (11) that the parameter M_2 does not have a source term from the domain wall structure, and therefore $M_2 = 0$ everywhere. Furthermore, one cannot directly solve these equations without the help of the constraint in Eq. (9). Therefore, it is more convenient to use this constraint to transform Eq. (11) to another set of differential equations for each of the components of M_i as in Ref. [40].

Taking the second derivative of the constraint in Eq. (9), we obtain

$$(\partial_x M_0)^2 - (\partial_x M_1)^2 - (\partial_x M_3)^2 + M_0\partial_x^2 M_0 - M_1\partial_x^2 M_1 - M_3\partial_x^2 M_3 = 0. \tag{12}$$

Substituting Eq. (12) to each component of Eq. (11) yields

$$\begin{aligned}&D\partial_x^2 M_j - 2\alpha'(x)DM_j(M_3\partial_x M_1 - M_1\partial_x M_3) + DM_j\sum_{k=0,1,3}(-1)^k(\partial_x M_k)^2 - \alpha'(x)^2 DM_j\left(M_1^2 + M_3^2\right) \\ &- 2M_jM_0(\omega_n\cos\theta + \Delta\sin\theta) + 2hM_jM_3\sin\theta - \left[\frac{1}{\tau_{so}} + \frac{1}{2\tau_{sf}}\cos(2\theta)\right]M_j\left(M_0^2 - \delta_{j0}\right) = S_j,\end{aligned} \tag{13}$$

where $j = 0, 1, 3$, and

$$S_j = \begin{cases} -2(\omega_n \cos\theta + \Delta \sin\theta) & j = 0 \\ -2\alpha'(x) D \partial_x M_3 + \alpha'(x)^2 D M_1 & j = 1 \\ 2\alpha'(x) D \partial_x M_1 + \alpha'(x)^2 D M_3 - 2h \sin\theta & j = 3 \end{cases}.$$

The differential equations in (10) and (13) have to be supplemented by the boundary conditions in Eq. (7) and the solutions at the regions far from the domain wall. With the parametrization in Eq. (8), Eq. (7) becomes

$$\begin{aligned} &\partial_x\theta|_{x_b^\pm} = \partial_x\theta|_{x_b^\mp} \\ &(M_i\partial_x M_0 - M_0\partial_x M_i)|_{x_b^\pm} - \alpha'(x) M_0 M_i'|_{x_b^\pm} \\ &\quad = (M_i\partial_x M_0 - M_0\partial_x M_i)|_{x_b^\mp}, \ i = 1, 3, \end{aligned} \tag{14}$$

where $M_{i'} = M_3$ for $i = 1$, and $M_{i'} = -M_1$ for $i = 3$.

E. Solutions of the Usadel equation

Without the exchange field $h = 0$, the solutions of the differential equations (10) and (13) give the regular results of the θ parametrization with $M_0 = 1$ and $M_i = 0$. In the case of a homogeneous exchange field $\boldsymbol{h} = h\hat{z}$, the values of θ and M_0 are changed, and $M_3 \neq 0$, due to the odd-frequency spin triplet superconductivity (with zero spin projection on the spin z axis) is induced. In the absence of spin relaxation terms

$$\begin{aligned} \tan\theta &= \frac{\sqrt{4\omega_n^2\Delta^2 + \left(h^2 + \omega_n^2 - \Delta^2\right)^2} - h^2 - \omega_n^2 + \Delta^2}{2\omega_n\Delta} \\ M_0 &= \frac{\omega_n + \Delta\tan\theta}{\sqrt{\omega_n^2 + (\Delta^2 - h^2)\tan^2\theta + 2\omega_n\Delta\tan\theta}} \\ M_3 &= \frac{h\tan\theta}{\sqrt{\omega_n^2 + (\Delta^2 - h^2)\tan^2\theta + 2\omega_n\Delta\tan\theta}} \\ M_1 &= 0. \end{aligned}$$

These results can be used to describe the solution of the differential equations far from the domain wall structure. For the inhomogeneous exchange field with a domain wall structure, however, the differential equations (10) and (13) cannot be solved analytically, but the numerical solutions are plotted in Fig. 2.

We can see that the domain wall structure brings certain changes to the homogeneous solutions. For θ, M_0, and M_3, the effect of the exchange field around the domain wall is reduced. This introduces a Gaussian functionlike structure for the solutions of these parameters as a function of position. At the center of the domain wall, the effect of the exchange field is reduced the most and the values of these parameters reach their homogeneous solutions gradually away from the domain wall. For a smaller domain wall, the reduction of the effect of the exchange field is more obvious, until for $\lambda \to 0$, the effect of the exchange field is completely lifted at the center of the domain wall. This is due to the existence of the spin-orbit relaxationlike term in Eq. (6) in the rotated Usadel equation with a relaxation rate $\alpha'(x)^2 D/2$ and $\alpha'(x) \propto \lambda^{-1}$.

The domain wall structure also introduces a nonzero solution of M_1 around the domain wall, due to the odd-frequency spin triplet superconductivity (with nonzero spin projection on the spin z axis) induced by the inhomogeneous exchange field. The maximum of M_1 appears at the boundary of the domain wall and gradually goes to zero away from it. It also changes sign at the two sides of the domain wall center. The amplitude of M_1 first increases and then decreases with increasing λ, the maximum taking place at $\lambda \approx 2\xi_0$.

Spin relaxation also brings many changes to the solutions of the differential equations. For the regions far from the domain wall, the consequence of spin relaxation is the same as with the case of homogeneous exchange field. The spin-orbit relaxation reduces the effect of the exchange field, therefore, the solutions in these regions approach the ones in the domain wall center. The spin-flip relaxation reduces the superconducting pair potential Δ, and therefore θ in these regions becomes smaller, and $M_{0/3}$ becomes larger with spin-flip relaxation. These can be seen from Figs. 3(a), 3(b) and 3(d).

For the regions around the domain wall, the spin relaxation brings minor changes. This is due to the fact that at the center of the domain wall, the effect of the exchange field is already reduced, and spin relaxation affects superconductivity similarly to the case without exchange field. This can be seen in Figs. 3(b) and 3(d). These behaviors can also be revealed in the physical quantities as discussed below.

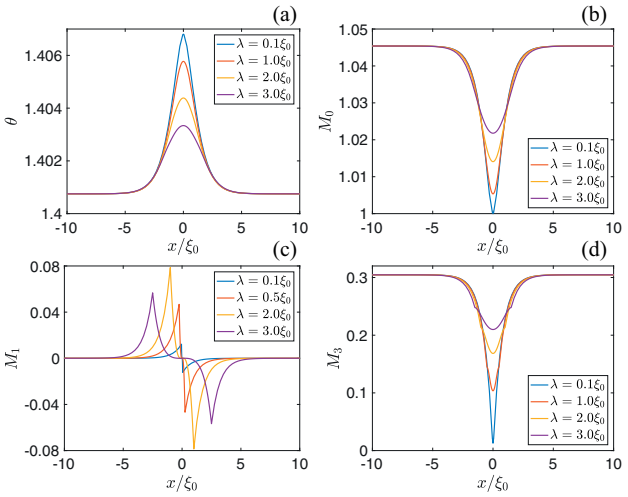

FIG. 2. Solutions of the differential equations in Eqs. (10) and (13) for different sizes of the domain wall. Here $\boldsymbol{h} = h(\cos\alpha(x), 0, \sin\alpha(x))$, $h = 0.3\Delta_0$, $\omega_n = \pi T$, $T = 0.05\Delta_0$, $\tau_{so/sf}^{-1} = 0$, Δ_0 is the superconducting pair potential at zero temperature and exchange field, and $\xi_0 = \sqrt{D/\Delta_0}$ is the superconducting coherence length.

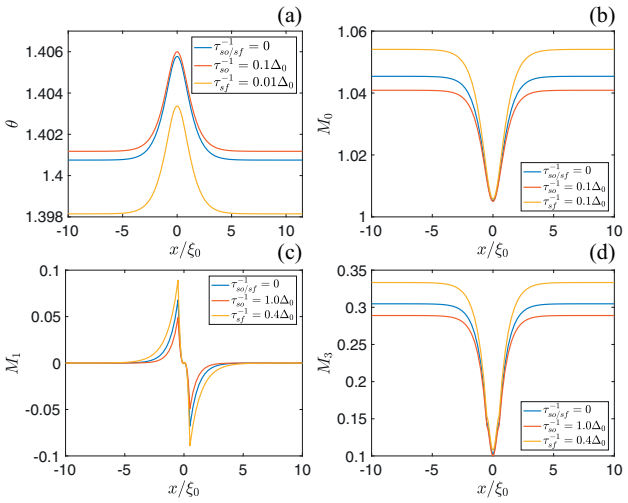

FIG. 3. Effect of spin relaxation on the solutions of the Usadel equation. Here $\boldsymbol{h} = h(\cos\alpha(x), 0, \sin\alpha(x))$, $h = 0.3\Delta_0$, $\omega_n = \pi T$, $T = 0.05\Delta_0$, and $\lambda = 1.0\xi_0$.

With these solutions, and using Eq. (3), the unrotated Green's function is

$$\begin{aligned}\check{g} = \cos\theta\hat{\tau}_3[M_0 + i\tan\theta\cos\alpha(x)\boldsymbol{M}\cdot\boldsymbol{\sigma} \\ + i\tan\theta\sin\alpha(x)(M_3\hat{\sigma}_1 - M_1\hat{\sigma}_3)] \\ + \sin\theta\hat{\tau}_1[M_0 - i\cot\theta\cos\alpha(x)\boldsymbol{M}\cdot\boldsymbol{\sigma} \\ - i\cot\theta\sin\alpha(x)(M_3\hat{\sigma}_1 - M_1\hat{\sigma}_3)].\end{aligned} \tag{15}$$

In the rest of the paper, we use this Green's function to calculate various physical quantities.

F. Self-consistent calculations

The superconducting pair potential in Eq. (4) has to be determined self-consistently. In the Matsubara representation, we have

$$\Delta = \frac{1}{2}\pi T\gamma\sum_{\omega_n>0}^{\omega_D}\mathrm{Tr}(\hat{\tau}_1\check{g}) = 2\pi T\gamma\sum_{\omega_n>0}^{\omega_D}M_0\sin\theta, \tag{16}$$

where $\check{g}$ is given by Eq. (15), γ is the coupling constant, and ω_D is the BCS cutoff energy. The latter gives a temperature dependent cutoff $N_D = \omega_D/(2\pi T)$ to the sum over n. Considering the relations

$$\begin{aligned}2\pi T\sum_{n=0}^{N_D(T)}\frac{1}{\omega_n} &= 2\pi T\left(\sum_{n=0}^{N_D(T_c)} + \sum_{N_D(T_c)}^{N_D(T)}\right)\frac{1}{\omega_n} \\ &= \frac{1}{\gamma} + \log\left(\frac{T_c}{T}\right)\end{aligned} \tag{17}$$

we can rewrite the self-consistency equation as

$$\Delta\log\left(\frac{T}{T_c}\right) = 2\pi T\sum_{\omega_n>0}\left(M_0\sin\theta - \frac{\Delta}{\omega_n}\right). \tag{18}$$

We can see that Δ does not explicitly depend on the rotation angle $\alpha(x)$. Its position dependence comes from the parameters M_0 and θ, whose solutions depend on $\alpha(x)$. This is because we only consider spin-singlet pairing in the self-consistent calculations.

The self-consistent pair potential in Eq. (18) is position dependent, $\Delta = \Delta(x)$. At the regions far from the domain wall, $\Delta(x = \pm\infty)$ is the same as in the case of homogeneous exchange field. A homogeneous exchange field brings many interesting effects on Δ. It suppresses Δ at a finite temperature and for $T \to 0$, $\Delta \to 0$ for a field $h > h_c$. Here $h_c = \Delta_0/\sqrt{2}$ when $T = 0$, called the Chandrasekhar-Clogston limit [3,4]. The superconducting pair potential is reduced by spin relaxation, and h_c is enhanced by the spin-orbit relaxation and suppressed by the spin-flip relaxation [25,26].

In the case of an inhomogeneous exchange field, the above properties are similar. However, in the domain wall region, the weak effect of the spin relaxation (Fig. 3) brings less changes to Δ, compared to the homogeneous case.

III. EQUILIBRIUM SPIN CURRENT DENSITY

One important consequence of the inhomogeneous exchange field is the equilibrium spin current density. Due to the inhomogeneity of the magnetization, the spin of the quasiparticles rotates following the local magnetization, which creates a flow of spin [41].

In the quasiclassical theory, the spin current can be calculated from

$$j_{k,i} = \frac{\sigma_N}{2e^2}\pi T i\sum_{\omega_n>0}\mathrm{Tr}[\hat{\tau}_0\hat{\sigma}_i(\check{g}\nabla_k\check{g})],$$

where $\sigma_N = 2e^2N_0D$ is the normal state conductivity and N_0 is the density of states at the Fermi level. The spin current density $j_{k,i}$ is a tensor, the index k represents the transport direction of spin, and i represents the spin component. With the parametrization in Eq. (15), we get the three components of the spin current density in the x direction,

$$\begin{aligned}j_{x,2} &= \frac{2\sigma_N}{e^2}\pi T\sum_{\omega_n>0}\left[\alpha'(x)\left(M_1^2 + M_3^2\right) + M_3\partial_xM_1 - M_1\partial_xM_3\right] \\ j_{x,1/3} &= 0,\end{aligned} \tag{19}$$

where $\alpha(x)$ is the rotation angle in Eq. (1). Since the rotation of the magnetization happens in the xz plane, the x and z spin components of the spin current density are absent, $j_{x,1/3} = 0$. The only nonzero spin component of the spin current density is in the y spin direction.

The spatial dependence of $j_{x,2}$ is shown in Fig. 4(a) for a domain wall size $\lambda = 0.5\xi_0$. We can see that a nonzero spin current density is created around the domain wall structure. Inside the domain wall, the maximum spin current density $j_{x,2}(0)$ is constant and smoothly goes to zero outside the domain wall. Both spin-orbit and spin-flip relaxations reduce the spin current density.

The constant spin current density $j_{x,2}(0)$ in the domain wall region is determined from the adiabatic solution of the parameter M_3 and the domain wall size λ. From Fig. 2(d) we know that M_3 describes the effect of the exchange field on superconductivity, and at the center of the domain wall $M_3 \to 0$ for a small domain wall size. Therefore, $j_{x,2}(0) \to 0$ for $\lambda \to 0$ and becomes large for a stronger exchange field. These are shown in Figs. 4(b) and 4(c). We can also see

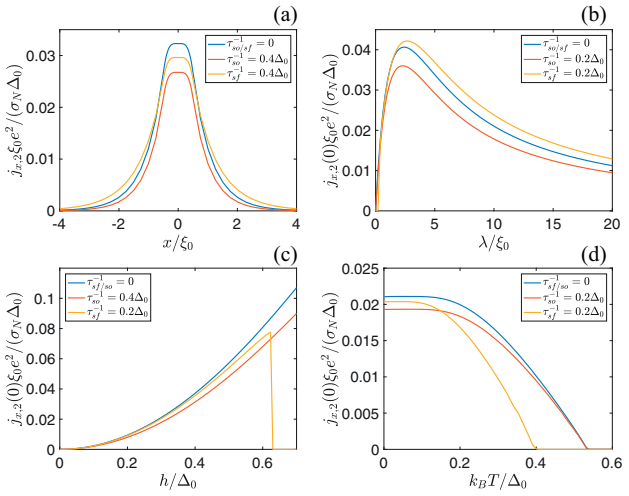

FIG. 4. Dependence of spin current density on (a) position, and the maximum spin current density $j_{x,2}(0)$ on (b) domain wall size, (c) exchange field, and (d) temperature. Here $\lambda = 0.5\xi_0$, $T = 0.05\Delta_0$, and $h = 0.3\Delta_0$ unless specified otherwise.

that for a small domain wall, both spin-orbit and spin-flip relaxation reduce $j_{x,2}(0)$. However, for large domain walls, spin-flip relaxation increases $j_{x,2}(0)$ for a fixed domain wall size, but it kills $j_{x,2}(0)$ at the Chandrasekhar-Clogston limit, where the superconductivity is suppressed [25,26].

The temperature dependence of $j_{x,2}(0)$ is shown in Fig. 4(d). It resembles the temperature dependence of the self-consistent pair potential Δ. This means $j_{x,2}(0) \sim \Delta$ for a fixed domain wall size and exchange field h. The effect of spin relaxation also resembles the temperature dependence of Δ.

From the spatial dependence of $j_{x,2}$ we can see that, strictly speaking, the spin current density is not conserved. The position dependence is related to the appearance of a spin-transfer torque [41]. It is exerted on the spins in order to reorient spin flow to follow the direction of local magnetization, namely, it represents the rotation of spins through the domain wall structure. Then in the continuity equation for spin density $\boldsymbol{n}_s$, we have [42]

$$\frac{d\boldsymbol{n}_s}{dt} + \nabla \cdot j_{k,i} = \mathcal{T},$$

where $\mathcal{T}$ is the spin-transfer torque and it is nonzero in the case of an inhomogeneous exchange field and spin relaxation.

In the static case $\nabla \cdot j_{k,i} = \mathcal{T}$. With the parametrization in Eq. (15),

$$\mathcal{T} = \partial_x j_{x,2} = \frac{4\sigma_N}{e^2 D}\pi T h \sum_{\omega_n>0} \sin\theta M_1. \tag{20}$$

It is nothing but the Matsubara sum of M_1 but constrained by superconductivity ($\sin\theta$). In the normal state $\theta \to 0$, then the torque is zero in equilibrium.

The expression of $\mathcal{T}$ in Eq. (20) also helps us to understand the properties of the spin current density. The spatial dependence follows Fig. 2(c), but the amplitude is constrained by $\sin\theta \sim \Delta$. That is why the temperature dependence of the spin current density is similar to that of the self-consistent pair potential [Fig. 4(d)]. The dependence on h explains the monotonous dependence on h of the spin current density [Fig. 4(c)].

The equilibrium spin-transfer torque $\mathcal{T}$ is related to the superconducting free energy by

$$\mathcal{T} = \frac{1}{V}\boldsymbol{h} \times \frac{\delta F_{sn}}{\delta \boldsymbol{h}}, \tag{21}$$

where V is the volume of the superconductor, $\boldsymbol{h}$ is the exchange field induced in the superconductor, and F_{sn} is given by

$$F_{sn} = W\int_{-\infty}^{\infty} f_{sn} dx, \tag{22}$$

where W is the cross sectional area of the superconductor and the superconducting free energy density [43–47] compared to its normal state f_{sn} is given by (see Appendix)

$$\begin{aligned} f_{sn} = f_s - f_n = \pi T N_0 \sum_{\omega_n>0} \mathrm{Tr}\Big\{ & (\omega_n + i\boldsymbol{h}\cdot\boldsymbol{\sigma})(\check{1} - \hat{\tau}_3\check{g}) \\ & - \frac{1}{2}(\Delta\hat{\tau}_+ + \Delta^*\hat{\tau}_-)\check{g} + \frac{D}{4}(\nabla\check{g})^2 \\ & + \frac{1}{16\tau_{so}}[3 - (\boldsymbol{\sigma}\check{g})\cdot(\boldsymbol{\sigma}\check{g})] \\ & + \frac{1}{16\tau_{sf}}[3 - (\boldsymbol{\sigma}\hat{\tau}_3\check{g})\cdot(\boldsymbol{\sigma}\hat{\tau}_3\check{g})]\Big\}. \end{aligned} \tag{23}$$

In the absence of spin relaxation and exchange field, this agrees with the result in Ref. [47]. Here $f_{sn} = f_{sn}[\boldsymbol{h}]$, and Δ and $\check{g}$ are the self-consistent values of the order parameter and the Green function. With the parametrization in Eq. (15), it becomes

$$\begin{aligned} f_{sn} = \pi T N_0 \sum_{\omega_n>0} \big\{ & 4\omega_n - 2M_0(2\omega_n\cos\theta + \Delta\sin\theta) \\ & + 4hM_3\sin\theta - D\big(M_1^2 + M_3^2\big)\alpha'(x)^2 \\ & + D[(\partial_x M_0)^2 - (\partial_x M_1)^2 - (\partial_x M_3)^2 + (\partial_x\theta)^2] \\ & - 2D(M_3\partial_x M_1 - M_1\partial_x M_3)\alpha'(x) \\ & + \tfrac{1}{4}\big[3\big(\tau_{so}^{-1} + \tau_{sf}^{-1}\big) - 3\big(\tau_{so}^{-1} + \tau_{sf}^{-1}\cos 2\theta\big)M_0^2 \\ & - \big(\tau_{so}^{-1} - \tau_{sf}^{-1}\cos 2\theta\big)\big(M_1^2 + M_3^2\big)\big]\big\}. \end{aligned} \tag{24}$$

From the relation in Eqs. (19) and (21), we obtain

$$f_{sn} = f_{sn}^0 - \frac{1}{2}\alpha'(x) j_{x,2} + \frac{1}{4}\alpha'(x)^2\frac{\delta j_{x,2}}{\delta\alpha'(x)}, \tag{25}$$

where f_{sn}^0 is the free-energy density in Eq. (24) with terms that do not directly depend on $\alpha'(x)$, and $f_{sn} - f_{sn}^0$ is nonzero only in the domain wall region. We can see that the spin current density contributes to the energetics of the system, which in turn influences the formation of the domain wall.

In nonequilibrium spin transport, spin-transfer torque leads to the domain wall motion and influences the orientation of the magnetization [41]. In our model, the equilibrium spin-transfer torque in Eq. (20) does not make the domain wall move, but it contributes to the superconducting free energy via

the spin current density [as in Eq. (25)], which in turn affects the domain wall size, as we discuss in the next section.

IV. EFFECT OF SUPERCONDUCTIVITY ON THE DOMAIN WALL SIZE

In the absence of the external magnetic field, the domain wall size in a ferromagnet is dictated by the competition between exchange and anisotropy energies [48]. Exchange energy tries to maintain the direction of the magnetization, while the anisotropy energy tends to align the magnetization to a particular direction.

The exchange energy density can be expressed by

$$U_{ex} = Q\sum_{i=1}^{3}\left(\frac{\partial m_i}{\partial x}\right)^2,$$

where m_i is the component of the magnetization unit vector, and Q is the exchange stiffness constant. Here $\boldsymbol{m} = (\cos\alpha, 0, \sin\alpha)$, where α is the rotation angle in Eq. (1). Substituting Eq. (1) to U_{ex} we get

$$U_{ex} = \frac{Q\pi^2}{\lambda^2}\Theta\left(x+\frac{\lambda}{2}\right)\Theta\left(\frac{\lambda}{2}-x\right). \tag{26}$$

The anisotropy energy density depends on the crystal structure of the system. Most of the ferromagnetic insulators have face centered cubic crystal structure [49]. The anisotropy energy density in this case is given by

$$U_{\text{aniso}} = K_{c1}\left(m_1^2m_2^2 + m_1^2m_3^2 + m_2^2m_3^2\right) + K_{c2}m_1^2m_2^2m_3^2,$$

where $K_{c1}, K_{c2} < 0$ for many ferromagnetic insulators, which makes the magnetization lie in one of the easy planes. In the case of thin films, the symmetry is broken in the direction perpendicular to the film plane and this energy density can be expressed by a uniaxial crystal structure as [50]

$$U_{\text{aniso}} = \left(K_1 + \frac{K_s}{t}\right)\sin^2\alpha + K_2\sin^4\alpha, \tag{27}$$

where $K_1 = K_{c1}$, $K_2 = -7K_{c1}/8 + K_{c2}/8$, and K_s is the surface anisotropy constant representing the rotation of the easy plane towards an easy axis magnetization with film thickness t.

Together with Eqs. (26) and (27), the domain wall energy is given by

$$F_1 = \int_{-\infty}^{\infty}(U_{ex}+U_{\text{aniso}})dx = \frac{Q\pi^2}{\lambda} + \frac{1}{2}K_{\text{eff}}\lambda, \tag{28}$$

where $K_{\text{eff}} = K_1 + K_s/t + 3K_2/4$. Minimization of this energy with respect to λ gives the domain wall size of the inhomogeneous exchange field in the ferromagnet

$$\lambda_0 = \sqrt{\frac{2Q}{K_{\text{eff}}}}\pi. \tag{29}$$

Then the minimized domain wall energy is

$$F_1^{\min} = \sqrt{2K_{\text{eff}}Q}\pi. \tag{30}$$

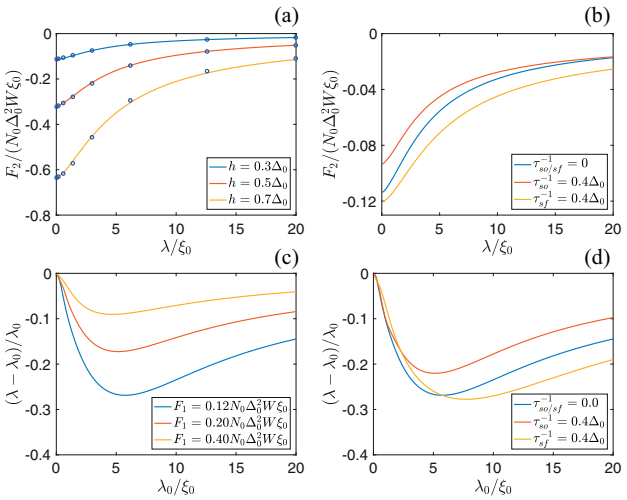

FIG. 5. (a) Superconducting free energy contribution F_2 to the domain wall energy at $T = 0.05\Delta_0$ for different exchange field strengths. The blue circles in (a) are the results of the fitted formula in Eq. (31). (b) Effect of spin relaxation on F_2 for $h = 0.3\Delta_0$ at $T = 0.05\Delta_0$. (c) Effect of superconductivity on the domain wall size for $h = 0.3\Delta_0$ with different domain wall energies F_1 in the ferromagnet. (d) The effect of spin relaxation on the same quantity as in (c) for $F_1 = 0.12N_0\Delta_0^2W\xi_0$.

In many studies, the domain wall structure is represented by the hyperbolic functions with [48]

$$\alpha(x) = \cos^{-1}\left[-\tanh\left(\frac{x-x_0}{\lambda'}\right)\right],$$

where $\lambda' = \sqrt{Q/K'_{\text{eff}}}$ and $K'_{\text{eff}} = K_1 + K_s/t + 2K_2/3$. The minimized energy is then given by $4\sqrt{K'_{\text{eff}}Q}$. Since $K'_{\text{eff}} \approx K_{\text{eff}}$, this is very close to $F_1^{\min}$ in Eq. (30). In other words, the domain wall structure in Eq. (1) gives the minimum energy which is only slightly larger than that of more complicated domain wall structures.

The contribution of superconductivity to the domain wall energy is given by the difference of the free energy in the cases of inhomogeneous and homogeneous magnetization

$$F_2 = F_{sn}(\boldsymbol{h}) - F_{sn}(\boldsymbol{h} = h\hat{z}),$$

where F_{sn} is given by Eq. (22). This energy cannot be expressed analytically, but the numerical result is plotted in Fig. 5(a). We can see that F_2 is negative. This is due to the fact that the existence of the domain wall structure enhances the superconducting condensation energy near the domain wall. This contribution is stronger for a smaller domain wall, since smaller domain wall reduces the effect of the exchange field more in the domain wall region. The effect of spin relaxation is plotted in Fig. 5(b). We can see that spin-orbit relaxation makes $|F_2|$ smaller. This is because spin-orbit relaxation reduces the effect of the exchange field, but it has less effect in the domain wall region. This makes the free energy difference $|F_{sn}(\boldsymbol{h}) - F_{sn}(\boldsymbol{h} = h\hat{z})|$ smaller. Spin-flip relaxation on the other hand, makes $|F_2|$ larger.

From Fig. 5(a) we can approximate F_2 as

$$F_2 = -\frac{a}{\lambda + 2\xi_0} + be^{-\lambda/\xi_0}, \tag{31}$$

where a, b are functions of temperature and exchange field strength and can be determined numerically. For example, for $h = 0.3\Delta_0$, $a = 0.4N_0\Delta_0^2 W\xi_0^2$ and $b = 0.085N_0\Delta_0^2 W\xi_0$.

Minimizing the total energy $F_1 + F_2$ with respect to λ, we get a compact analytical expression for two extreme limits

(i) $\lambda \ll \xi_0$

$$\lambda = \sqrt{\frac{2Q}{K_{\text{eff}} + \left(\frac{a}{2\xi_0^2} - \frac{2b}{\xi_0}\right)}}\pi.$$

(ii) $\lambda \gg \xi_0$

$$\lambda = \sqrt{\frac{2(Q - a/\pi^2)}{K_{\text{eff}}}}\pi, \text{ for } Q\pi^2 > a \tag{32}$$

$$\lambda = \frac{4a\xi_0}{a - \pi^2 Q}, \text{ for } Q\pi^2 < a.$$

In both limits superconductivity reduces the domain wall size. (i) For a small domain wall $\lambda \ll \xi_0$, superconductivity reduces the domain wall size by effectively increasing the anisotropy constant K_{eff}. (From the numerical results $a/(2\xi_0^2) > 2b/\xi_0$ holds for all h.) (ii) For the case of a large domain wall, the situation is more complicated. For a ferromagnet with strong stiffness $Q\pi^2 > a$, superconductivity reduces the domain wall size by effectively reducing the exchange stiffness constant Q. For a ferromagnet with weak stiffness $Q\pi^2 < a$, which also refers to the case of $K_{\text{eff}} \ll 1.0N_0\Delta_0^2 W$, the domain wall size is also reduced. However, in this case superconductivity dominates the domain wall energy and leads to a negative total energy $F_1 + F_2$, which introduces a dense domain structure with a domain length comparable with the domain wall size [51]. Since we are considering a single domain structure, here we only consider domain walls with positive domain wall energy.

In Fig. 5(c), we numerically minimize the domain wall energy $F = F_1 + F_2$ with respect to the domain wall size for the case of $h = 0.3\Delta_0$ and $T = 0.05\Delta_0$ and calculate the relative change of the domain wall size. To avoid a negative domain wall energy leading to a transition to a system with many domain walls, we set in each figure a constant $F_1 \geqslant 0.12N_0\Delta_0^2 W\xi_0$ so that $F > 0$ for each case considered. In other words, instead of varying K_{eff} and Q, we fix F_1 and vary λ_0 in the figures. The effect of superconductivity on the domain wall size is strongest for the lowest F_1. If we consider larger values of F_1, namely, a stronger ferromagnet, the effect of superconductivity on the domain wall size is smaller.

The effect of spin relaxation on the domain wall size is shown in Fig. 5(d). We see that for small domain walls, the spin relaxation brings very little effects on the domain wall size compared to the case without spin relaxation. However, for larger domain walls, the two types of spin-relaxation mechanisms lead to different effects on the domain wall size. Spin-orbit relaxation makes the effect smaller since it reduces the effect of the exchange field and makes $|F_2|$ smaller. Spin-flip relaxation makes the effect stronger, since $|F_2|$ is larger.

As we can see, the effect of superconductivity on the domain wall size is pronounced for weak ferromagnets with large domain walls. Domain wall sizes in ferromagnetic insulators are rarely reported, but with Eq. (29) we can evaluate a typical size. For materials with a face centered cubic structure, the exchange stiffness constant Q is related to the exchange integral J by $Q = 4S^2 J/a_0$, where S is spin and a_0 is the lattice constant [52]. With the values of the parameters for Q in Ref. [53] and for K_{eff} in Ref. [50], we get the domain wall size for a EuS thin film as 50 nm. Considering a typical coherence length of a conventional superconductor in the diffusive superconductors at zero temperature and exchange field between 15 nm and a few hundred nm, we can estimate in this case $\lambda_0 \sim 0.1 \ldots 5\xi_0$. Therefore, although perhaps in most cases $\lambda_0 < \xi_0$ is the most relevant limit, nothing as such seems to exclude the possibility of the opposite limit as well.

V. DENSITY OF STATES

The inhomogeneous exchange field also makes the local density of states (DoS) peculiar. Since the domain wall structure reduces the effect of the exchange field, the local DoS in the domain wall region is different from the one for homogeneous magnetization.

In the quasiclassical theory, the local DoS for each spin species is given by

$$N_s = \tfrac{1}{8}N_0 \text{Re}[\text{Tr}(\hat{\tau}_3 \pm \hat{\sigma}_3\hat{\tau}_3)\check{g}|_{\omega_n = -i\epsilon^+}],$$

where $\pm$ is for spin $\uparrow / \downarrow$. With the parametrization in Eq. (15), it becomes

$$N_s = \tfrac{1}{2}N_0 \text{Re}[\cos\theta M_0 \pm (\cos\alpha M_3 - \sin\alpha M_1) i \sin\theta]. \tag{33}$$

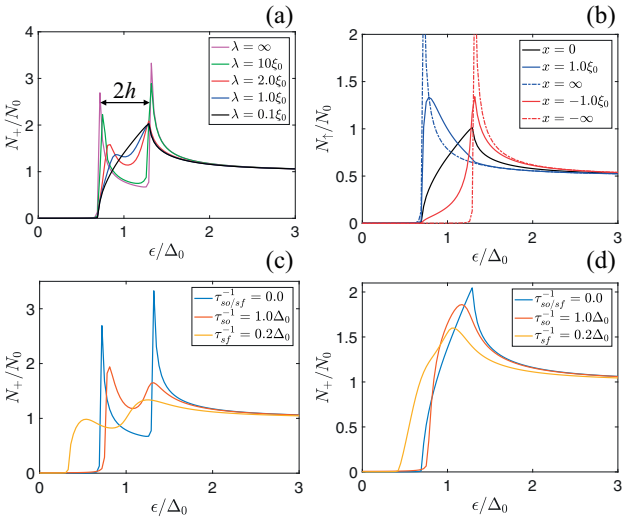

FIG. 6. (a) Local DoS at the center of the domain wall for different domain wall sizes. (b) Local DoS for spin $\uparrow$ at different positions for a domain wall size $\lambda = 0.1\xi_0$. (c) Local DoS in the presence of spin relaxation in the homogeneous exchange field (at $x = -\infty$) and (d) at the center of the domain wall ($x = 0$) for a domain wall size $\lambda = 0.1\xi_0$. The temperature and exchange field used in the calculations are $T = 0.05\Delta_0$, $h = 0.3\Delta_0$.

In Fig. 6(a) we show the local DoS $N_+ = N_\uparrow + N_\downarrow$ at the center of the domain wall for different domain wall sizes in the absence of spin relaxation. At the center of the domain wall $\alpha = \pi/2$ and $M_1 = 0$, then $N_\uparrow = N_\downarrow$ and $N_- = N_\uparrow - N_\downarrow = 0$ due to the symmetry of the model. For $\lambda \to \infty$, N_+ has two BCS peaks at $\Delta \pm h$. As the domain wall becomes smaller, the inner peak is shifted towards the outer one and forms a shark-fin structure for a very small domain wall size [$\lambda = 0.1\xi_0$ in Fig. 6(a)]. In this case, although $N_- = 0$, N_+ is different from the case with zero exchange field. Due to the spin-orbit relaxationlike effect of the inhomogeneous exchange field, the peaks are wider and the superconducting gap is smaller compared to the case of $h = 0$.

Since the magnetization direction is opposite on the two sides of the domain wall, N_s behaves differently in these two regions, such that $N_+(x) = N_+(-x)$ and $N_-(x) = -N_-(-x)$. In Fig. 6(b) we show $N_\uparrow$ at different location along the superconducting wire with a small domain wall $\lambda = 0.1\xi_0$, in the absence of spin relaxation. These results in are similar to those in Ref. [34], which concentrates on the limit $\lambda \ll \xi_0$. Here we further study the effect of spin relaxation on the local DoS in Figs. 6(c) and 6(d). The DoS in the presence of the two kinds of spin relaxation is plotted in Fig. 6(d) at the center of a domain wall with a size $\lambda = 0.1\xi_0$. For comparison, the DoS at $x = -\infty$, which also refers to the homogeneous exchange field, is plotted for the same parameters in Fig. 6(c). In both cases, spin-orbit relaxation broadens the peaks but keeps $\Delta(x)$ unchanged. Spin-flip relaxation also broadens the peaks, but it suppresses $\Delta(x)$. These properties of the local DoS are caused by the inhomogeneous magnetization and are needed for understanding the tunneling conductance as discussed in the next section.

VI. TUNNELING CONDUCTANCE

The local density of states is visible in measurements of a tunneling conductance through a barrier in contact with the FI/S bilayer. However, the results depend on whether the barrier itself is magnetic or not. Therefore, we consider either a nonmagnetic tunnel contact (NISFI) or tunneling through the FI containing the domain wall (SFIN). In either system the tunneling current can be written as

$$I = \frac{G_T}{e}\int_{-\infty}^{\infty} d\epsilon \bar{N}(\epsilon)[f(\epsilon - eV) - f(\epsilon)],$$

where G_T is the normal-state conductance, V is the applied voltage, and $f = [1 + \exp(\epsilon/k_BT)]^{-1}$ is the Fermi function. Here the averaged density of states $\bar{N}(\epsilon)$ over the tunneling area is given by [54]

$$\bar{N}(\epsilon) = \frac{1}{L}\int_{x_a}^{x_b} dx \sum_{s=\uparrow,\downarrow}[1 + sP(x)]N_s(\epsilon, x),$$

where $P(x)$ is the spin polarization of the junction, $L = x_b - x_a$ is the size of the tunneling barrier, and N_s is given in Eq. (33). Using the definition of $N_\pm = N_\uparrow \pm N_\downarrow$, we can also write

$$\bar{N}(\epsilon) = \frac{1}{L}\int_{x_a}^{x_b} dx[N_+ + P(x)N_-]. \quad (34)$$

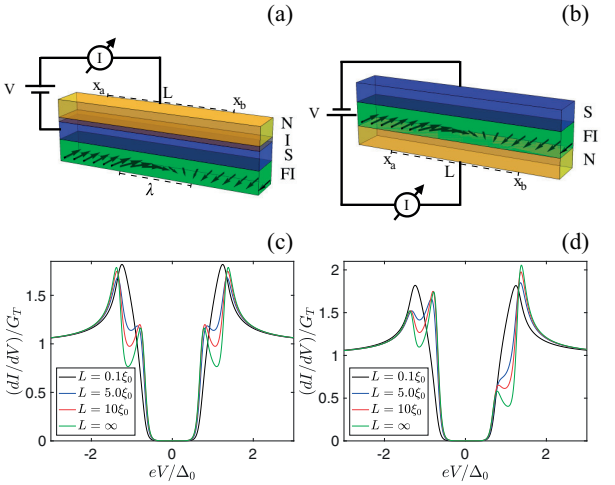

FIG. 7. Tunneling conductance for different sizes of the tunneling barriers for NISFI and NISFI contacts, respectively. Here the center of the tunneling barrier is located at the center of the domain wall, $x_b = -x_a = L/2$. The calculations are carried out for a domain wall size $\lambda = 0.1\xi_0$ at $T = 0.05\Delta_0$ and $h = 0.3\Delta_0$. In (d) the polarization is $P(x) = P_0 \cos\alpha$, where α is the rotation angle, and $P_0 = 0.5$.

The tunneling conductance is given by

$$\frac{dI}{dV}(V) = \frac{G_T}{e}\frac{d}{dV}\int_{-\infty}^{\infty} d\epsilon \bar{N}(\epsilon)[f(\epsilon - eV) - f(\epsilon)]. \quad (35)$$

In the case of a scanning tunneling microscope measurement with a small normal metal tip ($x_b - x_a \ll \xi_0$ and $P(x) = 0$), $\bar{N} = N_+$. In this case the tunneling conductance at $T \to 0$ gives the local DoS N_+ shown in Fig. 6.

For a planar tunneling spectroscopy measurement with a normal metal electrode having size $x_b - x_a \geqslant \xi_0$, $\bar{N}$ is the averaged N_+ since $P(x) = 0$. The tunneling conductance in this case is given in Fig. 7(c). We show the comparison of different sizes of tunneling barriers (centered at $x = 0$). Since we are considering a single domain wall structure, a large tunneling barrier produces tunneling conductance identical with the case of homogeneous magnetization (green curve). If we choose a smaller tunneling barrier, the effect of the domain wall is more obvious. It reduces the effect of the exchange field, becomes similar to the case for a small homogeneous exchange field strength h, and reshapes the peaks in the tunneling conductance (red and blue curves).

If the tunneling is through the ferromagnetic insulator, we need to include the effect of finite spin polarization. Assuming the polarization of the transmission to follow the local magnetization, the position dependent polarization P is related to the rotation angle of the magnetization as $P(x) = P_0 \cos\alpha$. The tunneling conductance is plotted in Fig. 7(d). The asymmetric dependence in the injection voltage in the conductance is a direct result of the polarization of the ferromagnet. Similar to Fig. 7(c), for a large tunneling barrier the tunneling conductance is the same for the case of a homogeneous exchange field h with a finite spin polarization P_0. The effect of the domain wall is again obvious for smaller tunneling barriers,

and the spin-orbit relaxationlike effect of the domain wall structure reduces the effect of the exchange field.

VII. CONCLUSION

In conclusion, we have studied various properties of a superconductor in contact to a ferromagnet with a domain wall. We have studied the equilibrium spin current density, which exists due to the inhomogeneity of the exchange field. It also contributes to the superconducting free energy, which in turn affects the domain wall size. We show that the domain wall size is reduced by the contribution of the superconducting free energy to the domain wall energy. We have also studied the peculiar density of states around the domain wall and the tunneling conductance. Our work can be a precursor to the study of the nonequilibrium effects, in particular domain wall motion.

ACKNOWLEDGMENTS

We thank F. S. Bergeret, M. Silaev, and S. Chakraborty for discussions. This project has received funding from the European Union's Horizon 2020 research and innovation programme under Grant agreement No. 800923 (SUPERTED) and the Academy of Finland Projects No. 305256 and No. 317118.

APPENDIX: EXPRESSION FOR THE FREE ENERGY

For completeness, we give now a brief argument for the form of the free energy in the superconducting state. There are several ways to arrive at such results, and below we follow a similar procedure as in Ref. [43]. The free energy density difference between superconducting and normal states can be written as [we set $N(0) = 1$ in the following] [55,56]

$$f_{sn} = -\int_0^\gamma d\gamma' \, \frac{\Delta|^2_{\gamma'}}{(\gamma')^2} = \int_\infty^{1/\gamma} dq \, \Delta|^2_{\gamma=1/q} \, . \tag{A1}$$

The integral could now in principle be computed numerically from Usadel equations, solving Δ self-consistently as a function of the coupling constant γ in the geometry considered. This is cumbersome, and also unnecessary, as the integral can be evaluated analytically as follows.

Suppose there exists a functional $R = \int d^3x \, r$,

$$r[q, \Delta, \vec{z}] = q\Delta^2 + p[\Delta, \vec{z}] \, , \tag{A2}$$

whose saddle point vs $\vec{z}$ and Δ defines $\Delta(q)$. In other words, the self-consistency (16) and Usadel equations (2) are defined by variations

$$\frac{\delta R}{\delta \Delta}|_* = 0 \, , \quad \frac{\delta R}{\delta z_j}|_* = 0 \, , \tag{A3}$$

and $\vec{z}$ is some parametrization of $\hat{g}$ under the constraint $\hat{g}^2 = 1$ of the Usadel equation. Now,

$$\frac{d}{dq}R|_* = \partial_q R|_* + \frac{\delta R}{\delta \Delta}|_* * \frac{d\Delta_*}{dq} + \frac{\delta R}{\delta \vec{z}}|_* * \frac{d\vec{z}_*}{dq} = \Delta_*^2 \, , \tag{A4}$$

where the last two terms vanish due to the saddle point conditions. Therefore,

$$f_{sn} = r[1/\gamma, \Delta_*, \vec{z}_*] - r[\infty, 0, \vec{z}_{*,n}] \, . \tag{A5}$$

This assumes there is a continuous solution branch connecting the normal and the superconducting states as the coupling constant γ (i.e., q) is changed.

The next step is to find a suitable R that satisfies Eqs. (A3). Its form can be guessed (or derived) based on σ-model results [45,46,57]:

$$\begin{aligned} r = q|\Delta|^2 - 2\pi T \sum_{\omega_n > 0} \frac{1}{2} \mathrm{tr} \Big\{ & -\frac{D}{4}(\nabla \check{g})^2 + (\omega_n + i\mathbf{h}\cdot\boldsymbol{\sigma})\hat{\tau}_3 \check{g} \\ & + (\Delta\hat{\tau}_+ + \Delta^*\hat{\tau}_-)\check{g} + \frac{1}{16\tau_{so}}(\boldsymbol{\sigma}\check{g})\cdot(\boldsymbol{\sigma}\check{g}) \\ & + \frac{1}{16\tau_{sf}}(\boldsymbol{\sigma}\hat{\tau}_3\check{g})\cdot(\boldsymbol{\sigma}\hat{\tau}_3\check{g}) \Big\} . \end{aligned} \tag{A6}$$

First, we can note that variation vs Δ^* (or Δ) gives the self-consistency relation (16). For variations with $\hat{g}$, we parametrize $\delta\hat{g} = e^{\delta\hat{W}}\hat{g}e^{-\delta\hat{W}} - \hat{g} \simeq \delta W\hat{g} - \hat{g}\delta\hat{W}$ to retain the normalization condition. Requiring variation vs $\hat{W}$ to vanish we find Eq. (2). Hence, the result has the property (A3).

The sum defining R is not convergent, and only the difference in Eq. (A5) is well defined. There's also an implicit Matsubara frequency cutoff in the term that appears in the self-consistency equation. We can eliminate this issue by substituting the self-consistency equation back into the $|\Delta|^2$ term in Eq. (A6). This results in Eq. (23) in the main text. Variation vs $\mathbf{h}$ still gives the correct quasiclassical expression for the magnetization, but Δ and $\hat{g}$ can no longer be varied and have to be taken at their saddle-point values.

[1] W. Meissner and R. Ochsenfeld, Naturwissenschaften **21**, 787 (1933).
[2] M. Tinkham, *Introduction to Superconductivity* (Dover Publications, 2004).
[3] B. Chandrasekhar, Appl. Phys. Lett. **1**, 7 (1962).
[4] A. M. Clogston, Phys. Rev. Lett. **9**, 266 (1962).
[5] R. Meservey, P. M. Tedrow, and P. Fulde, Phys. Rev. Lett. **25**, 1270 (1970).
[6] P. M. Tedrow and R. Meservey, Phys. Rev. Lett. **26**, 192 (1971).
[7] R. Meservey, P. M. Tedrow, and R. C. Bruno, Phys. Rev. B **11**, 4224 (1975).
[8] D. Paraskevopoulos, R. Meservey, and P. M. Tedrow, Phys. Rev. B **16**, 4907 (1977).
[9] R. Meservey, D. Paraskevopoulos, and P. M. Tedrow, Phys. Rev. B **22**, 1331 (1980).
[10] P. M. Tedrow, J. E. Tkaczyk, and A. Kumar, Phys. Rev. Lett. **56**, 1746 (1986).
[11] X. Hao, J. S. Moodera, and R. Meservey, Phys. Rev. B **42**, 8235 (1990).

[12] J. S. Moodera, T. S. Santos, and T. Nagahama, J. Phys.: Condens. Matter **19**, 165202 (2007).
[13] Y. M. Xiong, S. Stadler, P. W. Adams, and G. Catelani, Phys. Rev. Lett. **106**, 247001 (2011).
[14] K. Senapati, M. G. Blamire, and Z. H. Barber, Nat. Mater. **10**, 849 (2011).
[15] M. J. Wolf, C. Sürgers, G. Fischer, and D. Beckmann, Phys. Rev. B **90**, 144509 (2014).
[16] P. Machon, M. Eschrig, and W. Belzig, Phys. Rev. Lett. **110**, 047002 (2013).
[17] P. Machon, M. Eschrig, and W. Belzig, New J. Phys. **16**, 073002 (2014).
[18] A. Ozaeta, P. Virtanen, F. S. Bergeret, and T. T. Heikkilä, Phys. Rev. Lett. **112**, 057001 (2014).
[19] S. Kolenda, M. J. Wolf, and D. Beckmann, Phys. Rev. Lett. **116**, 097001 (2016).
[20] S. Kolenda, C. Sürgers, G. Fischer, and D. Beckmann, Phys. Rev. B **95**, 224505 (2017).
[21] C. Quay, D. Chevallier, C. Bena, and M. Aprili, Nat. Phys. **9**, 84 (2013).
[22] F. Hübler, M. J. Wolf, D. Beckmann, and H. v. Löhneysen, Phys. Rev. Lett. **109**, 207001 (2012).
[23] M. J. Wolf, F. Hübler, S. Kolenda, H. v. Löhneysen, and D. Beckmann, Phys. Rev. B **87**, 024517 (2013).
[24] M. Silaev, P. Virtanen, F. S. Bergeret, and T. T. Heikkilä, Phys. Rev. Lett. **114**, 167002 (2015).
[25] F. S. Bergeret, M. Silaev, P. Virtanen, and T. T. Heikkilä, Rev. Mod. Phys. **90**, 041001 (2018).
[26] T. T. Heikkilä, M. Silaev, P. Virtanen, and F. S. Bergeret, arXiv:1902.09297 (2019)
[27] A. I. Buzdin, L. N. Bulaevskii, and S. V. Panyukov, Zh. Eksp. Teor. Phys. **87**, 299 (1984) [Sov. Phys. JETP **60**, 174 (1984)].
[28] A. Y. Aladyshkin, A. I. Buzdin, A. A. Fraerman, A. S. Mel'nikov, D. A. Ryzhov, and A. V. Sokolov, Phys. Rev. B **68**, 184508 (2003).
[29] M. Houzet and A. I. Buzdin, Phys. Rev. B **74**, 214507 (2006).
[30] Z. Yang, M. Lange, A. Volodin, R. Szymczak, and V. V. Moshchalkov, Nat. Mater. **3**, 793 (2004).
[31] Z. Shomali, M. Zareyan, and W. Belzig, New J. Phys. **13**, 083033 (2011).
[32] I. Bobkova and A. Bobkov, JETP Lett. **109**, 1 (2019).
[33] D. S. Rabinovich, I. V. Bobkova, A. M. Bobkov, and M. A. Silaev, arXiv:1811.09304.
[34] E. Strambini, V. Golovach, G. De Simoni, J. Moodera, F. Bergeret, and F. Giazotto, Phys. Rev. Materials **1**, 054402 (2017).
[35] S. Komori, A. Di Bernardo, A. I. Buzdin, M. G. Blamire, and J. W. A. Robinson, Phys. Rev. Lett. **121**, 077003 (2018).
[36] F. S. Bergeret and I. V. Tokatly, Phys. Rev. Lett. **110**, 117003 (2013).
[37] F. S. Bergeret and I. V. Tokatly, Phys. Rev. B **89**, 134517 (2014).
[38] C. Gorini, P. Schwab, R. Raimondi, and A. L. Shelankov, Phys. Rev. B **82**, 195316 (2010).
[39] D. A. Ivanov and Y. V. Fominov, Phys. Rev. B **73**, 214524 (2006).
[40] T. E. Baker, A. Richie-Halford, and A. Bill, Phys. Rev. B **94**, 104518 (2016).
[41] D. C. Ralph and M. D. Stiles, J. Magn. Magn. Mater. **320**, 1190 (2008).
[42] Q. F. Sun and X. C. Xie, Phys. Rev. B **72**, 245305 (2005).
[43] G. Eilenberger, Z. Phys **214**, 195 (1968).
[44] K. D. Usadel, Phys. Rev. Lett. **25**, 507 (1970).
[45] A. Altland, B. D. Simons, and D. Taras-Semchuk, JETP Lett. **67**, 22 (1998).
[46] D. Taras-Semchuk and A. Altland, Phys. Rev. B **64**, 014512 (2001).
[47] P. Virtanen, F. Vischi, E. Strambini, M. Carrega, and F. Giazotto, Phys. Rev. B **96**, 245311 (2017).
[48] L. D. Landau, E. M. Lifshitz, and L. P. Pitaevskii, *Electrodynamics of Continuous Media*, 2nd ed. (Pergamon Press, 1984).
[49] Q. I. Yang, J. Zhao, L. Zhang, M. Dolev, A. D. Fried, A. F. Marshall, S. H. Risbud, and A. Kapitulnik, Appl. Phys. Lett. **104**, 082402 (2014).
[50] M. Li, C.-Z. Chang, B. J. Kirby, M. E. Jamer, W. Cui, L. Wu, P. Wei, Y. Zhu, D. Heiman, J. Li, and J. S. Moodera, Phys. Rev. Lett. **115**, 087201 (2015).
[51] A. I. Buzdin, Rev. Mod. Phys. **77**, 935 (2005).
[52] S. Chikazumi and C. D. Graham, *Physics of Ferromagnetism* (Oxford University Press, Oxford, 2009).
[53] W. Söllinger, W. Heiss, R. T. Lechner, K. Rumpf, P. Granitzer, H. Krenn, and G. Springholz, Phys. Rev. B **81**, 155213 (2010).
[54] F. S. Bergeret, A. Verso, and A. F. Volkov, Phys. Rev. B **86**, 214516 (2012).
[55] K. Maki and T. Tsuneto, Prog. Theor. Phys. **31**, 945 (1964).
[56] L. P. Gor'kov, Zh. Eksp. Teor. Fiz. **36**, 1918 (1959) [Sov. Phys. JETP **9**, 1364 (1959)].
[57] D. Belitz and T. R. Kirkpatrick, Rev. Mod. Phys. **66**, 261 (1994).

V

DOMAIN WALL MOTION IN A DIFFUSIVE WEAK FERROMAGNET

by

Faluke Aikebaier & T. T. Heikkilä

Submitted manuscript

https://arxiv.org/abs/1911.04121

Domain wall motion in a diffusive weak ferromagnet

Faluke Aikebaier[1,*] and Tero T. Heikkilä[1]

[1] *Department of Physics and Nanoscience Center, University of Jyväskylä, P.O. Box 35 (YFL), FI-40014 University of Jyväskylä, Finland*

(Dated: November 13, 2019)

We study the domain wall motion in a disordered weak ferromagnet, induced by injecting a spin current from a strong ferromagnet. Starting from the spin diffusion equation describing the spin accumulation in the weak ferromagnet, we calculate the force and torque acting on the domain wall. We also study the ensuing domain wall dynamics, and suggest a possible measurement method for detecting the domain wall motion via measuring the additional resistance.

I. INTRODUCTION

Current-driven domain wall motion has been an active field of research due to its applications in memory-storage devices[1]. Following a series of phenomenological theoretical works[2–5] and experimental confirmations,[6–10] a microscopic theory of domain wall motion was presented more than a decade ago.[11] The essential mechanism of such effects is the transfer of momentum and spin to the local magnetization due to a force and a (spin) torque, respectively, exerted by a spin polarized current passing through the domain wall.[12] However, spin-polarized currents may reduce the spin torque efficiency with an increasing temperature due to Joule heating.[13,14]

One suggestion to reduce the Joule heating is to replace the spin-polarized charge current with the pure spin current to induce the domain wall motion. Such pure spin currents have been realized in a lateral spin valve geometry,[15–17] see for example Fig. 1. The scenario in this case is as follows. A spin polarized current is injected from a ferromagnet to a nonmagnetic material, transported and absorbed by the second ferromagnet containing a domain wall. The absorbed pure spin current then induces a domain wall motion. It was shown that the domain wall motion in this case is also very efficient, in terms of the change of the magnetization at the interface of the ferromagnet where the spin current is absorbed. The force and torque in this structure have also been calculated for a case of weak impurity scattering,[18] but the ensuing domain wall dynamics have not yet been studied theoretically.

One important feature of the pure spin current compared to the spin-polarized current is that it decays within a length scale called spin-relaxation length, due to the spin-relaxation processes. In fact, spin relaxation significantly affects the current-driven domain wall motion.[12] For example, the spin relaxation of conduction electrons is one of the most relevant mechanisms for the damping of the domain wall motion. Moreover, it enhances the nonadiabaticity parameter of the domain walls close to the adiabatic limit.[19,20] In disordered ferromagnets, it has also been shown that the domain wall motion is very efficient even in the case of weak ferromagnetism with low spin polarization.[21] Therefore, studying the domain wall dynamics in the presence of pure spin current without the accompanied charge current may give rise to interesting new features.

Here we consider a similar structure with the one in Ref. 18, except that the nonmagnetic metal is replaced by a weak ferromagnet containing a domain wall, and a spin polarized current is injected from a strong ferromagnetic electrode. We define the concepts of the "weak" and "strong" ferromagnets based on the size of the spin polarization and the possibility of using the spin diffusion equation to describe the two systems. In particular, in the strong ferromagnet we assume a spin-polarized Fermi surface, described by spin-dependent densities of states N_σ, diffusion constants D_σ and conductivities $\sigma_\sigma = e^2 N_\sigma D_\sigma$.[22] In this case, we can study the spin polarized current in a homogeneous ferromagnet by writing diffusion equations separately for the two spin bands. On the other hand, the weak ferromagnet has a weakly spin-split Fermi surface (small exchange field) for which $\sigma_\uparrow = \sigma_\downarrow$. In this case we can include the Hanle precession term into the kinetic equations and therefore rigorously describe spin accumulation in the case of an inhomogeneous magnetization.

The spin polarized current injected from the strong ferromagnetic electrode creates a spin accumulation in the weak ferromagnet which decays exponentially due to the spin relaxation processes. This spin accumulation can be described by a spin diffusion equation with spin independent parameters, and it describes a spin current in a disordered wire. The solutions for the position dependent spin accumulation around the domain wall allows us to compute the force f and torque τ_z on the domain wall residing at a distance X from the injector. We show that they are characterized by three length scales: domain wall size λ, spin relaxation length ℓ_s, and the magnetic length ℓ_h. These length scales can in principle show up in any order, and we find how the force and torque depend on the order of those scales. In particular, due to the spin relaxation both the force and torque are exponentially decaying as functions of the distance of the domain wall from the injector, similar to the case in Ref. 18. We also study the resulting domain wall dynamics, and show that the domain wall motion with decaying force and torque has its characteristic features. In particular, the dynamics can cross between different dynamic regimes depending on the position of the domain wall, and de-

pending on the hierarchy of the length scales affecting the relative size of force and torque: In the case of a large torque and weak force, the domain wall motion can cross over from the unpinned motion for $\tau_z(X) > k_\perp \alpha_0$ to the limit of intrinsic pinning with $\tau_z(X) < k_\perp \lambda$, eventually stopping the domain wall. Here $k_\perp$ is a quantity characterizing the hard-axis anisotropy. On the other hand, if the force dominates and is large enough close to the injector, there is a crossover between oscillatory dynamics for $f(X) > \alpha_0 k_\perp$ and linearly (in time) decaying dynamics for $f(X) < \alpha_0 k_\perp$. Here α_0 describes damping.

We also suggest a possible measurement of the domain wall motion via the changes in the injection resistance, linked to the dependence of the injection resistance on the local spin accumulation at the position of the contact. Since the latter depends on the position of the domain wall, so does the injection resistance.

The outline of the paper is as follows. We first introduce the model, a weak ferromagnet containing a domain wall in contact with a spin-polarized ferromagnetic injector, in Sec. II. We also solve the spin diffusion equation with proper boundary conditions which describes the spin accumulation in this model. The force and torque due to the spin current are calculated in Sec. III. We study the domain wall dynamics in Sec. IV, and the possible measurement method accessing this dynamics in Sec. V before the conclusions in Sec. VI.

II. MODEL AND METHOD

We study the domain wall motion in the structure in Fig. 1. A spin polarized current is injected from a strong ferromagnet to a diffusive weak ferromagnet containing a domain wall. The injected current circulates on the left side of the injector, and a spin accumulation is induced in the weak ferromagnet. The decaying spin accumulation results in a spin current in both directions, capable of inducing a force and a torque on the domain wall.

On the right side of the injector, the weak ferromagnet contains a domain wall, and the magnetization is inhomogeneous. The inhomogeneity is shown in the exchange field as

$$\boldsymbol{h} = h(\sin\theta\cos\phi, \sin\theta\sin\phi, \cos\theta), \tag{1}$$

where h is the strength of the exchange splitting. Here θ and ϕ are the in-plane and out-of-plane components of the magnetization angle. For domain wall motion, ϕ is only a function of time,[11] and the rotation is described by the angle θ. A Néel domain wall is energetically favoured in thin films, namely, the rotation of the magnetization happens in the plane of the domain wall ($\phi = 0$). Then

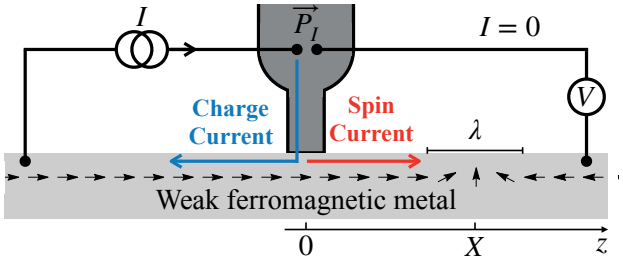

FIG. 1. Schematic view of the structure considered in this paper. A spin polarized current is injected from a strong ferromagnet to a diffusive weak ferromagnet containing a domain wall.

θ can be expressed by a variational ansatz[23]

$$\theta(z) = \pi\Theta\left(z - X - \frac{\lambda}{2}\right) + \frac{\pi}{\lambda}\left(z - X + \frac{\lambda}{2}\right)\Theta\left(z - X + \frac{\lambda}{2}\right)\Theta\left(X + \frac{\lambda}{2} - z\right), \tag{2}$$

where $\Theta(z)$ is the Heaviside step function, X is the position of the domain wall center, and λ is the domain wall size. The variational ansatz to the rotation angle, instead of the typically used hyperbolic functions[12] with slightly lower domain wall energy, brings certain conveniences to the analytical treatment of the problem while capturing the essential physics of the domain wall. Since the derivative of $\theta(x)$ is a constant inside the domain wall, the spin diffusion equation, which describes the nonequilibrium spin accumulation, can be simplified [see Eq. (4)]. The nonanalyticity of the derivative of $\theta(x)$ at the domain wall boundary can be transformed into boundary conditions of the spin diffusion equation [see Eq. (5) to Eq. (7)].

The spin accumulation in the weak ferromagnet is described by a spin diffusion equation in Eq. (A2). With the domain wall structure in Eq. (2), it can be written as

$$\hbar D\partial_z^2 \boldsymbol{s} = \frac{\hbar}{\tau_s}\boldsymbol{s} - 2\boldsymbol{h}\times\boldsymbol{s},$$

where D is the diffusion constant, τ_s is the spin-flip relaxation time, and $\boldsymbol{s} = (s_1, s_2, s_3)$ is a spin accumulation vector. The spin-relaxation length is defined as $\ell_s = \sqrt{D\tau_s}$.

We can use an SU(2) gauge transformation to treat the exchange field as homogeneous. We define a rotation matrix as

$$\hat{R} = e^{i\sigma_2\theta/2}e^{i\sigma_3\phi/2},$$

so that we can write the spin accumulation as

$$\boldsymbol{s} = \hat{R}^\dagger \boldsymbol{s}_0 \hat{R}. \tag{3}$$

Here the rotated spin accumulation $\boldsymbol{s}_0 = (s_1^0, s_2^0, s_3^0)$ satisfies the following spin diffusion equation

$$\hbar D\hat{\partial}_z^2 \boldsymbol{s}_0 = \frac{\hbar}{\tau_s}\boldsymbol{s}_0 - 2h\hat{z}\times\boldsymbol{s}_0, \tag{4}$$

where $\hat{z} = (0, 0, 1)$, $\hat{\partial}_z \cdot = \partial_z \cdot - [A, \cdot]$, and $A = i\sigma_2 \partial_z \theta(z)/2$ is an SU(2) type vector potential. The derivative of $\theta(z)$ devides the weak ferromagnet into three regions. In the domain wall region it is a constant, and to the left and the right sides of the domain wall region, $\theta'(z) = 0$. However, $\theta'(z)$ is discontinuous at the boundary of the domain wall. Therefore, we need a boundary condition to describe a continuous spin accumulation.

We can integrate Eq. (4) at the boundary of the domain wall, and obtain the boundary conditions

$$\partial_z s_1^0|_{z_b^\pm} - \partial_z s_1^0|_{z_b^\mp} = -\frac{\pi}{\lambda} s_3^0|_{z_b^\pm}, \tag{5}$$

$$\partial_z s_2^0|_{z_b^\pm} - \partial_z s_2^0|_{z_b^\mp} = 0, \tag{6}$$

$$\partial_z s_3^0|_{z_b^\pm} - \partial_z s_3^0|_{z_b^\mp} = \frac{\pi}{\lambda} s_1^0|_{z_b^\pm}. \tag{7}$$

At the domain wall edges $z = z_b = \pm(X \pm \lambda/2)$, and $\pm$ refers to the right and left sides of the domain wall boundary.

The second group of boundary conditions represent the injection of the spin polarized current. As we show in Appendix C, the spin injection from a contact with a strong ferromagnet with magnetization oriented in the z direction and biased with potential V can be described with the spin currents at the injection point,

$$\hbar D \partial_z s_1^0 = 0 \tag{8}$$

$$\hbar D \partial_z s_2^0 = 0 \tag{9}$$

$$\hbar D \partial_z s_3^0 = k_I \hbar D (s_3^0 - P_I \gamma V N_0), \tag{10}$$

where k_I is an injector transparency, P_I is an injector polarization (see Appendix C for precise definitions of these quantities in terms of the properties of a ferromagnetic injector wire), V is the voltage at the injector, and N_0 is the density of states at the Fermi level. The voltage is rescaled by a factor γ, due to fact that the spin accumulation in the weak ferromagnet is affected by the spin accumulation in the injector, see the details in Appendix C.

Making the equations dimensionless, we find that the domain wall physics is here described by three length scales: (i) domain wall size λ, (ii) spin relaxation length ℓ_s, and (iii) the magnetic length $l_h = \sqrt{\hbar D/h}$. The latter indicates the length within which a non-collinear component of the spin accumulation rotates a full period around the local magnetization direction. This is an important scale since both the force and the torque depend on such non-collinear components, as shown in Eqs. (16,17).

The "phase diagram" of different dynamical regimes depends on two dimensionless parameters corresponding to the ratios of these scales. In addition, the injector spin polarization P_I describes the efficiency of spin injection (the size of spin current for a given amount of charge current), whereas the interface transparency parameter k_I determines how strongly the resistance of the injector depends on the domain wall position.

In many strong ferromagnetic metals like iron and cobalt, the exchange splitting h is of the order of 1 eV.[24] This then leads to a very small l_h, of the order of the atomic lattice spacing. For a weak ferromagnet, for example CuNi, it is around 0.05 eV.[25] This leads to a magnetic length l_h between 10 to 25 nm.[25,26] On the other hand, depending on the exact materials or sample properties (e.g. thickness and concentration of Ni), the domain wall size λ and the spin-relaxation lengths ℓ_s of CuNi range from 15 to 25 nm[27] (estimated from measured anisotropy energy and exchange stiffness constants) and from 7 to 25 nm[28], respectively. This yields $\lambda/l_h \sim 0.5...1.5$ and $l_h/\ell_s \sim 0.4...3.6$. As there are also other materials with weak ferromagnetism, we also cannot exclude the other possibilities. In order to understand various properties of the domain wall motion induced from a spin current, we also consider these ratios outside of these ranges in the following discussions.

With the boundary conditions in Eq. (5) to Eq. (7) and in Eq. (8) to Eq. (10), we can solve the rotated spin diffusion equation in Eq. (4). They can be solved analytically (see Appendix B), but the solutions are in general quite lengthy. Rather, we plot the components of the spin accumulation for an example set of parameters as a function of position in Fig. 2(a,b). We can see that s_1^0 is a monotonously increasing (decreasing) function of position in region to the left (right) side of the domain wall, and reaches a minimum in the domain wall center. The second component of spin accumulation s_2^0 smoothly goes to zero away from the domain wall center. Compared to the spin accumulation in the case without the domain wall, s_3^0 changes sign in the domain wall region and exponentially decreases in region to the right of the domain wall.

The unrotated spin accumulation is given by Eq. (3). More specifically, we can write

$$s_1 = \cos\phi(s_1^0 \cos\theta + s_3^0 \sin\theta) - s_2^0 \sin\phi \tag{11}$$

$$s_2 = s_2^0 \cos\phi + \sin\phi(s_1^0 \cos\theta + s_3^0 \sin\theta) \tag{12}$$

$$s_3 = s_3^0 \cos\theta - s_1^0 \sin\theta. \tag{13}$$

The unrotated components of the spin accumulation are plotted for $\phi = 0$ in Fig. 2(c,d). Compared to the rotated solution, s_2 remains the same but s_1 changes sign on the two sides of the domain wall center, and s_3 also makes a difference compared to the case without the domain wall. In the next section, we use these spin accumulations to calculate the force and torque.

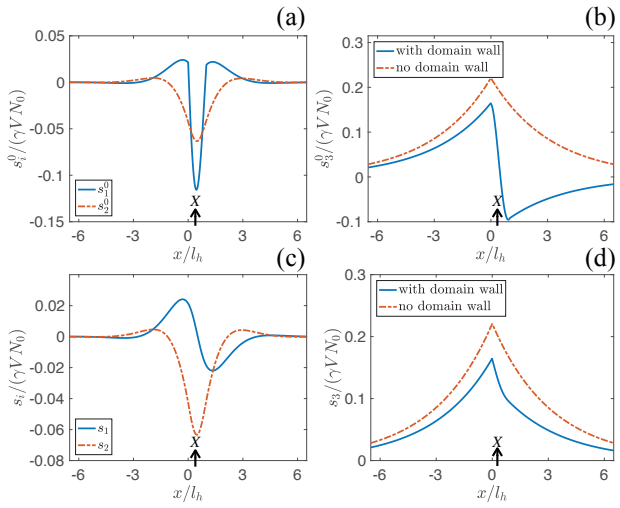

FIG. 2. Solutions of the spin diffusion equation. The solutions in the rotated space are shown in (a) and (b), and in the unrotated space are shown in (c) and (d). We also compare s_3^0 and s_3 with the spin accumulation in the case of homogeneous magnetization (no domain wall). Here the results are plotted for $\ell_s = 3.2l_h$, $P_I = 0.5$, $k_I l_h = 0.5$, and $\lambda = l_h$. The injector is placed at $x = 0$, whereas the domain wall center is at $X = 0.5\lambda$ marked in the figure.

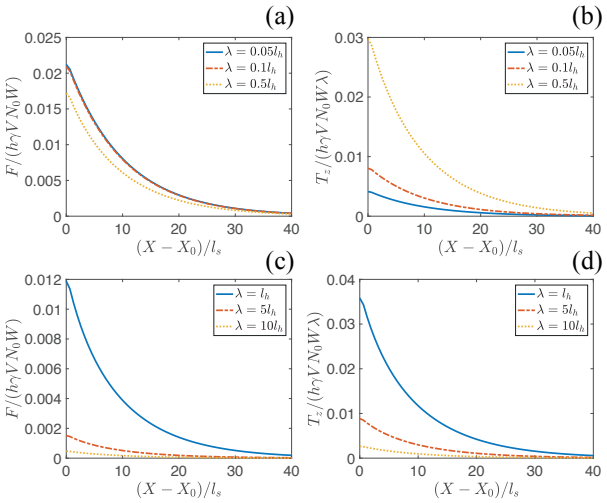

FIG. 3. Force and torque for smaller domain walls in (a,b), and for larger domain walls in (c,d), as a function of domain wall center position $X - X_0$, where $X_0 = \lambda/2$ is the shortest distance of the domain wall center to the right of the injector. Here the results are plotted for $\ell_s = 3.2l_h$, $P_I = 0.5$, and $k_I l_h = 0.5$.

III. FORCE AND TORQUE

The force and torque acting on the domain wall are given by[11,12]

$$F = -\int d^3z \nabla \boldsymbol{h} \cdot \boldsymbol{s} \tag{14}$$

$$T_z = -\int d^3z (\boldsymbol{h} \times \boldsymbol{s})_z, \tag{15}$$

where exchange field $\boldsymbol{h}$ is given in Eq. (1), and the components of the spin accumulation $\boldsymbol{s} = (s_1, s_2, s_3)$ are shown in Eq. (11) to Eq. (13). Substituting these to the force and torque in Eq. (14) and Eq. (15), we obtain

$$F = -\frac{h\pi W}{\lambda} \int dz s_1^0 \tag{16}$$

$$T_z = -hW \int dz s_2^0 \sin\theta, \tag{17}$$

where W is the cross sectional area of the weak ferromagnet.

The force and torque as a function of the domain wall position X are plotted in Fig. 3 for a few sets of parameters. The common feature of all the cases are that both decay exponentially as a function of X. This is due to the fact that the spin accumulation and the resulting spin current, which induces the domain wall motion, decays exponentially within the spin-relaxation length ℓ_s. These features are also very similar to the ones in Ref. 18. From Fig. 3(a,c), we can see that the force is independent of the domain wall size for small domain walls, and it is smaller for larger domain walls. On the other hand, the torque has a nonmonotonic dependence on the domain wall size λ, as shown in Fig. 3(b,d). It first increases as λ increases up to of the order of l_h, and then becomes smaller for larger domain walls. This is not the same with the case of current driven domain wall motion, where the torque is much larger than the force for larger domain walls.[12] This is due to the fact that when a spin relaxation length ℓ_s is smaller than the domain wall size λ ($\ell_s < \lambda$), due to the decaying spin current, less spins are transferred to the domain wall. This results in the smaller torque for larger domain wall sizes in Fig. 3(d).

The dependence of the force and the torque on the spin relaxation length are shown in Fig. 4. We can see that the torque is a monotonously decreasing function of the inverse relaxation length, i.e., decreasing spin relaxation increases the torque, as expected from the fact that torque results from spin transfer. On the other hand, the force is a non-monotonic function of l_h/ℓ_s. It also decays if the spin relaxation becomes strong (i.e., $l_h \gg \ell_s$). However, it also becomes small for a small magnetic length $l_h \ll l_s$. This is due to the fact that contrary to the torque, which within our model only comes from the domain wall region (that is where $\theta \neq 0$ in Eq. (17)), the force depends on the spin accumulation component s_1^0 also around the domain wall. However, for small l_h, this component oscillates rapidly, and thus the average force becomes small. Analogously, both the force and the torque become smaller

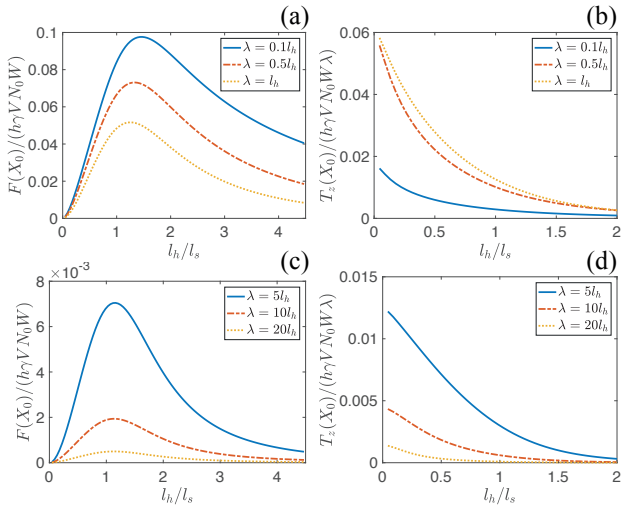

FIG. 4. Force and torque for smaller domain walls in (a,b), and for larger domain walls in (c,d), as a function of inverse spin relaxation length ℓ_s. Here the force and the torque are plotted for the domain wall position $X_0 = \lambda/2$. The parameters used in the calculations are $P_I = 0.5$ and $k_I l_h = 0.5$.

for larger λ/l_h. This is due to the oscillations of the spin accumulation inside the domain wall region.

In order to get a further insight on the relative magnitudes of the force and torque, we examine the adiabaticity parameter $\beta_s = \lambda F/T_z$ as a function of l_h/ℓ_s for different λ in Fig. 5. Since F and T_z both decay in the same manner, β_s is independent of the distance X from the injector. Comparing the values of β_s in Fig. 5(a) and (b), we can see that β_s is indeed smaller for larger domain walls, but the spin relaxation also plays an important role. We can see that $\beta_s \gg 1$ for strong spin relaxation, i.e., force is much larger than the torque. On the other hand, the torque is much larger than the force for large domain walls $\lambda \gtrsim l_h$, provided the spin relaxation length is also longer than l_h [Fig. 5(b)]. For small domain walls $\lambda \ll l_h$, β_s is proportional to λ^{-1}. We can estimate β_s in this limit for $l_h < \ell_s$ by

$$\beta_s = \frac{8}{\pi}\frac{l_h}{\lambda}\frac{l_h^2}{\ell_s^2}. \tag{18}$$

This is plotted in Fig. 5(a) as the black dashed curve.

This behavior can be compared to the case of strong ferromagnets in the ballistic limit[11]. There the only non-adiabaticity (non-vanishing β_s) comes from the finite λ_F/λ. The spin diffusion equation employed here assumes that the Fermi wavelength λ_F is much smaller than any other length scale. However, we see that in this case other length scales, such as l_h and ℓ_s govern the behavior of the adiabaticity parameter.

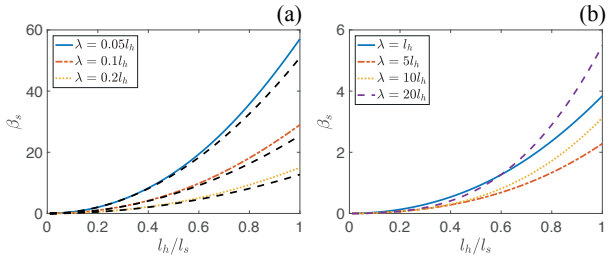

FIG. 5. Adiabaticity parameter β_s as a function of the inverse spin-relaxation length ℓ_s for different domain wall sizes. The results are plotted for $P_I = 0.5$ and $k_I l_h = 0.5$. The anlaytical estimate for β_s in Eq. (18) is shown as the black dashed curve in (a).

IV. DOMAIN WALL DYNAMICS

In the absence of an external pinning and a negligible domain wall mass,[29] the dynamic equations of domain wall motion are[11,12]

$$\dot{\phi} + \alpha_0 \frac{\dot{X}}{\lambda} = \frac{\lambda}{\hbar N S} F \tag{19}$$

$$\dot{X} - \alpha_0 \lambda \dot{\phi} = \frac{K_\perp \lambda}{2\hbar} S \sin(2\phi) + \frac{\lambda}{\hbar N S} T_z, \tag{20}$$

where ϕ is the out-of-plane angle in Eq. (1), α_0 is the Gilbert damping parameter of the local magnetization, $K_\perp$ is the perpendicular anisotropy energy, and S is the size of the localized spin. Also, $N = 2\lambda W/a_0^3$ is the number of spins in the domain wall, and a_0 is the lattice constant. The force and torque are given in Eq. (14) and in Eq. (15), respectively.

The unit of F and T_z/λ is $h\gamma V N_0 W$. In order to make the dynamic equations dimensionless, we multiply

$$t_0 = \frac{\hbar N S}{\lambda h \gamma V N_0 W} = \frac{2\hbar S}{a_0^3 N_0 h \gamma V}$$

to both sides of Eq. (19) and Eq. (20), and after reorganizing the terms, write

$$\frac{\dot{X}}{\lambda} = \frac{1}{1+\alpha_0^2}\left[\alpha_0 f + \frac{\tau_z}{\lambda} + k_\perp \sin(2\phi)\right] \tag{21}$$

$$\dot{\phi} = \frac{1}{1+\alpha_0^2}\left[f - \alpha_0 \frac{\tau_z}{\lambda} - \alpha_0 k_\perp \sin(2\phi)\right]. \tag{22}$$

Here we defined

$$f = -\frac{\pi}{\lambda \gamma V N_0} \int dx s_1^0$$

$$\tau_z = -\frac{1}{\gamma V N_0} \int dx s_2^0 \sin\theta$$

$$k_\perp = \frac{K_\perp S^2}{a_0^3 N_0 h\gamma V}.$$

We first discuss the case where the force is much larger than the torque ($\beta_s \gtrsim 1$). We can see from Fig. 5 that this is the case for small domain walls and large domain walls with strong spin relaxation $l_h \gg \ell_s$. For convenience we consider a small domain wall $\lambda \ll l_h$. The full numerical solutions of the dynamic equations of domain wall motion in Eq. (21) and Eq. (22) are shown in Fig. 6.

If the force is a constant $f = f_0$ in the absence of the torque, Eq. (22) yields $\dot\phi = 0$ for $f_0 < \alpha_0 k_\perp$. Then the domain wall moves with a constant velocity and a constant out-of-plane angle

$$\dot X = \frac{\lambda f_0}{\alpha_0}, \tag{23}$$

$$\phi = \frac{1}{2}\arcsin\left(\frac{f_0}{\alpha_0 k_\perp}\right). \tag{24}$$

In the spin current induced domain wall motion, the force decays as a function of the domain wall position X. If we write the force as $f = f_0 e^{-X/\ell_s}$, then $\dot\phi \to 0$ for $t \to \infty$, and this yields

$$\dot X = \frac{\lambda f_0}{\alpha_0} e^{-X/\ell_s}. \tag{25}$$

This equation can be solved as

$$X = X(0) + \ell_s \log\left[1 + \frac{f_0 \lambda t}{\ell_s \alpha_0}\right],$$

and

$$\dot X = \frac{f_0 \ell_s \lambda}{\ell_s \alpha_0 + f_0 \lambda t},$$

where $X(0)$ is the domain wall position where $\dot\phi \to 0$. This is exemplified by the curves in Fig. 6(a,b). There, the blue curve shows the behavior in the case where the force is everywhere below $\alpha_0 k_\perp$, and where $\dot\phi \to 0$ at around $t \approx 200 t_0$. From Eq. (22), we can also determine

$$\phi = \frac{1}{2}\arcsin\left[\frac{f_0 \ell_s}{k_\perp}\frac{e^{-X(0)/\ell_s}}{\ell_s\alpha_0 + f_0\lambda t}\right]. \tag{26}$$

If $f_0 > \alpha_0 k_\perp$, the constant force leads to an oscillatory domain wall velocity. This is known as the Walker breakdown.[30] The red dash-dotted curve in Fig. 6 shows the situation where the force is initially above this threshold, and only as the domain wall has moved further from the injector f gets below this threshold (around $t \gtrsim 1000 t_0$). After that the domain wall motion follows Eq. (25).

From Fig. 5, we can see that the torque is much larger than the force for large domain walls and weak spin relaxation. In the case of a constant torque in the absence of the force, the domain wall does not move if $\tau_z^0 < k_\perp \lambda$. The reason is that the perpendicular anisotropy energy

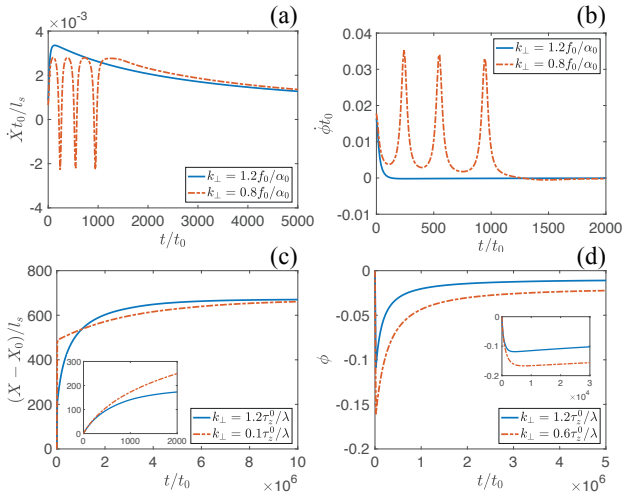

FIG. 6. Full numerical solutions of the dynamic equations of domain wall motion in Eq. (21) and Eq. (22). The case where the force is much larger than the torque is shown in (a,b), and the one where the torque is much larger than the force is shown in (c,d). In (a,b) we use $\lambda = 0.01 l_h$ and $\ell_s = 3.2 l_h$. In (c,d) $\lambda = 20 l_h$ and $\ell_s = 14 l_h$. The other parameters used in the calculations are $P_I = 0.5$, $k_I l_h = 0.5$, $X_0 = \lambda/2$, and $\alpha_0 = 0.2$. In the inset of (c,d), the results are shown for a smaller time scale.

described by the coefficient $k_\perp$ absorbs the torque completely. This is known as intrinsic pinning.[11] Otherwise, if $\tau_z^0 > k_\perp \lambda$, the domain wall moves with a finite velocity. Similar to the force, we can write the torque as $\tau_z = \tau_z^0 e^{-X/\ell_s}$. When the torque decays until $\tau_z(X(t)) < k_\perp \lambda$ so that $\dot\phi \to 0$, the domain wall stops moving. It takes a longer time for a smaller $k_\perp$ to absorb the torque completely. The domain wall position and the out-of-plane angle ϕ as a function of time for a decaying torque are plotted in Fig. 6(c,d).

We next examine the domain wall motion in the presence of both force and torque ($\beta_s \approx 1$). In the case of constant force and torque, a small force is enough to destroy the intrinsic pinning. The domain wall moves with a constant velocity, see Eq. (23). This is also the case with decaying force and torque with $f_0/\alpha_0 > \tau_z^0/\lambda$, and the domain wall motion follows Eq. (25). We can use Eq. (22) to obtain ϕ for $\dot\phi \to 0$ as

$$\phi = \frac{1}{2}\arcsin\left[\frac{1}{k_\perp}\left(\frac{f_0}{\alpha_0} - \frac{\tau_z^0}{\lambda}\right)\frac{\alpha_0 \ell_s}{\ell_s\alpha_0 + f_0\lambda t} e^{-X(0)/\ell_s}\right]. \tag{27}$$

For $f_0/\alpha_0 < \tau_z^0/\lambda$, however, the dynamic equations result a negative ϕ, and this leads to $\dot X \to 0$. The numerical solutions of the dynamic equations of the domain wall motion in Eq. (21) and Eq. (22) in the presence of both force and torque are plotted in Fig. 7(a,b)

In the above discussions, the voltage at the injector is considered to be positive $V > 0$. If the voltage changes sign at some instant of time, then the sign of the force

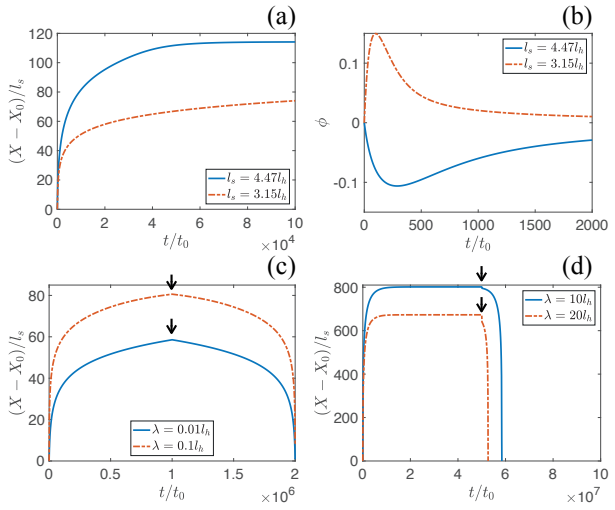

FIG. 7. Domain wall dynamics in the presence of both force and torque for different spin relaxation rates in (a,b). Forward and backward moving domain walls for different domain wall sizes in (c,d). In (a,b) we use $\lambda = l_h$. In (c) $\ell_s = 3.2l_h$, and in (d) $\ell_s = 14l_h$. The other parameters used in the calculations are $P_I = 0.5$, $k_I l_h = 0.5$, $X_0 = \lambda/2$, and $\alpha_0 = 0.2$. In the calculations we use $k_\perp = 1.2|f_0/\alpha_0 - \tau_z^0/\lambda|$. In (c,d) we use a small arrow to denote when the voltage changes sign.

and torque also changes, and they start pulling the domain wall instead of pushing it. This leads to the reversed motion of the domain wall. The reversed domain wall motion for small domain walls $\lambda < l_h$ are shown in Fig. 7(c). In this case, the domain wall reverses back to its original position $X = 0$ at an equal amount of time as the one needed to push it further. The reversed domain wall motion for large domain walls with weak spin relaxation is shown in Fig. 7(d). In this case the domain wall had stopped before the sign change of the injected spin current.

The above analysis is based on the dynamics described by Eqs. (19) and (20), with force and torque obtained from the solutions of the spin diffusion equations. Those equations were derived[12] by assuming a clean ferromagnet and an instant electronic response to the domain wall motion. It was recently shown[29] that taking into account the delayed electron dynamics, extra "inertial" terms proportional to $\ddot{\phi}$ and $\ddot{X}$ can also appear, leading for example to a hysteretic dynamics of the domain wall. The prefactor of those terms, an effective mass of the domain wall, is proportional to the time it takes for the electrons to traverse the domain wall width λ. If λ is large compared to the elastic mean free path, as assumed in the present manuscript, this effective mass is also likely to change from the ballistic limit considered in Ref. 29. This is why we did not yet consider its possible effect on the dynamics in the present manuscript.

V. DOMAIN WALL RESISTANCE

The current induced from the injector electrode is given by [see Appendix C, Eq. (C8)]

$$I = G[-\gamma V + P_I s_3(0)/N_0],$$

where G is the conductance of the injector. We can see from Appendix B that the spin accumulation is linear in the injection voltage V. Taking that into account allows us to include an extra resistance that depends on the relaxation of s_0 along the wire. In particular, we may study this extra resistance in the presence of the domain wall at position X, and without it (formally $X \to \infty$). This domain wall resistance provides a direct method to detect the domain wall motion.

If we denote the spin accumulation at the position of the injector as $s_3(0) = \mu_z P_I \gamma V N_0$, where $\mu_z = \mu_z(X, l_h, \ell_s, k_I, \lambda)$ is a dimensionless quantity, then the current through the contact can be written as $I = G(-1 + \mu_z P_I^2)\gamma V$. The spin accumulation thus adds a "spin resistance"

$$R_s = \frac{1}{G\mu_z P_I^2}. \tag{28}$$

The contribution of the domain wall to the spin resistance in Eq. (28) can be found by taking the difference of R_s with the resistance in the absence of the domain wall R_s^0 as $R_{\rm dw} = R_s - R_s^0$. Here

$$R_s^0 = \frac{1}{G\mu_z(X \to \infty)P_I^2} = \frac{2 + k_I \ell_s}{G P_I^2 k_I \ell_s},$$

where $\mu_z(X \to \infty)$ is determined from Eq. (B1), and k_I is the injector transparency. Again the analytic formula for $R_{\rm dw}$ is long, but we show its behavior for some selected parameters in Fig. 8.

We can see that the domain wall contribution to the resistance $R_{\rm dw}$ reduces exponentially as the domain wall moves away from the injector, as is natural due to the fact that $R_{\rm dw}$ depends on the size of the spin accumulation around the domain wall. Close to the injector $X = \lambda/2$ [Fig. 8(c)], the domain wall contribution is maximal for $l_h \ll \ell_s$ and for $\lambda \approx l_h$.

VI. CONCLUSION

In conclusion, we have studied the domain wall motion in weak ferromagnets in a non-local spin-injection setup. We have used a spin-diffusion equation to calculate the spin accumulation and evaluated the force and torque acting on the domain wall. Both decay exponentially as a function of domain wall position. We have studied the domain wall dynamics and have showed that the domain wall motion exhibits interesting features due to the decaying force and torque. For example, if the force close to the injector is larger than the torque and a threshold

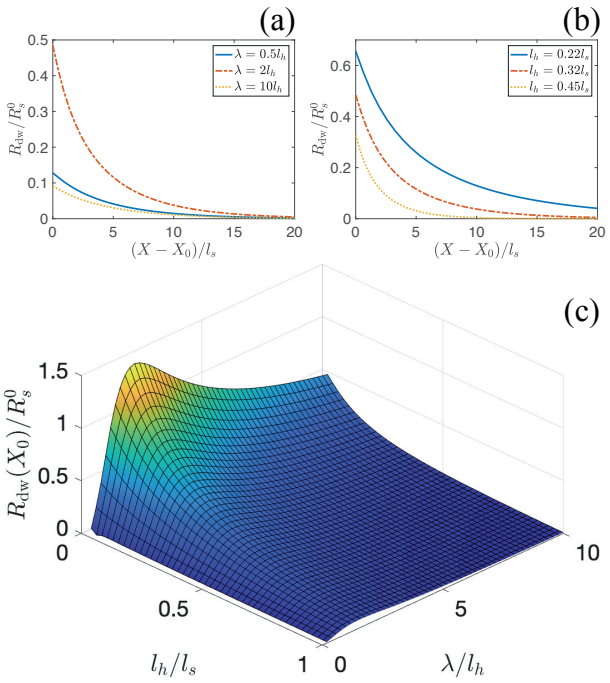

FIG. 8. The additional resistance $R_{\rm dw}$ introduced from the domain wall plotted as a function of the domain wall position in (a,b), and the dependence of the maximum $R_{\rm dw}$ at X_0 plotted as a function of λ and ℓ_s^{-1} in (c). In (a) $R_{\rm dw}$ is plotted for different domain wall sizes and $\ell_s = 3.2l_h$, and in (b) for different spin relaxation lengths for $\lambda = 2l_h$. The other parameters used in the calculations are $k_I l_h = 0.5$, $P_I = 0.5$, and $X_0 = \lambda/2$.

for Walker breakdown, the domain wall exhibits first an oscillatory dynamics, but further from the injector spin relaxation necessarily takes the force below that threshold value, resulting into an algebraically decaying domain wall speed. On the other hand, for a large torque close to the injector, compared to both the force and an intrinsic pinning value due to anisotropy, the relatively steady initial motion ceases when the torque becomes smaller than the intrinsic pinning value, and the domain wall essentially stops. Since the sign of both the force and the torque depend on the sign of the injection current, the domain wall motion can be reversed by reversing the sign of the current. This is why the pure spin current can also be used to pull the domain wall back towards the injector. Besides the analysis of the force and torque and their result on the dynamics, we have also described a means to detect the domain wall position via monitoring the injection resistance that depends on the domain wall position.

Our model is an alternative description of domain wall motion compared to majority of the models[12] dealing with essentially ballistic electron systems. In those cases the only relevant length scales are the domain wall size and the Fermi wavelength. We show how in disordered systems and weak ferromagnets there may be also other essential length scales governing the domain wall dynamics, especially the magnetic length l_h and the spin relaxation length ℓ_s. Our approach is made possible by the use of the spin diffusion equation also in the presence of inhomogeneous magnetism, which would not be straightforward when the spin polarization in the ferromagnet is large. To be able to use this equation, we hence need to assume weak ferromagnetism, which limits the applicability range of our approach. On the other hand, it provides hints on the types of effects expected also in the case of strong ferromagnets for which, to our knowledge, an analogous theory does not exist.

ACKNOWLEDGMENTS

We thank M. Silaev for discussions. This work was supported by the Academy of Finland project number 317118.

Appendix A: Spin diffusion equation

As a useful tool in describing the electronic transport properties of magnetic materials, we start by the spin dependent Boltzmann equation in the diffusive limit[22,31]

$$(\partial_t - D\nabla^2) f_z(\boldsymbol{r}, \epsilon, t) = -\frac{1}{\tau_s} f_z(\boldsymbol{r}, \epsilon, t), \qquad \text{(A1)}$$

where D is the diffusion constant (in a weak ferromagnet assumed independent of the spin index), $f_z = f_\uparrow - f_\downarrow$ and f_σ is the distribution function of electrons with spin $\sigma = \uparrow / \downarrow$, and τ_s is the spin-flip relaxation time. This equation has been widely used in spintronics, for example in the description of the spin accumulation at an interface between a ferromagnet and a nonmagnetic metal.[32]

In the case of an inhomogeneous exchange field, other spin components should be taken into account, and we can replace f_s by $\boldsymbol{f} \cdot \boldsymbol{\sigma} = (f_x, f_y, f_z) \cdot \boldsymbol{\sigma}$, where $\boldsymbol{\sigma} = (\sigma_1, \sigma_2, \sigma_3)$ is a vector of Pauli spin matrices. Considering the Heisenberg equation of motion for $\boldsymbol{f} \cdot \boldsymbol{\sigma}$, and substituting back to the Boltzmann equation (see a similar derivation in Refs. 33 and 34, except that those articles write an opposite sign of the Zeeman energy term) we obtain for a steady state

$$D\nabla^2 \boldsymbol{f} = \frac{1}{\tau_s} \boldsymbol{f} + \frac{i}{\hbar} \left[\frac{g\mu_B}{2} \boldsymbol{B} \cdot \boldsymbol{\sigma}, \boldsymbol{f} \cdot \boldsymbol{\sigma} \right],$$

where the other component of the commutator is the Zeeman energy. There, $g = 2$ is the g-factor, μ_B is the Bohr magneton, and $\boldsymbol{B}$ is the magnetic field. By denoting $\boldsymbol{h} = g\mu_B \boldsymbol{B}/2$ and reorganizing the terms, we obtain

$$\hbar D\nabla^2 \boldsymbol{f} = \frac{\hbar}{\tau_s} \boldsymbol{f} - 2\boldsymbol{h} \times \boldsymbol{f},$$

where we used the relation $(\boldsymbol{a} \cdot \boldsymbol{\sigma})(\boldsymbol{b} \cdot \boldsymbol{\sigma}) = 2i(\boldsymbol{a} \times \boldsymbol{b})$. This equation is an extension of Eq. (A1) to the case with

inhomogeneous magnetization, as it reduces to Eq. (A1) for the case of homogeneous magnetization in the steady state.

Integrating over energy on the two sides, we finally obtain the spin-diffusion equation

$$\hbar D\nabla^2 \boldsymbol{s} = \frac{\hbar}{\tau_s}\boldsymbol{s} - 2\boldsymbol{h}\times\boldsymbol{s}, \tag{A2}$$

where

$$\boldsymbol{s}(\boldsymbol{r}) = N_0 \int d\epsilon \boldsymbol{f}(\boldsymbol{r},\epsilon)$$

is the spin accumulation at position $\boldsymbol{r}$. The spin diffusion equation was used to describe the spin Hanle effect in ferromagnet-normal metal-ferromagnet systems.[33,35,36] Here we use it to calculate the spin accumulation in a weak ferromagnet, including the Hanle effect from the inhomogeneous exchange field.

The spin current is given by the derivative of the spin accumulation

$$\boldsymbol{j}(\boldsymbol{r}) = \hbar D\nabla \boldsymbol{s}(\boldsymbol{r}).$$

The spin current is a tensor, as it depends on position for all three spin components. This spin current plays an important role in the domain wall motion.

Appendix B: Spin accumulation with inhomogenous magnetization

Since the rotation angle in Eq. (2) is a step function, the spin diffusion equation in Eq. (4) is separated into three regions. On the left and right side of the domain wall, the general solution of Eq. (4) is given by

$$s_1^0 = \frac{1}{\eta}\{\cosh(z\eta\nu)\left[\eta C_{1i}\cos(z\eta\mu) + (\mu C_{2i} + \nu C_{4i})\sin(z\eta\mu)\right] + \left[(\nu C_{2i} - \mu C_{4i})\cos(z\eta\mu) + \eta C_{3i}\sin(z\eta\mu)\right]\sinh(z\eta\nu)\}$$

$$s_2^0 = \frac{1}{\eta}\{\cosh(z\eta\nu)\left[\eta C_{3i}\cos(z\eta\mu) + (-\nu C_{2i} + \mu C_{4i})\sin(z\eta\mu)\right] + \left[(\mu C_{2i} + \nu C_{4i})\cos(z\eta\mu) - \eta C_{1i}\sin(z\eta\mu)\right]\sinh(z\eta\nu)\}$$

$$s_3^0 = e^{z/\ell_s}C_{5i} + e^{-z/\ell_s}C_{6i},$$

where $i = 1, 3$ refers to the left and right side of the domain wall, and C_{ni} are constants which are determined from the boundary conditions. Here we also defined

$$\eta = \left[\frac{4}{l_h^4} + \frac{1}{\ell_s^4}\right]^{1/4}$$

$$\mu = \sin\left[\frac{1}{2}\arctan\left(\frac{2\ell_s^2}{l_h^2}\right)\right]$$

$$\nu = \cos\left[\frac{1}{2}\arctan\left(\frac{2\ell_s^2}{l_h^2}\right)\right].$$

In the domain wall region the solutions are given by

$$\begin{aligned} s_1^0 = &-\frac{C_{12}e^{zk_1}[\alpha^2 + \ell_s^{-2} - k_1^2]}{2\alpha\sqrt{N_1}k_1} + \frac{C_{22}e^{-zk_1}[\alpha^2 + \ell_s^{-2} - k_1^2]}{2\alpha\sqrt{N_1}k_1} - \frac{C_{32}e^{zk_2}[\alpha^2 + \ell_s^{-2} - k_2^2]}{2\alpha\sqrt{N_2}k_2} \\ &+ \frac{C_{42}e^{-zk_2}[\alpha^2 + \ell_s^{-2} - k_2^2]}{2\alpha\sqrt{N_2}k_2} - \frac{C_{52}e^{zk_2^*}[\alpha^2 + \ell_s^{-2} - k_2^{*2}]}{2\alpha\sqrt{N_2}k_2^*} + \frac{C_{62}e^{-zk_2^*}[\alpha^2 + \ell_s^{-2} - k_2^{*2}]}{2\alpha\sqrt{N_2}k_2^*} \end{aligned}$$

$$s_2^0 = \frac{C_{12}e^{zk_1}al_h^2}{36\alpha\beta^2\sqrt{N_1}k_1} - \frac{C_{22}e^{-zk_1}al_h^2}{36\alpha\beta^2\sqrt{N_1}k_1} + \frac{C_{32}e^{zk_2}bl_h^2}{72\alpha\beta^2\sqrt{N_2}k_2} - \frac{C_{42}e^{-zk_2}bl_h^2}{72\alpha\beta^2\sqrt{N_2}k_2} + \frac{C_{52}e^{zk_2^*}b^*l_h^2}{72\alpha\beta^2\sqrt{N_2}k_2^*} - \frac{C_{62}e^{-zk_2^*}b^*l_h^2}{72\alpha\beta^2\sqrt{N_2}k_2^*}$$

$$s_3^0 = \frac{C_{12}e^{zk_1}}{\sqrt{N_1}} + \frac{C_{22}e^{-zk_1}}{\sqrt{N_1}} + \frac{C_{32}e^{zk_2}}{\sqrt{N_2}} + \frac{C_{42}e^{-zk_2}}{\sqrt{N_2}} + \frac{C_{52}e^{zk_2^*}}{\sqrt{N_2}} + \frac{C_{62}e^{-zk_2^*}}{\sqrt{N_2}},$$

where

$$\alpha = \frac{\pi}{\lambda}$$

$$\beta = \left[\alpha^6 + \frac{90\alpha^2}{l_h^4} + \frac{36\alpha^4}{\ell_s^2} + \frac{1}{2}\sqrt{-4\left(\alpha^4 - \frac{12}{l_h^4} - \frac{12\alpha^2}{\ell_s^2}\right)^3 + 4\left(\alpha^6 + \frac{90\alpha^2}{l_h^4} + \frac{36\alpha^4}{\ell_s^2}\right)^2}\right]^{1/3}$$

and

$$k_1 = \sqrt{\frac{1}{3}\left[-2\alpha^2 + \beta + \frac{3}{\ell_s^2} + \frac{\alpha^4 - 12/l_h^4 - 12\alpha^2/\ell_s^2}{\beta}\right]}$$

$$k_2 = \sqrt{\frac{1}{12}\left[-8\alpha^2 + 2i(i+\sqrt{3})\beta + \frac{12}{\ell_s^2} + \frac{2(1+i\sqrt{3})(-\alpha^4 + 12/l_h^4 + 12\alpha^2/\ell_s^2)}{\beta}\right]}$$

are the solutions of the following characteristic equation

$$\alpha^4\left(k^2 - \frac{1}{\ell_s^2}\right) + \left[\frac{4}{l_h^4} + \left(k^2 - \frac{1}{\ell_s^2}\right)^2\right]\left(k^2 - \frac{1}{\ell_s^2}\right) - 2\alpha^2\left[\frac{2}{l_h^4} - k^4 + \frac{1}{\ell_s^4}\right] = 0.$$

The other coefficients are

$$a = \left[\alpha^4 + \alpha^2\beta + \beta^2 - \frac{12}{l_h^4}\right]^2 + \frac{12\alpha^2}{\ell_s^2}\left[-2\alpha^4 - 2\alpha^2\beta + \beta^2 + \frac{24}{l_h^4}\right] + \frac{144\alpha^4}{\ell_s^4}$$

$$\begin{aligned} b =& -(1-i\sqrt{3})\alpha^8 - (1+i\sqrt{3})\beta^4 - \frac{48\beta^2}{l_h^4} - \frac{144(1-i\sqrt{3})}{l_h^8} + \alpha^6\left[-2\left(1+i\sqrt{3}\right)\beta + \frac{24}{\ell_s^2}\left(1-i\sqrt{3}\right)\right] \\ &+ 2\alpha^2\left[-(1-i\sqrt{3})\beta^3 + \frac{12(1+i\sqrt{3})\beta}{l_h^4} + \frac{12\beta^2}{\ell_s^2} - \frac{144(1-i\sqrt{3})}{l_h^4\ell_s^2}\right] \\ &+ 6\alpha^4\left[\beta^2 + \frac{4(1+i\sqrt{3})\beta}{\ell_s^2} + 4(1-i\sqrt{3})\left(\frac{1}{l_h^4} - \frac{6}{\ell_s^4}\right)\right] \end{aligned}$$

$$N_1 = \frac{(1+l_h^2k_1^2)\left\{a^2l_h^4 + 324\beta^4\left[\alpha^4 - (k_1^2 - \ell_s^{-2})^2 + 2\alpha^2(k_1^2 + \ell_s^{-2})\right]\right\}}{1296\alpha^2\beta^4k_1^2}$$

$$N_2 = \frac{(1+l_h^2|k_2|^2)\left\{|b|^2l_h^4 + 1296\beta^4\left[\alpha^4 + |k_2^2|^2 - \ell_s^{-4} - 2\ell_s^{-2}\mathrm{Re}(k_2^2) + \alpha^2(2\ell_s^{-2} - 2\mathrm{Re}(k_2^2) + 4|k_2|^2)\right]\right\}}{5184\alpha^2\beta^4|k_2|^2}.$$

The unknown coefficients are determined from the boundary conditions. Although one can determine $C_{51} = C_{53} = 0$ straightforwardly, since s_3^0 only decays as a function of domain wall position, other components have too long expressions to be printed here and rather have to be shown numerically.[37] We plot some of the coefficients for different values of the domain wall size λ in Fig. 9.

The solutions also yield $C_{52} = C_{32}^*$ and $C_{62} = C_{42}^*$, which also imply real-valued spin accumulation. Moreover, the coefficients in region $i = 3$ are very similar with those in region $i = 1$, but with opposite signs (C_{13}, C_{33} and C_{63}). For $X \gg \ell_s$, we also find

$$C_{61} = -C_{63} = \frac{k_I\ell_sP_IVN_0}{2 + k_I\ell_s}, \tag{B1}$$

but in general the expression is more complicated.

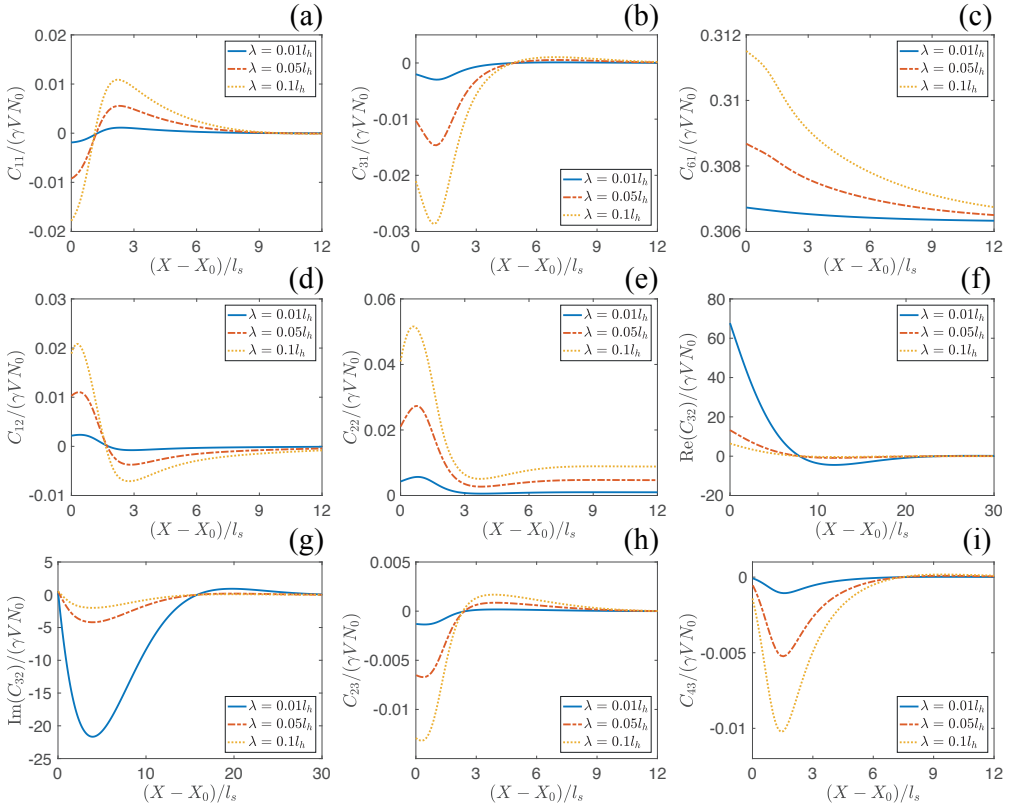

FIG. 9. Coefficients in the general solutions of the spin diffusion equation. Here the results are plotted for $\ell_s = 3.2l_h$, $P_I = 0.5$, $k_I l_h = 0.5$, and $X_0 = \lambda/2$.

The solutions in the domain wall region can hence be written as

$$s_1^0 = -\frac{\alpha^2 + \ell_s^{-2} - k_1^2}{2\alpha\sqrt{N_1}k_1}\left(C_{12}e^{zk_1} - C_{22}e^{-zk_1}\right) - \mathrm{Re}\left[\frac{\alpha^2 + \ell_s^{-2} - k_2^2}{\alpha\sqrt{N_2}k_2}\left(C_{32}e^{zk_2} - C_{42}e^{-zk_2}\right)\right] \tag{B2}$$

$$s_2^0 = \frac{al_h^2}{36\alpha\beta^2\sqrt{N_1}k_1}\left(C_{12}e^{zk_1} - C_{22}e^{-zk_1}\right) + \mathrm{Re}\left[\frac{bl_h^2}{36\alpha\beta^2\sqrt{N_2}k_2}\left(C_{32}e^{zk_2} - C_{42}e^{-zk_2}\right)\right] \tag{B3}$$

$$s_3^0 = \frac{1}{\sqrt{N_1}}\left(C_{12}e^{zk_1} + C_{22}e^{-zk_1}\right) + \frac{2}{\sqrt{N_2}}\mathrm{Re}\left(C_{32}e^{zk_2} + C_{42}e^{-zk_2}\right). \tag{B4}$$

The unrotated spin accumulation is given by the transformation in Eq. (3). We use these results to calculate the force and torque in the equations of domain wall motion.

Appendix C: Description of the injector

We consider the case where the spin polarized current is injected to the weak ferromagnet from a strong ferromagnet attached to it a position $z = 0$. Since we assume the injector magnetization to be homogeneous, we can write the spin diffusion equation separately in the two spin directions collinear with the magnetization of the strong ferromagnet. If we assume that the current is injected into the weak ferromagnet from a wire placed in the y direction, the spin-diffusion equation in the injector becomes[34]

$$\partial_y^2 s_\sigma^I = \frac{s_\sigma^I - s_{\bar{\sigma}}^I}{2l_\sigma^2},$$

where $\bar{\sigma}$ is the opposite spin to $\sigma = \uparrow / \downarrow$ and $l_\sigma = \sqrt{D_\sigma \tau_\sigma}$ is the spin-dependent spin relaxation length. The general

solution of this equation can be written as

$$s^I_{\uparrow/\downarrow} = \frac{l^2_\downarrow(C_1 + C_2 y) + l^2_\uparrow(C_3 + C_4 y)}{l^2_{\rm tot}} \pm \frac{l^2_{\downarrow/\uparrow}}{l^2_{\rm tot}}\left[(C_3 - C_1)\cosh\left(\frac{y}{l}\right) + l(C_4 - C_2)\sinh\left(\frac{y}{l}\right)\right],$$

where $l^2_{\rm tot} = l^2_\uparrow + l^2_\downarrow$ and $l = \sqrt{2} l_\uparrow l_\downarrow / l_{\rm tot}$. The unknown coefficients can be determined from the boundary condition[31]

$$\sigma^I_{\uparrow/\downarrow} A_T \partial_y s^I_{\uparrow/\downarrow}(0) = \frac{1}{R_I}\left[s^w_{\uparrow/\downarrow}(0) - s^I_{\uparrow/\downarrow}(0)\right], \qquad \text{(C1)}$$

where $\sigma^I_\sigma = e^2 N_\sigma D_\sigma$ is the spin dependent conductivity in the injector, N_σ is the density of states of spin σ at the Fermi level, A_T is the cross-sectional area of the tunnelling junction, R_I is the resistance of the contact between the injector and the wire, and s^w_σ is the spin density for spin σ created at the weak ferromagnet. If the voltage is applied at a distance L away from the contact, then we have two more boundary conditions

$$s^I_\uparrow(-L) + s^I_\downarrow(-L) = V N_0$$

$$s^I_\uparrow(-L) - s^I_\downarrow(-L) = 0,$$

where the upper equation states that the average potential of the electrons at the distance L is V ($e = 1$), and the lower indicates the vanishing of the spin accumulation in the electrode where the voltage is applied.

With the determined coefficients, we can write the chemical potential and the spin accumulation at the position of injection by assuming $\tanh(L/l) \to 1$, valid when $L \gg l$

$$\mu_I(0) N_0 = s^I_\uparrow(0) + s^I_\downarrow(0) = \frac{a_I l l^2_{\rm tot}\left[V\sigma^I_\downarrow + 2a_I L \mu_w(0)\right] N_0 + 2a_I(2Ll^2_\uparrow - l l^2_{\rm min})\sigma^I_\downarrow s^w_\uparrow(0) + \sigma^I_\uparrow\left[l^2_{\rm tot} V N_0\left(a_I l + 2\sigma^I_\downarrow\right) + 2a_I\left(2Ll^2_\downarrow + l l^2_{\rm min}\right) s^w_\downarrow(0)\right]}{2a_I\left[a_I l L l^2_{\rm tot} + \left(Ll^2_\uparrow + l l^2_\downarrow\right)\sigma^I_\downarrow\right] + 2\sigma^I_\uparrow\left[a_I\left(Ll^2_\downarrow + l l^2_\uparrow\right) + l^2_{\rm tot}\sigma^I_\downarrow\right]} \qquad \text{(C2)}$$

$$s^I_3(0) = s^I_\uparrow(0) - s^I_\downarrow(0) = \frac{a_I l l^2_{\rm tot}\left\{\sigma^I_\uparrow\left[V N_0 - 2s^w_\downarrow(0)\right] - \sigma^I_\downarrow\left[V N_0 - 2s^w_\uparrow(0)\right] + 2a_I L s^w_3(0)\right\}}{2a_I\left[a_I l L l^2_{\rm tot} + \left(Ll^2_\uparrow + l l^2_\downarrow\right)\sigma^I_\downarrow\right] + 2\sigma^I_\uparrow\left[a_I\left(Ll^2_\downarrow + l l^2_\uparrow\right) + l^2_{\rm tot}\sigma^I_\downarrow\right]}, \qquad \text{(C3)}$$

where $a_I = 1/(R_I A_T)$ and $l^2_{\rm min} = l^2_\uparrow - l^2_\downarrow$. Here we also defined the chemical potential and the spin accumulation in the weak ferromagnet as $\mu_w(0) N_0 = s^w_\uparrow(0) + s^w_\downarrow(0)$ and $s^w_3(0) = s^w_\uparrow(0) - s^w_\downarrow(0)$.

We assume for simplicity that the injector and the weak ferromagnetic wire cross sections are equal. Defining the injector transparency $\kappa_I = 1/(\sigma^w R_I A_T)$, we can write the boundary condition analogous to Eq. (C1) for the weak ferromagnet wire as

$$\partial_z s^w_{\uparrow/\downarrow}(0) = \kappa_I\left[s^w_{\uparrow/\downarrow}(0) - s^I_{\uparrow/\downarrow}(0)\right],$$

where σ^w is the conductivity in the weak ferromagnet. We then write this boundary condition in terms of $\mu_w(0)$ and $s^w_3(0)$, and choose the zero point of potential so that $\mu_w(0) = 0$. By substituting $s^I_{\uparrow/\downarrow}(0)$ in Eq. (C2) and Eq. (C3), we obtain for $l_\uparrow = l_\downarrow$

$$\begin{pmatrix}\partial_z \mu_w(0) N_0 \\ \partial_z s^w_3(0)\end{pmatrix} = \kappa_I \begin{pmatrix} \frac{a_I l \sigma^I_F}{\delta} & \frac{a_I L \sigma^I_F + \sigma^I_\uparrow \sigma^I_\downarrow}{\delta}\frac{\sigma^I_\uparrow - \sigma^I_\downarrow}{\sigma^I_\uparrow + \sigma^I_\downarrow} \\ \frac{a_I l \sigma^I_F}{\delta}\frac{\sigma^I_\uparrow - \sigma^I_\downarrow}{\sigma^I_\uparrow + \sigma^I_\downarrow} & \frac{a_I L \sigma^I_F + \sigma^I_\uparrow \sigma^I_\downarrow}{\delta} \end{pmatrix} \begin{pmatrix} -V N_0 \\ s^w_3(0)\end{pmatrix},$$

where $\sigma^I_F = (\sigma^I_\uparrow + \sigma^I_\downarrow)/2$, and $\delta = a^2_I L l + a_I(L + l)\sigma^I_F + \sigma^I_\uparrow \sigma^I_\downarrow$.

This equation leads to an Onsager relation for the current through the contact

$$\begin{pmatrix}\partial_z \mu_w(0) N_0 \\ \partial_z s^w_3(0)\end{pmatrix} = \begin{pmatrix} k_I & P_I k_I \\ P_I k_I & k_I \end{pmatrix} \begin{pmatrix} -\gamma V N_0 \\ s^w_3(0)\end{pmatrix}, \qquad \text{(C4)}$$

where the injector polarization and transparency are defined as

$$P_I = \frac{\sigma_\uparrow^I - \sigma_\downarrow^I}{\sigma_\uparrow^I + \sigma_\downarrow^I} \tag{C5}$$

$$\begin{aligned} k_I &= \kappa_I \frac{a_I L \sigma_F^I + (\sigma_F^I)^2(1-P_I^2)}{\delta} \\ &= \frac{1}{\sigma^w} \frac{L\sigma_F^I + (\sigma_F^I)^2(1-P_I^2)R_I A_T}{Ll + (L+l)\sigma_F^I R_I A_T + (\sigma_F^I)^2(1-P_I^2)R_I^2 A_T^2} \\ &\xrightarrow{R_I \ll l\sigma_{\uparrow/\downarrow}^I/A_T} \frac{\sigma_F^I}{\sigma^w l} \end{aligned} \tag{C6}$$

$$\gamma = \frac{a_I l}{a_I L + \sigma_F^I(1-P_I^2)} = \frac{l}{L + \sigma_F^I R_I A_T (1-P_I^2)}. \tag{C7}$$

The second row of Eq. (C4) yields the boundary condition for the spin-diffusion equation, whereas the first row in the Onsager relation yields the current through the contact. Multiplying the first row by $\sigma^w W/N_0$, where W is the cross-sectional area of the weak ferromagnet, we obtain

$$I = G[-\gamma V + P_I s_3^w(0)/N_0], \tag{C8}$$

where

$$I = \sigma^w W \partial_z \mu_w(0)$$

and

$$G = k_I \sigma^w W.$$

Since $s_3^w(0)$ is linear in VN_0 as shown in Eq. (B1), the spin accumulation contributes an additional resistance to the total resistance.

* faluke.aikebaier@jyu.fi

[1] S. S. P. Parkin, M. Hayashi, and L. Thomas, Science **320**, 190 (2008).
[2] L. Berger, Journal of Applied Physics **49**, 2156 (1978).
[3] L. Berger, Journal of Applied Physics **55**, 1954 (1984).
[4] L. Berger, Journal of Applied Physics **71**, 2721 (1992).
[5] L. Berger, Phys. Rev. B **54**, 9353 (1996).
[6] J. Grollier, D. Lacour, V. Cros, A. Hamzic, A. Vaurs, A. Fert, D. Adam, and G. Faini, Journal of Applied Physics **92**, 4825 (2002).
[7] J. Grollier, P. Boulenc, V. Cros, A. Hamzić, A. Vaurès, A. Fert, and G. Faini, Applied Physics Letters **83**, 509 (2003).
[8] M. Kläui, C. A. F. Vaz, J. A. C. Bland, W. Wernsdorfer, G. Faini, E. Cambril, and L. J. Heyderman, Applied Physics Letters **83**, 105 (2003).
[9] N. Vernier, D. A. Allwood, D. Atkinson, M. D. Cooke, and R. P. Cowburn, Europhysics Letters (EPL) **65**, 526 (2004).
[10] A. Yamaguchi, T. Ono, S. Nasu, K. Miyake, K. Mibu, and T. Shinjo, Phys. Rev. Lett. **92**, 077205 (2004).
[11] G. Tatara and H. Kohno, Phys. Rev. Lett. **92**, 086601 (2004).
[12] G. Tatara, H. Kohno, and J. Shibata, Physics Reports **468**, 213 (2008).
[13] M. Laufenberg, W. Bührer, D. Bedau, P.-E. Melchy, M. Kläui, L. Vila, G. Faini, C. A. F. Vaz, J. A. C. Bland, and U. Rüdiger, Phys. Rev. Lett. **97**, 046602 (2006).
[14] F. Junginger, M. Kläui, D. Backes, U. Rüdiger, T. Kasama, R. E. Dunin-Borkowski, L. J. Heyderman, C. A. F. Vaz, and J. A. C. Bland, Applied Physics Letters **90**, 132506 (2007).
[15] D. Ilgaz, J. Nievendick, L. Heyne, D. Backes, J. Rhensius, T. A. Moore, M. A. Niño, A. Locatelli, T. O. Menteş, A. v. Schmidsfeld, A. v. Bieren, S. Krzyk, L. J. Heyderman, and M. Kläui, Phys. Rev. Lett. **105**, 076601 (2010).
[16] N. Motzko, B. Burkhardt, N. Richter, R. Reeve, P. Laczkowski, W. Savero Torres, L. Vila, J.-P. Attané, and M. Kläui, Phys. Rev. B **88**, 214405 (2013).
[17] A. Pfeiffer, R. M. Reeve, M. Voto, W. Savero-Torres, N. Richter, L. Vila, J. P. Attané, L. Lopez-Diaz, and M. Kläui, Journal of Physics: Condensed Matter **29**, 085802 (2017).
[18] K. Hosono, J. Shibata, H. Kohno, and Y. Nozaki, Phys. Rev. B **87**, 094404 (2013).
[19] S. Zhang and Z. Li, Phys. Rev. Lett. **93**, 127204 (2004).
[20] A. Thiaville, Y. Nakatani, J. Miltat, and Y. Suzuki, Europhysics Letters (EPL) **69**, 990 (2005).
[21] Y. Ban and G. Tatara, Phys. Rev. B **80**, 184406 (2009).
[22] T. Valet and A. Fert, Phys. Rev. B **48**, 7099 (1993).
[23] F. Aikebaier, P. Virtanen, and T. Heikkilä, Phys. Rev. B **99**, 104504 (2019).
[24] E. Wohlfarth (Elsevier, 1980) pp. 1 – 70.
[25] V. A. Oboznov, V. V. Bolginov, A. K. Feofanov, V. V. Ryazanov, and A. I. Buzdin, Physical review letters **96**, 197003 (2006).
[26] V. V. Ryazanov, V. A. Oboznov, A. Y. Rusanov, A. V. Veretennikov, A. A. Golubov, and J. Aarts, Phys. Rev. Lett. **86**, 2427 (2001).
[27] D. López González, Y. Shirahata, B. Van de Wiele, K. J. A. Franke, A. Casiraghi, T. Taniyama, and S. van Dijken, AIP Advances **7**, 035119 (2017).
[28] S.-Y. Hsu, P. Holody, R. Loloee, J. M. Rittner, W. P. Pratt, and P. A. Schroeder, Phys. Rev. B **54**, 9027 (1996).
[29] H. M. Hurst, V. Galitski, and T. T. Heikkilä, arXiv:1908.02299 (2019).
[30] N. L. Schryer and L. R. Walker, Journal of Applied Physics **45**, 5406 (1974).
[31] T. Heikkilä, *The Physics of Nanoelectronics: Transport and Fluctuation Phenomena at Low Temperatures*, Oxford Master Series in Physics (OUP Oxford, 2013).
[32] P. C. van Son, H. van Kempen, and P. Wyder, Phys. Rev. Lett. **58**, 2271 (1987).
[33] D. Huertas Hernando, Y. V. Nazarov, A. Brataas, and G. E. W. Bauer, Phys. Rev. B **62**, 5700 (2000).
[34] A. Brataas, G. E. Bauer, and P. J. Kelly, Phys. Rep. **427**, 157 (2006).
[35] F. J. Jedema, A. Filip, and B. Van Wees, Nature **410**, 345 (2001).

[36] F. J. Jedema, M. S. Nijboer, A. T. Filip, and B. J. van Wees, Phys. Rev. B **67**, 085319 (2003).

[37] The Mathematica codes used to solve for the coefficients will be provided together with the published paper.